

School of Earth and Planetary Sciences

Precise Orbit Determination of CubeSats

Amir Allahvirdizadeh

0000-0002-3722-4417

**This thesis is presented for the Degree of
Doctor of Philosophy
of
Curtin University**

July 2022

Declaration

To the best of my knowledge and belief, this thesis contains no material previously published by any other person except where due acknowledgment has been made. This thesis contains no material which has been accepted for the award of any other degree or diploma in any university.

Amir Allahviridi-Zadeh

20 July 2022

Abstract

Low Earth Orbiting (LEO) satellites are usually complex, large, and expensive spacecraft built for different space missions and earth science applications. Precise orbits of LEO satellites with accuracy at a few cm to dm levels are essential for some of these applications and are achievable using precise orbit determination (POD) methods. Technology advancements brought the opportunity to build and launch smaller satellites from the commercial-off-the-shelf (COTS) components in 10 cm-sized cubes, known as CubeSats. It would significantly reduce the complexity and the cost of having more satellites in orbit and expand space missions to research institutes and the private sector capable of building these miniature satellites. However, CubeSats are faced with some limitations, mainly due to 1) the limited onboard power and 2) the quality of COTS sensors. These limitations significantly reduce CubeSats' applicability in missions requiring high orbital accuracy. Therefore, the aim of this thesis is to investigate the limitations of the CubeSats in the POD and develop algorithms and remedies to reach high orbital and clock accuracies. The outputs would help in increasing CubeSats' applicability in future space missions.

Investigating the first limitation shows that the limited onboard power causes the duty cycles in the power budget of sensors in the bus and payload. Consequently, applying various data constraints, such as the unavailability of GNSS observations and attitude information, is inevitable for low-power CubeSats. An efficient post-mission POD based on various data constraints is developed in the thesis and implemented in Bernese GNSS software. The validations confirm that the sub-dm level of orbital accuracy is achievable with observations collected under various duty cycles. Adding simultaneous data constraints such as lower sample intervals or the limited number of channels for tracking GNSS satellites negatively impacts the orbital accuracy. Other constraints, such as the lack of attitude information, the arc length, and the latency of the required orbits, are extensively analysed in the thesis. Based on the analysis of these factors, recommendations are provided for the CubeSats developers and mission designers to find appropriate combinations for the data constraint to achieve the required orbital accuracy in post-mission mode.

The quality of the COTS components is the second limitation that affects CubeSats POD and is investigated in the thesis. It starts with developing a new weighting model based on Signal-to-Noise-Ratio (SNR) to optimally represent the stochastic behaviour of the onboard observations due to the inter-satellite geometry in space, something which is not achievable using the widely-used elevation angle-dependant models. The internal validation methods, such as comparing overlapping arcs, the goodness of fit, and residual analysis, confirm the orbital improvements due to applying the proposed weighting model in the POD of CubeSats.

The short-term stabilities of the estimated clocks in CubeSat's POD, which is crucial for high-rate applications such as GNSS Radio Occultation (GNSS-RO), is another investigated point relevant to the quality of COTS components. The limitations in 1) the CubeSats POD and 2) the quality of COTS components are specified as the main sources for clock instabilities. The primary reasons for these limitations are categorised as the presence of a significant number of outliers, biases due to thermal variations, unmodelled phase centre variations, the J2 effect, and the quality of the onboard oscillators. The impacts of each factor are analysed, and the applicable remedies with the analysis of their influences on stability improvements are provided. A practical method to solve the issue of time-tagging the high-rate GNSS-RO observations using unstable clocks is addressed. Evaluating the GNSS-RO product from the Spire Global constellation confirms the quality of the CubeSats' products and the benefits of replacing large and expensive LEO satellites with CubeSats.

Besides the abovementioned limitations, the onboard POD using GNSS observations requires real-time corrections for clocks and orbits of GNSS satellites in space. In this sense, the accuracy and the stability of corrections from the new generation of Australian and New Zealand Satellite-Based Augmentation Systems (AU/NZ SBAS, known as, SouthPAN) and the Japanese navigation system (QZSS) are studied. The limitations and the structure of these corrections with the implementation points in the POD are addressed. Extending the CubeSats POD to the real-time mode and using these corrections result in achieving sub dm to dm levels of orbital accuracy.

Considering CubeSat's limitations for onboard processing, a new software for absolute and relative kinematic POD, named LeoPod, was developed during this PhD study. The structure and models implemented in LeoPod are thoroughly explained in the thesis. A relative kinematic POD approach augmented with the precise inter-satellite ranges from the ground-based reduced-dynamic POD is developed to remove the receiver-dependent errors and meet the limited processing capacity of CubeSats in formation flying scenarios. The structure of implementing this approach and the derived orbital accuracy based on the length of the inter-satellite ranges are discussed.

Although the significant limitations of CubeSats and their impacts on the POD are discussed in this dissertation, some areas need further investigation. It includes extending the CubeSats POD to the use of multi-frequency multi-constellation GNSS mode, using undifferenced-uncombined observations, and applying the concept of PPP-IAR and the array-aided PPP for integer ambiguity resolution and precise attitude determination using GNSS.

Acknowledgements

I would like to express my deepest gratitude to my main supervisor, Professor Ahmed El-Mowafy, who gave me this chance to work on the prestigious Australian Research Council (ARC) Discovery Project: Tracking Formation-Flying of Nanosatellites Using Inter-Satellite Links (DP 190102444). I appreciate all of his support during these years; that is indeed beyond the supervisory duties. He is a true leader for the GNSS-SPAN Group at Curtin University and a great mentor for me since I started my PhD in Australia. The funding received from the ARC project and Curtin University to fund my PhD research program is acknowledged.

I would like to especially thank Professor Kan Wang, who helped me a lot when I arrived at Curtin University. I was impressed by her brilliant mind and hard-working character. I appreciate her friendly behaviour and enjoyed our scientific discussions during these years.

I would like to thank Professor Peter Teunissen, a distinguished scientist in GNSS positioning and navigation. Although my time under his supervision was short due to the COVID-19 pandemic, I was impressed by his strong view of the theory of estimation and observation modelling.

My most profound appreciation is to my family for their support, and finally, I dedicate this thesis to my beloved wife, Afsaneh, for her kindness and great support during my PhD.

Acknowledgement of Country

We acknowledge that Curtin University works across hundreds of traditional lands and custodial groups in Australia and with First Nations people around the globe. We wish to pay our deepest respects to their ancestors and members of their communities, past, present, and to their emerging leaders. Our passion and commitment to work with all Australians and peoples from across the world, including our First Nations peoples, are at the core of the work we do, reflective of our institutions' values and commitment to our role as leaders in the Reconciliation space in Australia.

List of Publications

This thesis by compilation comprises four first-author and one second-author peer-reviewed papers and two chapters discussing the model implementations and software development and modifications during this PhD. The copyright authorizations, author contribution declarations, and proof of peer-reviewed publications are provided in Appendix A, B, and C, respectively.

1. **Allahvirdi-Zadeh, A.**, Wang, K., & El-Mowafy, A. (2022). Precise Orbit Determination of LEO Satellites Based on Undifferenced GNSS Observations. *Journal of surveying engineering*, 148(1), 03121001. DOI: 10.1061/(ASCE)SU.1943-5428.0000382
2. Wang, K., **Allahvirdi-Zadeh, A.**, El-Mowafy, A., & Gross, J. N. (2020). A sensitivity study of POD using dual-frequency GPS for CubeSats data limitation and resources. *Remote Sensing*, 12(13), 2107. DOI: 10.3390/rs12132107
3. **Allahvirdi-Zadeh, A.**, El-Mowafy, A., Wang, K. (2022). Precise Orbit Determination of CubeSats Using Proposed Observations Weighting Model. In: *International Association of Geodesy Symposia*. Springer, Berlin, Heidelberg. DOI: 10.1007/1345_2022_160
4. **Allahvirdi-Zadeh, A.**, Awange, J., El-Mowafy, A., Ding, T., & Wang, K. (2022). Stability of CubeSat Clocks and Their Impacts on GNSS Radio Occultation. *Remote Sensing*, 14(2), 362. DOI: 10.3390/rs14020362
5. **Allahvirdi-Zadeh, A.**, Wang, K., & El-Mowafy, A. (2021). POD of small LEO satellites based on precise real-time MADOCA and SBAS-aided PPP corrections. *GPS solutions*, 25(2), 1-14. DOI: 10.1007/s10291-020-01078-8

Table of Contents

| | |
|--|-----|
| Declaration | 1 |
| Abstract | 2 |
| Acknowledgements | 4 |
| Acknowledgement of Country | 5 |
| List of Publications | 6 |
| Table of Contents | 7 |
| List of Figures | 9 |
| List of Tables | 14 |
| List of Abbreviations | 16 |
| 1 Introduction..... | 20 |
| 1.1 Background..... | 20 |
| 1.2 Research Questions..... | 23 |
| 1.3 Objectives | 23 |
| 1.4 Outline of the Thesis..... | 24 |
| 2 Precise Orbit Determination of LEO Satellites Based on Undifferenced GNSS Observations . | 30 |
| 3 Post-mission CubeSats POD..... | 44 |
| 4 A sensitivity study of POD using dual-frequency GPS for CubeSats data limitation and resources | 55 |
| 5 Precise Orbit Determination of CubeSats Using Proposed Observations Weighting Model | 77 |
| 6 Stability of CubeSat Clocks and Their Impacts on GNSS Radio Occultation | 86 |
| 7 POD of small LEO satellites based on precise real-time MADOCA and SBAS-aided PPP corrections..... | 113 |
| 8 Real-time CubeSats POD with a new software | 128 |
| 8.1 Kinematic POD using LeoPod software..... | 128 |
| 8.2 Relative Kinematic POD using LeoPod software | 135 |

| | | |
|-----|---|-----|
| 9 | Conclusions..... | 139 |
| 9.1 | Summary of the thesis outcomes | 139 |
| 9.2 | Recommendations and future work | 143 |
| | References..... | 145 |
| | Appendix A: Copyright Permission Statements | 148 |
| | Appendix B: Statement of Contributions by Co-Authors..... | 157 |
| | Appendix C: Proof of Peer-Reviewed and Accepted Publications..... | 160 |

List of Figures

Since the thesis includes mainly publications in Chapters with figure numbers starting from 1 in each, the list of figures is listed below according to their Chapter.

Chapter 2

| | |
|--|----|
| Figure 1 Flowchart of the paper's structure | 32 |
| Figure 2 Questions that will be addressed in each section..... | 33 |
| Figure 3 Flowchart of reduced-dynamic POD computation procedure..... | 36 |
| Figure 4 Flowchart for the EKF reduced-dynamic POD | 39 |

Chapter 3

| | |
|---|----|
| Figure 1 Flowchart of CubeSat POD using Bernese software package. The relevant step numbers are provided in parentheses | 53 |
|---|----|

Chapter 4

| | |
|---|----|
| Figure 1 (a) Distribution of the tracked satellite numbers per epoch and (b) the time history of the satellite numbers having both the L1/L2 observations and at least the L1 observations. The data was collected from the CubeSat STF-1 from 15:39:37 in GPS time (GPST) on 27 February 2019 to 3:55:10 on 28 February 2019 | 58 |
| Figure 2 Flow-diagram of the processing procedure and the estimated parameters. n and m are the numbers of the stochastic parameter vectors considered during the estimation in Step 3 and 4, respectively | 61 |
| Figure 3 3D orbital errors of the code-based kinematic (red) and reduced-dynamic daily arc (blue) with a sampling interval of 10 s. The IGS final products were used for the GPS satellites. | 63 |
| Figure 4 3D orbital errors for different duty-cycles (from 20% to 80%) of the phase-based reduced-dynamic orbits using data of GRACE FO-1 with a sampling interval of 10 s. The elevation mask was set to 5 degrees with a mean satellite number of about 9..... | 63 |
| Figure 5 (a) Distribution of the satellite numbers per epoch (observing at least P1 and P2 observations) applying different elevation mask angles and (b) the corresponding 3D orbital errors of the phase-based reduced-dynamic orbits with a duty-cycle of 100% and mean satellite numbers of 7 and 6 | 64 |
| Figure 6 3D RMSE of the reduced-dynamic orbits under different duty-cycles, observation sampling intervals, and mean satellite numbers using the IGS final products. The cases having 9, 7, and 6 satellites (on average) are given between each pair of the dashed lines | 65 |
| Figure 7 Differences in the between-satellite clocks for G02 and G32 between the IGS final and rapid clocks | 67 |

- Figure 8 3D orbital errors of the phase-based reduced-dynamic orbits using data of GRACE FO-1 with a 100% duty-cycle, a mean satellite number of 9, and a sampling interval of 10 s (having the IGS final as the reference). Different IGS products were applied. 67
- Figure 9 3D RMSE of the reduced-dynamic orbits under different duty-cycles, observation sampling intervals and mean satellite numbers using (a) the IGR and (b) the IGC products. The cases having 9, 7, and 6 satellites (on average) are given between each pair of the dashed lines. 68
- Figure 10 The antenna reference frame (ARF, shown in red), the satellite reference frame (SRF, shown in yellow), and the radial, along-track, and cross-track (RSW, shown in green) system. t_1 and t_2 represent two conservative time epochs for the same satellite. The figure is scaled for a better presentation 69
- Figure 11 Angle differences between the east, north, and up directions in the antenna reference frame (ARF) and the opposite along-track direction, the cross-track direction, and the radial direction. The data for GRACE FO-1 was used for the plot. Note that the blue line is almost overwritten by the green dashed line. 69
- Figure 12 3D orbital errors not applying the antenna attitude information. The IGS final products were used for observations with a duty-cycle of 100%, a sampling interval of 10 s, and a mean satellite number of 9. 70
- Figure 13 3D orbital errors computed with different arc lengths using (a) the IGS final products and (b) the IGS rapid products. A duty-cycle of 100%, an observation interval of 10 s, and a mean satellite number of 9 were assumed for the processing. The arc length experiment here refers to the processing using e.g., k hours of data in each processing round, and in each hour of these k hours, data are tracked in $X\%$ of the time. 71
- Figure 14 3D RMSE of the reduced-dynamic orbits when processing with the arc lengths of 24 h, 12 h, and 6 h applying (a) the IGS final products, (b) the IGS rapid (IGR) products, and (c) the IGS real-time (IGC) products. Between each pair of the dashed lines, the cases are sorted from the highest duty-cycle of 100% to the lowest duty-cycle of 20%, first for the mean satellite number of 9, and then similarly for the mean satellite numbers of 7 and 6, respectively. 72

Chapter 5

- Figure 1 Structure of the Spire 3U RO CubeSat (Credit: Spire Global, Inc.) 79
- Figure 2 Observation weights from the SNR- and the elevation-dependent weighting models for one month (16/12/2020–15/01/2021) of L1C (left) and L2L (right) signals from all available GPS satellites as observed on CubeSat PRN099 80
- Figure 3 3D-RMS of differences between RD-POD and Kinematic POD (Kin-POD) for all CubeSats. Each segment related to each CubeSat PRN contains all processed file during one month (16/12/2020–15/01/2021) 81
- Figure 4 Overlapped arc between two consecutive orbits. The red cross hatches indicate the arc boundaries. 81
- Figure 5 RMS of overlapping validation for RD-POD (a) and Kin-POD (b). (Dark colours: using the SNR-based model – Light colours: using the elevation-dependent model) 82

| | |
|---|-----|
| Figure 6 RMS of the a-posteriori sigma for all CubeSats for RD-POD (top) and Kin-POD (bottom). (Dark colours: using the SNR-based model— Light colours: using the elevation-dependent model) | 83 |
| Figure 7 The RMS of IF phase residuals from the RD-POD (top) and the Kin-POD (bottom) for CubeSat PRN099. The RMS values are derived from one month of all observations of all GPS satellites | 84 |
| Chapter 6 | |
| Figure 1 Structure of the Spire 3U RO CubeSat (source: Spire Global, Inc.) | 92 |
| Figure 2 MDEV of the estimated clocks of all 17 CubeSats from the RD-POD over the testing period (31 days: 16 Dec 2020–15 Jan 2021). Different colours are dedicated to the different observation segments | 92 |
| Figure 3 Flowchart indicating CubeSats' clock instability assessment and the proposed remedies | 93 |
| Figure 4 MDEV of the 17 CubeSats' clocks for short averaging times plotted against the percentage of the observations that are considered outliers in the pre-processing steps. In the subfigures, each dot represents the MDEV of one observation segment for one CubeSat over the testing period. The subfigures (a–d) indicate averaging times 1, 5, 10, and 30 s, respectively. | 94 |
| Figure 5 Cylindrical model for detecting CubeSats located in the shadow of the earth..... | 95 |
| Figure 6 PCV patterns with 5 resolution for the CubeSat antenna (Lemur 3.1.0) from the antenna calibration (left) and the inflight observations using the residual approach (right). The inner circles are marked with the elevation angles, and the azimuth values are tagged on the outer circle. The azimuth 0 coincides with the positive x-axis of the CubeSats' body frame (approximately the positive velocity direction) in the zero-quaternion case..... | 96 |
| Figure 7 Estimated clock offsets from all observation segments of CubeSat 099 (top) and COSMIC-2A 1 (bottom) over the testing period. Several millisecond jumps are observed for CubeSat's oscillator compared to the USO's onboard COSMIC-2. Some of the clocks are plotted in bold for better visibility | 99 |
| Figure 8 Mean of the improvements in comparing the estimated CubeSats' clocks before and after applying the proposed corrections in the RD-POD procedure. The lines inside each bar show the minimum and maximum RMS of the improvements over the testing period..... | 100 |
| Figure 9 Mean of the MDEV reductions in the short-term stabilities after applying the proposed corrections compared to the first estimation of clocks, i.e., before applying the proposed remedies. Each CubeSat has four bars related to short averaging times (1, 5, 10, and 30 s, respectively). They are tagged for CubeSat 099 as an example | 100 |
| Figure 10 MDEV of the estimated clocks of COSMIC-2 satellites. Different colours are dedicated to the different observation segments of each COSMIC-2 satellite. The duration of the observation segments is varied from 30 min to 2 h, generally around 1.5 h with a sample interval of 10 s | 101 |
| Figure 11 COSMIC-2 satellite structure (credit: Surrey Satellite Technology) | 102 |

| | | |
|------------------|---|-----|
| Figure 12 | Number of occultations for the COSMIC-2 constellation and 17 CubeSats (top), Geographical coverage of the 17 tested CubeSats (bottom left), and COSMIC-2 constellation (bottom right) over the testing period (16 December 2020–15 January 2021) | 104 |
| Figure 13 | Comparing the CubeSats and COSMIC-2 with radiosonde observations as a reference in terms of temperature and height. The profiles related to each site are provided in subfigures (a–d)..... | 105 |
| Figure 14 | Comparing CubeSats and COSMIC-2 with the radiosonde observations as a reference in terms of the temperature and pressure. The profiles related to each site are provided in subfigures (a-d)..... | 106 |
| Figure 15 | Comparing CubeSats and COSMIC-2 in terms of the refractivity and height. The profiles related to each date are provided in subfigures (a–d)..... | 106 |
| Figure 16 | Locations of the radiosonde stations used for the validation using KGE metric | 107 |
| Chapter 7 | | |
| Figure 1 | RMSE of the orbits in MADOCA L6E PPP service (red) and SBAS-aided L5 PPP service (blue) with respect to IGS final orbits in the radial (top), along-track (2nd row), cross-track (3rd row) directions, and the 3D RMS (bottom) for August 14–20, 2018. The area of each day is divided into 31 sections, representing 31 PRNs. Each dot represents the result of one GPS satellite on the corresponding day | 116 |
| Figure 2 | Standard deviations of the satellite clock residuals from MADOCA L6E PPP service (red) and SBAS-aided L5 PPP service (blue) from August 14–20, 2018. The clocks are compared with IGS final satellite clocks. The area of each day is divided into 31 sections, representing 31 PRNs. Each dot represents the result of one GPS satellite on the corresponding day | 117 |
| Figure 3 | Modified Allan deviation ($-MDEV$) of all GPS clocks from CODE final products (top), MADOCA L6E PPP service (middle), and SBAS-aided L5 PPP service (bottom) from August 14–20, 2018 | 117 |
| Figure 4 | Network distribution of MADOCA (red) and AU/NZ SBAS services (blue) | 118 |
| Figure 5 | Flowchart of the reduced-dynamic POD | 119 |
| Figure 6 | Orbital differences between the reduced-dynamic orbits and the reference orbits applying (left) MADOCA L6E PPP products and (right) SBAS-aided L5 PPP products. The data of GRACE-FO 1 on August 15, 2018, were used for the plot | 121 |
| Figure 7 | Average 3D RMSE of the reduced-dynamic orbits applying different duty cycling (shown as the colored percentage in the legend) for (left) GRACE-FO 1 and (right) Sentinel-3B using different GPS products from August 14–20, 2018. The line segments inside each bar illustrate the minimum and maximum daily 3D RMSE over the test period. The abbreviations in the x-axis are given in Table 4 | 122 |
| Figure 8 | Maximum 3D errors of the reduced-dynamic orbits within a certain percentage of all 3D orbital errors from August 14–20, 2018, after using different providers of GNSS observation | |

corrections for (left) GRACE-FO1 and (right) Sentinel-3B. The duty cycle is set to 100%
 122

Figure 9 Average velocity RMSE in the along-track direction for (left) GRACE-FO 1 and (right) Sentinel-3B using different GPS products from August 14–20, 2018. The line segments inside each bar illustrate the minimum and maximum daily velocity RMSE in the alongtrack direction over the test period. The legend refers to the percentage values for duty cycling
 122

Figure 10 Kinematic and reduced-dynamic orbits for GRACE-FO-1 on August 15, 2018, using (left) MADOCA L6E PPP products and (right) SBAS-aided L5 PPP products 123

Figure 11 Average RMSE of the kinematic orbits (for the 3D, crosstrack, along-track, and radial directions) for (left) GRACE-FO 1 and (right) Sentinel-3B using different GPS products from August 14–20, 2018. The line segments inside each bar illustrate the minimum and maximum daily RMSE over the test period 124

Figure 12 Maximum 3D errors of the kinematic orbits within a certain percentage of all 3D orbital errors from August 14–20, 2018, using different providers of GPS observation corrections for (left) GRACE-FO 1 and (right) Sentinel-3B satellites. The duty cycle is set to 100%
 124

Chapter 8

Figure 1 Flowchart of CubeSat POD using LeoPod software. The relevant step numbers are provided in parentheses 134

Figure 2 Flowchart for the relative POD augmented with the precise inter-satellite ranges 136

List of Tables

Since the thesis includes mainly publications in Chapters with table numbers starting from 1 in each, the list of tables is listed below according to their Chapter.

Chapter 2

Table 1 Examples of dynamic models used in the reduced-dynamic POD 35

Table 2 Summary of LEO POD results in different studies 36

Table 3 Comparison of the POD methods that are typically used in the postprocessing and real-time modes 40

Chapter 4

Table 1 Processing details for the reduced-dynamic orbit determination..... 61

Table 2 Mean number of satellites used in SPP and percentiles of valid SPP solutions applying different elevation masks. Note that the mean satellite numbers are given as rounded values. The real values of the mean satellite numbers amount to about 8.5, 7.4, and 5.7 for an elevation mask of 5, 15, and 25 degrees, respectively..... 64

Table 3 3D RMSE (in cm) of the phase-based reduced-dynamic orbits under different duty-cycles and mean satellite numbers..... 65

Table 4 Information on different IGS products and the 3D orbital RMSE using 10 s observation data 66

Table 5 3D RMSE of the phase-based reduced-dynamic orbits with different arc lengths and using different IGS products. 10 s observation data with a duty-cycle of 100% and a mean satellite number of 9 were used for the processing 71

Table 6 Increase in the 3D RMSE (in cm) of phase-based reduced-dynamic orbits when shortening the arc length from 24 h to 12 h. The IGS final products were used..... 71

Chapter 5

Table 1 CubeSats POD processing models and parameters 80

Table 2 Mean percentage of the RMS reduction due to the proposed SNR-based model compared to the elevation-dependent model for all CubeSats in all directions 82

Table 3 Mean value of the a-posteriori STD of all CubeSats from RDPOD and Kin-POD..... 83

Chapter 6

Table 1 POD processing models and parameters..... 90

Table 2 Specifications of seventeen CubeSats employed in this study. SSO: Sun-Synchronous Orbit, LTAN: Local Time of Ascending Node, LTDN: Local Time of Descending Node (provided by Spire Global Inc.)..... 91

| | |
|--|-----|
| Table 3 Mean values of the MDEV changes of the CubeSats' clocks when the numbers of stochastic accelerations are doubled compared to the default settings for the CubeSats observations with a high rate of outliers (>50%)..... | 94 |
| Table 4 Mean values of MDEV differences between when the CubeSats are in the shadow and when they are out of the shadow region..... | 95 |
| Table 5 Mean values of the MDEV reductions after applying new PCV patterns in the RD-POD for short averaging times..... | 97 |
| Table 6 Mean values of the clock differences between with/without applying J2 corrections in the RD-POD..... | 98 |
| Table 7 COSMIC-2 satellite specifications (the ESA Earth Observation Portal (eoPortal))..... | 102 |
| Table 8 Mean and standard deviation (STD) of the differences between the CubeSats and COSMIC-2 temperature values and the radiosonde observations for different heights..... | 104 |
| Table 9 Mean and standard deviation (STD) of the differences between CubeSats and COSMIC-2 temperature values and the radiosonde observations for different pressures levels..... | 105 |
| Table 10 KGE values for the CubeSats and COSMIC-2 profiles against the radiosonde observations..... | 107 |

Chapter 7

| | |
|---|-----|
| Table 1 Average orbital RMSE of MADOCA L6E and SBAS-aided L5 PPP services from August 14–20, 2018..... | 116 |
| Table 2 Mean MDEV of the CODE, MADOCA, and SBAS-aided PPP (L5) clocks for all Block IIF satellites with different averaging times..... | 118 |
| Table 3 LEO POD processing models and parameters..... | 119 |
| Table 4 Details of different GPS products used for the processing..... | 120 |
| Table 5 Average RMSE of the reduced-dynamic orbits from August 14–20, 2018, using MADOCA L6E PPP products and SBAS-aided L5 PPP products..... | 121 |
| Table 6 RMSE of the kinematic orbits from August 14–20, 2018, using MADOCA L6E PPP products and SBAS-aided L5 PPP products..... | 123 |

Chapter 8

| | |
|--|-----|
| Table 1 The specifications of the CPU used for relative POD testing compared to a real CubeSat CPU..... | 136 |
| Table 2 RMS values for comparison of CubeSats orbits generated from the augmented relative POD with the reduced-dynamic POD for baselines less than 1000 km..... | 137 |

List of Abbreviations

A

| | |
|------------|---|
| ADCS | Attitude determination and Control System |
| AIUB | Astronomical Institute of the University of Bern |
| ARP | antenna reference point |
| AU/NZ-SBAS | Australia/New Zealand Satellite-Based Augmentation System |

B

| | |
|------|--------------------------------|
| BLUE | Best Linear Unbiased Estimator |
|------|--------------------------------|

C

| | |
|----------|---|
| C-CSAC | Cesium Chip-Scale Atomic Clock |
| CDF | Cumulative distribution function |
| CHOMPTT | CubeSat Handling of Multisystem Precision Time Transfer |
| CLAS | Centimeter Level Augmentation Service |
| CNES | Centre National d'Etudes Spatiales |
| CODE | Center for Orbit Determination in Europe |
| CoM | center-of-mass |
| CORS | continuously operating reference stations |
| COSMIC-2 | Constellation Observing System for Meteorology, Ionosphere, and Climate |
| COTS | Commercial Off-The-Shelf |
| CRF | CubeSat's reference frame |

D

| | |
|-------|---|
| DCB | Differential Code Biases |
| DD | double differences |
| DF | dual-frequency |
| DLR | German Space Operations Center |
| DOF | degrees of freedom |
| DORIS | Doppler Orbitography and Radiopositioning Integrated by Satellite |

E

| | |
|------|----------------------------|
| ECEF | earth-centered earth-fixed |
| ECOM | Empirical CODE orbit Model |
| EGM | earth gravitational model |

| | |
|-----|------------------------------|
| EKF | extended Kalman filter |
| EOP | earth orientation parameters |
| ESA | European Space Agency |

F

| | |
|------|--------------------------------|
| FDE | fault detection and exclusion |
| FES | Finite Element Solution |
| FPGA | Field Programmable Gate Arrays |

G

| | |
|----------|--|
| GAST | Greenwich Apparent Sidereal Time |
| GEO | geostationary earth orbit |
| GHOST | GPS high precision orbit determination software tools |
| GNSS | Global Navigation Satellite Systems |
| GNSS-RO | Global Navigation Satellite Systems' radio occultation |
| GPC | ground processing centre |
| GPST | GPS time |
| GRACE | Gravity Recovery and Climate Experiment |
| GRACE-FO | GRACE Follow-On |
| GRAPHIC | Group and phase ionospheric correction |
| GRAS | GNSS Receiver for Atmospheric Sounding |
| GSN | GRAS Support Network |

I

| | |
|--------|--|
| IAR | Integer ambiguity resolution |
| IAU | International Astronomical Union |
| ICRF | International Celestial Reference Frame |
| IERS | International earth rotation and reference systems service |
| IF | Ionosphere-free |
| IGS | International GNSS Service |
| IMU | Inertial measurement unit |
| In-SAR | Interferometric synthetic aperture radar |
| ITOE | Inertial true of epoch frame |
| ITRF | International terrestrial reference frame |
| IV&V | Independent Verification and Validation |

J

| | |
|--------|---|
| JAXA | Japan Aerospace Research and Development Agency |
| JPL | Jet Propulsion Laboratory |
| JPL DE | Jet Propulsion Laboratory Development Ephemeris |

K

| | |
|---------|-------------------------------|
| KBR | K-band ranging |
| KGE | Kling-Gupta Efficiency metric |
| Kin | kinematic |
| Kin-POD | Kinematic POD |

L

| | |
|------|-------------------------------|
| LEO | Low Earth Orbit |
| LINZ | Land Information New Zealand |
| LTAN | Local Time of Ascending Node |
| LTDN | Local Time of Descending Node |

M

| | |
|--------|---|
| MADOCA | Multi-GNSS Advanced Demonstration Tool for Orbit and Clock Analysis |
| MDEV | modified Allan deviation |
| MetOp | Meteorological Operational |

N

| | |
|------|--|
| NCEI | National Centers for Environmental Information |
| NEU | North, East Up |
| NWP | numerical weather prediction |

O

| | |
|-----|-------------------------|
| O-C | observed-minus-computed |
|-----|-------------------------|

P

| | |
|-----|-------------------------------------|
| PCO | phase center offsets |
| PCV | phase center variations |
| PNT | Positioning, Navigation, and Timing |
| POD | Precise orbit determination |
| PPP | Precise point positioning |

Q

| | |
|------|-------------------------------|
| QWG | Quality Working Group |
| QZSS | Quasi-Zenith Satellite System |

R

| | |
|---------|--|
| RD | reduced-dynamic |
| RD-POD | reduced-dynamic POD |
| RETICLE | Real-Time Clock Estimation system |
| R-MAC | Rubidium Miniature Atomic Clock |
| RMS | root mean square |
| RMSE | root-mean-squared error |
| RO | Radio Occultation |
| RTCM | radio technical commission for maritime services |
| RTS | IGS real-time service |

S

| | |
|-------|----------------------------|
| SDR | software-defined radio |
| SLR | satellite laser ranging |
| SNR | Signal-to-Noise Ratio |
| SPP | single point positioning |
| SRF | satellite reference frame |
| SRP | solar radiation pressure |
| SSR | State Space Representation |
| STD | standard deviation |
| STF-1 | Simulation To Flight-1 |

T

| | |
|-----|-------------------|
| TLE | two-line elements |
|-----|-------------------|

U

| | |
|------|--|
| UCAR | University of Corporation for Atmospheric Research |
| UKF | unscented Kalman filter |
| USO | ultra-stable oscillator |
| UTLS | Upper troposphere-lower stratosphere |

1 Introduction

1.1 Background

Human beings have an old desire to explore the outer part of the Earth. This desire motivated the design of space missions and the building of complex spacecraft. Most of these satellites are launched in the Low Earth Orbit (LEO), particularly with an altitude of 300-1500 km, which is suitable for remote sensing and communicating applications. Based on the considered application, the orbits of these satellites should be determined with a certain level of accuracy. The word “orbit” here refers to the spacecraft's location in its motion around the Earth.

LEO satellites are below the Medium Orbit Earth (MEO) satellites of the Global Navigation Satellite Systems (GNSS). To benefit from this fact, LEO satellites nowadays are equipped with GNSS antennas and receivers to coarsely determine their position using code observations in a Single Point Positioning (SPP) solution with an accuracy of several meters. The satellite's motion mainly results from the Earth's central gravitational force and is disturbed by various forces acting on the satellite. Knowing and using more information about these forces result in higher accuracy in determining the satellite's orbit. Therefore, the estimated orbit onboard a LEO satellite from GNSS sensors can be integrated with the force models that affect the dynamics of the satellite in space to reach a better orbit determination accuracy. However, forces on miniature LEO satellites, such as CubeSats, are modelled with low degrees and orders due to the limitation in their onboard processing. Combining this procedure with the output of other sensors in the satellite, mainly the Attitude Determination and Control System (ADCS), can result in orbit determination with meter-level accuracy. However, this accuracy level does not fulfill the requirements of many applications.

Precise orbits with accuracy at the cm- to dm-level are achievable for large LEO satellites equipped with powerful ADCS in the post-mission mode. In this process, the GNSS observations collected onboard these satellites should first be screened for outliers. Next, the filtered observations are corrected for known delays and errors that affect the GNSS signals in space. These steps are similar to the Precise Point Positioning with Integer Ambiguity Resolution (PPP-IAR) method used for ground applications, except for the tropospheric delays that are not considered for the LEO satellites as they are flying above this layer (Zhang et al. 2021). Dynamic models are also used to deal with the acting forces on satellites, and stochastic accelerations are estimated to compensate for the deficiencies in the models. This procedure results in estimating the precise orbits of LEO satellites.

Reaching a high level of orbital accuracy for large LEO satellites is indebted to the use of refined POD algorithms and the satellite's high-quality bus and payload components. Although GNSS receivers and antennas represent only a small fraction of the cost of the satellites, the combined high-

quality sensors and complexity in design, build, and launch leads to an increased cost of building large LEO satellites, the so-called geodetic satellites, in space. Examples of these expensive missions are:

- GRACE-FO: \$520 million (Smith 2018)
- Sentinel 1-6: \$3.83 billion (ESA 2019)
- COSMIC 1-2: \$560 million (Yen 2014)

However, the recent technology advancements in Commercial-Off-The-Shelf (COTS) sensors and related developments in satellite launchers opened a new era for building small satellites, particularly CubeSats. These satellites are built from COTS components in 10 cm-sized cube units ($10 \times 10 \times 10$ cm = 1U) and are usually categorized as nanosatellites. Their applicability increases with increasing their sizes, such as 3U and 6U, as more payloads and better quality sensors can be used. Currently, the cost of having a CubeSat in space varies from \$20k to \$ 200k based on the size of the CubeSat and its payloads, which is considerably smaller than the costs mentioned earlier for large LEO satellites. This low-cost feature makes CubeSats affordable and favourable among space research centres and interested industries, which would increase the CubeSats' applicability in space exploration, remote sensing, weather forecasting, Earth monitoring, environmental activities, and many more.

Most missions mentioned above need highly accurate orbits at the decimetre level or, even better, with low latencies of a few hours or less. In GNSS radio occultation, for example, orbital accuracy of 5-20 cm and velocity accuracy of 0.05-0.2 mm/s, as well as the short-term stabilities of the onboard oscillators, are required in near-real-time (Kursinski et al. 1997, Montenbruck 2017). The accuracy of the orbits required for SAR missions is at the decimetre level (Eineder et al. 2011). In satellite altimetry, the mean sea level is determined with mm- to cm accuracy, and the uncertainties in the satellite position, i.e. its orbit determination, in the radial direction should be less than 1-2 cm (Cerri et al. 2010). Therefore, the orbital accuracy of CubeSats needs to be determined with high accuracy to make them usable in these missions.

The low-cost feature of CubeSats comes at the cost of experiencing some limitations that significantly affect the orbital and clock accuracy either in post-mission or for the onboard POD. Like the large LEO satellites, the CubeSats' orbits determined onboard are mostly performed using code-only observations, which cannot provide accuracy better than several meters (Gangestad et al. 2013, Kovář et al. 2022). In contrast to the large LEO satellites, CubeSats have less power and processing capabilities. Therefore, the dynamic models that can be applied for POD are compromised, which

may not even be an option for low-power CubeSats (e.g. 1U). Most of the existing CubeSats have a limited power budget which cannot operate all sensors at the same time, and thus the power is required to be rotated among various sensors, called duty-cycling. This limitation affects the capability of continuously using spaceborne receivers and collecting GNSS observations (Mander and Bisnath 2013, Foster et al. 2015, Wesam et al. 2017, Wang et al. 2020), especially in the eclipse regions. The interrupted observations significantly reduce the orbital accuracy and can sometimes terminate the POD. In the absence of GNSS observations, integrating a two-body orbital model can thus be used to approximate the position of the CubeSat in space. However, the resulting orbit is prone to drift over time due to external disturbances and should be corrected by switching on the receiver; its accuracy can otherwise be degraded to the km level (Personal Communication with CubeSat developers).

Another issue for CubeSats is the quality of the COTS components used (Roscoe et al. 2018), including the onboard oscillator and ADCS, which can substantially affect the orbital accuracy. Moreover, due to the limited power and processing budget onboard these satellites, most CubeSats are equipped with a single-frequency GPS-only receiver (Omar et al. 2018, Vidal-Valladares et al. 2022), providing fewer observations compared to the use of dual-frequency receivers. The low number of satellite tracking channels that resulted in a low number of GNSS observations is another issue that may affect the final orbit.

Storing and transmitting the required information for POD to the ground station may also be interrupted for various reasons. In such a case, the CubeSat's orbit is computed using Two-Line Elements (TLE) data and some simplified general perturbations (SGP) models such as the SGP4 software package (Vallado and Crawford 2008, San-Juan et al. 2017). The TLEs consist of CubeSat ID, epoch, six Keplerian orbital elements (eccentricity, semimajor axis, inclination, longitude of ascending node of the orbit, argument of Perigee, and true anomaly of the satellite), and an atmospheric drag coefficient term called the ballistic coefficient. The CubeSat operators use the TLEs to avoid collision between CubeSats or between CubeSats and space debris by applying proper manoeuvres. The TLE parameters for most CubeSats are available online at <http://celestrak.com> and <https://space-track.org>. The accuracy of these orbits is typically at km-level (Kahr et al. 2013, Li et al. 2021), which is not usable for CubeSats positioning in Earth science missions such as space meteorology, satellite altimetry, and gravimetry.

POD of CubeSats should fulfil the critical requirements of control and guidance, the linkage between the onboard sensors, the parameters being sensed in space, and the ground stations that support data collection and facilitate dissemination. None of the current methods discussed above is appropriate

for high-accuracy applications. Precisely determining the CubeSats' orbit for future space applications is essential and, thus, is investigated in this thesis.

1.2 Research Questions

The main research problem addressed in this study is: Can we achieve high-precision orbits for CubeSats at a close level to geodetic LEO satellites? To be more specific, the following research questions are defined:

1. What are the gaps in the existing POD methods to be utilized for CubeSat?
2. What are the main limitations in CubeSats that may affect the POD?
3. What are the requirements for achieving high-precision orbits for CubeSats in post-mission and real-time modes?

1.3 Objectives

Answering the above research questions requires addressing the challenges associated with the CubeSats' limitations and developing POD methods suitable for them, which form the main objectives of this research. POD accuracy at sub dm- to dm-level is targeted, compared to the current accuracy of several meters to even kilometres for CubeSats. The following specific objectives are identified to address the research questions of this thesis:

1. Investigate state-of-the-art POD methods for LEO satellites and define the specifications of each method based on CubeSats' limitations
2. Develop and validate an efficient post-mission POD approach for CubeSats that experience data constraints
3. Develop and validate a novel weighting model suitable for the observations collected by COTS sensors
4. Investigate the parameters affecting the receiver clock estimation as an associated process to the CubeSat POD
5. Demonstrate the potential of replacing the geodetic satellites with CubeSats using a real-data example
6. Extend the CubeSats POD for (near) real-time application based on using real-time PPP corrections received in space and investigate the accuracy and limitations of these products
7. Develop real-time absolute and relative Kinematic POD algorithms that address the CubeSats processing limitations

The realization of this framework will help in achieving autonomous guidance and control systems for CubeSats and would expand the CubeSats' applicability in many space missions. The thesis is among the first to address the CubeSats POD and its applications in space missions and Earth sciences.

1.4 Outline of the Thesis

In summary, after the introduction, this research starts with a comprehensive review of POD methods, including the dynamic, kinematic, and reduced-dynamic approaches in Chapter 2. It identifies the gaps for achieving continuous and precise CubeSat POD considering the limitations of these satellites. A reduced-dynamic and kinematic POD based on interrupted observations and other constraints that may impact CubeSats are developed and implemented using Bernese GNSS software. These steps are extensively explained in Chapter 3 to provide a framework for post-mission POD, using CubeSats' limited data and resources, for the rest of the thesis. A sensitivity analysis is carried out in Chapter 4 with the developed reduced-dynamic and kinematic POD considering CubeSats data constraints due to the power limitations. The quality of the COTS components is another limiting factor of CubeSats that affects POD results. The stochastic behaviour of the GNSS observations collected by COTS sensors onboard CubeSats requires better models than the traditional stochastic functions. Therefore, an SNR-based weighting function is developed and evaluated in Chapter 5 using actual CubeSats data from the Spire Global constellation. The receiver clock offset is another output of the CubeSats POD process, which is significantly impacted by the quality of the onboard oscillators and deficiencies in the CubeSats POD. The short-term stability of the receiver clocks required for high-rate applications such as GNSS-RO is investigated in Chapter 6. All suspected factors in the hardware part and the POD models are comprehensively analysed, and some remedies are proposed to overcome these limitations. The replacement of geodetic satellites with CubeSats for the GNSS-RO mission is also studied in Chapter 6. The atmospheric products of LEO and CubeSats constellations are compared and evaluated using external observations, and the benefits of using CubeSats constellations are explained. Real-time PPP corrections in space make the (near) real-time POD possible; therefore, the developed POD methods for CubeSats in the previous chapters are extended in Chapter 7 to implement these corrections through space links. Next, the real-time POD based on sequential least-squares filtering is developed in Chapter 8 and extended to the relative POD augmented by the precise inter-satellite ranges, which will aid the onboard CubeSats POD either for a single CubeSat or a set of CubeSats in a formation flying. The conclusions and a summary of the results obtained in the thesis are given in Chapter 9, with a look at future potential studies in this field. The validations are performed using GPS observations since, at the time of preparing the thesis, there was no available multi-GNSS receiver onboard a CubeSat.

The detailed structure of the thesis is as follows:

Chapter 2: Precise Orbit Determination of LEO Satellites Based on Undifferenced GNSS Observations

The first objective of the thesis listed above is addressed in the following publication forming Chapter 2 of the thesis:

- Allahviridi-Zadeh, A., Wang, K., & El-Mowafy, A. (2022). Precise Orbit Determination of LEO Satellites Based on Undifferenced GNSS Observations. *Journal of Surveying Engineering*, 148(1) (pp 1-13), 03121001. DOI: 10.1061/(ASCE)SU.1943-5428.00003

This review paper investigates the fundamental knowledge of precise orbit determination of LEO satellites. The principles of dynamic orbit determination are based on solving the equation of motion of the satellite as a second-order differential equation, and the affecting physical forces on this equation are introduced. After pointing out the deficiencies in the pure dynamic method, the kinematic and the reduced-dynamic POD are explained in detail for both post-mission and real-time processing modes. This procedure includes providing the used measurement, dynamic, and error models, discussing the data screening steps, and addressing possible solution and validation approaches. The benefits and drawbacks of each solution method in both the post-mission and real-time modes are discussed from the perspective of small, low-power CubeSats. This study discusses the essential points that need to be considered in the POD, considering CubeSats' limitations, such as data interruption, low quality of sensors, and limited processing capability and capacity. An efficient CubeSats POD in post-mission based on these limitations is developed in the next chapter.

Chapter 3: Post-mission CubeSats POD

The power and quality of the COTS sensors are the main constraints of CubeSats that may affect the POD. Therefore, a reduced-dynamic POD factoring these limitations is developed in this chapter and implemented in the Bernese GNSS Software v5.2 (Dach et al. 2015). The model is extended for Kinematic POD, which is useful for periods with uninterrupted GNSS observations. All models required for data processing, screening steps, transformations between frames, propagating the orbits and estimating the variational equations, and estimating the unknowns are extensively explained to provide fundamental knowledge and processing tools for the rest of the chapters. The developed POD method addresses the second objective of the thesis. The next chapter will study different constraints in data acquisition and their impacts on the CubeSats POD.

Chapter 4: A sensitivity study of POD using dual-frequency GPS for CubeSats data limitation and resources

The following publication covers this chapter to complement addressing the second objective of the thesis:

- Wang, K., Allahviridi-Zadeh, A., El-Mowafy, A., & Gross, J. N. (2020). A sensitivity study of POD using dual-frequency GPS for CubeSats data limitation and resources. *Remote Sensing*, 12(13) (pp 1-21), 2107. DOI: 10.3390/rs1213210

The paper provides an extensive sensitivity analysis of the CubeSat POD concerning the continuity of GNSS observations, which is limited by the onboard power budgets and duty cycle tasks. This analysis starts with discussing the shortage of observations for real CubeSats due to duty cycling and its impact on POD. The variation of duty cycles and the resulting orbital accuracies are discussed based on utilizing phase-based reduced-dynamic POD. The GRACE-FO 1 is used as an example of LEO satellites to generate the duty-cycled data, investigate their impact, and test the developed POD in various scenarios. These scenarios include the orbital accuracy assessment when:

- 1) Specific elevation mask-angles are set to remove the satellites with low elevations;
- 2) The number of tracked GNSS satellites is limited to a specific number in the receivers;
- 3) Storing and broadcasting GNSS observations at lower sample intervals, which are inevitable due to power issues or broadcasting limitations;
- 4) Applying different latency requirements of the final precise orbits in the mission, which would require using various GNSS precise orbit and clock products;
- 5) Considering the case when attitude information from the star tracker sensor is not available for the CubeSats due to duty cycling or broadcasting issues;
- 6) Considering the varying arc lengths in POD computations, which are inevitable because of CubeSats' limitations.

The outcome of this paper is helpful for the CubeSats developers and the mission planners to ensure achieving the required orbital accuracy in post-mission mode.

In addition to the data constraints due to the power limitations, the quality of COTS components and the changing inter-satellite geometry of GNSS satellites with respect to the CubeSats have high impacts on the quality of CubeSats POD. The next chapter provides a new model to cope with the GNSS observations collected by the COTS sensors in the CubeSats POD.

Chapter 5: Precise Orbit Determination of CubeSats Using Proposed Observations Weighting Model

The following publication covers the third objective of the thesis in this chapter:

- Allahviridi-Zadeh, A., El-Mowafy, Wang, K. (2022). Precise Orbit Determination of CubeSats Using Proposed Observations Weighting Model. In: International Association of Geodesy Symposia. Springer, Berlin, Heidelberg. DOI: 10.1007/1345_2022_160

This paper proposes a new weighting model for the CubeSats POD based on the Signal-to-Noise Ratio (SNR) and evaluates the proposed model by testing its POD performance with actual CubeSats observations. The results show that the new model outperforms the elevation-angle dependent weighting functions, and the targeted sub-dm to dm-level accuracy is achievable for the tested CubeSats.

The receiver clock offsets are the other outputs of the CubeSats POD process, which are influenced by the quality of the COTS sensors, i.e., the onboard oscillators, and the deficiencies in the CubeSats POD. The next chapter is dedicated to the investigation of this primary issue.

Chapter 6: Stability of CubeSat Clocks and Their Impacts on GNSS Radio Occultation

The following publication addresses the fourth and fifth objectives of the thesis:

- Allahviridi-Zadeh, A., Awange, J., El-Mowafy, A., Ding, T., & Wang, K. (2022). Stability of CubeSat Clocks and Their Impacts on GNSS Radio Occultation. *Remote Sensing*, 14(2) (pp 1-26), 362. DOI: 10.3390/rs14020362

In the first part of this publication, the parameters that affect the stability of CubeSat clocks are deeply investigated, and the impact of each parameter in the receiver clock estimation in CubeSats POD is specified. Remedies are suggested to reduce the instabilities in the estimated clocks. The impacts of these remedies on the stability improvements are investigated.

The second part of the paper covers the fifth objective of this dissertation. The quality of the GNSS radio occultation (RO) products, i.e., the atmospheric profiles, are compared to the similar products of a large LEO constellation. It is shown that CubeSats' profiles can compete with large LEO satellites, and they could cover the entire Earth at a significantly lower cost compared with a constellation of large LEO satellites. This is a clear example of the potential and benefit of replacing expensive and complicated LEO satellites with CubeSats for some applications.

To this point in the thesis, the limitations in CubeSats POD in post-mission modes, mainly due to the data constraints and the quality of COTS sensors, are extensively investigated. The algorithms to cope with these limitations are developed, and the remedies are proposed, resulting in achieving the targeted accuracy for CubeSats POD. Extending the developed CubeSats POD to the real-time scenario based on using the space-based PPP corrections is the topic of the next chapter.

Chapter 7: POD of small LEO satellites based on precise real-time MADOCA and SBAS-aided PPP corrections

The following publication covers this chapter to address the sixth objective of this dissertation:

- Allahviridi-Zadeh, A., Wang, K., & El-Mowafy, A. (2021). POD of small LEO satellites based on precise real-time MADOCA and SBAS-aided PPP corrections. *GPS solutions*, 25(2), (pp 1-14). DOI: 10.1007/s10291-020-01078-8

In the absolute positioning, precise orbits and clocks of the GNSS satellites estimated from the processing of a global network are used to correct the orbital errors and the satellite clock offsets of the GNSS satellites. These products are now available in space thanks to, for example, the new generation of the Australian/New Zealand SBAS, known as the SouthPAN service (Geoscience of Australia 2020), and the Japanese Quasi-Zenith Satellite System (QZSS). This step is significant toward reaching high accuracy in real-time POD for LEO satellites, including CubeSats. The chapter extensively analyses the products broadcasted in space under the so-called “SBAS-aided L5 PPP” and “MADOCA L6E PPP” services. The network density and constellations, the different update intervals, the dynamic models used for the network adjustment, and the bandwidth limitation for the GEO link used were discussed to address the better quality of the used MADOCA products compared to the testbed SouthPAN products. The structure of both products and the way to apply them in the POD are provided in Chapter 8 (cf. section 8.1, point 1a). These products (SouthPAN and QZSS) are tested for the near-real-time POD of LEO satellites with the onboard observations affected by different duty cycles. The accuracy achieved can fulfil most applications that need near-real-time orbits of the LEO satellites. The targeted sub-dm- to dm- level of accuracy is fulfilled.

Real-time POD requires an efficient algorithm to be developed based on all limitations for onboard processing. The aim of the next chapter is to implement that algorithm in a new POD software.

Chapter 8: Real-time CubeSats POD with a new software

Bernese software used for the previous chapter processes the orbits in a batch least-squares adjustment and generates the orbits with high accuracies. However, it is not suitable for real-time scenarios and onboard processing. Therefore, a new software, named “LeoPod”, is developed to perform real-time POD based on sequential least-squares filtering in both the absolute and relative kinematic modes. In developing this software, the limitation of the processing units of CubeSats is considered and tested with the low-power CPUs that may be available onboard CubeSats. This chapter explains the structure of LeoPod software and the models used to perform the CubeSats POD. A kinematic relative POD method is also developed and augmented by suggested precise inter-satellite ranges derived from reduced-dynamic POD. The proper structure for implementing this

approach for a formation flying or a constellation of CubeSats is proposed, and the results are provided based on the length of the inter-satellite ranges. The proposed approach would be a step toward augmented navigation using smart constellations of CubeSats.

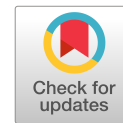
Chapter 9: Conclusions

The last chapter summarises the outputs of this thesis and provides the potential direction of studies and future works related to achieving high accuracy and reliable POD of CubeSats.

2 Precise Orbit Determination of LEO Satellites Based on Undifferenced GNSS Observations

This thesis starts by comprehensively investigating the state-of-the-art POD methods and the required observation, dynamic, and stochastic models. This investigation includes studying the benefits and drawbacks of each method in post- and real-time processing for CubeSats limitations. The chapter provides essential fundamentals of POD of CubeSats for the rest of this PhD research and is covered by the following publication:

Allahvirdi-Zadeh, A., Wang, K., & El-Mowafy, A. (2022). Precise Orbit Determination of LEO Satellites Based on Undifferenced GNSS Observations. *Journal of Surveying Engineering*, 148(1) (pp 1-13), 03121001. DOI: 10.1061/(ASCE)SU.1943-5428.00003



Precise Orbit Determination of LEO Satellites Based on Undifferenced GNSS Observations

Amir Allahviridi-Zadeh¹; Kan Wang²; and Ahmed El-Mowafy³

Abstract: Precise orbit determination (POD) is the procedure for determining the orbit of a satellite with high accuracy. Compared with global navigation satellite systems (GNSS), the low Earth orbit (LEO) satellites have some different features in space, mainly due to perturbations caused by dynamic forces related to their altitudes. Methods for POD of LEO satellites have been developed over the last decades. Nowadays, postprocessed precise orbits are used in different space applications such as radio occultation, satellite altimetry, and interferometric synthetic-aperture radar missions. The advancements in technology decrease the size of LEO satellites and developments in theory increase their orbital accuracy. In recent years, onboard POD has become a hot topic in the navigation and positioning field, which is crucial for, e.g., formation flying of small satellites and GNSS-aided LEO megaconstellations for positioning purposes. This contribution reviews LEO POD methods based on undifferenced GNSS observations in both postmission and real-time data processing. It comprises the quality control step, the models used and their limitations, processing algorithms, and different validation methods. To have a clear insight into the current and the future state of the LEO POD, the most recent developments and important achievements are also discussed. DOI: 10.1061/(ASCE)SU.1943-5428.0000382. This work is made available under the terms of the Creative Commons Attribution 4.0 International license, <https://creativecommons.org/licenses/by/4.0/>.

Author keywords: Precise orbit determination (POD); Precise point positioning (PPP); Kinematic POD; Reduced-dynamic POD; Onboard POD; POD with integer ambiguity resolution.

Introduction

The low Earth orbit (LEO) satellites, including CubeSats, have an orbital altitude that ranges from 300 to 1,500 km. They are used in different space missions, including satellite gravimetry, interferometric synthetic aperture radar (In-SAR), global navigation satellite systems (GNSS) radio occultation, satellite altimetry, global Earth mapping and monitoring, formation flying, and positioning using megaconstellations. Orbits with high accuracy, mainly at the subdecimeter level, are required for almost all these missions (Montenbruck 2017). Precise orbit determination (POD) methods are categorized into three main types: dynamic, kinematic, and reduced-dynamic POD.

The dynamic POD incorporates dynamic models of forces that affect the satellite motion. Such models are used to solve the satellite equation of motion [Eq. (1)] using numerical integration to determine the best-fitting orbit. The equation of motion for a LEO satellite can be considered as a second-order differential equation relating its movement to the accelerations (\mathbf{a}) that perturb the orbit. These perturbation accelerations depend on time (t), position (\mathbf{r}), velocity (\mathbf{v}), and physical forces (\mathbf{f}) affecting the motion. The equation of motion is expressed as follows (Dach et al. 2015):

$$\frac{d^2\mathbf{r}}{dt^2} = \mathbf{a}(t, \mathbf{r}, \mathbf{v}, \mathbf{f}) = -GM \frac{\mathbf{r}}{\|\mathbf{r}\|^3} + \mathbf{a}_p \quad (1)$$

where \mathbf{a} = total acceleration; GM = product of the gravitational constant and the mass of the Earth, the vector \mathbf{r} denotes the position vector of LEO satellite; and $\|\cdot\|$ forms the norm of a vector. The first term on the right side of Eq. (1) is the central gravity term, which has the dominant effect on the LEO satellite. The other perturbations, represented as \mathbf{a}_p , are caused by other physical forces that impact the LEO motion. These forces are categorized into gravitational (\mathbf{f}_g) and nongravitational (\mathbf{f}_{ng}) forces. The gravitational forces include higher-order terms of the Earth gravity (\mathbf{f}_{ho}), the gravitational attractions by the Sun, Moon, and the other celestial planets (\mathbf{f}_{smp}), the solid Earth, pole, and ocean tidal effects (\mathbf{f}_{ti}), and the general relativistic effects (\mathbf{f}_{rel}), combined into the following equation:

$$\mathbf{f}_g = \mathbf{f}_{ho} + \mathbf{f}_{smp} + \mathbf{f}_{ti} + \mathbf{f}_{rel} \quad (2)$$

The nongravitational forces are independent of the satellite mass and include the atmospheric drag (\mathbf{f}_d), solar radiation pressure (SRP) denoted as (\mathbf{f}_r), and the Albedo effect (\mathbf{f}_{al}) as follows:

$$\mathbf{f}_{ng} = \mathbf{f}_d + \mathbf{f}_r + \mathbf{f}_{al} \quad (3)$$

The atmospheric drag is the friction of the satellite with the Earth atmosphere, the SRP is the acceleration due to the absorption or reflection of solar photons, and the Albedo effect is caused by the solar energy flux reflected from the Earth. The aforementioned forces have been discussed in detail by Montenbruck and Gill (2000), and approximate values of these accelerations on an example of LEO satellites were given in Table 32.2 of Montenbruck (2017). To solve the equation of motion and achieve precise orbits, arc-by-arc, different stepwise numerical integration methods are used (Montenbruck and Gill 2000).

The accuracy of the dynamic POD is highly dependent on the accuracy of physical force models used, and the deficiencies in

¹Ph.D. Candidate, School of Earth and Planetary Sciences, Curtin Univ., GPO Box U1987, Perth, WA 6845, Australia. ORCID: <https://orcid.org/0000-0002-3722-4417>. Email: amir.allahviridizadeh@curtin.edu.au

²Associate Professor, School of Earth and Planetary Sciences, Curtin Univ., GPO Box U1987, Perth, WA 6845, Australia; National Time Service Center, Chinese Academy of Sciences, Xi'an 710600, China; Univ. of Chinese Academy of Sciences, Beijing 100049, China (corresponding author). Email: wangkan@ntsc.ac.cn

³Associate Professor, School of Earth and Planetary Sciences, Curtin Univ., GPO Box U1987, Perth, WA 6845, Australia. ORCID: <https://orcid.org/0000-0001-7060-4123>. Email: A.El-Mowafy@curtin.edu.au

Note. This manuscript was published online on October 18, 2021. Discussion period open until March 18, 2022; separate discussions must be submitted for individual papers. This paper is part of the *Journal of Surveying Engineering*, © ASCE, ISSN 0733-9453.

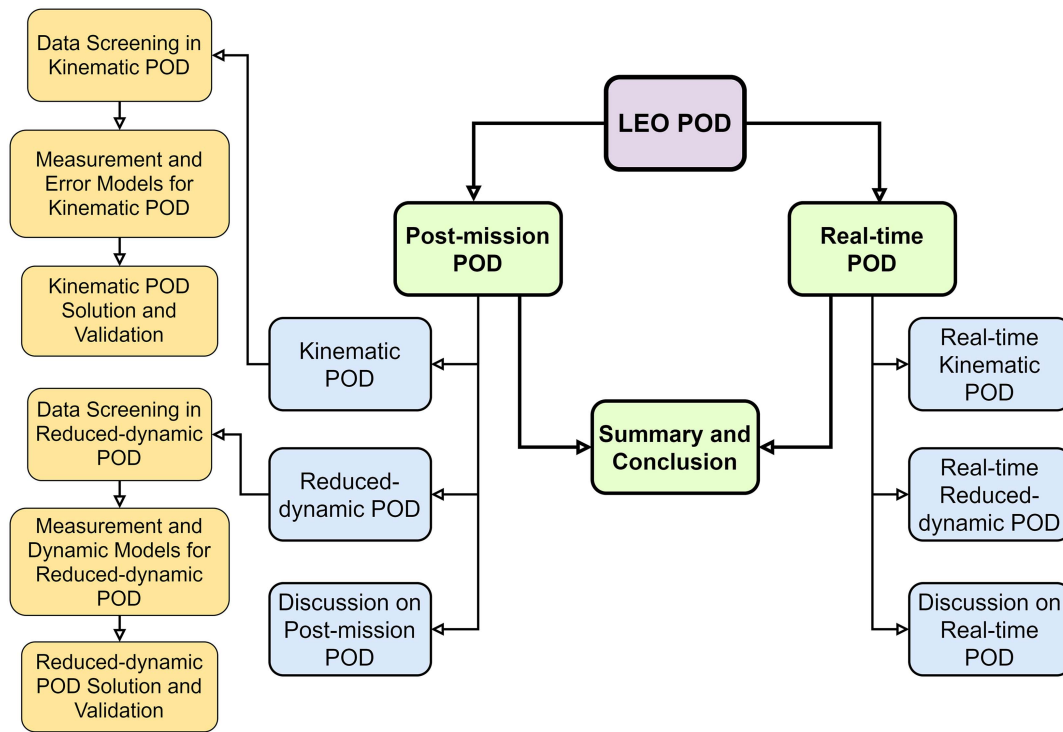


Fig. 1. Flowchart of the paper's structure.

these models cause systematic errors in the POD that grow with the arc length. These deficiencies are related mostly to the nongravitational part, including atmospheric drag and SRP. Accurate modeling of the atmospheric drag depends on the accuracy of the information on the density of the upper atmosphere, detailed knowledge of the interaction of the atmospheric particles with the satellite surface, and the satellite attitude in space. The SRP depends on the satellite shape, surface coating materials, and the orientation. These dependencies cause accuracy degradation in the dynamic POD for the LEO satellites because the drag and SRP coefficients should be estimated during the POD to model these accelerations accurately, which is not happening for the purely dynamic POD. Therefore, the kinematic POD using only GNSS measurements, and the reduced-dynamic POD that uses both dynamic models and GNSS observations, have been developed during the previous 2 decades to improve the orbital accuracy of LEO satellites.

In this paper, the kinematic and reduced-dynamic POD using undifferenced measurements are discussed and compared in detail in the next section from the postmission viewpoint and based on the batch least-squares solution. For each method, the functional, stochastic, and dynamic models, as well as the preprocessing, post-mission solution, and validation steps are given. The concept of real-time POD based on filtering is discussed in the section "Real-Time POD." At the end of each section, a discussion about the latest studies related to each topic is provided. Finally, an outlook on the POD of LEO satellites based on undifferenced GNSS observations, along with a comparison of the discussed methods, is given in the conclusion. A flow diagram of the paper structure including the section headings is provided in Fig. 1 to help readers follow the content.

Postmission POD

The postmission precise LEO orbits are essential in many geoscience applications. Depending on the applications, the precise orbits

may be available with different latencies, from several hours for weather forecasting or urgent satellite imagery, to several days for nonemergency applications that require the highest possible accuracy. The POD of such missions is performed in processing centers using different software packages such as GipsyX from the Jet Propulsion Laboratory (JPL) (Bertiger et al. 2020), Bernese GNSS software from the Astronomical Institute of the University of Bern (AIUB) (Dach et al. 2015), GHOST from the German Space Operations Center (DLR) (Wermuth et al. 2010), and PANDA from Wuhan University (Chuang et al. 2008). In this section, a general algorithm for the postmission POD based on the kinematic and reduced-dynamic methods is discussed. The main issues and questions that the reader could encounter in postmission POD are summarized in Fig. 2 and are discussed subsequently.

Kinematic POD

The kinematic POD method estimates the orbit by processing only the GNSS measurements with a precise positioning approach without considering the dynamic models. Hence, it is susceptible to satellite geometry, measurement errors, noise, and data outages, and orbit estimation will not be accurate or even available when the GNSS data have large biases or gaps. This something could happen in small LEO satellites with limited power capability, such as CubeSats (Wang et al. 2020). Kinematic POD is a popular method in recovering the gravity field information because a priori knowledge of the involved physical forces is not required (Jäggi et al. 2016). The use of this method for the gravity field determination was demonstrated by Švehla and Rothacher (2003b), and the first gravity field model based on kinematic orbits was calculated by Gerlach et al. (2003).

The kinematic POD in postmission mode starts with the quality control of the observations, followed by orbit determination based on the precise point positioning (PPP) approach. These steps are discussed subsequently.

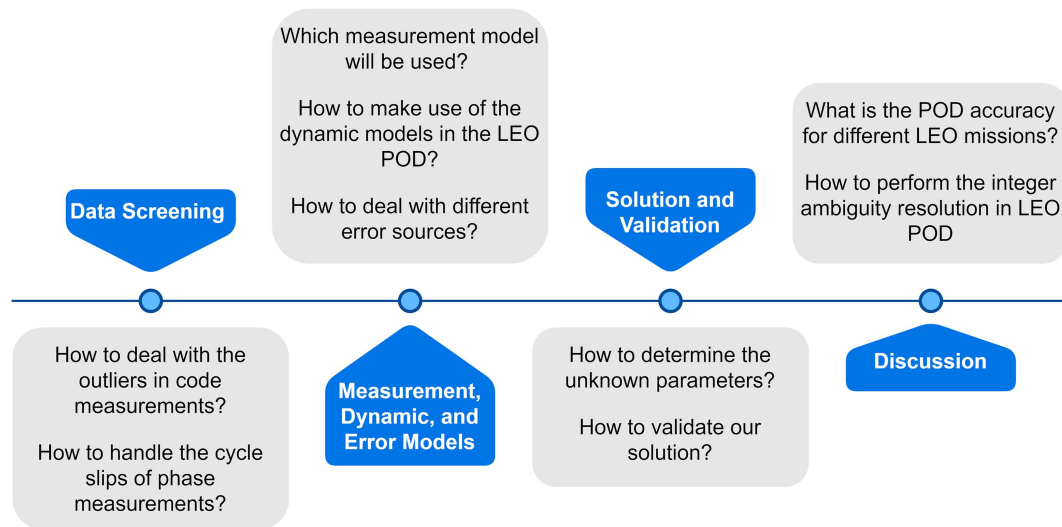


Fig. 2. Questions that will be addressed in each section.

Data Screening in Kinematic POD

The orbital periods of LEO satellites are around 90–120 min, where a typical GPS satellite is visible for them for less than 40 min (Ren and Schön 2018). This short period is due to the low orbital altitude of the LEO satellite and its higher velocity (~ 8 km/s) than the GNSS satellites (~ 4 km/s). During this period, weak GNSS signals and the possible ionospheric scintillations may cause signal loss-of-lock and cycle slips, which would reduce the strength of the model. As such, to achieve precise kinematic orbits, the GNSS measurements should be preprocessed through, e.g., the so-called fault detection and exclusion (FDE) method (El-Mowafy 2014).

The FDE concept is based on testing the null hypothesis that expresses the error-free model against the alternative hypotheses that refer to the possibility of the presence of outliers in observations. It can be summarized as follows:

- Detect the presence of outliers in observations using the overall test statistic $T_q = \hat{\mathbf{e}}^T \mathbf{Q}_y^{-1} \hat{\mathbf{e}}$, which follows a central chi-square distribution in the fault-free mode, where $\hat{\mathbf{e}}$ denotes the observation residuals, assumed to be normally distributed, and \mathbf{Q}_y denotes the covariance matrix of the observations. If $T_q \geq \chi_{\alpha}^2(df, 0)$, the null hypothesis is rejected, indicating the presence of outliers; $\chi_{\alpha}^2(df, 0)$ represents the central chi-square distribution function for a predefined significance level α and the observations' degrees of freedom df .
- Identify the observation that causes this model error using, e.g., the Baarda w-test statistic (Baarda 1968). The identified code observation will be excluded from the rest of the processing, and a new ambiguity will be introduced in the unknown vector for the identified phase observation.

Besides the FDE method, there are other approaches for the cycle slip detection that can be considered for the POD of LEO satellites (e.g., Ren and Schön 2018).

Measurement and Error Models for Kinematic POD

A simplified measurement model for code (P) and phase observations (Φ) between the GNSS satellite s and the LEO spaceborne receiver r at frequency j is expressed

$$\begin{aligned} P_{r,j}^s &= \rho_r^s + c(dt_r - dt^s) + \mu_j I_{r,1}^s + c(d_{r,j} - d_j^s) + e_j \\ \Phi_{r,j}^s &= \rho_r^s + c(dt_r - dt^s) - \mu_j I_{r,1}^s + c(\delta_{r,j} - \delta_j^s) + \lambda_j n_{r,j}^s + \varepsilon_j \end{aligned} \quad (4)$$

where ρ_r^s = receiver-satellite range (m); c = speed of light (m/s); dt_r and dt^s = receiver and satellite clock offsets (s); $\mu_j = f_1^2/f_j^2$ is the unitless coefficient to be multiplied with the ionospheric delay on L1 ($I_{r,1}^s$ in meters) for the frequency f_j ; $d_{r,j}$ and $\delta_{r,j}$ = receiver code and phase hardware biases (s); and d_j^s and δ_j^s = satellite code and phase hardware biases (s), respectively. The receiver code hardware biases are lumped with the receiver clocks, and the phase hardware biases, which are considered constant in time, are lumped with ambiguities. The phase ambiguity parameter $n_{r,j}^s$ is transformed from cycles to the range by multiplying with the wavelength λ_j . Noises and remaining mismodeled errors such as multipath are denoted by e_j and ε_j for code and phase, respectively. The shape of the solar panels and the position of the patch antenna are two main sources of multipath error for the LEO satellites. The tropospheric delays are not present for the LEO satellites due to their altitudes (Hofmann-Wellenhof et al. 2008). For the multi-GNSS receivers, the inter-system biases (ISBs) need to be considered in the processing to compensate for differences in time references and hardware biases between GNSS (Kouba et al. 2017).

GNSS Precise Orbits and Clocks. Precise GNSS orbits and clocks are essential for POD because using the broadcast ephemeris can deliver POD accuracy at the meter to submeter (Montenbruck and Ramos-Bosch 2008). This precise information is available from, e.g., International GNSS Service (IGS) or Center for Orbit Determination in Europe (CODE) with different sampling intervals. Higher-order Lagrange polynomials can be used to interpolate the GNSS satellite orbits with the large sampling intervals of, e.g., 15 min (Feng and Zheng 2005), but interpolating clocks could degrade their accuracy dramatically. As such, analysis centers like the CODE also deliver high-rate clock products. The high-sampled clocks also deliver the possibility to access the short-term stability of the onboard clocks, which is crucial for different applications (Hauschild et al. 2013).

Antenna Phase Center. The LEO satellite antenna phase center offsets (PCOs) and phase center variations (PCVs) can be determined from the consistent nominal antenna models achieved before the launch using a robotic measurement system (Montenbruck et al. 2009). However, these models do not reflect the actual space environment, such as experiencing the effect of the near-field multipath. Neglecting or incorrect modeling of the antenna PCOs and PCVs could cause systematic errors in the LEO POD. To compensate for

this limitation and generate the correct phase center pattern to improve the consistency of the POD solutions, the LEO observations can be used in the empirical inflight calibration methods, i.e., the so-called residual and direct approaches. In the residual approach, phase residuals are used to derive the empirical PCVs as binwise mean values, whereas in the direct approach, the PCV values are considered as the unknowns and estimated in the processing (Jäggi et al. 2009). As an example, Van Den Ijssel et al. (2015) used the residual approach to derive PCVs for the Swarm constellation.

Ionospheric Errors. There are two main approaches to deal with the ionospheric error in the POD process. The first approach removes the first-order term of the ionospheric delay by forming the ionosphere-free (IF) linear combination using dual-frequency GNSS measurements. This combination increases the noise level by a factor of $\sqrt{(f_i^4 + f_j^4)/(f_i^2 - f_j^2)^2}$, e.g., approximately three orders of magnitude for L1 and L2. The corresponding GNSS satellite differential code biases (DCBs) need to be considered if the formed IF combination is different from the one contained in the precise GNSS satellite clocks. Despite using the IF combination, the higher-order ionospheric terms are not removed. The magnitude of these terms is in the range of few millimeters to several centimeters depending on the solar activity conditions, carrier frequency, and relative orientation of the LEO satellite to the magnetic field (Hoque and Jakowski 2007). These errors are generally neglected in most POD processing approaches.

The second approach in dealing with the ionospheric delay is to use the uncombined measurements and estimate ionospheric delays as the unknown parameters. It allows for extensions to an arbitrary number of frequencies and could strengthen the model by implementing the spatial and temporal constraints on the ionospheric parameters (Odijk et al. 2016). Because the first approach, i.e., forming IF combination, is used in most POD studies, it will be used in the rest of this paper.

Regardless of the method used to deal with the ionospheric delay, the ionospheric scintillation can degrade or even interrupt the GNSS tracking (Kintner et al. 2007). Such performance reduction is observed in the Swarm GPS receiver, and several modifications in the tracking loop and the antenna field of view were performed after launch to solve the problem (Van den Ijssel et al. 2016).

Unknown Parameter Vector. The unknown parameter vector in the postmission kinematic POD is defined as $\mathbf{x} = (\mathbf{r}^T, dt, \mathbf{b}^T)^T$ where for epoch t with m satellites, the vector $\mathbf{r} = (x_t, y_t, z_t)^T$ is the LEO satellite position, the term dt contains the LEO clock offsets in range, and $\mathbf{b} = (b_t^{s_1}, \dots, b_t^{s_m})^T$ includes the IF ambiguities that are lumped with the corresponding hardware biases.

Kinematic POD Solution and Validation

Estimation. To determine the unknown parameters at epoch t (for $t = 1, \dots, k$), the IF combination of code (P_{IF}) and phase (Φ_{IF}) measurements are considered in the observation vector $\mathbf{y} = (y_1^T, y_2^T, \dots, y_k^T)^T$, where $y_t = (P_{IF}^t, \Phi_{IF}^t)^T$. In a batch least-squares estimation, the observation linearized model is expressed

$$E\{\Delta\mathbf{y}\} = \mathbf{J}\Delta\mathbf{x}; \quad D\{\Delta\mathbf{y}\} = \mathbf{Q}_y \quad (5)$$

where E and D = mathematical expectation and dispersion operators, respectively; and \mathbf{J} = partial derivative of the observations concerning the unknown parameters that form the design matrix. Different observation weighting models including the equal and the elevation-dependent weighting models are often applied to form the variance-covariance matrix of the observations \mathbf{Q}_y . However,

giving equal weights to all observations may not be optimal for all satellites and the correct calculation of the elevation angels requires the attitude information recorded by the satellites that may not be available for low-power satellites. Using a weighting model based on signal-to-noise ratio is a possible solution that was proposed by Allahviridi-Zadeh et al. (2021). Eq. (5) can be efficiently solved using the parameter pre-elimination and back substitution.

Validation. After the data screening and processing steps, the output orbits should be validated using internal and external validation methods. The internal validation method uses a precise reference orbit, which can, e.g., be prepared from the reduced-dynamic POD method with the single-difference integer ambiguity resolution. Besides, the overlap analysis between subsequent orbits is often used to assess the internal consistency (Montenbruck 2017). In this method, two orbits (arcs) are generated while they have time overlap, e.g., daily arcs that are 30 h long. The differences between two orbits in the overlapping period should be small enough to validate the processing results.

The external validation method uses the non-GNSS technique such as the satellite laser ranging (SLR) and K-band ranging (KBR) system to compare the measured range with that computed from the POD (Arnold et al. 2019). Some LEO altimetry missions such as Sentinel-3, which require high accuracy in the radial direction, are equipped with a Doppler Orbitography and Radiopositioning Integrated by Satellite (DORIS) antenna (Auriol and Tourain 2010). It can be used for both the DORIS POD and as an external validation tool (Fernández 2019).

The external validation methods are mainly available for the large LEO satellites such as GOCE (Bock et al. 2014) and Sentinel-3 (Fernández et al. 2016) that are equipped with the required costly sensors. This may not be possible for small satellites, such as CubeSats. The internal validation and self-consistency POD tests, such as the analysis of residuals and the orbit overlaps, are thus considered for these satellites.

Reduced-Dynamic POD

As discussed previously, the dynamic and kinematic POD have some limitations. The former requires comprehensive dynamic models that are not precisely available for LEO satellites (especially the nongravitational-force models), and the latter is sensitive to data outages and weak GNSS satellite geometry. The reduced-dynamic POD, however, can benefit from both sides, i.e., the availability of dynamic models, as well as GNSS observations. In this method, the initial conditions, force model parameters, and possible stochastic accelerations are estimated instead of the epochwise LEO positions in the kinematic POD.

Because this POD method delivers more accurate orbital positions than the other two approaches, it has been used as the primary method to determine the orbit of different LEO missions, such as TOPEX/Poseidon (Yunck et al. 1994), CHAMP (Švehla and Rothacher 2003b) Jason-1 (Haines et al. 2004), GRACE (Kang et al. 2003), GOCE (Bock et al. 2014), Swarm (Van Den Ijssel et al. 2015), HY-2A (Guo et al. 2015), FY-3C (Zhang et al. 2018), Sentinel (Fernández 2019), and GRACE-FO (Kang et al. 2020). In the following, different steps of this approach are discussed.

Data Screening in Reduced-Dynamic POD

As explained in the “Data Screening for Kinematic POD” section, similar methods can be performed to screen GNSS data before starting the POD processing. However, some POD software packages, such as Bernese, perform the data screening step along with the POD steps. Such procedure is mentioned in the “Reduced-Dynamic POD Solution and Validation” section, Step 2.

Measurement and Dynamic Models for Reduced-Dynamic POD

Based on the measurement models given in Eq. (4), the LEO receiver clocks and ambiguities are estimated together with the elements used to propagate the LEO orbits, i.e., the satellite initial conditions, force model parameters, and possible stochastic accelerations. The latter two terms can be used to form the improved orbital accelerations. The dynamic model, expressed by the equation of motion [Eq. (1)], is a second-order differential equation. With the unknowns mentioned previously estimated in a least-squares adjustment, the LEO satellite trajectory can be propagated for any arbitrary time point with the improved accelerations and the initial state vector $\mathbf{S}_0 = (\mathbf{r}_0^T, \mathbf{v}_0^T)^T$ by using numerical integration of the equation of motion. The initial position \mathbf{r}_0 and velocity \mathbf{v}_0 vectors can be defined based on Keplerian elements (Dach et al. 2015). **Variational Equations.** Due to the nonlinearities, the partial derivatives of the state vector at an arbitrary time t with respect to the initial state vector and the force model parameters need to be numerically integrated. These partials represent a transition matrix $\tilde{\Phi} = \partial_{\mathbf{S}_0} \mathbf{S}_t$, which is the partial derivatives of the current state using the initial state vector, and a sensitivity matrix $\tilde{\mathbf{S}} = \partial_{\mathbf{p}} \mathbf{S}_t$, which is the partial derivatives with respect to the force model parameters \mathbf{p} . They can be computed using numerical integration of the following so-called variational equations (Montenbruck and Gill 2000):

$$\begin{aligned} \frac{d}{dt} \begin{pmatrix} \tilde{\Phi} \\ \tilde{\mathbf{S}} \end{pmatrix} &= \begin{pmatrix} \partial_{\mathbf{r}} \mathbf{v} & \partial_{\mathbf{v}} \mathbf{v} \\ \partial_{\mathbf{r}} \mathbf{a} & \partial_{\mathbf{v}} \mathbf{a} \end{pmatrix}_{6 \times 6} \begin{pmatrix} \tilde{\Phi} \\ \tilde{\mathbf{S}} \end{pmatrix} + \begin{pmatrix} 0 & \partial_{\mathbf{p}} \mathbf{v} \\ 0 & \partial_{\mathbf{p}} \mathbf{a} \end{pmatrix}_{6 \times (6+n_p)} \\ &= \begin{pmatrix} 0 & \mathbf{I} \\ \partial_{\mathbf{r}} \mathbf{a} & \partial_{\mathbf{v}} \mathbf{a} \end{pmatrix}_{6 \times 6} \begin{pmatrix} \tilde{\Phi} \\ \tilde{\mathbf{S}} \end{pmatrix} + \begin{pmatrix} 0 & 0 \\ 0 & \partial_{\mathbf{p}} \mathbf{a} \end{pmatrix}_{6 \times (6+n_p)} \end{aligned} \quad (6)$$

where n_p = number of the dynamic parameters estimated during the orbit determination to account for effects like the atmospheric drag and SRP. Here, $\partial_{\mathbf{r}} \mathbf{v}$ is zero because \mathbf{r} and \mathbf{v} are two independent components in the state vector. Likewise, \mathbf{v} does not depend explicitly on \mathbf{p} , and $\partial_{\mathbf{p}} \mathbf{v}$ is zero. This variation equation is numerically integrated by using existing force models and improved model parameters (in the last iteration) to generate the corresponding partial derivatives at an arbitrary time point. Examples of the existing force models are given in Table 1.

Empirical Accelerations. Despite using available force models, deficiencies could still exist in the models for the SRP and air drag. For example, the drag force model depends on the satellite body (shape, size, and orientation), the distribution of atmospheric layer density, and the predictive assessment of this density (Vallado and

Finkleman 2014). The possible model deficiencies can thus be compensated by using empirical accelerations (Montenbruck et al. 2005). The empirical accelerations are estimated in the orbit determination procedure as the unknown parameters in the radial $\alpha_{\mathbf{R}}$, along-track $\alpha_{\mathbf{AT}}$, and cross-track $\alpha_{\mathbf{CT}}$ directions. They can be lumped in the term $\alpha_{\mathbf{EMP}}$ as follows:

$$\alpha_{\mathbf{EMP}} = \alpha_{\mathbf{R}} \mathbf{e}_{\mathbf{R}} + \alpha_{\mathbf{AT}} \mathbf{e}_{\mathbf{AT}} + \alpha_{\mathbf{CT}} \mathbf{e}_{\mathbf{CT}} \quad (7)$$

where $\mathbf{e}_{\mathbf{R}}$, $\mathbf{e}_{\mathbf{CT}}$, and $\mathbf{e}_{\mathbf{AT}}$ represent the unit vectors in the radial, cross-track, and along-track directions, respectively. The accelerations can be estimated as piecewise constants for a time interval ($t_{i-1} \leq t < t_i$) (Jäggi et al. 2005). The drawback of this concept is that the changes in the improved orbit are not differentiable at t_i . Therefore, the concept of piecewise-linear accelerations was introduced by Jäggi et al. (2006) to overcome this limitation and allow one to set up continuous piecewise accelerations, which improves orbital accuracy. As an alternative approach, small velocity changes at the predefined epochs, the so-called pseudostochastic pulses, can be estimated. However, the improvement could be discontinuous at the time epochs introducing the pulses (Jäggi et al. 2006).

Stochastic parameters in the reduced-dynamic POD can be parametrized as a combination of the aforementioned approaches. One procedure, which is used in the GHOST (GPS high precision orbit determination software tools) package, starts with computing SRP and drag accelerations using simple models (Table 1), then adjusts scale factors (coefficients) for these accelerations during the orbit determination, and finally estimates the piecewise-constant empirical accelerations for the predefined subintervals to compensate for model deficiencies. Another possible procedure, e.g., that used in the Bernese GNSS software, is based on different parameterizations of the stochastic parameters in the different processing steps of the reduced-dynamic POD procedures. This procedure is explained in the following section.

Reduced-Dynamic POD Solution and Validation

The postmission solution of the unknown parameters can be performed with the following steps, taking the example of the Bernese GNSS version 5.2 software for the LEO POD using dual-frequency GPS observations, with a flowchart of these steps shown in Fig. 3:

- Step 1: The solution starts from a single point positioning using code observations passing the outlier detection step. The collocation method, as the numerical integration method in Bernese (Dach et al. 2015), is then used to generate a code-based reduced-dynamic orbit, fitting the kinematic positions. These outputs will be used for the GNSS phase observations' preprocessing in the following step.

Table 1. Examples of dynamic models used in the reduced-dynamic POD

| Item | Description |
|--|--|
| Earth's gravity | EGM 2008 (Pavlis et al. 2008) |
| Tides (solid Earth tides, pole tides, and ocean tides) | IERS 2010 (Petit and Luzum 2010) |
| Other planets' ephemeris | JPL Development Ephemeris (JPL DE405) (Standish 1998) |
| Radiation pressure | Cannon-ball model (Montenbruck and Gill 2000), cylindrical Earth shadow (Allahverdi-Zadeh et al. 2016) |
| Atmospheric drag | Jacchia 71 density model (Jacchia 1971) |
| Antenna offset | Daily solar flux and hourly geomagnetic activity (Xiong et al. 2018) Constant phase center coordinate in the SRF (Rothacher and Schmid 2010) Attitude information of the satellite (Giorgi 2017) |
| Empirical acceleration | Pseudostochastic pulses, piecewise constant/continuous accelerations (Jäggi et al. 2006) |
| Terrestrial reference frame | ITRF2014 (Altamimi et al. 2016) |
| Earth orientation | IAU precession, nutation, and sidereal time models (Petit and Luzum 2010), IERS polar bulletin (Luzum et al. 2001) |
| Inertial reference frame | ICRF (J2000.0) (Ma et al. 1998) |

Note: EGM = earth gravitational model; IERS = International earth rotation and reference systems service; SRF = satellite reference frame; ITRF2014 = International terrestrial reference frame 2014; IAU = International Astronomical Union; and ICRF = International Celestial Reference Frame.

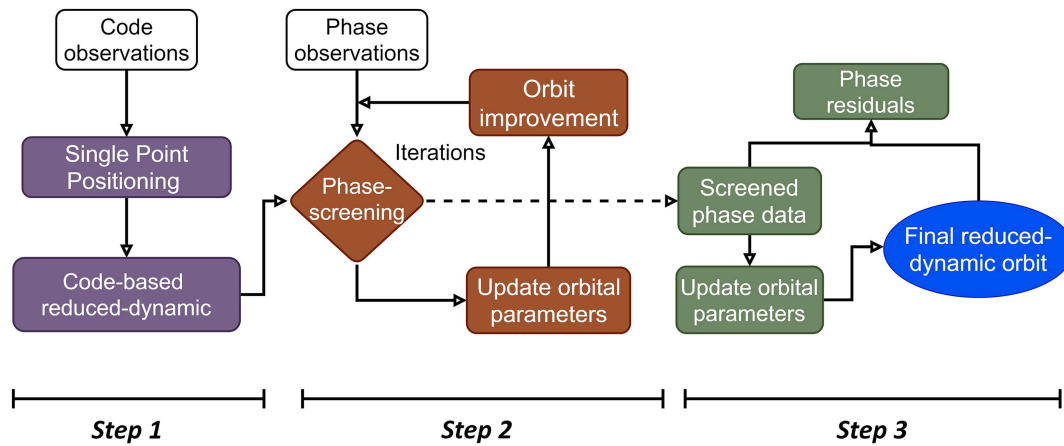


Fig. 3. Flowchart of reduced-dynamic POD computation procedure.

- Step 2: Phase observations are screened and used to improve the orbital accuracy in an iterative process. The entire orbit is divided into n_α intervals with equal time periods, and in each iteration, the stochastic velocity changes are determined for each interval. For a LEO satellite with an orbital period of 90–120 min and the GNSS measurements with a sampling interval of 10–30 s, the orbit interval could be set to, e.g., 15 min. The estimated velocity pulses are used along with the estimated initial conditions and force model parameters in a numerical integration step to improve the orbit. The updated orbit in the last iteration and the screened phase data will be used in the final reduced-dynamic POD.
- Step 3: In the final POD, another round of least-squares estimation is performed using the fault-free phase observations and considering reduced time intervals, e.g., from 15 to 6 min, to estimate piecewise constant accelerations. The numerically integrated orbit is considered as the final reduced-dynamic orbit. The validation methods discussed in the “Kinematic POD Solution and Validation” section can also be used to validate the final reduced-dynamic orbit.

Discussion on Postmission POD

The kinematic and the reduced-dynamic POD using single- and dual-frequency observations are used in different LEO satellite-related studies. Table 2 presents a selection of LEO POD accuracies achieved with the different validation methods based on undifferenced dual-frequency measurements with both the kinematic and reduced-dynamic methods used in different missions. These results were obtained from different studies over a rather long timespan (2005–2020). The presented POD accuracies are therefore affected by the progress in the gravitational force modeling achieved by different gravity field missions over these years. Satellites in higher orbits often have lower root mean square (RMS) errors, mainly due to the harsh dynamical environment of satellites in the lower altitudes (e.g., Swarm-B satellite in Table 2 that has a higher altitude than Swarm-A and Swarm-C).

The orbital accuracy of the kinematic POD method is correlated to the epochwise receiver clock offset determination. There is a high correlation between the radial component of the orbit and the receiver clock parameters (Weinbach and Schön 2012). Stable oscillators thus enable a robust clock model and can stabilize the radial orbital component. This concept is simulated for the GRACE mission to model the receiver clock offset, and a 40% improvement in the radial direction is shown (Yang et al. 2014).

In all the aforementioned studies, the first-order ionospheric delay is removed by forming the IF linear combination. However, as

Table 2. Summary of LEO POD results in different studies

| Mission | Accuracy in terms of RMS with respect to the reference solution (cm) | POD | References |
|--------------|--|------------------|--|
| CHAMP | SLR RMS: 2.7 | Kin ^a | Švehla and Rothacher (2005b) |
| | SLR RMS: 2.5 | RD ^b | |
| GRACE-A | SLR RMS: 2.2 | RD | Jäggi et al. (2007) |
| | SLR RMS: 3.0 | Kin | |
| GRACE-B | SLR RMS: 1.9 | RD | |
| | SLR RMS: 2.8 | Kin | |
| GRACE | K-band RMS: 1.1 | RD | |
| | K-band RMS: 2.0 | Kin | |
| GOCE | SLR RMS: 2.3 | Kin | Bock et al. (2011) |
| | SLR RMS: 2.0 | RD | |
| Swarm | SLR RMS: 4-5 | Kin | Van Den Ijssel et al. (2015) |
| | SLR RMS: 2 | RD | |
| Swarm-A | SLR RMS: 3.2 | Kin | Jäggi et al. (2016) |
| Swarm-B | SLR RMS: 2.7 | | |
| Swarm-C | SLR RMS: 3.1 | | |
| Fengyun-3C | Overlapping 3D RMS: 3.4 | RD | Li et al. (2017) |
| TG02 | Overlapping 3D RMS: 1.4SLR RMS <3.5 | RD | Li et al. (2018) |
| Sentinel 1-A | QWG 3D RMS ^c <2.5 | RD | Peter et al. (2017), Fernández et al. (2018), Fernández (2019) |
| Sentinel 1-B | QWG 3D RMS <4 | | |
| Sentinel 2-A | QWG 3D RMS <2.5 | | |
| Sentinel 2-B | QWG 3D RMS <2 | | |
| Sentinel 3-A | QWG 3D RMS <3 SLR RMS <1.5 | | |
| Sentinel 3-B | QWG 3D RMS <3 SLR RMS <1.5 | | |
| GRACE-FO C | SLR RMS: 1.5 | RD | Kang et al. (2020) |
| GRACE-FO D | SLR RMS: 1.5 | | |
| GRACE-FO | K-band RMS: 0.5 | | |

^aKin = kinematic.

^bRD = reduced-dynamic.

^cQWG = QWG 3D RMS values achieved by comparing Copernicus POD solutions with the POD Quality Working Group (QWG) as external solutions.

discussed in the “Measurement and Error Models of Kinematic POD” section, the uncombined observations can also be applied in the POD. The kinematic POD with raw measurements, considering the higher-orders of the ionospheric delays, provided similar orbital

accuracy compared with using the IF combination (Zehentner and Mayer-Gürr 2016).

Although this paper reviews LEO POD methods based on using undifferenced GNSS measurements, it is worth mentioning that differencing of the GNSS observables were also used for LEO POD, where GNSS observations collected on a LEO satellite are differenced with GNSS observations at a known ground reference station. The double differencing of GPS phase measurements with ambiguity resolution for the kinematic POD of CHAMP was carried out by Švehla and Rothacher (2003a). The double differences (DD) were formed between the IGS permanent stations and the LEO satellite to reduce the orbit- and clock-related errors from the observation model. However, with such long baselines, the remaining orbital and clock errors still need to be considered. Besides, tropospheric errors need to be considered for the observations at the ground stations. Furthermore, the concept of DD between two GRACE satellites formed the first GPS baseline in space with the millimeter-accuracy after performing ambiguity resolution (Švehla and Rothacher 2004). Such a baseline can be used for the orbit validation and gravity recovery in the GRACE-FO mission (Kang et al. 2020).

Single receiver integer ambiguity resolution (IAR) can effectively improve the positioning accuracy; however, it requires corrections for the hardware biases to recover the integer nature of the ambiguities. Different IAR methods were reviewed comprehensively by Teunissen and Khodabandeh (2015). Among the available single-receiver-based IAR methods, the methods proposed by Laurichesse et al. (2009) and Bertiger et al. (2010) are usually used for the LEO POD. The former method is based on identifying the satellite wide-lane biases, using them to estimate the undifferenced wide-lane ambiguities for a network, and finally fixing L1 ambiguities for these receivers.

A similar approach has been tested for GRACE and Jason-1, i.e., their wide-lane measurements were corrected by the GPS fractional wide-lane corrections provided by the network. Next, the GPS satellite integer clocks derived from the network were used to estimate the IF phase residuals. Finally, by forming between-satellite single differences of these residuals, the receiver clock offset was removed and the integer ambiguities were estimated. The orbits of these satellites determined by the unambiguous measurements were shown to be more accurate than the orbits from float solutions, i.e., those estimated with float ambiguities.

In the method proposed by Bertiger et al. (2010), GPS orbit errors and clock offsets, dual-frequency phase biases, and corresponding wide-lane values were estimated in a network solution and were used to form integer constraints in the LEO data processing. The method has been tested for the Jason-2 mission, and it was shown that the radial orbital accuracy increased significantly, i.e., reaching below 1 cm, fulfilling the altimetry requirements.

The wide-lane ambiguities have a longer wavelength than the original ambiguities, which eases the ambiguity resolution by reducing the number of potential ambiguity candidates. In addition to the aforementioned methods, the IAR for Sentinel-3A data has been performed by Montenbruck et al. (2018) using the wide-lane bias products and the integer phase clock offset corrections from the Centre National d'Etudes Spatiales (CNES). The orbit generated with fixed ambiguities outperformed the orbit of float solutions. The RMS value (validated by the SLR) reached 5 mm, which has a 30% improvement. The systematic biases in the cross-track direction were also revealed through the IAR due to the errors in the antenna PCOs, which can be absorbed by the ambiguities in the float solution.

In addition to the kinematic and the reduced-dynamic methods, a fourth POD approach was introduced by Švehla and Rothacher (2005a), called the reduced-kinematic POD. However, it has not

been developed further because it was used inside the kinematic POD only for the gravity field determination (Švehla 2018).

In summary, both the kinematic and the reduced-dynamic POD in the postmission processing can deliver orbital accuracy at the centimeter-level, which can be improved by the IAR. This accuracy fulfills the requirements of most postprocessed LEO applications (Montenbruck 2017). The reduced-dynamic POD makes use of the strong dynamic models and can normally deliver higher orbital accuracy than the kinematic mode. However, the extensive dynamic modeling requires high computational load, which is not a big issue in postmission by the ground-based processing centers, but could be an issue for onboard processing, especially for small satellites such as CubeSats.

Real-Time POD

The real-time POD of LEO satellites is an essential requirement for their control and guidance. It provides a valid link between the data collected using the onboard sensors and the ground monitoring stations that support data collection and facilitate dissemination. However, there are some challenges in the onboard POD. For example, due to the limited power and memory budget, especially for small LEO satellites such as CubeSats, the onboard algorithms should consider the trade-off among computational load, onboard power resources, and the required orbit accuracy (Montenbruck and Ramos-Bosch 2008). Therefore, using dynamic models with a high degree and time-/memory-consuming estimation approaches, such as the batch least-squares adjustment, might not be preferable for CubeSats. One thus often needs to simplify the dynamic model by, e.g., utilizing the Earth's gravity model with a lower degree, and perform the POD based on a real-time filter. The same applies to additional information, e.g., the attitude information, which requires more sensors and payload, but would be important for achieving good accuracy and availability of the POD results.

The real-time POD algorithms are based on recursive methods for the nonlinear models, including the extended Kalman filter (EKF) and the unscented Kalman filter (UKF). The EKF method is based on linearization of the dynamic and measurement models, whereas the UKF approach relies on a nonlinear transformation (the so-called unscented transformation) to propagate the mean and covariance information without using linearizing models. The UKF is developed for highly nonlinear problems, but the real-time filter performs close to linearity if proper initial conditions and accurate force models are considered in the filter (Montenbruck 2017). Therefore, the EKF method, as the most common method used in the onboard POD, is explained in this paper. It is followed by a discussion about the limitations of the real-time POD and the latest studies in this field. The algorithms for the orbit determination based on UKF were explained by, e.g., Pardal et al. (2010).

Real-Time Kinematic POD

The state vector for the kinematic POD at each epoch t is expressed as $\mathbf{x} = (\mathbf{r}^T, dt, \mathbf{b}^T)^T$. The processing is initialized with the initial values of the filter state (\mathbf{x}_0) and its covariance matrix (\mathbf{Q}_0), which are typically estimated using the least-squares adjustment. Because no dynamic model was used in the kinematic POD, an identity matrix is considered as the transition matrix ($\Phi_t^{\text{KIN}} = \mathbf{I}$, where KIN refers to kinematic) to update the clock offset and ambiguities combined in $\hat{\mathbf{x}}'$ as follows:

$$\begin{aligned}\hat{\mathbf{x}}'_{t|t-1} &= \Phi_t^{\text{KIN}} \hat{\mathbf{x}}'_{t-1|t-1} \\ \hat{\mathbf{Q}}'_{t|t-1} &= \Phi_t^{\text{KIN}} \mathbf{Q}'_{t-1|t-1} \Phi_t^{\text{KIN}T} + \mathbf{Q}_t^{\text{KIN}}\end{aligned}\quad (8)$$

where the process noise matrix is diagonal, i.e., $\mathbf{Q}_t^{\text{KIN}} = \text{diag}(\sigma_{dt}^2, \sigma_b^2)$, which represents the process noise of the clock offset modeled as random-walk, with the term \mathbf{b} due to the hardware biases included in it. If cycle slips take place, the temporal link of the ambiguities is interrupted.

Before applying the measurement update, data screening process discussed in the ‘‘Data Screening for Kinematic POD’’ section should be performed. During the measurement update, the predicted states can be considered as pseudo-observations that aid GNSS observations of the current epoch, and the unknowns can be estimated using a sequential least-squares adjustment, with the measurement and stochastic models expressed as follows:

$$\begin{aligned} E \begin{pmatrix} \hat{\mathbf{x}}'_{t|t-1} \\ \mathbf{y}_t \end{pmatrix} &= \begin{pmatrix} \mathbf{0} & \mathbf{I} \\ \mathbf{J}_r & \mathbf{J}_{x'} \end{pmatrix} \begin{pmatrix} \mathbf{r}_t \\ \mathbf{x}'_t \end{pmatrix}; \\ D \begin{pmatrix} \hat{\mathbf{x}}'_{t|t-1} \\ \mathbf{y}_t \end{pmatrix} &= \begin{pmatrix} \hat{\mathbf{Q}}_{t|t-1} & \mathbf{0} \\ \mathbf{0} & \mathbf{Q}_{y_t} \end{pmatrix} \end{aligned} \quad (9)$$

where \mathbf{J}_r and $\mathbf{J}_{x'}$ = partial derivatives of the observations with respect to the kinematic orbits and the combined clocks and ambiguities, respectively. Although expressed in different forms, the aforementioned sequential least-squares adjustment is equivalent to EKF (Humpherys and West 2010), provided that the same temporal link is considered.

Real-Time Reduced-Dynamic POD

The vector $\mathbf{x} = (\mathbf{r}_0^T, \mathbf{v}_0^T, \mathbf{p}^T, \boldsymbol{\alpha}_{\text{EMP}}^T, dt, \mathbf{b}^T)^T$ is the EKF state vector in the reduced-dynamic POD, where $\mathbf{p} = (c_r, c_d)^T$ contains the SRP and drag coefficients. For m number of satellites, there are $12 + m$ unknowns at each epoch (six satellite state components, two coefficients for the SRP and air drag, three empirical accelerations, one clock offset, and m phase ambiguities). The propagation in time update involves a simple integration method to compute both the satellite trajectory and the partial derivatives concerning the state vector and the term \mathbf{p} . The empirical acceleration parameters $\boldsymbol{\alpha}_{\text{EMP}}$ are updated using a Gauss-Markov process, expressed

$$\boldsymbol{\alpha}_{\text{EMP}_{t|t-1}} = l \boldsymbol{\alpha}_{\text{EMP}_{t-1|t-1}} \quad \text{where } l = e^{-\frac{|\Delta_{t,t-1}|}{\tau}} \quad (10)$$

where $\Delta_{t,t-1}$ = time difference between the current and previous epochs; τ = time constant; and l = exponential damping factor. Other state parameters of the filter remain constant during this step with a white process noise model. Considering $\partial_{(x,y,z,v_x,v_y,v_z)} \boldsymbol{\alpha}_{\text{EMP}_{t|t-1}} = \mathbf{0}$ and $\partial_{\boldsymbol{\alpha}_{\text{EMP}_{t-1|t-1}}} \boldsymbol{\alpha}_{\text{EMP}_{t|t-1}} = l$, the full structure of the reduced-dynamic EKF transitions matrix $\boldsymbol{\Phi}_t^{\text{RD}}$, where the superscript RD denotes reduced dynamic, is expressed

$$\begin{aligned} \boldsymbol{\Phi}_t^{\text{RD}} &= \partial_{\mathbf{x}_{t-1|t-1}} \mathbf{x}_{t|t-1} \\ &= \begin{bmatrix} \tilde{\boldsymbol{\Phi}}_{6 \times 6} & \tilde{\mathbf{S}}_{6 \times 2} & \tilde{\mathbf{S}}_{6 \times 3} & \mathbf{0}_{6 \times 1} & \mathbf{0}_{6 \times m} \\ \mathbf{0}_{2 \times 6} & \mathbf{I}_{2 \times 2} & \mathbf{0}_{2 \times 3} & \mathbf{0}_{2 \times 1} & \mathbf{0}_{2 \times m} \\ \mathbf{0}_{3 \times 6} & \mathbf{0}_{3 \times 2} & l \times \mathbf{I}_{3 \times 3} & \mathbf{0}_{3 \times 1} & \mathbf{0}_{3 \times m} \\ \mathbf{0}_{1 \times 6} & \mathbf{0}_{1 \times 2} & \mathbf{0}_{1 \times 3} & 1 & \mathbf{0}_{1 \times m} \\ \mathbf{0}_{m \times 6} & \mathbf{0}_{m \times 2} & \mathbf{0}_{m \times 3} & \mathbf{0}_{m \times 1} & \mathbf{I}_{m \times m} \end{bmatrix}_{(12+m) \times (12+m)} \end{aligned} \quad (11)$$

where $\tilde{\boldsymbol{\Phi}}$ and $\tilde{\mathbf{S}}$ are obtained from the numerical integration of the variational equation. The covariance update is expressed

$$\mathbf{Q}_{t|t-1} = \boldsymbol{\Phi}_t^{\text{RD}} \mathbf{Q}_{t-1|t-1} \boldsymbol{\Phi}_t^{\text{RD}T} + \mathbf{Q}_t^{\text{RD}} \quad (12)$$

where the process noise matrix \mathbf{Q}_t^{RD} is determined based on assumptions and simulations that are designed to prevent filter divergence. An example of such a matrix has been given by Montenbruck and Ramos-Bosch (2008), where the empirical accelerations and the receiver clock offsets were modeled using Gauss-Markov and random walk processes, respectively.

Next, the measurement update is performed to improve the filter state vector with the newly available observations, after data screening and cycle slip detection process, as follows:

$$\begin{aligned} \mathbf{K}_t &= \mathbf{Q}_{t|t-1} \mathbf{J}_t^T (\mathbf{Q}_{y_t} + \mathbf{J}_t \mathbf{Q}_{t|t-1} \mathbf{J}_t^T)^{-1} \\ \hat{\mathbf{x}}_{t|t} &= \hat{\mathbf{x}}_{t|t-1} + \mathbf{K}_t (\mathbf{y}_t - \mathbf{j}_t(\hat{\mathbf{x}}_{t|t-1})) \\ \mathbf{Q}_{t|t} &= (\mathbf{I}_m - \mathbf{K}_t \mathbf{J}_t) \mathbf{Q}_{t|t-1} \end{aligned} \quad (13)$$

The gain matrix \mathbf{K}_t depends on the covariance matrix of the measurements \mathbf{Q}_{y_t} and the propagated covariance from the time update step $\mathbf{Q}_{t|t-1}$. The term \mathbf{J}_t is the partial derivative for the filter state vector, and $\mathbf{j}_t(\hat{\mathbf{x}}_{t|t-1})$ contains the computed values of the observations.

Finally, an integration method, such as the fourth-order Runge-Kutta (Butcher 2016), can be used to propagate the trajectory of the LEO satellite over a fixed time step to the desired output sampling interval (Montenbruck and Ramos-Bosch 2008). A flowchart of these steps is given in Fig. 4. It is possible to simplify the aforementioned algorithm to meet the computational budget of the small satellites such as CubeSats by considering drag and SRP coefficients as modeled values rather than estimating them, and not estimating empirical accelerations, as explained by Yang et al. (2016). However, it reduces the orbital accuracy to a meter level.

Discussion on Real-Time POD

Different studies were carried out to overcome the limitations of real-time POD. One of these limitations is the poor accuracy of GPS orbits and clock offsets provided by the broadcast ephemeris. It was reported by Montenbruck and Ramos-Bosch (2008) that depending on the satellite altitude, an accuracy [defined by the daily three-dimensional (3D) RMS] of 40–60 cm was achieved using GPS dual-frequency observations and broadcast ephemeris. The simulated multi-GNSS measurements from GPS, Galileo, and Beidou-3 satellites were tested by Hauschild and Montenbruck (2020) with a flight-proven algorithm developed by Montenbruck et al. (2008). It was reported that combining all measurements deliver LEO satellite orbits with 10.4-cm 3D RMS error when using broadcast ephemeris.

Real-Time GNSS Precise Orbits and Clocks

One of the recent advancements of PPP is the availability of real-time GNSS precise orbit and clock corrections that can be provided by geostationary (GEO) satellites. There are some commercial services, such as G4 from Fugro (Tegedor et al. 2017) and TerraStar-D (Jokinen et al. 2014) that can provide such a service. In addition to the commercial services, the Japanese Quasi-Zenith Satellite System (QZSS) also provides the orbits and clock corrections through the L6 signal broadcast by the navigation satellites (Cabinet Office 2020) within the Multi-GNSS Advanced Demonstration Tool for Orbit and Clock Analysis (MADOCA) service. Moreover, the new-generation Australia/New-Zealand Satellite-Based Augmentation System (AU/NZ-SBAS) broadcasts real-time precise orbit and clock corrections to enable PPP through a GEO link (Barrios et al. 2018). These two free-of-charge services are available only over the Asia-Pacific region. However, it is expected that such services can be available globally in the future by combining different SBASs and

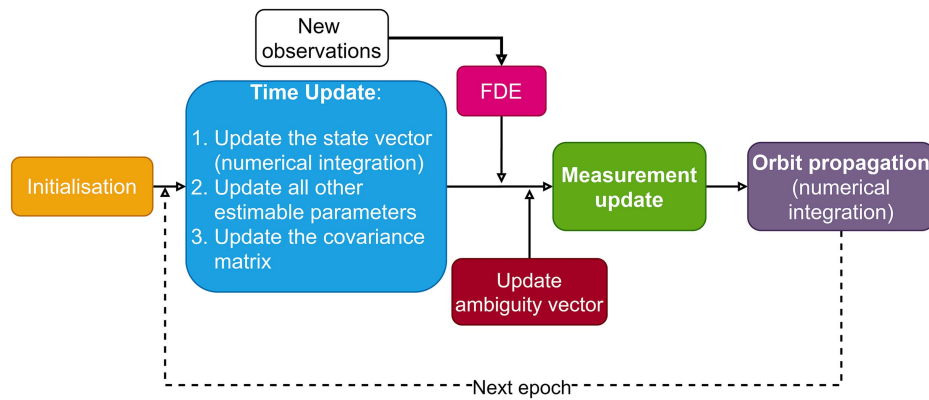


Fig. 4. Flowchart for the EKF reduced-dynamic POD.

some by the new generation of GNSS (e.g., Galileo). The MADOCA and the AU/NZ SBAS products and their impacts on the POD of small LEO satellites with limited data were investigated by Allahviridi-Zadeh et al. (2021)

However, even with high-precision real-time orbit and clock corrections available in space, some limitations should be considered for the onboard POD. For instance, most LEO satellites, especially those used for remote-sensing applications, are in highly inclined polar orbits, which limits their ability to receive real-time GPS orbits and clock parameters via GEO satellites when the LEO satellite is over the polar region. The concept of using multiantennas has been proposed by Giordano et al. (2017) to overcome the weak communication links above this region. Moreover, sudden communication breaks could result in discontinuities in receiving the required orbit and clock offset corrections. In such cases, using outdated corrections is inevitable.

An alternative solution is predicting the orbit and clock corrections with, e.g., high-order polynomials (El-Mowafy et al. 2017). It was reported by Hauschild et al. (2016) that the predicted corrections improved the real-time POD of the SWARM-C satellite compared with the case when using broadcast ephemeris. The real-time orbit and clock corrections could also contain faults or significant errors, which decrease their accuracy. To solve this problem, the orbits and clocks may be modeled as additional quasi-observations and be checked independently from the observations in a FDE (El-Mowafy 2018). Moreover, switching from one GEO satellite transmitter to other providers could also cause problems because different providers may apply different models and initial values in the orbit and clock correction production.

Real-Time POD of Small LEO Satellites and LEO Megaconstellations

Recent low-cost GNSS receivers will be used in the future to test real-time POD in the low-power CubeSats (Palomo et al. 2019). Real-time POD is also essential for the LEO augmentation systems, which can be used to aid positioning in challenging areas with low GNSS visibility and to improve the PPP convergence time for ground users (Li et al. 2019b). The generating procedure of the required orbital products for LEO constellations was proposed by Wang and El-Mowafy (2020). In addition to the orbits, prediction of the LEO clocks is also essential for positioning applications using LEO constellations. The clock prediction is affected by different factors such as the stability of the onboard frequency oscillator and the time reference, as well as the estimation errors and residuals in the POD procedure. The relevant factors and their potential influences were discussed and analyzed by Wang and El-Mowafy (2021) for certain LEO clock types.

Based on the altitude of the LEO region, covering the whole Earth using a megaconstellation of large and expensive LEO satellites requires a huge budget. The available constellations of the small communication LEO satellites such as OneWeb, McLean, Virginia and Starlink, Hawthorne, California can be used to improve the positioning coverage and performance for urban areas, and possibility indoor applications and intelligent transportation systems by providing additional positioning signals if supplied by navigation payloads (Reid et al. 2019), or with their signals used as signal-of-opportunity (Psiaki 2020). However, the onboard POD is a challenging task, especially for the low-power satellites.

Other information, such as intersatellite links, could be used to strengthen the model. This approach has been tested by Li et al. (2019a) for different simulated LEO satellite constellations using simulated intersatellite links. The subcentimeter to decimeter accuracies achieved in this method depends on the number of links and their ranging accuracies. The other issue in the constellation of the small LEO satellites, especially for the low-cost CubeSats, is the stability of the onboard frequency oscillator, which is essential for the clock modeling of these satellites. Unstable oscillators prevent clock prediction, and epoch-by-epoch clock estimation is required in the real-time POD procedure that should be performed either on board or by the ground user.

Real-Time POD with Integer Ambiguity Resolution

Although the POD based on IAR improves orbital accuracy post-mission, performing the actual onboard POD with IAR is a challenging task and requires real-time phase corrections in space. As an example, the QZSS satellites broadcast these phase biases over Japan via the L6 signal (Cabinet Office 2020) under the Centimeter Level Augmentation Service (CLAS). With the availability of such phase corrections in space, the onboard POD of the LEO satellites with PPP-IAR and its impacts on actual onboard POD can be tested in the near future.

Summary and Conclusion

In this paper, two main LEO POD methods, the kinematic and the reduced-dynamic POD, in two processing modes, postmission and real-time processing, have been reviewed and discussed. The kinematic POD uses only GNSS measurements, and it is appropriate for applications such as gravity missions that do not consider the dynamic forces affecting the LEO satellites. On the other hand, the reduced-dynamic POD is a more accurate method because the dynamic models and estimated empirical accelerations can strengthen the measurement model and thus improve POD accuracy. In the

Table 3. Comparison of the POD methods that are typically used in the postprocessing and real-time modes

| Item | Postmission POD | | Real-time POD | |
|-------------|--|--|--|--|
| | Kinematic | Reduced-dynamic | Kinematic | Reduced-dynamic |
| Inputs | GNSS observation, GNSS satellite orbits and clock corrections | Dynamic models, GNSS observations + GNSS satellite orbits and clock corrections | GNSS observation, broadcast ephemeris | Simplified dynamic models, GNSS observation, broadcast ephemeris |
| Outputs | Satellite positions, LEO receiver clock offsets, phase ambiguities | Keplerian elements (initial state), force model parameters, empirical accelerations, LEO receiver clock offsets, phase ambiguities | Satellite positions, LEO receiver clock offsets, phase ambiguities | Keplerian elements (initial state), force model parameters, empirical accelerations, LEO receiver clock offsets, phase ambiguities |
| Limitations | Data problems and gaps | Model deficiencies | Data problems and gaps | Computational load |
| Advantages | Computational effectiveness, not relying on dynamic models | High accuracy and continuity | Computational effectiveness, not relying on dynamic models | High accuracy and continuity |
| Usability | Gravity missions | Most geoscience and remote sensing missions | Onboard positioning and navigation | Onboard positioning and navigation |
| Accuracy | <10 cm | <5 cm | Meter | Submeter |

postprocessing mode, both the kinematic and the reduced-dynamic POD methods provide accurate orbits at several centimeters, fulfilling the required accuracy for most LEO missions. For example, gravity missions require kinematic orbits with an accuracy of a few centimeters. Other applications such as altimetry, atmospheric sounding, and InSAR also use high-accuracy reduced-dynamic orbits, from one to several centimeter levels.

The numerical integration in the reduced-dynamic POD requires high computational efforts. Consequently, the reduced-dynamic POD is more time-consuming than the kinematic POD. With the powerful computation units in the processing centers available, the computational load is not a significant factor for postprocessing and even near-real-time applications. However, it has a considerable impact on the onboard processing because there could be not enough computational capacity in space, in particular for small LEO satellites such as CubeSats.

The kinematic POD is not available in the epochs experiencing data gaps, which is common for small LEO satellites with power limitations, such as CubeSats, because power sometimes has to be rotationally allocated among different sensors onboard. For these satellites, the reduced-dynamic POD is the proper method; however, simplified dynamic models can be considered to facilitate onboard POD. The reduced-dynamic POD is also the primary method for the reference orbit determination of LEO satellites in the orbit determination centers such as CODE and JPL.

Besides reviewing the postmission procedures, recent advancement in the onboard POD, such as using real-time precise orbits and clock corrections in space, and its limitations in terms of availability, accuracy, continuity, and reliability, have been addressed. The onboard POD is based on using filtering approaches. In applying comprehensive dynamic models and precise satellite orbits and clock corrections, the final output of the EKF after solution convergence can reach a similar level as that using the batch least-squares in the postprocessing mode. However, due to the onboard processing limitations, simplified dynamic models are often used in the real-time POD, resulting in a degraded accuracy compared with the postmission processing mode. Table 3 provides a comparison between the kinematic and the reduced-dynamic POD for both the postmission and real-time modes.

Real-time POD and the corresponding challenges for the small low-capacity power satellites with limited data such as CubeSats are among our future works. The LEO POD-enabled IAR, which has been tested in the postprocessing mode, is considered as an appropriate tool for improving real-time POD performance. However, it requires real-time phase corrections in space for the onboard

satellite positioning, which is currently limited and not tested yet in real-world LEO missions, but it is of high interest to the LEO community. The onboard POD is essential for formation flying of LEO satellites and LEO megaconstellations as a positioning augmentation system to GNSS. This is a new topic in navigation, remote-sensing, and geoscience applications.

Data Availability Statement

All data, models, and code generated or used during the study appear in the published article.

Acknowledgments

The work is funded by the Australian Research Council Discovery Project: Tracking Formation-Flying of Nanosatellites Using Inter-Satellite Links (DP 190102444), and the Chinese Academy of Sciences (CAS) “Light of West China” Program (No. XAB2018YDYL01).

References

- Allahverdi-Zadeh, A., J. Asgari, and A. R. Amiri-Simkooei. 2016. “Investigation of GPS draconitic year effect on GPS time series of eliminated eclipsing GPS satellite data.” *J. Geod. Sci.* 6 (1): 2016. <https://doi.org/10.1515/jogs-2016-0007>.
- Allahverdi-Zadeh, A., K. Wang, and A. El-Mowafy. 2021. “Precise orbit determination of CubeSats using proposed observations weighting model.” In *Proc., Geodesy for a Sustainable Earth, Scientific Assembly of the International Association of Geodesy (IAG 2021)*. Beijing.
- Altamimi, Z., P. Rebischung, L. Métivier, and X. Collilieux. 2016. “ITRF2014: A new release of the international terrestrial reference frame modeling nonlinear station motions.” *J. Geophys. Res. Solid Earth* 121 (8): 6109–6131. <https://doi.org/10.1002/2016JB013098>.
- Arnold, D., O. Montenbruck, S. Hackel, and K. Sošnica. 2019. “Satellite laser ranging to low Earth orbiters: Orbit and network validation.” *J. Geod.* 93 (11): 2315–2334. <https://doi.org/10.1007/s00190-018-1140-4>.
- Auriol, A., and C. Tourain. 2010. “DORIS system: The new age.” *Adv. Space Res.* 46 (12): 1484–1496. <https://doi.org/10.1016/j.asr.2010.05.015>.
- Baarda, W. 1968. *A testing procedure for use in geodetic networks*. Delft, Netherlands: Netherlands Geodetic Commission.
- Barrios, J., J. Caro, J. Calle, E. Carbonell, J. Pericacho, G. Fernández, V. Esteban, M. Fernández, F. Bravo, and B. Torres. 2018. “Update

- on Australia and New Zealand DFMC SBAS and PPP system results.” In *Proc., 31st Int. Technical Meeting of the Satellite Division of The Institute of Navigation (ION GNSS+ 2018)*, 1038–1067. Manassas, VA: Institute of Navigation.
- Bertiger, W., Y. Bar-Sever, A. Dorsey, B. Haines, N. Harvey, D. Hemberger, M. Heflin, W. Lu, M. Miller, and A. W. Moore. 2020. “GipsyX/RTGx, A new tool set for space geodetic operations and research.” *Adv. Space Res.* 66 (3): 469–489. <https://doi.org/10.1016/j.asr.2020.04.015>.
- Bertiger, W., S. D. Desai, B. Haines, N. Harvey, A. W. Moore, S. Owen, and J. P. Weiss. 2010. “Single receiver phase ambiguity resolution with GPS data.” *J. Geod.* 84 (5): 327–337. <https://doi.org/10.1007/s00190-010-0371-9>.
- Bock, H., A. Jäggi, G. Beutler, and U. Meyer. 2014. “GOCE: Precise orbit determination for the entire mission.” *J. Geod.* 88 (11): 1047–1060. <https://doi.org/10.1007/s00190-014-0742-8>.
- Bock, H., A. Jäggi, U. Meyer, P. Visser, J. van den Ijssel, T. van Helleputte, M. Heinze, and U. Hugentobler. 2011. “GPS-derived orbits for the GOCE satellite.” *J. Geod.* 85 (11): 807. <https://doi.org/10.1007/s00190-011-0484-9>.
- Butcher, J. C. 2016. *Numerical methods for ordinary differential equations*. West Sussex, UK: Wiley.
- Cabinet Office. 2020. “Quasi-zenith satellite system interface specification centimeter level augmentation service.” IS-QZSS-L6-003. Accessed September 17, 2021. <https://qzss.go.jp/en/technical/download/pdf/ps-is-qzss/is-qzss-l6-003.pdf?t=1606870849719>.
- Chuang, S., Z. Qile, G. Jianghui, L. Yidong, G. Maorong, and L. Jingnan. 2008. “Recent development of PANDA software in GNSS data processing.” In *Proc., Int. Conf. on Earth Observation Data Processing and Analysis (ICEODPA)*. Bellingham, WA: International Society of Optics and Photonics. <https://doi.org/10.1117/12.816261>.
- Dach, R., S. Lutz, P. Walser, and P. Fridez. 2015. *Bernese GNSS software Version 5.2*. Bern, Switzerland: Univ. of Bern.
- El-Mowafy, A. 2014. “GNSS multi-frequency receiver single-satellite measurement validation method.” *GPS Solut.* 18 (4): 553–561. <https://doi.org/10.1007/s10291-013-0352-6>.
- El-Mowafy, A. 2018. “Real-time precise point positioning using orbit and clock corrections as quasi-observations for improved detection of faults.” *J. Navig.* 71 (4): 769–787. <https://doi.org/10.1017/S0373463317001023>.
- El-Mowafy, A., M. Deo, and N. Kubo. 2017. “Maintaining real-time precise point positioning during outages of orbit and clock corrections.” *GPS Solut.* 21 (3): 937–947. <https://doi.org/10.1007/s10291-016-0583-4>.
- Feng, Y., and Y. Zheng. 2005. “Efficient interpolations to GPS orbits for precise wide area applications.” *GPS Solut.* 9 (4): 273–282. <https://doi.org/10.1007/s10291-005-0133-y>.
- Fernández, J., C. Fernández, P. Féménias, and H. Peter. 2016. “The Copernicus Sentinel-3 mission.” Accessed September 17, 2021. https://cdsis.nasa.gov/lw20/docs/2016/papers/P32-Fernandez_paper.pdf.
- Fernández, J., H. Peter, J. Berzosa, L. J. Gallardo, E. J. Calero, and P. Féménias. 2018. “Copernicus POD service: First orbit determination results for Sentinel-3B.” Accessed September 17, 2021. <https://sentinel.esa.int/documents/247904/3372613/25-years-progress-radar-altimetry-first-orbit-determination-results-sentinel-3b>.
- Fernández, M. 2019. “Sentinel-3 properties for GPS POD, Copernicus sentinel-1, -2 and -3 precise orbit determination service.” Accessed September 17, 2021. <https://sentinels.copernicus.eu/documents/247904/3372613/Sentinel-3-GPS-POD-Properties.pdf>.
- Gerlach, C., N. Sneeuw, P. Visser, and D. Švehla. 2003. “CHAMP gravity field recovery with the energy balance approach: First results.” In *First CHAMP mission results for gravity, magnetic and atmospheric studies*, edited by C. Reigber, H. Lühr, and P. Schwintzer, 134–139. Berlin: Springer.
- Giordano, P., P. Zoccarato, M. Otten, and M. Crisci. 2017. “P2OD: Real-time precise onboard orbit determination for LEO satellites.” In *Proc., 30th Int. Technical Meeting of the Satellite Division of The Institute of Navigation (ION GNSS+ 2017)*, 1754–1771. Manassas, VA: Institute of Navigation. <https://doi.org/10.33012/2017.15190>.
- Giorgi, G. 2017. “Attitude determination.” In *Springer handbook of global navigation satellite systems*, edited by P. J. G. Teunissen and O. Montenbruck, 561–582. Berlin: Springer.
- Guo, J., Q. Zhao, X. Guo, X. Liu, J. Liu, and Q. Zhou. 2015. “Quality assessment of onboard GPS receiver and its combination with DORIS and SLR for Haiyang 2A precise orbit determination.” *Sci. China Earth Sci.* 58 (1): 138–150. <https://doi.org/10.1007/s11430-014-4943-z>.
- Haines, B., Y. Bar-Sever, W. Bertiger, S. Desai, and P. Willis. 2004. “One-centimeter orbit determination for Jason-1: New GPS-based strategies.” *Mar. Geod.* 27 (1–2): 299–318. <https://doi.org/10.1080/014904104904465300>.
- Hauschild, A., and O. Montenbruck. 2020. “Precise on-board navigation of LEO satellites with GNSS broadcast ephemerides.” In *Proc., 33rd Int. Technical Meeting of the Satellite Division of The Institute of Navigation (ION GNSS+ 2020)*, 3866–3874. Manassas, VA: Institute of Navigation. <https://doi.org/10.33012/2020.17752>.
- Hauschild, A., O. Montenbruck, and P. Steigenberger. 2013. “Short-term analysis of GNSS clocks.” *GPS Solut.* 17 (3): 295–307. <https://doi.org/10.1007/s10291-012-0278-4>.
- Hauschild, A., J. Tegeedor, O. Montenbruck, H. Visser, and M. Markgraf. 2016. “Precise onboard orbit determination for LEO satellites with real-time orbit and clock corrections.” In *Proc., 29th Int. Technical Meeting of The Satellite Division of the Institute of Navigation (ION GNSS 2016)*, 3715–3723. Manassas, VA: Institute of Navigation. <https://doi.org/10.33012/2016.14717>.
- Hofmann-Wellenhof, B., H. Lichtenegger, and E. Wasle. 2008. *GNSS—Global navigation satellite systems: GPS, GLONASS, Galileo, and more*. Berlin: Springer.
- Hoque, M. M., and N. Jakowski. 2007. “Higher order ionospheric effects in precise GNSS positioning.” *J. Geod.* 81 (4): 259–268. <https://doi.org/10.1007/s00190-006-0106-0>.
- Humpherys, J., and J. West. 2010. “Kalman filtering with Newton’s method [Lecture Notes].” *IEEE Control Syst. Mag.* 30 (6): 101–106. <https://doi.org/10.1109/MCS.2010.938485>.
- Jacchia, L. G. 1971. “Revised static models of the thermosphere and exosphere with empirical temperature profiles.” SAO Special Report 332. Accessed September 17, 2021. <http://articles.adsabs.harvard.edu/pdf/1971SAOSR.332.....J>.
- Jäggi, A., G. Beutler, and U. Hugentobler. 2005. “Efficient stochastic orbit modeling techniques using least squares estimators.” In *Proc., A Window on the Future of Geodesy*, 175–180. Berlin: Springer.
- Jäggi, A., R. Dach, O. Montenbruck, U. Hugentobler, H. Bock, and G. Beutler. 2009. “Phase center modeling for LEO GPS receiver antennas and its impact on precise orbit determination.” *J. Geod.* 83 (12): 1145. <https://doi.org/10.1007/s00190-009-0333-2>.
- Jäggi, A., C. Dahle, D. Arnold, H. Bock, U. Meyer, G. Beutler, and J. van Den Ijssel. 2016. “Swarm kinematic orbits and gravity fields from 18 months of GPS data.” *Adv. Space Res.* 57 (1): 218–233. <https://doi.org/10.1016/j.asr.2015.10.035>.
- Jäggi, A., U. Hugentobler, and G. Beutler. 2006. “Pseudo-stochastic orbit modeling techniques for low-Earth orbiters.” *J. Geod.* 80 (1): 47–60. <https://doi.org/10.1007/s00190-006-0029-9>.
- Jäggi, A., U. Hugentobler, H. Bock, and G. Beutler. 2007. “Precise orbit determination for GRACE using undifferenced or doubly differenced GPS data.” *Adv. Space Res.* 39 (10): 1612–1619. <https://doi.org/10.1016/j.asr.2007.03.012>.
- Jokinen, A., C. Ellum, J. Neumann, D. Chan, I. Webster, S. Masterson, and T. Morley. 2014. “Kinematic performance of NovAtel CORRECT with Terrastar-D precise point positioning (PPP) service.” In *Proc., 27th Int. Technical Meeting of the Satellite Division of the Institute of Navigation (ION GNSS+ 14)*, 1020–1034. Manassas, VA: Institute of Navigation.
- Kang, Z., S. Bettadpur, P. Nagel, H. Save, S. Poole, and N. Pie. 2020. “GRACE-FO precise orbit determination and gravity recovery.” *J. Geod.* 94 (9): 85. <https://doi.org/10.1007/s00190-020-01414-3>.
- Kang, Z., P. Nagel, and R. Pastor. 2003. “Precise orbit determination for GRACE.” *Adv. Space Res.* 31 (8): 1875–1881. [https://doi.org/10.1016/S0273-1177\(03\)00159-5](https://doi.org/10.1016/S0273-1177(03)00159-5).
- Kintner, P. M., B. M. Ledvina, and E. R. de Paula. 2007. “GPS and ionospheric scintillations.” *Space Weather.* 5 (9): 27. <https://doi.org/10.1029/2006SW000260>.

- Kouba, J., F. Lahaye, and P. Tétreault. 2017. "Precise point positioning." In *Springer handbook of global navigation satellite systems*, edited by P. J. Teunissen and O. Montenbruck. Cham, Switzerland: Springer. https://doi.org/10.1007/978-3-319-42928-1_25.
- Laurichesse, D., F. Mercier, J. P. Berthias, P. Broca, and L. Cerri. 2009. "Integer ambiguity resolution on undifferenced GPS phase measurements and its application to PPP and satellite precise orbit determination." *Navigation* 56 (2): 135–149. <https://doi.org/10.1002/j.2161-4296.2009.tb01750.x>.
- Li, K., X. Zhou, W. Wang, Y. Gao, G. Zhao, E. Tao, and K. Xu. 2018. "Centimeter-level orbit determination for TG02 Spacelab using onboard GNSS data." *Sensors* 18 (8): 2671. <https://doi.org/10.3390/s18082671>.
- Li, M., W. Li, C. Shi, K. Jiang, X. Guo, X. Dai, X. Meng, Z. Yang, G. Yang, and M. Liao. 2017. "Precise orbit determination of the Fengyun-3C satellite using onboard GPS and BDS observations." *J. Geod.* 91 (11): 1313–1327. <https://doi.org/10.1007/s00190-017-1027-9>.
- Li, X., Z. Jiang, F. Ma, H. Lv, Y. Yuan, and X. Li. 2019a. "LEO precise orbit determination with inter-satellite links." *Remote Sens.* 11 (18): 2117. <https://doi.org/10.3390/rs11182117>.
- Li, X., F. Ma, X. Li, H. Lv, L. Bian, Z. Jiang, and X. Zhang. 2019b. "LEO constellation-augmented multi-GNSS for rapid PPP convergence." *J. Geod.* 93 (5): 749–764. <https://doi.org/10.1007/s00190-018-1195-2>.
- Luzum, B. J., J. R. Ray, M. S. Carter, and F. J. Josties. 2001. "Recent improvements to IERS bulletin a combination and prediction." *GPS Solut.* 4 (3): 34–40. <https://doi.org/10.1007/PL00012853>.
- Ma, C., E. F. Arias, T. M. Eubanks, A. L. Fey, A. M. Gontier, C. S. Jacobs, O. J. Sovers, B. A. Archinal, and P. Charlot. 1998. "The international celestial reference frame as realized by very long baseline interferometry." *Astron. J.* 116 (1): 516–546. <https://doi.org/10.1086/300408>.
- Montenbruck, O. 2017. "Space applications." In *Handbook of global navigation satellite systems*, edited by P. J. G. Teunissen and O. Montenbruck, 933–964. Berlin: Springer.
- Montenbruck, O., M. Garcia-Fernandez, Y. Yoon, S. Schön, and A. Jäggi. 2009. "Antenna phase center calibration for precise positioning of LEO satellites." *GPS Solut.* 13 (1): 23–34. <https://doi.org/10.1007/s10291-008-0094-z>.
- Montenbruck, O., and E. Gill. 2000. *Satellite orbits: Models, methods and applications*. Berlin: Springer.
- Montenbruck, O., S. Hackel, and A. Jäggi. 2018. "Precise orbit determination of the Sentinel-3A altimetry satellite using ambiguity-fixed GPS carrier phase observations." *J. Geod.* 92 (7): 711–726. <https://doi.org/10.1007/s00190-017-1090-2>.
- Montenbruck, O., M. Markgraf, J. Naudet, S. Santandrea, K. Gantois, and P. Vuilleumier. 2008. "Autonomous and precise navigation of the Proba-2 spacecraft." In *Proc., AIAA/AAS Astrodynamics Specialist Conf. and Exhibit*. Reston, VA: American Institute of Aeronautics and Astronautics.
- Montenbruck, O., and P. Ramos-Bosch. 2008. "Precision real-time navigation of LEO satellites using global positioning system measurements." *GPS Solut.* 12 (3): 187–198. <https://doi.org/10.1007/s10291-007-0080-x>.
- Montenbruck, O., T. van Helleputte, R. Kroes, and E. Gill. 2005. "Reduced dynamic orbit determination using GPS code and carrier measurements." *Aerosp. Sci. Technol.* 9 (3): 261–271. <https://doi.org/10.1016/j.ast.2005.01.003>.
- Odijk, D., B. Zhang, A. Khodabandeh, R. Odolinski, and P. J. G. Teunissen. 2016. "On the estimability of parameters in undifferenced, uncombined GNSS network and PPP-RTK user models by means of S-system theory." *J. Geod.* 90 (1): 15–44. <https://doi.org/10.1007/s00190-015-0854-9>.
- Palomo, J. M., P. D'Angelo, P. F. Silva, A. J. Fernández, P. Giordano, P. Zoccarato, J. Tegeador, O. Oerpen, L. B. Hansen, C. Hill, and T. Moore. 2019. "Space GNSS receiver performance results with precise real-time on-board orbit determination (P2OD) in LEO missions." In *Proc., 32nd Int. Technical Meeting of the Satellite Division of The Institute of Navigation (ION GNSS+ 2019)*, 1172–1186. Manassas, VA: Institute of Navigation. <https://doi.org/10.33012/2019.17082>.
- Pardal, P., H. Kuga, and R. V. de Morales. 2010. "Comparing the extended and the sigma point Kalman filters for orbit determination modeling using GPS measurements." In *Proc., 23rd Int. Technical Meeting of the Satellite Division of The Institute of Navigation (ION GNSS 2010)*, 2732–2742. Manassas, VA: Institute of Navigation.
- Pavlis, N., S. Kenyon, J. Factor, and S. Holmes. 2008. "Earth gravitational model 2008." In *SEG technical program expanded abstracts 2008*, 761–763. Tulsa, OK: Society of Exploration Geophysicists.
- Peter, H., et al. 2017. "Sentinel-1A—First precise orbit determination results." *Adv. Space Res.* 60 (5): 879–892. <https://doi.org/10.1016/j.asr.2017.05.034>.
- Petit, G., and B. Luzum. 2010. "IERS conventions." Accessed September 17, 2021. <https://www.iers.org/IERS/EN/Publications/TechnicalNotes/tm36.html>.
- Psiaki, M. L. 2020. "Navigation using carrier Doppler shift from a LEO constellation: TRANSIT on steroids." In *Proc., 33rd Int. Technical Meeting of the Satellite Division of The Institute of Navigation (ION GNSS+ 2020)*. Manassas, VA: Institute of Navigation. <https://doi.org/10.33012/2020.17667>.
- Reid, T., K. Gunning, A. Perkins, L. O. Sherman, and T. Walter. 2019. "Going back for the future: Large/mega LEO constellations for navigation." In *Proc., 32nd Int. Technical Meeting of the Satellite Division of The Institute of Navigation (ION GNSS+ 2019)*. Manassas, VA: Institute of Navigation. <https://doi.org/10.33012/2019.17123>.
- Ren, L., and S. Schön. 2018. "PPP-based Swarm kinematic orbit determination." *Ann. Geophys.* 36 (5): 1227–1241. <https://doi.org/10.5194/angeo-36-1227-2018>.
- Rothacher, M., and R. Schmid. 2010. "ANTEX: The antenna exchange format version 1.4." Accessed September 17, 2021. <ftp://igs.org/pub/station/general/antex14.txt>.
- Standish, E. 1998. "JPL planetary and lunar ephemerides." *Astron. Astrophys.* 336: 381–384.
- Švehla, D. 2018. *Geometrical theory of satellite orbits and gravity field*. Berlin: Springer.
- Švehla, D., and M. Rothacher. 2003a. "CHAMP double-difference kinematic POD with ambiguity resolution." In *First CHAMP mission results for gravity, magnetic and atmospheric studies*, edited by C. Reigber, H. Lühr, and P. Schwintzer, 70–77. Berlin: Springer.
- Švehla, D., and M. Rothacher. 2003b. "Kinematic and reduced-dynamic precise orbit determination of low Earth orbiters." *Adv. Geosci.* 1 (Apr): 47–56. <https://doi.org/10.5194/adgeo-1-47-2003>.
- Švehla, D., and M. Rothacher. 2004. "Formation flying of LEO satellites using GPS." Accessed September 17, 2021. <https://ui.adsabs.harvard.edu/abs/2004AGUFMSF53A07355>.
- Švehla, D., and M. Rothacher. 2005a. "Kinematic positioning of LEO and GPS satellites and IGS stations on the ground." *Adv. Space Res.* 36 (3): 376–381. <https://doi.org/10.1016/j.asr.2005.04.066>.
- Švehla, D., and M. Rothacher. 2005b. "Kinematic precise orbit determination for gravity field determination." In *Proc., A Window on the Future of Geodesy*, 181–188. Berlin: Springer.
- Tegeador, J., O. Ørpen, T. Melgard, D. Lapucha, and H. Visser. 2017. "G4 multi-constellation precise point positioning service for high accuracy offshore navigation." *TransNav* 11 (3): 425–429. <https://doi.org/10.12716/1001.11.03.05>.
- Teunissen, P. J. G., and A. Khodabandeh. 2015. "Review and principles of PPP-RTK methods." *J. Geod.* 89 (3): 217–240. <https://doi.org/10.1007/s00190-014-0771-3>.
- Vallado, D. A., and D. Finkleman. 2014. "A critical assessment of satellite drag and atmospheric density modeling." *Acta Astronaut.* 95 (Apr): 141–165. <https://doi.org/10.1016/j.actaastro.2013.10.005>.
- Van den Ijssel, J., B. Forte, and O. Montenbruck. 2016. "Impact of swarm GPS receiver updates on POD performance." *Earth Planets Space* 68 (1): 85. <https://doi.org/10.1186/s40623-016-0459-4>.
- Van Den Ijssel, J., J. Encarnação, E. Doornbos, and P. Visser. 2015. "Precise science orbits for the Swarm satellite constellation." *Adv. Space Res.* 56 (6): 1042–1055. <https://doi.org/10.1016/j.asr.2015.06.002>.
- Wang, K., A. Allahviridi-Zadeh, A. El-Mowafy, and J. N. Gross. 2020. "A sensitivity study of POD using dual-frequency GPS for Cubesats data limitation and resources." *Remote Sens.* 12 (13): 2107. <https://doi.org/10.3390/rs12132107>.
- Wang, K., and A. El-Mowafy. 2020. "Proposed orbital products for positioning using mega-constellation LEO satellites." *Sensors* 20 (20): 5806. <https://doi.org/10.3390/s20205806>.

- Wang, K., and A. El-Mowafy. 2021. "LEO satellite clock analysis and prediction for positioning applications." *Geo Spat Inf. Sci.* 2021 (Jun): 1–20. <https://doi.org/10.1080/10095020.2021.1917310>.
- Weinbach, U., and S. Schön. 2012. "Improved GPS receiver clock modeling for kinematic orbit determination of the GRACE satellites." In *Proc., 2012 European Frequency and Time Forum*, 157–160. New York: IEEE.
- Wermuth, M., O. Montenbruck, and T. Van Helleputte. 2010. "GPS high precision orbit determination software tools (GHOST)." In *Proc., 4th Int. Conf. on astrodynamics tools and techniques*, 3–6. Madrid, Spain: Citeseer.
- Xiong, C., H. Lühr, M. Schmidt, M. Bloßfeld, and S. Rudenko. 2018. "An empirical model of the thermospheric mass density derived from CHAMP satellite." In *Proc., Annales Geophysicae*, 1141–1152. Göttingen, Germany: Copernicus.
- Yang, Y., X. Yue, and A. G. Dempster. 2016. "GPS-based onboard real-time orbit determination for LEO satellites using consider Kalman filter." *52 (2)*: 769–777. <https://doi.org/10.1109/TAES.2015.140758>.
- Yang, Y., X. Yue, J. Yuan, and C. Rizos. 2014. "Enhancing the kinematic precise orbit determination of low Earth orbiters using GPS receiver clock modelling." *Adv. Space Res.* 54 (9): 1901–1912. <https://doi.org/10.1016/j.asr.2014.07.016>.
- Yunck, T. P., W. I. Bertiger, S. C. Wu, Y. E. Bar-Sever, E. J. Christensen, B. J. Haines, S. M. Lichten, R. J. Muellerschoen, Y. Vigue, and P. Willis. 1994. "First assessment of GPS-based reduced dynamic orbit determination on TOPEX/Poseidon." *Geophys. Res. Lett.* 21 (Jan): 541. <https://doi.org/10.1029/94GL00010>.
- Zehentner, N., and T. Mayer-Gürr. 2016. "Precise orbit determination based on raw GPS measurements." *J. Geod.* 90 (3): 275–286. <https://doi.org/10.1007/s00190-015-0872-7>.
- Zhang, Q., X. Guo, L. Qu, and Q. Zhao. 2018. "Precise orbit determination of FY-3C with calibration of orbit biases in BeiDou GEO satellites." *Remote Sens.* 10 (3): 382. <https://doi.org/10.3390/rs10030382>.

3 Post-mission CubeSats POD

In the following chapters in this thesis, the requirements for estimating precise orbits of CubeSats, considering their limitations, are extensively discussed, mainly in a post-mission mode. Currently, there are different software packages to perform POD in post-mission (cf. Chapter 2); for example, the Bernese GNSS Software has been widely used in the past decades by various institutions for this purpose. Bernese performs the POD based on the reduced-dynamic and kinematic approaches using batch least-squares adjustment. The procedure of the CubeSat POD using Bernese in post-mission mode and the applied modifications implemented in the thesis are explained in this chapter.

Note: The symbols used in the following equations are already defined in the previous chapter and inside the relevant paper. New symbols are defined inside the text.

A general flowchart of the Reduced-Dynamic POD (RD-POD) in Bernese for LEO satellites is provided in, e.g., Chapter 2, Fig. 3. In the following, a detailed explanation of the processing steps with the relevant equations and the modifications that are required for CubeSats POD are provided.

- 1- The first step is to prepare the input files, including the precise orbits and clocks of GNSS satellites, the Earth Orientation Parameters (EOP), and the Differential Code Biases (DCB). In this thesis, different orbit and clock products of GNSS satellites are used, including those provided by the following:
 - International GNSS Service (IGS) (Johnston et al. 2017)
 - Center for Orbit Determination in Europe (CODE) (Dach et al. 2020)
 - Centre National d'Etudes Spatiales (CNES) (Laurichesse et al. 2013)
 - Multi-GNSS Advanced Demonstration Tool for Orbit and Clock Analysis (MADOCA) (JAXA 2020)
 - Australia/New Zealand Satellite-Based Augmentation System (SBAS) known as SouthPAN (Barrios et al. 2018, Geoscience of Australia 2020)

These products are provided in precise standard formats for the post-mission POD, i.e., with SP3 and clock RINEX files. However, real-time POD based on the MADOCA and SouthPAN PPP products require some modifications that are explained in section 8.1. The only modification in the SouthPAN SBAS products is transforming the orbits from the antenna phase centre (APC) to the Centre of Mass (CoM) (cf. Equation 1, Chapter 7).

- 2- These products should be transformed into the Bernese format, including:

- a. Transforming the EOP files provided by IERS (C04, Bulletin A, Bulletin B) into ERP files.
- b. Transforming the precise orbits of GNSS satellites from the Earth-Centered Earth-Fixed (ECEF) frame (X_{ECEF}) into the inertial frame (J2000) ($X_{Inertial}$) and extracting the clock data from the SP3 format if the precise clocks are not provided in a separate clock RINEX file:

The transformation matrix from the inertial to the Earth-fixed frames (U) consists of the rotation matrices of Precession (P_r), Nutation (N_u), Earth rotation (E_r), and polar motion (P_m) as follows:

$$U = P_r N_u E_r P_m \quad (3.1)$$

The models used to derive P_r and N_u are provided in, e.g., Table 1 in Chapter 4. The term $E_r = R_3(GAST)$ is the rotation about the celestial ephemeris pole and $GAST$ denotes the Greenwich Apparent Sidereal Time. The coordinates of conventional international origin provided by the IERS are used to compute the polar motion $P_m = R_2(-x_p)R_1(-y_p)$. Considering the orthogonality of the transformation matrix, i.e., $U^{-1} = U^T$, the transformation between two frames is applied using the following equation:

$$X_{Inertial} = U^T X_{ECEF} \quad (3.2)$$

- c. Generating a continuous orbit for the GNSS satellites: The equation of motion for GNSS satellites (cf. Equation 1 in Chapter 2) is numerically solved in this step in four iterations using the collocation method. Solving the equation of motion requires the partial derivatives of the satellite positions and velocities with respect to the orbital parameters, which are derived based on numerical integration using the variational equations (cf. Equation 6 in Chapter 2, where velocity-dependent forces are assumed zeros). This procedure is performed by dividing the GNSS orbits into 24 hourly sub-intervals and solving the following polynomial for the required coefficients (r_{0_i}) with setting up initial values for each sub-interval:

$$\begin{aligned}
r(t) &= \sum_{i=0}^{10} (t-t_0)^i r_{0,i} \\
r_{0,i} &= \frac{\partial r_0(t)}{\partial p_i}
\end{aligned} \tag{3.3}$$

The coefficients are the partial derivatives of the initial values with respect to the dynamic parameters p_i . These initial values for the left boundary of each sub-interval are the solution of the previous sub-interval. Due to the computational efficiency, the variational equation is numerically solved for 6-h subintervals with higher polynomial degrees, e.g., 12. However, the force models used in this procedure are similar to those provided in Table 1 in Chapter 4, with different degrees and orders. The dynamic parameters in this step include the solar radiation pressure in the direction of the sun to the satellite (D), the direction of the solar panel axis is defined as the y-bias (Y), and the perpendicular to D and Y is (X). They are estimated from the following Empirical CODE orbit Model (ECOM) (Arnold et al. 2015) using the constant (D_0 , Y_0 , X_0) and periodic (D_{2c} , D_{2s} , D_{4c} , D_{4s} , X_c , X_s) coefficients derived from numerical integrations:

$$\begin{aligned}
D &= D_0 + D_{2c} \cos 2u + D_{2s} \sin 2u + D_{4c} \cos 4u + D_{4s} \sin 4u \\
Y &= Y_0 \\
X &= X_0 + X_c \cos u + X_s \sin u
\end{aligned} \tag{3.4}$$

where u is the argument of latitude of the satellite.

The last point in this step is to estimate the instantaneous velocity changes (stochastic pulses Δv) every two hours in the radial (R), along-track (S), and cross-track (W) directions to enhance the orbit quality by solving the following variational equation set ($VE_{\Delta v}$) with zero initial values (Jäggi et al. 2006):

$$VE_{\Delta v} = \frac{\partial r_0(t)}{\partial \Delta v_i} \Delta v_i + \delta(t-t_i) (e_R, e_S, e_W)^T \tag{3.5}$$

where $\delta(t-t_i)$ denotes Dirac's delta distribution. The eclipsing periods are also determined to remove the observations of the satellites that cannot keep their nominal yaw attitude during the shadow of the Earth and moon (Allahverdi-Zadeh 2013, Allahverdi-Zadeh et al. 2016).

- d. Next, transform precise clocks from the RINEX format into the Bernese format.

e. Last, import the observations of CubeSats while the following steps are performed to screen the raw observations for the detection of outliers:

- Checking the large gaps in data and introducing new ambiguities;
- Detecting clock jumps;
- Detecting outliers and cycle slips using the following Melbourne-Wübbena Linear Combination (MW) and considering the GNSS observation equations (cf. Equation 4 in Chapter 2):

$$MW = \frac{f_1 \Phi_{r,1}^s - f_2 \Phi_{r,2}^s}{f_1 - f_2} - \frac{f_1 P_{r,1}^s + f_2 P_{r,2}^s}{f_1 + f_2} \quad (3.6)$$

- Detecting the outliers using the difference of IF combination between the phase and code observations and checking these values against a pre-set threshold based on their assumed statistical distribution:

$$\Phi_{r,IF}^s - P_{r,IF}^s = \frac{f_1^2 \Phi_{r,1}^s - f_2^2 \Phi_{r,2}^s - f_1^2 P_{r,1}^s + f_2^2 P_{r,2}^s}{f_1^2 - f_2^2} \quad (3.7)$$

The duty-cycled observations are also generated in this step.

3- The next step is to generate an initial orbit of the CubeSats using code observations:

- a. The epoch-wise kinematic coordinates and the receiver clock offsets of CubeSats are estimated using IF code observations in an iterative least-squares adjustment. Iterative outlier detection and exclusion of faulty code observations are also performed based on comparing the RMS of the estimated coordinates with a pre-defined threshold. If it exceeds the threshold, the suspected observations are removed, and the least-squares adjustment is repeated for the remaining observations.
- b. The estimated kinematic coordinates are converted into the SP3 format and then are used to generate a continuous orbit as explained above in steps 2-b and 2-c. However, compared with the GNSS orbits and due to the possible harsh atmosphere environments of the LEO region, higher degrees of the Earth's potential and ocean tides are considered for the CubeSats orbit estimation. The interval for solving the equation of motion and variational equation amounts to 1 and 12 minutes, respectively. The estimated dynamic parameters do not follow Equation (3.4), but equations 2-5 in Chapter 4.

- 4- The next step is to use the computed code-based reduced-dynamic orbit from the previous step for an iterative screening of phase observations for outliers as explained in the following:
- a. The general data screening procedure in Bernese starts with marking the observations under a pre-defined elevation mask angle. However, the number of observations may be limited for low-power CubeSats, and based on the discussions given in Chapter 5 (see Figure 2 of Chapter 5), removing observations from low-elevation angles is not optimal for CubeSats. Therefore, applying the elevation mask angle is disabled, and all observations are weighted based on the proposed weighting model in this thesis (cf. Equation 1 in Chapter 5). A new module is developed to perform the observation weighting functions by computing the SNR-dependant observation variance (cf. Chapter 5) at the undifferenced level. This function is used to update the covariance matrix.
 - b. Next, the data intervals with no cycle slips are identified using linear polynomials fitted to the between-satellite single-differenced Observed-minus-Computed (O-C) terms of the IF phase observations at each epoch. Considering Equation 4 in Chapter 2, the following O-C term is defined:

$$\Phi_{r,IF}^{s_1 s_2} - \rho_r^{s_1 s_2} - c(dt^{s_1 s_2} + \delta_{IF}^{s_1 s_2}) - \lambda_{IF} n_{r,IF}^{s_1 s_2} = \varepsilon_{IF}^{s_1 s_2} \quad (3.8)$$

After removing the impact of the receiver clock offsets, this equation is expected to be smooth with a few centimetres of random errors (noise) and fitted to the linear polynomials. The epoch-difference solution using the Equation (3.8) is then used to check for cycle slips.

- c. The epoch difference of the IF residuals using values from the previous step are generated as follows:

$$v_{IF,t_2-t_1} = \left(\Phi_{r,IF}^{s_1 s_2}(t_2) - \hat{\Phi}_{r,IF}^{s_1 s_2}(t_2) \right) - \left(\Phi_{r,IF}^{s_1 s_2}(t_1) - \hat{\Phi}_{r,IF}^{s_1 s_2}(t_1) \right) \quad (3.9)$$

where $\hat{\Phi} = J\hat{x}$ indicates the computed observations from the least-squares adjustment that are tested by considering the following condition with the pre-defined standard deviation values (σ_{L_1} , σ_{L_2}) to detect cycle slips:

$$|v_{IF,t_2-t_1}| \leq 6 \sqrt{\left(\frac{f_1^2}{f_1^2 - f_2^2} \sigma_{L_1} \right)^2 + \left(\frac{f_2^2}{f_1^2 - f_2^2} \sigma_{L_2} \right)^2} \quad (3.10)$$

- d. If significant jumps occur in the receiver clock, they should be detected and introduced as cycle slips for the phase observations used in this step. The variations in the estimated receiver clocks are checked for this purpose.
- e. In this step, the screened phase observations, the code-based reduced-dynamic orbit, the orbital partial derivatives from solving the variational equation, and the attitude information of CubeSats are used to estimate the improved CubeSats orbital parameters in a batch least-squares adjustment (cf. Equation 2 in Chapter 6). These parameters include six Keplerian elements at the initial epoch, nine constant and periodic coefficients for the dynamic models in the RSW directions (cf. Equation 2-5 in Chapter 4), and three velocity changes (stochastic pulses) at pre-defined epochs (see Equation (3.5)). The following matrices are required to solve the batch least-squares adjustment:

- Observation weighting matrix: In Bernese, the inverse of the covariance matrix of the observations is considered as the weighting matrix, making the Best Linear Unbiased Estimator (BLUE) (Teunissen 2000), expressed as:

$$Q_y = 3\sigma_{L_1}^2 \times I_n \quad (3.11)$$

where I is the identity matrix with the size of satellites (n). Multiplying with three is due to the higher noise level in IF observations. In this thesis, the Equation (3.11) is replaced with the proposed SNR weighting model (cf. Equation 1 in Chapter 5).

- Design matrix: The design matrix required for the reduced-dynamic POD contains the partial derivatives of the state vector with respect to the Keplerian elements x_k , the dynamic parameters x_d , and n_s stochastic pulses x_a estimated from solving the equation of motion and the variational equation explained above (cf. Equation 6 in Chapter 2). The design matrix also includes the partial derivatives of the IF phase observations $\partial \tilde{\Phi}_{r,IF}^s$ with respect to the receiver clock offset dt_r and b , the IF ambiguities are lumped with the corresponding phase biases as follows:

$$A = \begin{bmatrix} \frac{\partial r}{\partial x_k} & \frac{\partial r}{\partial x_d} & \frac{\partial r}{\partial x_a} & \frac{\partial \tilde{\Phi}_{r,IF}^s}{\partial dt_r} & \frac{\partial \tilde{\Phi}_{r,IF}^s}{\partial b} \end{bmatrix} \quad (3.12)$$

- Unknown Parameters: The unknown parameters, which comprise 6 Keplerian elements, 9 dynamic parameters, 3 stochastic accelerations, receiver clock and ambiguities, for the reduced-dynamic POD in post-mission mode are read as follows:

$$x = \left[x_{K_{6 \times 1}}^T \quad x_{d_{9 \times 1}}^T \quad x_{a_{3 \times n_s}}^T \quad dt_r \quad b_{n \times 1}^T \right]^T \quad (3.13)$$

In the batch mode, all epochs are considered in the least-squares, and the dimension of the normal equation, i.e., $N = A^T Q_y^{-1} A$, is therefore large. The optimized solution is to reconstruct the following normal equation:

$$\begin{bmatrix} A_{dt}^T Q_y^{-1} A_{dt} & A_{dt}^T Q_y^{-1} A_{pb} \\ A_{pb}^T Q_y^{-1} A_{dt} & A_{pb}^T Q_y^{-1} A_{pb} \end{bmatrix} \begin{bmatrix} dt \\ (p \ b)^T \end{bmatrix} = \begin{bmatrix} A_{dt}^T Q_y^{-1} \hat{\Phi}_{r,IF}^{s_1 s_2} \\ A_{pb}^T Q_y^{-1} \hat{\Phi}_{r,IF}^{s_1 s_2} \end{bmatrix} \quad (3.14)$$

where A_{dt} and A_{pb} are the design matrices related to the receiver clock offsets dt_r , the combined dynamic parameters and the ambiguities $(p \ b)^T$, respectively. The clock offsets are pre-eliminated epoch-wise, and the combined dynamic and ambiguities after this elimination are updated as follows:

$$(p \ b)^T = \left(A_{pb}^T Q_y^{-1} A_{pb} - (A_{pb}^T Q_y^{-1} A_{dt}) (A_{dt}^T Q_y^{-1} A_{dt})^{-1} (A_{dt}^T Q_y^{-1} A_{pb}) \right)^{-1} \cdots \quad (3.15)$$

$$\left(A_{pb}^T Q_y^{-1} \hat{\Phi}_{r,IF}^{s_1 s_2} - (A_{pb}^T Q_y^{-1} A_{dt}) (A_{dt}^T Q_y^{-1} A_{dt})^{-1} (A_{dt}^T Q_y^{-1} \hat{\Phi}_{r,IF}^{s_1 s_2}) \right)$$

The equation (3.15) is then solved, and the estimated dynamic parameters and ambiguities are introduced into the observation equation for each epoch. For a detailed explanation of reconstructing the normal matrices and solving Equation (3.15), refer to Chapter 6.3 in Jäggi (2006). The output of the batch least-squares contains the improved orbital elements and the stochastic parameters.

- An improved reduced-dynamic orbit is computed using the estimated orbital and stochastic parameters in the previous step. This orbit is used in the next iteration to screen the observations and find possible cycle slips.

The procedure explained in Step 4 should be repeated, e.g. three times, to clean the observations and find all cycle slips. A pre-final reduced-dynamic orbit is generated in the last iteration and used in step 6 for the final improvement update.

- 5- The next step is to test the residuals to find any observation that does not fit the model. The following IF residuals (v_{IF}) are computed using the screened observations and the orbit generated in the last iteration of the data screening in step 4.

$$v_{IF} = \Phi_{r,IF}^s - \hat{\Phi}_{r,IF}^s \quad (3.16)$$

The residuals larger than a pre-defined threshold, e.g., 4 cm, are used for outlier detection and exclusion.

- 6- The computed reduced-dynamic orbit from the data screening step is transformed to the precise ephemeris file format and then propagated with a new parametrisation, i.e., six Keplerian elements and only three constant coefficients in the RSW directions. This selection allows parametrizing the final reduced-dynamic orbit independently from the orbit parametrization used for the data screening. The partial derivatives with respect to the new parametrization are also estimated in this step.
- 7- Constant stochastic accelerations for shorter sub-intervals are estimated in another round of batch least-squares to generate the final reduced-dynamic orbit of the CubeSats. For a sample interval $t_{i-1} \leq t < t_i$, the relevant variational equation for these piece-wise constant accelerations, which is valid only in this interval, is defined as follows:

$$VE_{a_i} = \frac{\partial r_0(t)}{\partial a_i} a_i + (e_R, e_S, e_W)^T \quad (3.17)$$

These partial derivatives in Bernese are computed as a linear combination of partial derivatives of the Keplerian parameters (Dach et al. 2015). Therefore, the number of dynamic parameters in x_d is reduced to 3, referring to only constant coefficients in the RSW directions, and the stochastic pulses in x_a are replaced with the n_p piece-wise constant accelerations in shorter sub-intervals, i.e., 6 min. The unknown vector (3.13) with new parametrisations is expressed as:

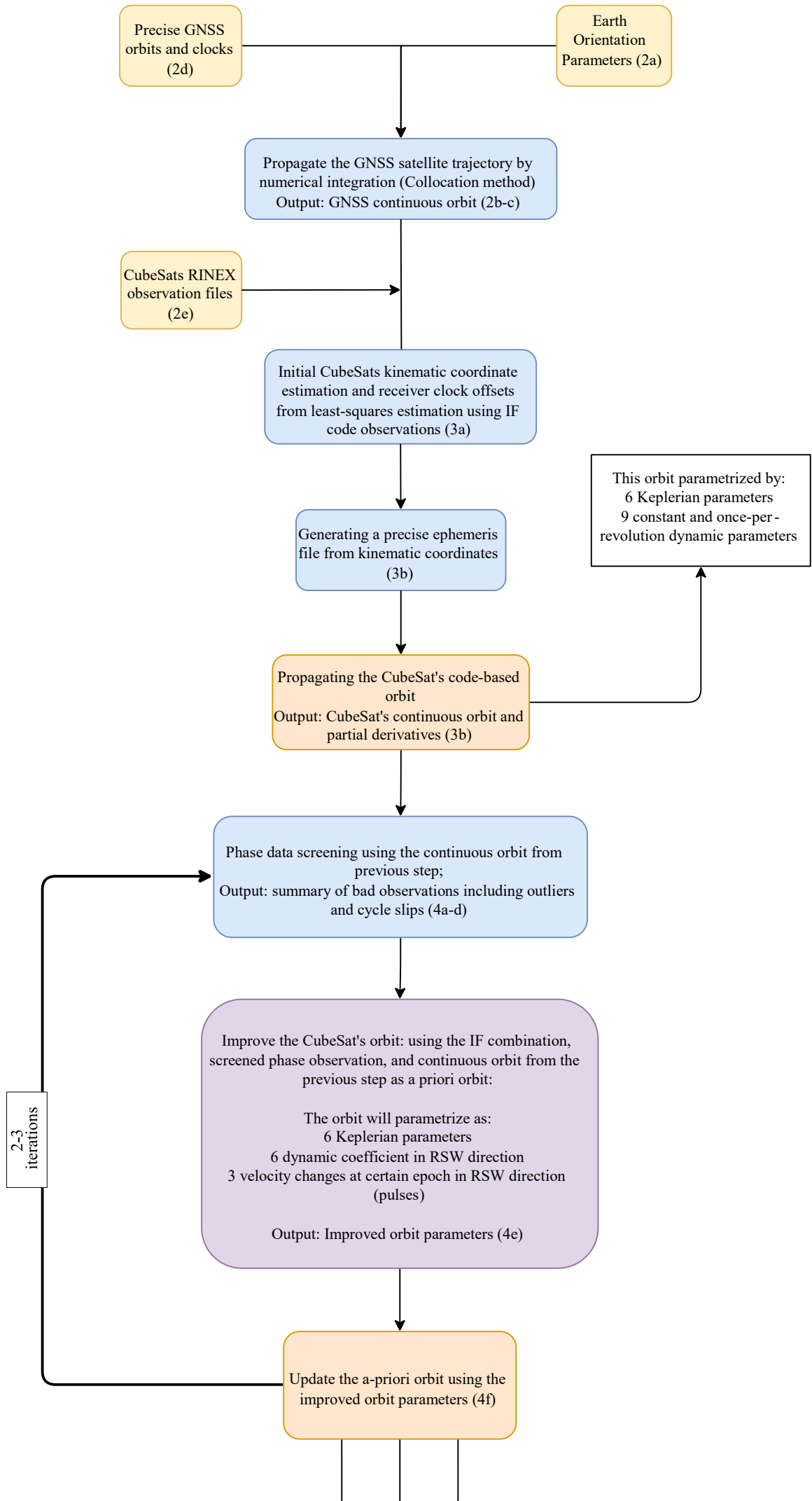
$$x = \left[x_{K_{6 \times 1}}^T \quad x_{d_{3 \times 1}}^T \quad x_{a_{3 \times n_p}}^T \quad dt_r \quad b_{n \times 1}^T \right]^T \quad (3.18)$$

These parameters are used to update the pre-final orbit and generate CubeSats' final reduced-dynamic precise orbit. This final reduced-dynamic orbit is used to generate the final IF phase residuals (3.16).

- 8- The cleaned IF phase observations and the final-reduced dynamic orbit are considered in another round of the batch least-squares adjustment to estimate the kinematic orbits. However, since this is a purely kinematic estimation, no dynamic parameters and stochastic accelerations (or pulses) are estimated. The unknown vector for the kinematic POD contains the epoch-wise coordinates of CubeSat, receiver clock offsets, and phase ambiguities lumped with phase biases:

$$x = \left[x_{3 \times 1}^T \quad dt_r \quad b_{n \times 1}^T \right]^T \quad (3.19)$$

The reduced-dynamic orbit can extend the CubeSats' orbits and velocities at arbitrary time points. Therefore, the reduced-dynamic orbit is continuous. However, this is not the case for the kinematic orbit since it includes the estimated coordinates only at the epochs when GNSS observations are available. The detailed flowchart of these steps is provided in Figure 1.



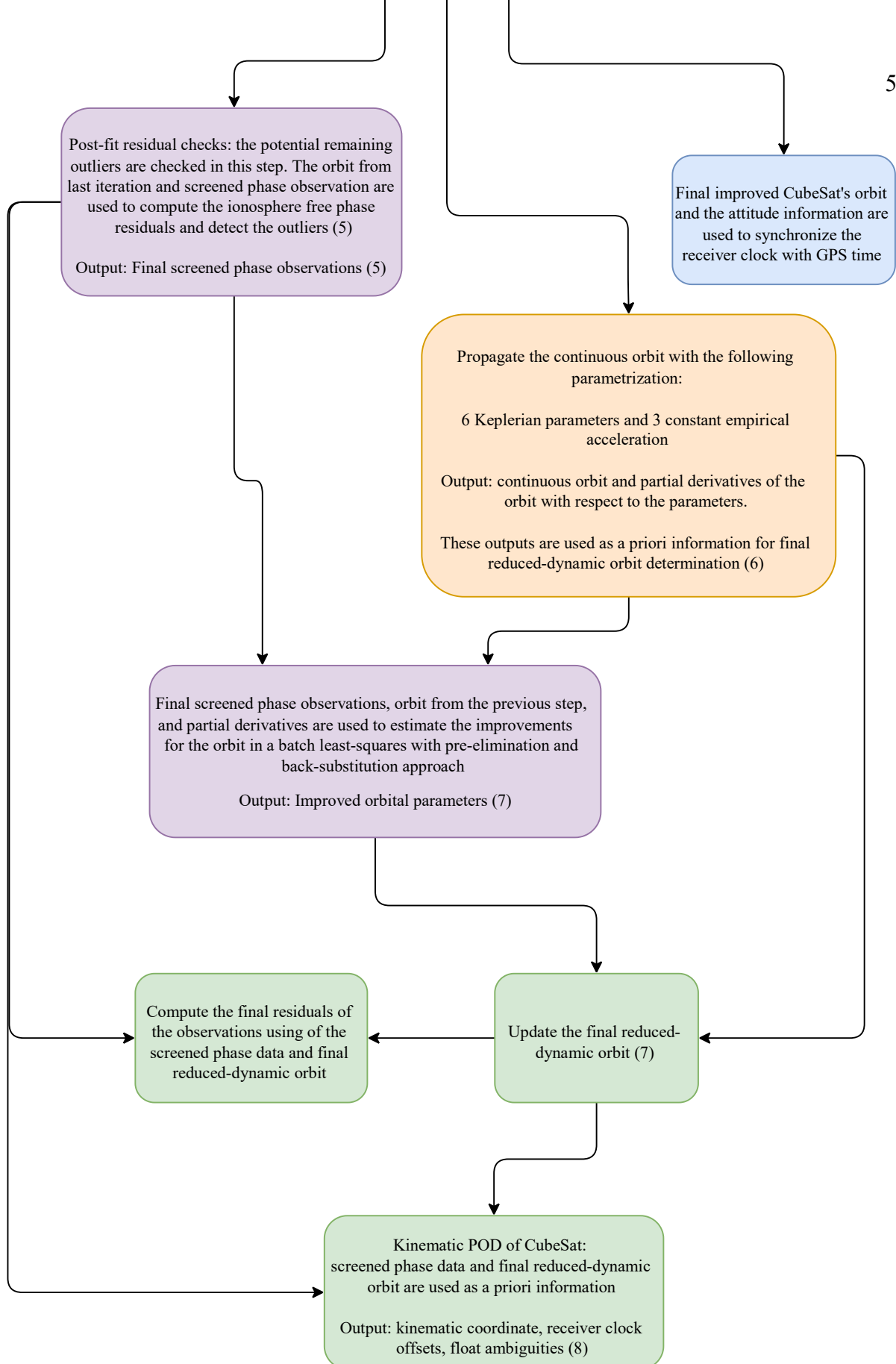


Figure 1 Flowchart of CubeSat POD using Bernese software package. The relevant step numbers are provided in parentheses

4 A sensitivity study of POD using dual-frequency GPS for CubeSats data limitation and resources

Data interruption is the primary limitation for many small CubeSats in the POD procedure. This interruption is not only for the Attitude Determination and Control System (ADCS) but also for the whole sensors' data in the bus, which resulted in the unavailability of GNSS observations and attitude information. The impact of this limitation is extensively studied in this chapter, and the required algorithms to reach different accuracies are discussed. The sensitivity analysis of different constraints and their impacts on the POD is discussed in the following publication, where the detailed software implementation is provided in Chapter 3:

Wang, K., **Allahviridi-Zadeh, A.**, El-Mowafy, A., & Gross, J. N. (2020). A sensitivity study of POD using dual-frequency GPS for CubeSats data limitation and resources. *Remote Sensing*, 12(13) (pp 1-21), 2107. DOI: 10.3390/rs1213210

Article

A Sensitivity Study of POD Using Dual-Frequency GPS for CubeSats Data Limitation and Resources

Kan Wang ^{1,*} , Amir Allahviridi-Zadeh ¹ , Ahmed El-Mowafy ¹  and Jason N. Gross ² 

¹ School of Earth and Planetary Sciences, Curtin University, GPO Box U1987, WA 6845 Perth, Australia; amir.zadeh@postgrad.curtin.edu.au (A.A.-Z.); A.El-Mowafy@curtin.edu.au (A.E.-M.)

² Department of Mechanical and Aerospace Engineering, West Virginia University, 1306 Evansdale Drive, PO Box 6070, Morgantown, WV 26506-6070, USA; Jason.Gross@mail.wvu.edu

* Correspondence: kan.wang@curtin.edu.au

Received: 10 June 2020; Accepted: 27 June 2020; Published: 1 July 2020



Abstract: Making use of dual-frequency (DF) global navigation satellite system (GNSS) observations and good dynamic models, the precise orbit determination (POD) for the satellites on low earth orbits has been intensively investigated in the last decades and has achieved an accuracy of centimeters. With the rapidly increasing number of the CubeSat missions in recent years, the POD of CubeSats were also attempted with combined dynamic models and GNSS DF observations. While comprehensive dynamic models are allowed to be used in the postprocessing mode, strong constraints on the data completeness, continuity, and restricted resources due to the power and size limits of CubeSats still hamper the high-accuracy POD. An analysis of these constraints and their impact on the achievable orbital accuracy thus needs to be considered in the planning phase. In this study, with the focus put on the use of DF GNSS data in postprocessing CubeSat POD, a detailed sensitivity analysis of the orbital accuracy was performed w.r.t. the data continuity, completeness, observation sampling interval, latency requirements, availability of the attitude information, and arc length. It is found that the overlapping of several constraints often causes a relatively large degradation in the orbital accuracy, especially when one of the constraints is related to a low duty-cycle of, e.g., below 40% of time. Assuming that the GNSS data is properly tracked except for the assumed constraints, and using the International GNSS Service (IGS) final products or products from the IGS real-time service, the 3D orbital accuracy for arcs of 6 h to 24 h should generally be within or around 1 dm, provided that the limitation on data is not too severe, i.e., with a duty-cycle not lower than 40% and an observation sampling interval not larger than 60 s.

Keywords: CubeSat; precise orbit determination; GNSS; low earth orbit

1. Introduction

Combining strong dynamic models and observations of global navigation satellite system (GNSS) collected onboard, the processing strategies used for the low Earth orbit (LEO) reduced-dynamic precise orbit determination (POD) have been intensively investigated in the last decades [1–5]. Compared to the dynamic orbits based on the dynamic models only and the kinematic orbits based on the GNSS observations only, the reduced-dynamic orbit determination has the advantage that it is more robust against model deficiencies for the former case, and possible data constraints, e.g., data in-continuity for the latter case. Following the need for the POD by a range of applications, such as the studies in the Earth gravity field [6,7], the atmospheric sounding [8], the altimetry [9], and the Interferometric Synthetic Aperture Radar (InSAR) [10], the LEO orbital accuracy based on undifferenced GNSS observations can reach a few centimeters [11,12], and even better at mm-level in case of baseline processing for formation-flying [12–14]. For undifferenced POD, the highest accuracy is often realized

in postprocessing mode applying good dynamic models, precise GNSS satellite orbits, and clocks, and under the condition that the GPS dual-frequency phase and code data are tracked and collected with a good continuity and completeness. The antenna attitude information is often well monitored by extra sensors like star cameras and inertial measurement unit (IMU), and eventually will be used to correctly apply the antenna sensor offsets, the antenna phase centre offsets (PCOs), and variations (PCVs) [15].

The number of CubeSat missions has dramatically increased in this decade. By April 2020, there are over 1000 CubeSats successfully launched into their low earth orbits [16]. In addition to educational purposes, CubeSats are nowadays also used for the demonstration of new technologies and scientific researches [17,18]. Compared to large or medium LEO satellites, the CubeSats are mostly cost-effective and occupy a much smaller size and weight, i.e., typically from below 1 kg (0.25U) to more than 20 kg (12U). This often leads to smaller battery volume and smaller size of the solar panels. In addition to the two-line elements (TLEs), other sensors like sun sensors and magnetometers have been used for orbit determination of CubeSats with relatively low accuracy, i.e., at km-level [19]. In the case of higher positioning accuracy requirements, the GNSS-based processing has been demonstrated as a useful method for the CubeSat POD, for which successful postprocessed position fix was achieved with a meter-level accuracy [20]. While the onboard positioning normally utilizes simplified dynamic models due to the limitation of the computational load [21,22], the data postprocessing allows the usage of comprehensive dynamic models and the estimation of enough additional dynamic parameters to compensate remaining model deficiencies. However, even for the postprocessing mode, strongly constrained satellite size and power need to be shared among all sensors onboard. The capacity for data tracking, storage, and transfer is thus restricted, which limits the accuracy of orbit determination. The GNSS satellites may not be able to be fully tracked continuously due to these limitations, which could yield a duty-cycle smaller than 100% [20,21,23], and lead to fewer data available for the processing and more ambiguities to be set up. The size of the data collected between each data dump could also be limited [20]. The collected GNSS observations are most likely to be temporarily stored onboard and transferred back to the ground processing centre (GPC) every orbital cycle or a few cycles during a limited ground contact time, while information of tasks other than positioning is required to be stored and transferred at the same time. This may implicitly limit the GNSS data amount during the downlink. Due to these constraints and the potential limit on computational load in case of the real-time onboard processing, a relatively low sampling rate might be preferable for CubeSat POD, or low in general but only high in specific areas [24]. Furthermore, one may need to prepare for a low number of tracked satellites in case of assigning channels for the purpose of initial signal acquisitions [20] and in case of improper data tracking due to possible antenna control problems, which will be discussed later in this section.

In addition to the data continuity and availability, other information required for the POD may also be limited for CubeSat missions. Due to the limitation of the CubeSats in terms of their size, power, and capacity to install extra sensors, the antenna attitude information may not be well measured, estimated, documented, and transferred back to the GPC with sufficient details. For example, due to power management needs, the IMU under its own high-accuracy experiment [25] onboard the CubeSat Simulation To Flight-1 (STF-1), investigated by NASA's Katherine Johnson Independent Verification and Validation (IV&V) Facility and West Virginia University [21,26], was unable to be activated during the GNSS data collection. Depending on the latency requirements of the CubeSat orbits, the high-accuracy GNSS satellite orbits and clocks might not be available for the processing, e.g., the international GNSS service (IGS) final products [27,28], which has a latency of 12–18 days. As explained in [11], this could lead to dramatic accuracy differences already in case of good data continuity and availability, mainly due to the decreased sampling rates of the satellite clocks. Moreover, instead of processing orbits with long arcs of 24 h or 12 h (which accounts for about 16 and 8 orbital cycles for an orbital period of 1.5 h), rapid processing may also be used to compute the orbit with shorter arcs of several hours. While some conditions mentioned above may not significantly influence the orbital accuracy when individually

being considered, large degradation of different levels could happen when several conditions happen together. Therefore, at the planning phase of a CubeSat mission, it is important to assess the orbital accuracy under different scenarios, so that one can properly compromise between the limits on diverse resources and the expected orbital accuracy.

The GNSS-based orbit determination of small satellites is often performed with single-frequency signals [23,24,29,30], which leads to an accuracy of decimeters to meters depending on the data availability and the dynamic models used. In recent years, to enable a higher POD accuracy, the usage of dual-frequency code and phase GPS data has been attempted and planned in CubeSat missions, even for a multi-constellation scenario [31]. Having dual-frequency phase and code observations at hand, the first-order ionospheric delays, which amounts to about 99% of the total ionospheric delays [32], can be eliminated by forming the ionosphere-free (IF) combination instead of the group and phase ionospheric correction (GRAPHIC) combination, which is often formed in the single-frequency case involving both the code and phase signals. While having the second frequency should theoretically enables better POD accuracy, a higher challenge for data tracking, storage, and transfer is also associated with the use of the dual-frequency GNSS in CubeSat missions. In addition to the planned constraints on diverse resources, the actual data collection of the dual-frequency CubeSat missions may not fulfil the expectation due to the lower robustness compared to the large LEO satellites. As an example, Figure 1 shows the real data condition of the 3U CubeSat STF-1 experimented by NASA's Katherine Johnson IV&V Facility and West Virginia University, which was expected to collect dual-frequency GPS data with a duty-cycle of 100% during a specific 12 h period. The actual data condition, however, did not meet the expectation, possibly due to the lack of the antenna attitude control. Due to the limitations in the antenna system, reports of short data pieces and frequent cycle slips, which hampers the high-accuracy POD, can also be found for the triple-CubeSat CanX-2 [20]. As such, not only for the planning purpose but also to get prepared for the possible sub-optimal real data collection, investigations of the CubeSat POD accuracy with diverse constraints on data and resources are important. A proper compromise is very possibly needed between the limiting resources, the suboptimal data conditions, and the requirements on orbital accuracy.

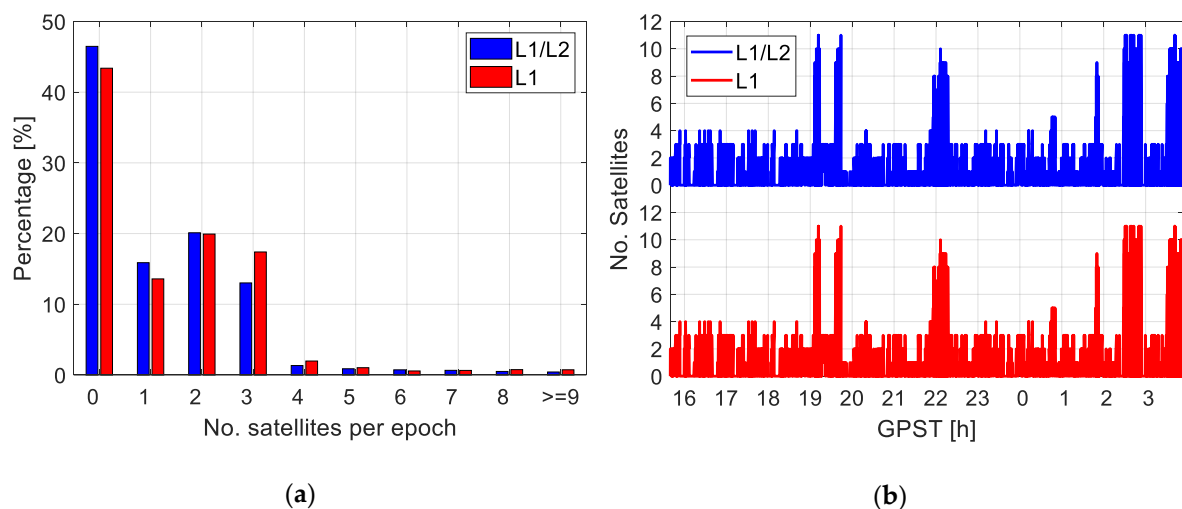


Figure 1. (a) Distribution of the tracked satellite numbers per epoch and (b) the time history of the satellite numbers having both the L1/L2 observations and at least the L1 observations. The data was collected from the CubeSat STF-1 from 15:39:37 in GPS time (GPST) on 27 February 2019 to 3:55:10 on 28 February 2019.

For the dual-frequency CubeSat POD, which is the focus of this study, it was pointed out by previous studies that the discontinuity of the observation data with a low duty-cycle may significantly degrade the orbital accuracy in both the real-time and the postprocessing modes [21,33]. In this study,

we restrict focus on postprocessing reduced-dynamic dual-frequency CubeSat POD, which relieves the strong constraints of the computational load onboard the CubeSat and allows for the usage of good dynamic models. In the experiments of CanX-2 [20] and STF-1 [21], geodetic grade receivers NovAtel OEM4-G2 and OEM615 tracking dual-frequency GPS signals were mounted onboard the CubeSats. With the expectation that in future CubeSat missions, dual-frequency measurements can be properly tracked in each duty-cycle by geodetic receivers with a mean average satellite number of at least 5 to 6, this study performs a sensitivity analysis of different limitations on the data availability, continuity, resources, latencies, and arc lengths with respect to the orbital accuracy. The overlapping effect of different constraints is investigated, and a compromise between these factors and the orbital accuracy is discussed. In addition to CubeSats, the analysis should also benefit the POD of other small satellites that need to bare similar constraints on data, power, and resources.

2. Processing Strategy

In this study, the final LEO orbits (where CubeSats are classified as LEO) are postprocessed following the reduced-dynamic LEO processing scheme of the Bernese GNSS Software V5.2 [34]. After correcting the antenna PCOs, PCVs, and the offsets between the antenna reference point (ARP) and the satellite center-of-mass (CoM), the determined final orbit in this study is referred to the satellite CoM. For the sensitivity analysis purpose, the final reduced-dynamic orbits are produced assuming different observation sampling rates, duty cycling, varying mean number of satellites by changing the elevation mask as will be explained in the next section, arc lengths, using different types of the IGS products, with and without the antenna attitude information. The processing procedure can generally be summarized in the following steps, which is also given in Figure 2 as a flow diagram:

1. Compute kinematic orbits using single point positioning (SPP) employing the IF combination of the code observations. These kinematic orbits, denoted as vector \hat{r}_K , are discrete and have an accuracy of meters.
2. Computation of the code-based reduced-dynamic orbits. The reduced-dynamic orbits are computed with accelerations based on a series of gravitational and nongravitational terms, such as the Earth gravitational terms, the Earth tidal terms, the gravitational attraction from the sun, moon, and other planets, as well as the general relativistic term. Note that mis-modeled effects like the solar radiation pressure and the air drag will be largely absorbed by the estimated dynamic parameters and the stochastic velocity changes or accelerations set up later in the processing [35]. Details of the processing and the dynamic models are given in Table 1. Making use of the kinematic code orbits from the first step, the six Keplerian elements at the initial condition (the semi-major axis of the orbit, the orbital eccentricity, the inclination of the orbital plane, the right ascension of the ascending node, the argument of perigee, and the argument of latitude at the initial condition), and a remaining part of the dynamic models are estimated with a batch least-squares adjustment, which includes at this step nine flight-oriented dynamic parameters. These estimable dynamic parameters contain three constant terms (a_{R0} , a_{S0} , and a_{W0}) and six periodic terms (a_{RC} , a_{SC} , a_{WC} , a_{RS} , a_{SS} , and a_{WS}) in the radial (R), along-track (S) and cross-track (W) directions. The total acceleration a can then be distributed into the term a_0 , which is assumed known by applying the models given in Table 1, and an additional dynamic term a_{dyn} that is to be adjusted:

$$a = a_0 + a_{dyn}, \quad (1)$$

With

$$a_{dyn} = a_R e_R + a_S e_S + a_W e_W, \quad (2)$$

$$a_R = a_{R0} + a_{RC} \cos(U) + a_{RS} \sin(U), \quad (3)$$

$$a_S = a_{S0} + a_{SC} \cos(U) + a_{SS} \sin(U), \quad (4)$$

$$a_W = a_{W0} + a_{WC} \cos(U) + a_{WS} \sin(U), \quad (5)$$

where e_R , e_S , and e_W represent the unit vectors in the radial, along-track, and cross-track directions, respectively. U denotes the satellite argument of latitude. The code-based kinematic orbits \hat{r}_K obtained from the first step are used as observations to adjust the 15 parameters mentioned above in a least-squares sense. The linearized observation equation at the epoch t_i can be formulated as:

$$E(\hat{r}_K - \hat{r}_0) = [A_{rk}, A_{rd}][x_k, x_d]^T, \quad (6)$$

where \hat{r}_0 is the a priori orbit vector obtained based on numerical integration on hand the a_0 , and the \hat{a}_{dyn} and the Keplerian elements estimated from the last iteration. The vectors x_k and x_d contain the increments of the six Keplerian elements and the nine dynamic parameters, respectively, and the design matrices A_{rk} and A_{rd} contain the partial derivatives of the position vectors with respect to x_k and x_d . The partial derivatives are computed with numerical integration of the variational equations [36,37]. E is the expectation operator. The reduced-dynamic orbit can be interpolated for time epochs with higher sampling rates and produced for periods with data gaps. In this study, all orbits are resampled into time epochs with 10 s sampling interval for assessment, regardless of which duty-cycles and observation sampling rates are applied in the processing.

3. Phase preprocessing and orbit improvements. This step preprocesses the raw phase observations to detect cycle slips and mark bad observations. The preprocessing goes through several iterations to improve the LEO orbit quality. The orbit improvement is realized through estimation of stochastic velocity changes [38] in addition to the 15 parameters mentioned in the second step, and is performed in a least-squares adjustment making use of the IF combination of the phase observations. One set of the stochastic velocity changes is considered in each predefined time interval, e.g., every 15 min. The linearized phase observation equation at the epoch t_i can be expressed as:

$$E(\Delta\varphi_{IF}) = [A_{lk}, A_{ld}, A_{lv}][x_k, x_d, x_v]^T + c \times \Delta t_r + \lambda_{IF} N_{IF}, \quad (7)$$

With

$$\lambda_{IF} = \frac{c}{f_1 + f_2}, \quad (8)$$

$$N_{IF} = \frac{f_1^2 \lambda_1 N_1 - f_2^2 \lambda_2 N_2}{c(f_1 - f_2)}, \quad (9)$$

where $\Delta\varphi_{IF}$ represents the observed-minus-computed (O-C) term of the IF phase observations. c and Δt_r denote the speed of light and the receiver clock error, respectively. λ_j , f_j , and N_j represent the wavelength, the frequency, and the ambiguity on frequency j ($j = 1, 2$), respectively. Note that N_{IF} is not an integer. The receiver clock error is estimated epoch-wise independently, and the ambiguity is assumed constant before the detection of a cycle slip. Note that new ambiguities are setup for estimation at the beginning of each round of duty cycling. x_v stands for the vector containing all stochastic velocity changes in the RSW directions from the first to the current epoch and note that x_v is constrained to zero with a predefined a priori standard deviation. The design matrices A_{lk} , A_{ld} , and A_{lv} contain the partial derivatives of the O-C terms with respect to the x_k , x_d , and x_v , respectively. To be estimated are the vector $[x_k, x_d, x_v]^T$, the receiver clock offset Δt_r , and the term N_{IF} . Note that very little code observations are used to avoid the problem of matrix singularity between the receiver clock offset and the ambiguity terms. Note that the ambiguities on L1 and L2 are not attempted to be fixed in this study.

4. Generation of final orbits. With the preprocessed phase observations, the six Keplerian elements, the three constant dynamic parameters (a_{R0} , a_{S0} , and a_{W0}) are estimated together with stochastic

accelerations in the RSW directions. The accelerations are set up in shorter time intervals compared to those in Step 3. The linearized phase observation equation is thus formulated as:

$$E(\Delta\varphi_{IF}) = [A_{Ik}, A_{Id0}, A_{Ia}][x_k, x_{d0}, x_a]^T + c \times \Delta t_r + \lambda_{IF} N_{IF}, \quad (10)$$

where x_{d0} and x_a denote the increment vector of the three constant dynamic parameters and all the stochastic accelerations from the first to the current epoch, respectively. x_a is constrained to zero with a predefined a priori standard deviation (selected as 5×10^{-9} m/s² in all the three directions based on the default setting for GRACE satellites in the Bernese software, as real data from the GRACE Follow-on mission is used for test purposes in this study, which will be explained later. This value may vary for satellites of other missions). A_{Id0} and A_{Ia} correspond to the partial derivatives of the phase O-C terms with respect to the x_{d0} and x_a , respectively. Note that very little code observations are used to avoid singularity mentioned above.

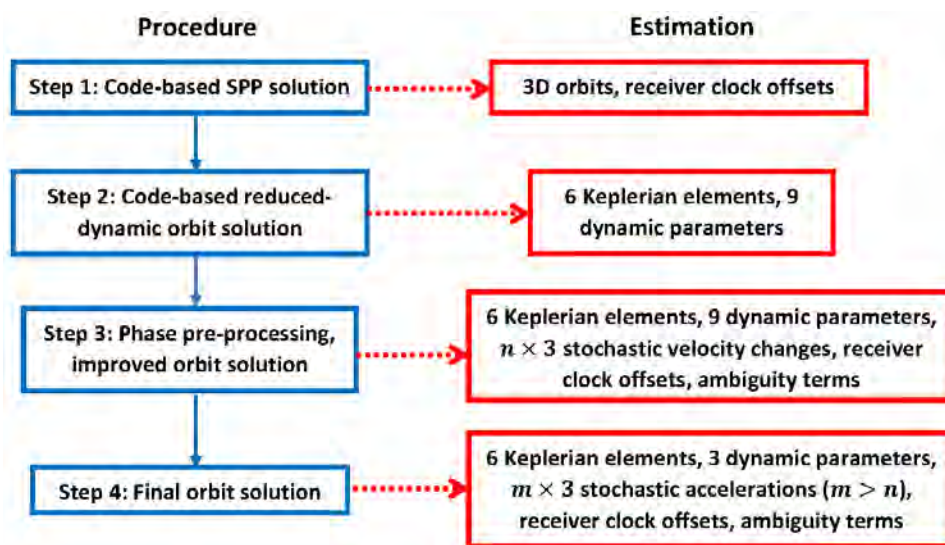


Figure 2. Flow-diagram of the processing procedure and the estimated parameters. n and m are the numbers of the stochastic parameter vectors considered during the estimation in Step 3 and 4, respectively.

Table 1. Processing details for the reduced-dynamic orbit determination.

| | |
|----------------------------------|---|
| Measurement Model | GPS code P1 + P2, phase L1 + L2 |
| | IF linear combination |
| | Sampling interval: 10 s, 20 s, 30 s, 60 s, 120 s |
| | Elevation mask: 5°, 15°, 25° (for different mean satellite numbers) |
| | Arc length: 6 h, 12 h, 24 h |
| Dynamic Model | GPS orbits and clocks: IGS final, rapid, real-time products |
| | Earth gravity: EGM2008 [39], Earth potential degree: 120 |
| | N-body gravity: JPL DE405 [40] (Planetary ephemeris) |
| | Solid Earth tides: IERS Conventions 2010 |
| | Pole tides: IERS Conventions 2010 [41] |
| | Ocean tides: FES2004 [42] |
| Reference Frame | General relativistic term |
| | IGS14, J2000.0 (Julian epoch) |
| Coordinate Transformation | Nutation and precession: IAU2000R06 [34] |
| | Sub-daily pole variations: IERS Conventions 2010 [41] |
| | Earth rotation parameters: IGS final, rapid, ultra-rapid products |

In this study, the data from the LEO satellite of the GRACE Follow-on mission [43], the GRACE FO-1, which continuously tracked dual-frequency code and phase GPS observations on L1 and L2, are used for different scenarios simulating conditions with limited data and resources on 22 August 2018. For the purpose of consistency, the processed orbits are differenced with the best-case scenario in this study (as the reference for comparison), i.e., the phase-based reduced dynamic orbits with a duty-cycle of 100%, an observation sampling interval of 10 s, an elevation mask of 5 degrees (default setting in Bernese for LEO processing), using the IGS final products and processed in a 24 h arc. The use of our best-case scenario as a reference for comparing different tested cases is justified by comparing it with the reference orbits provided by the Jet Propulsion Laboratory (JPL) [44] for the same day, where good consistency with a 3-dimensional (3D) root-mean-squared error (RMSE) of below 2 cm was achieved. Nevertheless, it should be noted that in this study, the 3D RMSE computed under different scenarios refer to the accuracy difference compared with the best-case scenario, but not the absolute orbital accuracy. Note that for LEO missions, independent techniques like the satellite laser ranging (SLR) and the K-band ranging (KBR) are often utilized to validate the accuracy of reference orbits. As a large number of variants with respect to different observation sampling rates, duty-cycles, satellite numbers, latencies, availability of the attitude information, and arc lengths are tested, this study does not attempt to study long-term variation of results. As a consistency check, the POD results of the best-case scenario from 14 to 21 August 2018 were compared with the JPL reference orbits, and no significant difference from those of the test day in this study can be observed, i.e., at a few millimeters. As such, we consider the simulations based on the test day are representative.

3. Orbit Determination under Different Scenarios

As a start point of our analysis, let us look at the results of code-based processing and see the impact of using a reduced-dynamic model. Figure 3 shows the 3D positional errors of the kinematic orbits (red) based on the code observations on P1 and P2 forming the IF combination (Step 1 in Section 2), and when computing the same data with the reduced-dynamic orbits (blue, Step 2 in Section 2) for GRACE FO-1 for the tested 1 day of data. As complete dual-frequency CubeSats data for a long period needed in our analysis are currently not available, the data from a typical LEO satellite that may share similar orbit conditions with CubeSats, in this study GRACE FO-1, were used for simulation of the best-case scenario of the CubeSat processing [33]. For the tested LEO satellite, the dual-frequency GPS data are tracked in a complete and continuous manner with an observation sampling interval of 10 s. A duty-cycle of 100% and a mean satellite number of about 9 above the elevation mask of 5 degrees were available for the processing of a daily arc using the IGS final products. The 3D RMSE of the code-based kinematic (Step 1 in Section 2) and reduced-dynamic orbits (Step 2 in Section 2) amount to about 1.6 m and 0.2 m, respectively, which clearly shows the value of employing strong dynamic models. When reducing the data availability and continuity, the accuracy of the reduced-dynamic orbit could degrade to the sub-meter level.

For high-accuracy POD, as discussed in Section 2, the code-based orbits are only used as the a priori orbits for the phase processing. Therefore, in the rest of the sections, the sensitivity analysis will focus on the final phase-based reduced-dynamic orbits.

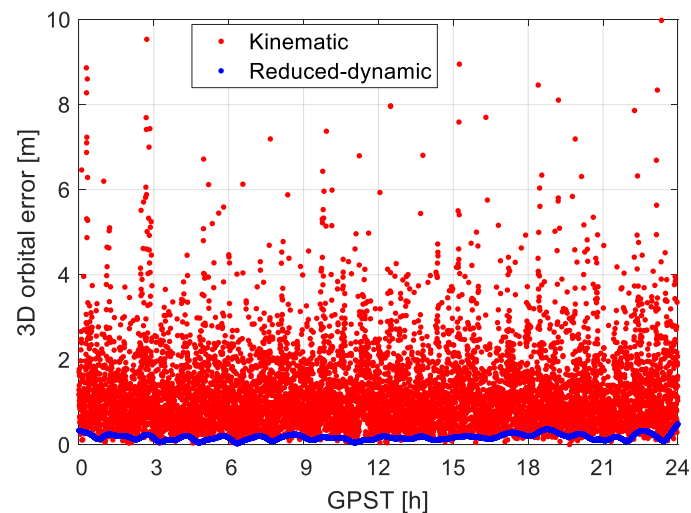


Figure 3. 3D orbital errors of the code-based kinematic (red) and reduced-dynamic daily arc (blue) with a sampling interval of 10 s. The IGS final products were used for the GPS satellites.

3.1. Duty Cycling and Satellite Numbers

As mentioned before, due to the constraints of the CubeSats on the power, the data storage, and the time of active attitude control possibly during the sunlight, the GNSS observations might have breaks, and are collected in pieces of different length [20]. In this study, observation data are assumed to be collected with different duty-cycles, i.e., with the power turned on only for a part of the time. The duty-cycle D is defined here as a percentage of time data was available out of the total time considered. The sensitivity analysis is performed assuming the D varying from 20% to 100%. In our tests, a duty-cycle implies that the data are available in the first $60 \times D$ min of each hour. The 3D orbital errors are shown in Figure 4 with varying D . The observation sampling interval was 10 s. Recall that the phase-based reduced-dynamic orbit with a duty-cycle of 100% was our best-case scenario and was used as the reference for comparison as mentioned in Section 2. The RMSE increases from about 1.6 cm with a D of 80% to about 3.5 cm with a D of 20%. Note that the RMSE is computed from the beginning of the first power-on period to the end of the last power-on period of the test day.

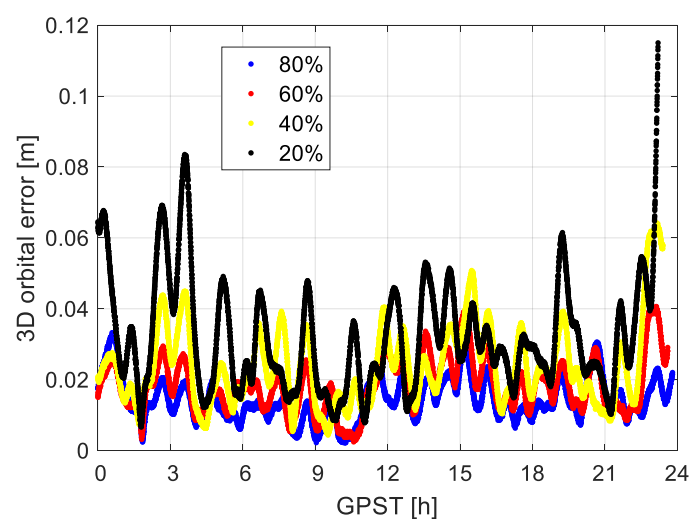


Figure 4. 3D orbital errors for different duty-cycles (from 20% to 80%) of the phase-based reduced-dynamic orbits using data of GRACE FO-1 with a sampling interval of 10 s. The elevation mask was set to 5 degrees with a mean satellite number of about 9.

As shown in Figure 1 and discussed in [19], the number of satellites that can be properly tracked (at least for the P1 and P2 observations) by the CubeSat receiver could be lower than expected due to different reasons, such as the antenna stabilization problems or specific channel assignment. Therefore, to resemble this practical issue, a simplified approach is performed in this simulation to reduce the number of satellites observed under good conditions by excluding satellites with low elevation angles. The elevation mask is increased from 5 to 25 degrees in the test, resulting in a reduction of the mean satellite number from about 9 to 6 (see Table 2). The Figure 5a illustrates the distribution of the satellite numbers applying different elevation masks for GRACE FO-1 for the test period. A gradual reduction of the satellite numbers can be observed when increasing the elevation mask. The percentile of valid SPP solutions is reduced correspondingly from nearly 100% to about 83% due to the reduction in redundancy.

Table 2. Mean number of satellites used in SPP and percentiles of valid SPP solutions applying different elevation masks. Note that the mean satellite numbers are given as rounded values. The real values of the mean satellite numbers amount to about 8.5, 7.4, and 5.7 for an elevation mask of 5, 15, and 25 degrees, respectively.

| Elevation Mask [Degree] | Mean Integer Number of Satellites | Percentile of Valid SPP Solutions |
|-------------------------|-----------------------------------|-----------------------------------|
| 5 | 9 | 99.9% |
| 15 | 7 | 99.1% |
| 25 | 6 | 82.9% |

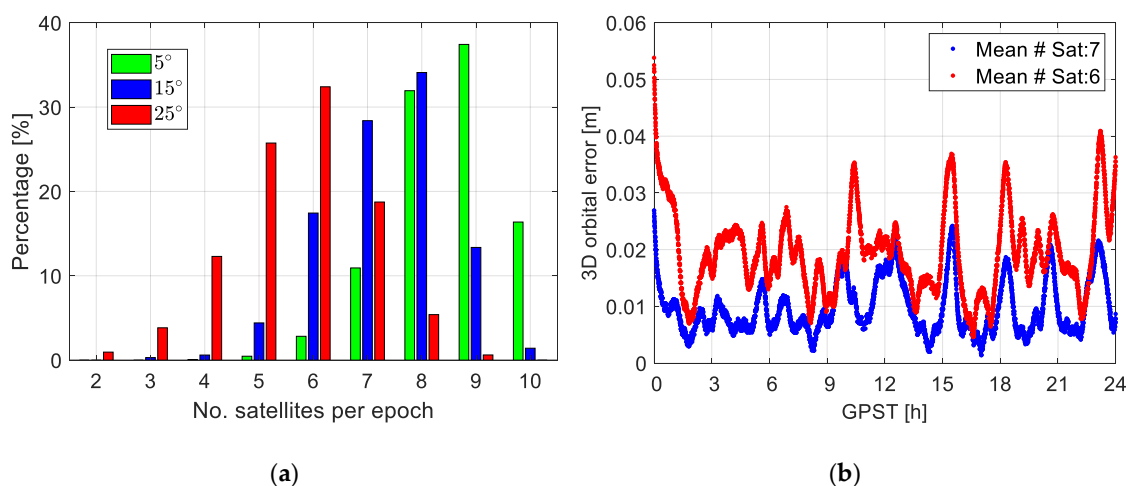


Figure 5. (a) Distribution of the satellite numbers per epoch (observing at least P1 and P2 observations) applying different elevation mask angles and (b) the corresponding 3D orbital errors of the phase-based reduced-dynamic orbits with a duty-cycle of 100% and mean satellite numbers of 7 and 6.

Having a duty-cycle of 100%, as shown in Figure 5b, decreasing the number of the received satellites from, e.g., 7 to 6, degrades the RMSE from about 1.1 to 2.1 cm. Note that the case with the mean satellite number of 9 having an elevation mask of 5 degrees is our best-case scenario and is used as the reference for comparison, in other words, the RMSE represent the solution discrepancy between the cases of using 7 or 6 satellites and when using 9 satellites.

Although the differences observed in Figures 4 and 5 are not large, coupling a reduction in the duty-cycle with a reduction in the number of received satellites would cause larger problems. Table 3 shows the 3D RMSE of the orbits applying different duty-cycles and mean satellite numbers, assuming an observation sampling interval of 10 s still. As mentioned earlier, the solution obtained with a duty-cycle of 100% and the mean satellite number of 9 is used as the reference for assessing the solutions by computing their discrepancies. It can be observed that with a duty-cycle equal or above 60%, even when the observed satellites are limited, the RMSE is still below 3 cm. With lower

duty-cycles, however, observing all or almost all visible satellites would be essential to maintain a low RMSE at this level. With a duty-cycle of 20%, decreasing the mean satellite number to 6 would increase the RMSE to about 5 cm.

Table 3. 3D RMSE (in cm) of the phase-based reduced-dynamic orbits under different duty-cycles and mean satellite numbers.

| Duty-Cycle/Mean # Satellite | 9 Satellites | 7 Satellites | 6 Satellites |
|-----------------------------|--------------|--------------|--------------|
| 100% | – | 1.1 | 2.1 |
| 80% | 1.6 | 1.9 | 2.4 |
| 60% | 2.0 | 2.1 | 2.7 |
| 40% | 2.6 | 2.9 | 3.5 |
| 20% | 3.5 | 3.9 | 4.8 |

3.2. Sampling Rate of the Observations

In Section 3.1, the GPS observations onboard the LEO satellite with a sampling interval of 10 s were used for producing the reduced-dynamic orbits. Depending on the capacity of the CubeSat missions, the data might need to be stored and transferred to the GPC with a lower sampling rate. A compromise thus needs to be considered between the duty-cycles, the data completeness, and the sampling rate. Figure 6 illustrates the 3D RMSE of the orbits with the sampling interval varying from 10 to 120 s and the duty-cycle varying from 100% to 20%. The cases having mean satellite numbers of 9, 7, and 6 are given between each pair of dashed lines. Recall that the number of satellites is controlled by adjusting the elevation mask (Section 3.1). In the case of a duty-cycle of 20%, the orbits generated with an observation sampling interval of 120 s (red line) are not produced due to the extremely low number of continuous observations in each data patch. Note that all the RMSE are computed based on orbits resampled to 10 s sampling intervals.

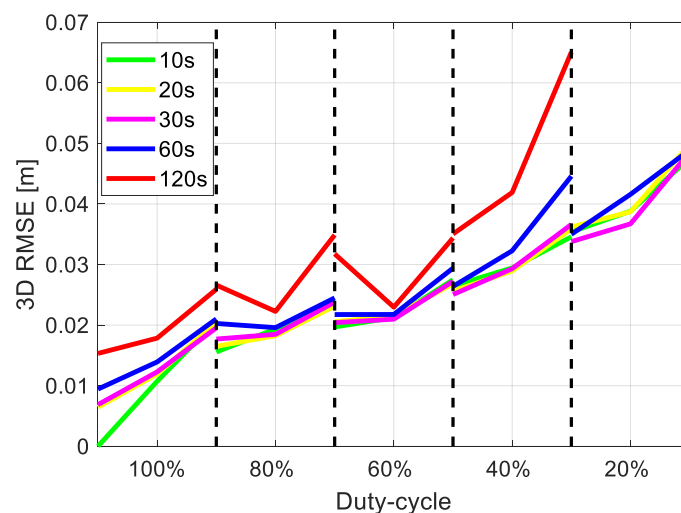


Figure 6. 3D RMSE of the reduced-dynamic orbits under different duty-cycles, observation sampling intervals, and mean satellite numbers using the IGS final products. The cases having 9, 7, and 6 satellites (on average) are given between each pair of the dashed lines.

From Figure 6 it can be observed that the values in general gradually increase from the left to the right side, i.e., from the cases with good data continuity, completeness, to those with bad data conditions. With less data available for the processing in the Steps 3 and 4 (Section 2), the estimable parameters, including the six Keplerian elements, the additional dynamic parameters, and the stochastic parameters, are determined with lower precision. This results in a lower accuracy of the numerically integrated

orbits. At the same time, it can also be observed that the differences between having observation sampling intervals of 10 s (green), 20 s (yellow), and 30 s (magenta) are small. This can be attributed to the 30 s GPS clocks provided in the IGS final products, where interpolation into high-sampled time epochs would introduce biases within a higher percentage of the processing time (to be discussed in the next subsection). Provided that the receiver has a high duty-cycle not lower than 60%, even with a limited number of observed satellites and a high sampling interval of 120 s, the 3D RMSE is still below or around 3 cm. However, with lower duty-cycles, the degradation of the orbit accuracy could be dramatic when the observations are only available with a low sampling rate and when the observed satellites are limited.

3.3. Latency Applying Different GPS Products

In Sections 3.1 and 3.2, the IGS final products for GPS satellite orbits and clocks were used for the estimation of the reduced-dynamic orbits. The IGS final products are produced weekly and have a latency of 12 to 18 days. In case that the CubeSat orbits are required within a shorter time, the IGS (or one of its analysis centres) rapid products or products from the IGS real-time service (RTS) [45,46] can be used instead. Table 4 gives the latencies of different IGS products. In this study, the decoded IGS real-time stream IGC01, which is denoted as the IGC products and available at [47], is used for simulation of the scenario retrieving the GPS products in (near)-real-time. Products of the single IGS analysis centers, e.g., the real-time products from the National Centre for Space Studies (CNES), are also of high quality [48]. In this study, for consistency purpose, we used the IGS products of different latencies and satellite clock sampling rates.

Table 4. Information on different IGS products and the 3D orbital RMSE using 10 s observation data.

| Orbits/Clocks | Identifier | Latency | Accuracy [cm] Orbit/Clock | Satellite Clock Sampling Interval [s] | 3D RMSE [cm] |
|---------------|------------|------------------|------------------------------|--|--------------|
| IGS Final | IGS | 12–18 days | 2.5/2.25 | 30 | – |
| IGS rapid | IGR | 17–41 h | 2.5/2.25 | 300 | 4.8 |
| IGS RTS | IGC | (Near)-real-time | 2–5/3–5 | 30 | 3.2 |

Despite the accuracy differences [46,49], from Table 4 it can also be seen that the sampling rate of the IGR satellite clocks is lower than the other two products. In [11], the sampling interval of GPS satellite clock-offset corrections was identified as a limiting factor for the LEO orbital accuracy. This possibly explains the fact that the 3D orbital RMSE using the IGR products are not better than those using the IGC products. Figure 7 shows the differences of the between-satellite clock corrections for G02 and G32 between the IGS final and rapid clocks. The between-satellite clock differences are shown to remove possible inconsistencies between the reference time scales of different products. The blue dots indicate the differences at the given sampling interval of the rapid clocks, i.e., 300 s. The red dots illustrate the differences at a sampling interval of 30 s, where the rapid clocks were linearly interpolated using the nearest epochs to this higher sampling rate. From Figure 7 it can be observed that although the differences are generally at centimeters for the blue dots with the given sampling rate of the rapid clocks, after interpolation, the differences are increased to dm-level (see the red dots). For the test day, the average RMS of the clock differences for all satellites between the IGS and IGR final products, divided by $\sqrt{2}$ for the between-satellite differencing, amount to about 2 cm. Note that the large pattern of the red dots is caused by the stochastic behaviors of the clocks, and an interpolation over a longer period with a higher-order polynomial does not help to reduce the biases. As an example, interpolation with a quadratic polynomial within each half hour increases the average RMS by several millimeters.

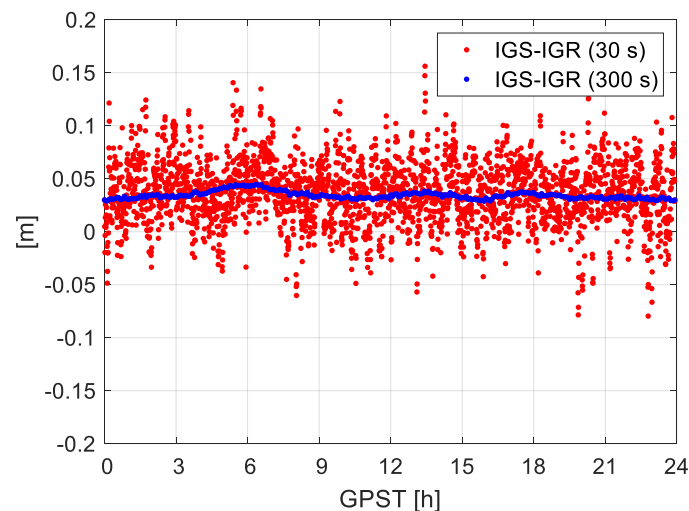


Figure 7. Differences in the between-satellite clocks for G02 and G32 between the IGS final and rapid clocks.

Assuming a duty-cycle of 100%, an observation sampling interval of 10 s, and a mean satellite number of 9, the last column of Table 4 shows the 3D RMSE of the final LEO orbits determined using different IGS products compared with the best-case scenario, i.e., using the IGS final products. A 3D RMSE of several centimeters can be achieved for the IGR and IGC products. This is further illustrated by Figure 8, which shows the time series of the 3D orbital errors applying the IGR and IGC products.

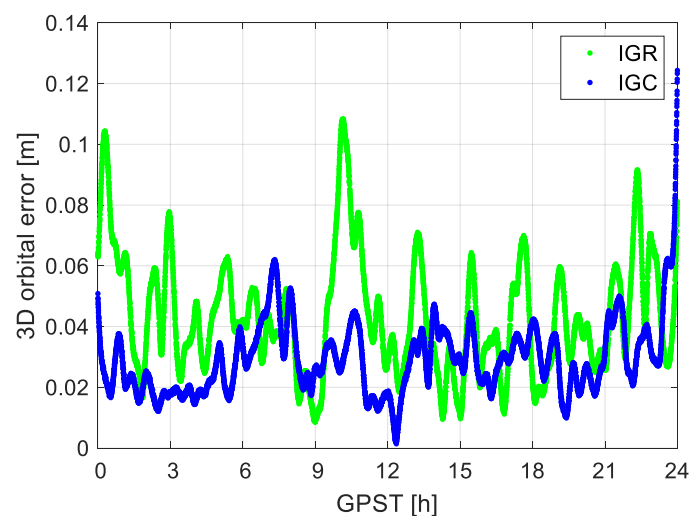


Figure 8. 3D orbital errors of the phase-based reduced-dynamic orbits using data of GRACE FO-1 with a 100% duty-cycle, a mean satellite number of 9, and a sampling interval of 10 s (having the IGS final as the reference). Different IGS products were applied.

In the case of having limited data available, i.e., with short duty-cycles, limited satellite numbers and sampling rate, the orbital accuracy using the IGR and IGC products would not be as good as shown in Figure 8 anymore. In the case of using the IGR and IGC products, Figure 9 illustrated the 3D RMSE of the difference between phase-based reduced-dynamic orbits and the best-case scenario when applying different duty-cycles, mean satellite numbers, and observation sampling rates. Note that the cases having different satellite numbers (9, 7, and 6) are given between each pair of the dashed lines. Compared to Figure 6 using the IGS final products, the 3D RMSE has generally increased due to the reduced accuracy of the GPS products and the higher sampling interval of the GPS clocks (for IGR products). As discussed for the IGS final products, when using the IGC products (Figure 9b), one can

similarly observe that a high observation sampling interval of, e.g., 10 s (green) or 20 s (yellow), is not helpful to reduce the RMSE due to the GPS clock sampling of 30 s. For the cases when using the IGR products (Figure 9a) with a higher GPS clock sampling interval of 300 s (Table 4), no obvious degradation can be concluded even when having an observation sampling interval of 120 s.

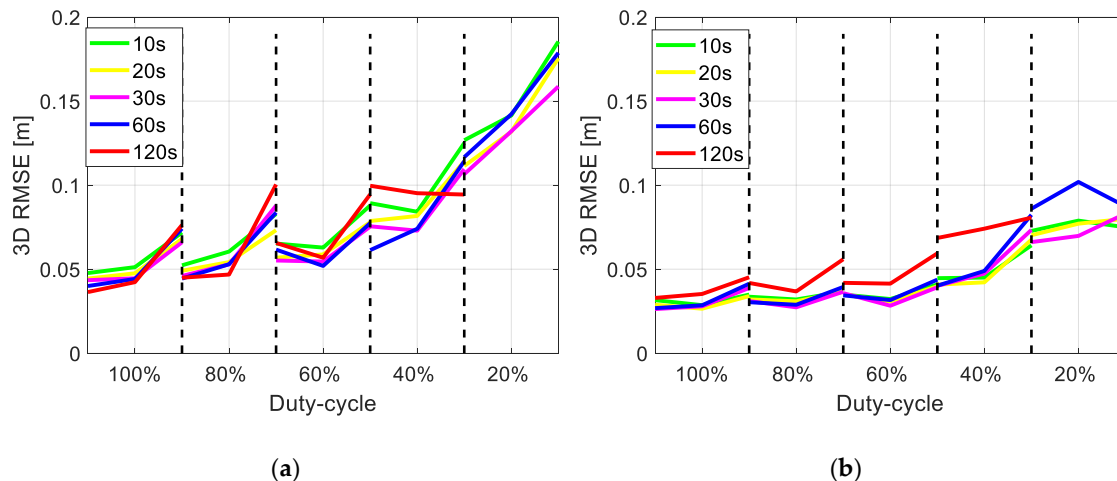


Figure 9. 3D RMSE of the reduced-dynamic orbits under different duty-cycles, observation sampling intervals and mean satellite numbers using (a) the IGR and (b) the IGC products. The cases having 9, 7, and 6 satellites (on average) are given between each pair of the dashed lines.

3.4. Antenna Attitude

As shown in the example in Figure 1, it is suspected that the poor data tracking condition is caused by the lack of antenna stabilization. Good antenna stabilization is essential to keep the antenna in a favorable orientation for GNSS tracking, i.e., approximately toward the radial direction. High-accuracy attitude control is expected to be realized also for CubeSats, as found to be feasible in the tests simulating different CubeSat scenarios in [50] and achieved for the CubeSat CanX-2 [20]. Under the condition of appropriate antenna stabilization, the antenna attitude information is often measured by extra sensors like star cameras or IMU on LEO/CubeSats satellites. For CubeSats, however, the limited size and power may limit its capacity to properly measure, store, or transfer the attitude information back to the GPC. As mentioned in Section 1, the data from the IMU onboard the CubeSat STF-1, e.g., was not collected during the GNSS data tracking because of the power allocation, where the IMU used was of a special type tested for a high-accuracy experiment that was carried out at a different time. The attitude information of the satellite (and antenna) is sometimes even ignored in CubeSat simulation studies [21]. Under such circumstances, where no attitude information is available, the antenna attitude could be estimated based on the satellite positions and velocities. Taking the GRACE FO-1 as an example, the antenna was fixed on the satellite and its up direction generally points toward the radial direction from the earth to the LEO satellite. Note that the X-axis in the satellite reference frame (SRF) is here approximately in the anti-flight direction, as GRACE FO-1 is the leading satellite in the test period. Figure 10 depicts the RSW system (green) in the radial, along-track and cross-track directions with the origin in the satellite centre-of-mass, and the antenna reference frame (ARF, red), e.g., for GRACE FO-1, in the north, east, and up (NEU) directions with the origin in the antenna reference point (ARP). To evaluate the differences between the expected and the actual orientations, the angle differences are computed with the help of the east (e_E) and the opposite along-track (e_S) unit vectors, the north (e_N) and the cross-track (e_W) unit vectors, and the up (e_U) and the radial (e_R) unit vectors in the inertial system:

$$\alpha_E = \arccos(-e_E^T e_S), \quad \alpha_N = \arccos(e_N^T e_W), \quad \alpha_U = \arccos(e_U^T e_R). \quad (11)$$

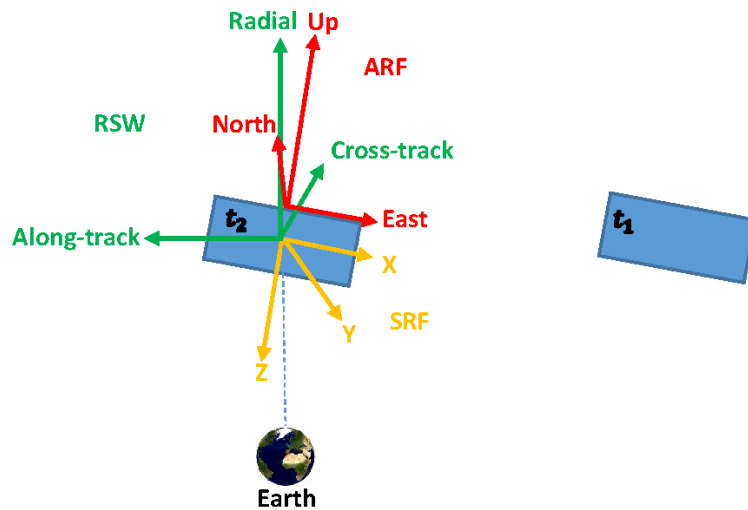


Figure 10. The antenna reference frame (ARF, shown in red), the satellite reference frame (SRF, shown in yellow), and the radial, along-track, and cross-track (RSW, shown in green) system. t_1 and t_2 represent two conservative time epochs for the same satellite. The figure is scaled for a better presentation.

In Equation (11), the unit vectors e_R and e_S are calculated based on the satellite position and velocity vectors, and e_W completes the left-hand system. As the antenna is fixed on the satellite, the antenna NEU unit vectors e_N , e_E , and e_U are calculated based on the satellite orientations, which are tracked by extra sensors and documented in an attitude file with quaternions. The rotation matrix R_{SRF} transforming from the SRF to the inertial system can be computed with these quaternions [51]. Based on the definition of the SRF as illustrated in Figure 10 in yellow, the e_N , e_E , and e_U can be obtained with:

$$e_E = R_{SRF}[1, 0, 0]^T, e_N = R_{SRF}[0, -1, 0]^T, e_U = R_{SRF}[0, 0, -1]^T \tag{12}$$

The angle differences α_E , α_N , and α_U are given in Figure 11. It can be observed that these angle differences are not large. In case that the antenna attitude file is not given, or the attitude information is not accurately documented, one could approximate the antenna orientation using the RSW directions.

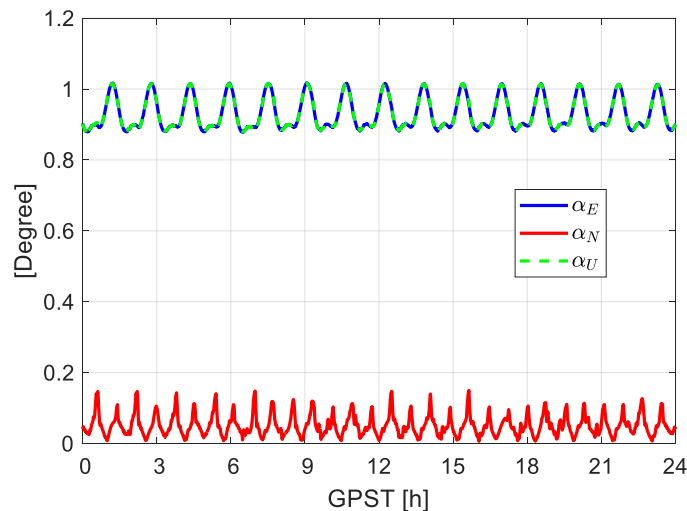


Figure 11. Angle differences between the east, north, and up directions in the antenna reference frame (ARF) and the opposite along-track direction, the cross-track direction, and the radial direction. The data for GRACE FO-1 was used for the plot. Note that the blue line is almost overwritten by the green dashed line.

Benefiting from the fact that the angle differences between the actual and the expected antenna orientation are small, even without having the attitude information available, differences less than 10 mm can mostly be observed in the final orbits provided that the observation data is complete and continuous (see Figure 12), i.e., with a 3D RMSE amounting to 8 mm. Applying the IGS final products, for other cases with reduced duty-cycles and mean satellite numbers, the differences in the RMSE (referenced to the best-case scenario) with and without applying the attitude file are also mostly at several millimeters. This applies also to the cases when using the IGR and IGC products. This suggests that good attitude control can maintain the POD accuracy even when the attitudes are not properly determined or transferred back to the GPC.

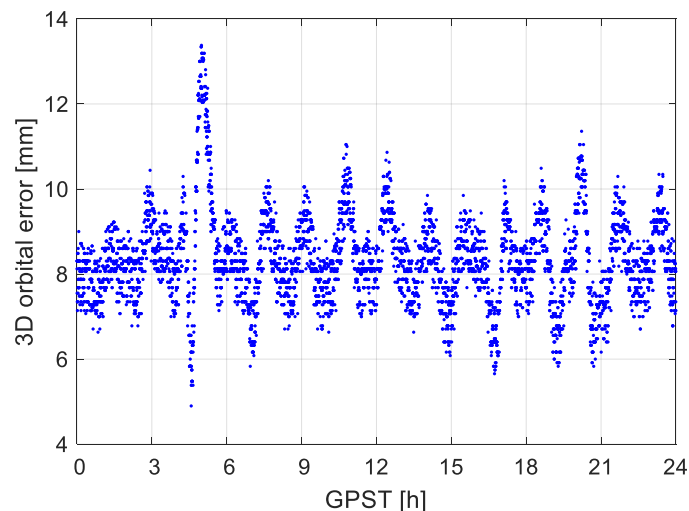


Figure 12. 3D orbital errors not applying the antenna attitude information. The IGS final products were used for observations with a duty-cycle of 100%, a sampling interval of 10 s, and a mean satellite number of 9.

3.5. Length of Arc

The orbital period of a LEO satellite is typically around 1.5 h, depending on its altitude from the Earth's surface. Taking the GRACE FO-1 as an example, based on the semi-major axis estimated in the final reference orbit, its orbital period is approximately 1 h 34 min 29 s for the test day. A 24 h arc for data analysis thus contains about roughly 15.2 orbital periods. By reducing the length of the processed arc in case of rapid processing, the amount of the data used for estimation of the orbital parameters may cover, e.g., only several orbital cycles. For an observation model with a good strength, e.g., having data with a high sampling rate, a high duty-cycle, a relatively loose latency requirement, and a high number of observed satellites, the influence of the arc length could be small. However, a long arc might be essential for scenarios with weaker model strengths. To analyze this correlation, this section presents results of a varying arc length from 24 h to 12 h and 6 h. The influences of the arc length on different scenarios are investigated in detail.

Using the best scenario with a duty-cycle of 100%, a mean satellite number of 9, and an observation sampling interval of 10 s, the 3D RMSE of the final orbits are given in Table 5 for different arc lengths and using different IGS products. For arcs shorter than 24 h, multiple arcs were processed covering the entire test day.

Table 5. 3D RMSE of the phase-based reduced-dynamic orbits with different arc lengths and using different IGS products. 10 s observation data with a duty-cycle of 100% and a mean satellite number of 9 were used for the processing.

| Arc Length/Products | IGS Final [cm] | IGR [cm] | IGC [cm] |
|---------------------|----------------|----------|----------|
| 24 h | – | 4.8 | 3.2 |
| 12 h | 0.6 | 5.1 | 3.1 |
| 6 h | 1.0 | 5.6 | 3.5 |

From Table 5 it can be observed that in case of good data condition, the accuracy differences are very small when reducing the arc length. Having a closer look at the 3D orbital errors with an arc length of 6 h and 12 h using, e.g., the IGS final products (see Figure 13a), border effects of the short arcs, i.e., the degradation of the orbital accuracy at the edges of the corresponding arcs, are the main reason of the degradation [11]. Applying the IGS rapid products (see Figure 13b), the degradation at borders is less obvious due to the generally much larger orbital errors.

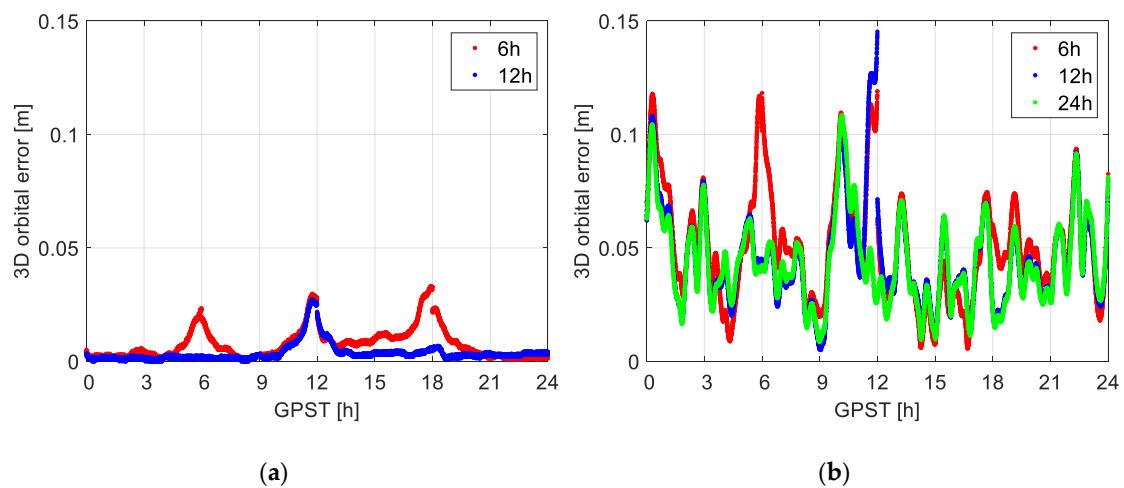


Figure 13. 3D orbital errors computed with different arc lengths using (a) the IGS final products and (b) the IGS rapid products. A duty-cycle of 100%, an observation interval of 10 s, and a mean satellite number of 9 were assumed for the processing. The arc length experiment here refers to the processing using e.g., k hours of data in each processing round, and in each hour of these k hours, data are tracked in $X\%$ of the time.

For cases with lower data availability, the degradation caused by shortening the arcs could be higher. For scenarios simulating different data conditions, the increase in the 3D RMSE when shortening the arc length from 24 h to 12 h is given in Table 6 as an example applying the IGS final products. While most of the increase is still at millimeters, increase of several centimeters is also observed for the cases with very limited data.

Table 6. Increase in the 3D RMSE (in cm) of phase-based reduced-dynamic orbits when shortening the arc length from 24 h to 12 h. The IGS final products were used.

| Duty-Cycle/Mean # Satellite Sampling Interval [s] | 8 Satellites 10/20/30/60/120 | 7 Satellites 10/20/30/60/120 | 5 Satellites 10/20/30/60/120 |
|--|---------------------------------|---------------------------------|---------------------------------|
| 100% | 0.6/0.2/0.1/0.2/–0.1 | 0.1/0.1/0.2/0.2/0.2 | 0.1/0.0/0.1/0.1/0.2 |
| 80% | 0.2/0.1/0.5/0.4/–0.4 | 0.1/0.1/0.2/0.2/0.5 | 0.2/0.2/0.2/0.3/0.4 |
| 60% | 0.1/0.0/0.3/1.0/–0.4 | 0.1/0.1/0.2/0.2/0.5 | 0.0/0.1/0.1/0.1/1.0 |
| 40% | 0.2/0.3/0.3/0.6/0.8 | 0.2/0.0/0.2/0.7/1.7 | 0.2/0.3/0.5/2.0/3.5 |
| 20% | 2.0/2.2/2.8/3.3/– | 1.6/2.2/3.0/3.6/– | 2.9/2.0/3.4/4.8/– |

When shortening the arcs to 6 h and applying worse IGS products, a larger increase in the RMSE can be observed. Figure 14 shows the 3D RMSE when processing with the arc lengths of 24 h, 12 h, and 6 h applying different IGS products. The x-intervals between each two vertical dashed lines represent different cases having the same sampling interval, which are sorted from the highest duty-cycle of 100% to the lowest duty-cycle of 20% first for the mean satellite number of 9, and then similarly for the mean satellite numbers of 7 and 6, respectively. The peaks observed in Figure 14 are thus mostly caused by the low duty-cycles of 40% and 20%. From Figure 14 it can be observed that when shortening the arcs from 24 h (green) to 12 h (blue) or 6 h (red), the increase in the 3D RMSE could be dramatic under bad data conditions, especially when using the IGR and IGC products. While this increase is still limited to around 1 dm when shortening the arcs from 24 h to 12 h, cases with increase above 2 dm appear when shortening the arcs to 6 h and when applying the IGR or IGC products. In cases that the duty-cycle is not lower than 40% and the sampling interval is not larger than 60 s, the 3D RMSE is generally within or around 1 dm when applying the IGS final products or the IGC products, even when processing with arcs with a length of 6 h. Due to the large sampling interval of the IGR satellite clocks, reaching a 3D RMSE of this level generally requires a duty-cycle not lower than 60% when processing 6 h arcs applying the IGR products.

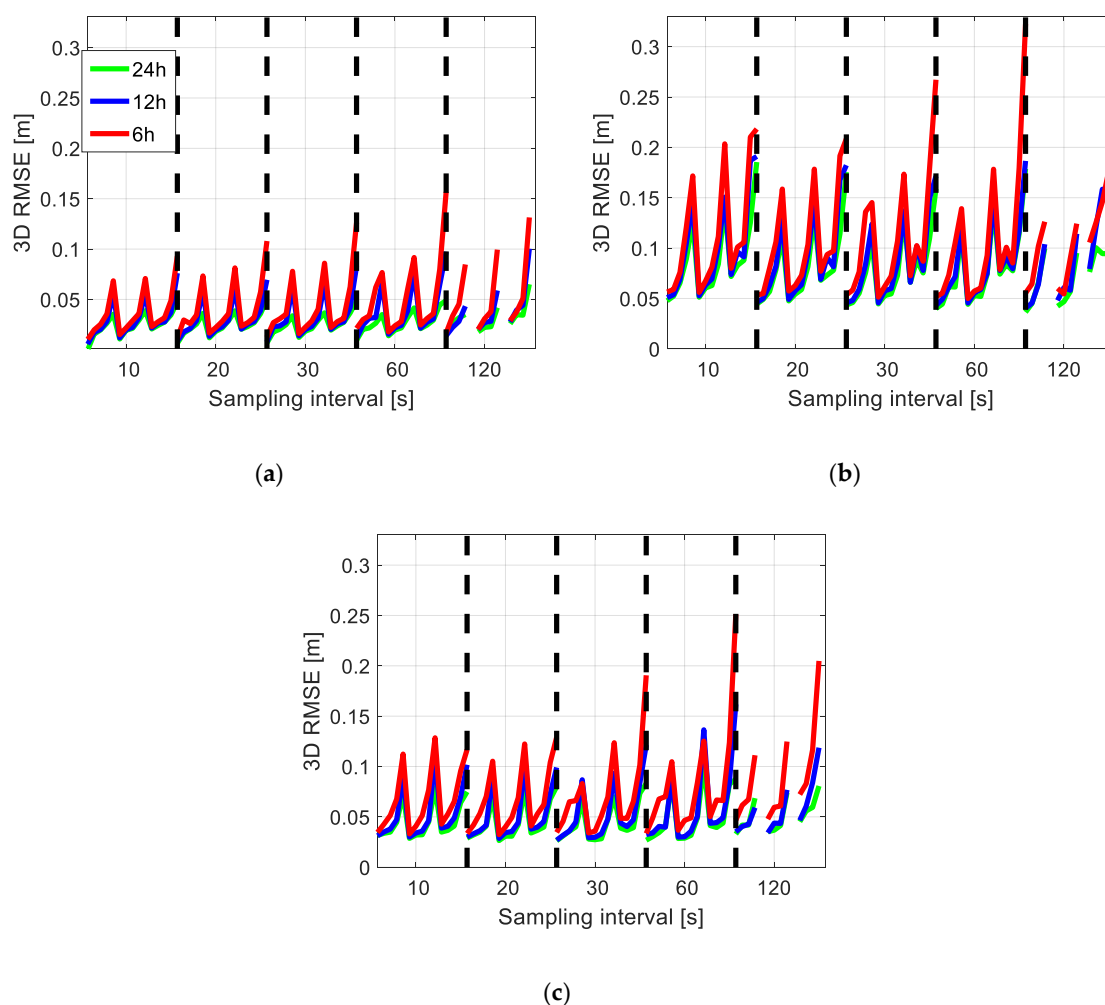


Figure 14. 3D RMSE of the reduced-dynamic orbits when processing with the arc lengths of 24 h, 12 h, and 6 h applying (a) the IGS final products, (b) the IGS rapid (IGR) products, and (c) the IGS real-time (IGC) products. Between each pair of the dashed lines, the cases are sorted from the highest duty-cycle of 100% to the lowest duty-cycle of 20%, first for the mean satellite number of 9, and then similarly for the mean satellite numbers of 7 and 6, respectively.

4. Conclusions

The CubeSat missions have attempted to determine their precise orbits combining dynamic models and dual-frequency GNSS observations. While such kind of reduced-dynamic orbits can reach high accuracy of centimeters for large LEO satellites, the limited size, power, and capacity of CubeSats always set strong constraints on the availability of data and different resources, thus limiting the achievable accuracy of the determined orbits. As an important step at the planning phase of the CubeSat missions, a proper compromise needs to be carefully considered between these constraints and the orbital accuracy, so that limited resources can be better managed and saved for other tasks of CubeSat missions under the required POD accuracy.

In this contribution, with the focus put on the dual-frequency postprocessed CubeSat POD, a detailed sensitivity analysis was performed between the orbital accuracy and different constraints, i.e., the data continuity, the data completeness, the observation sampling interval, the attitude information, the latency of the required orbital products, as well as the processed arc length. It was found that the accuracy degradation of the orbits could be large when several constraints are overlapped with each other, especially when one of the constraints is related to very low duty-cycle, e.g., below 40%. It was also found that the accuracy influences of the observation sampling interval is related to the sampling interval of the GPS satellite clock products used for the processing. In case that the data is otherwise tracked in good condition after considering the assumed constraints, the 3D orbital accuracy for arc lengths of 6 h to 24 h should generally be within or around 1 dm when applying the IGS final products or products from the IGS RTS, provided that the duty-cycle is not lower than 40% and the observation sampling interval is not larger than 60 s.

Author Contributions: K.W. and A.E.-M. designed the work, K.W. and A.A.-Z. contributed to the data processing, K.W. analyzed the data, K.W.; A.A.-Z.; A.E.-M.; and J.N.G. contributed to the writing of the paper. All authors have read and agreed to the published version of the manuscript.

Funding: The work is funded by the Australian Research Council Discovery Project: Tracking Formation-Flying of Nanosatellites Using Inter-Satellite Links (DP 190102444).

Acknowledgments: We would like to thank West Virginia University for providing the GNSS data of CubeSat STF-1.

Conflicts of Interest: The authors declare no conflict of interest.

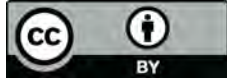
References

1. Yunck, T.P.; Wu, S.C.; Wu, J.T.; Thornton, C.L. Precise tracking of remote-sensing satellites with the global positioning system. *IEEE Trans. Geosci. Remote Sens.* **1990**, *28*, 108–116. [[CrossRef](#)]
2. Montenbruck, O. An epoch state filter for use with analytical orbit models of low earth satellites. *Aerosp. Sci. Technol.* **2000**, *4*, 277–287. [[CrossRef](#)]
3. Svehla, D.; Rothacher, M. Kinematic and reduced-dynamic precise orbit determination of low earth orbiters. *Adv. Geosci. EGU* **2003**, *2003*, 1, 47–56.
4. Jäggi, A.; Hugentobler, U.; Bock, H.; Beutler, G. Precise orbit determination for GRACE using undifferenced or doubly differenced GPS data. *Adv. Space Res.* **2007**, *39*, 1612–1619. [[CrossRef](#)]
5. Haines, B.; Bar-Sever, Y.; Bertiger, W.; Desai, S.; Willis, P. One-Centimeter Orbit Determination for Jason-1: New GPS-Based Strategies. *Mar. Geod.* **2004**, *27*, 299–318. [[CrossRef](#)]
6. Tapley, B.D.; Bettadpur, S.; Watkins, M.; Reigber, C. The gravity recovery and climate experiment: Mission overview and early results. *Geophys. Res. Lett.* **2004**, *31*. [[CrossRef](#)]
7. Drinkwater, M.R.; Floberghagen, R.; Haagmans, R.; Muzi, D.; Popescu, A. GOCE: ESA's first earth explorer core mission. In *Earth Gravity Field from Space—From Sensors to Earth Sciences*; Beutler, G., Drinkwater, M.R., Rummel, R., Von Steiger, R., Eds.; Part of the Space Sciences Series of ISSI Book Series (Volume 17); Springer: Dordrecht, The Netherlands, 2003; pp. 419–432.
8. Wickert, J.; Reigber, C.; Beyerle, G.; König, R.; Marquardt, C.; Schmidt, T.; Grunwaldt, L.; Galas, R.; Meehan, T.K.; Melbourne, W.G.; et al. Atmosphere sounding by GPS radio occultation: First results from CHAMP. *Geophys. Res. Lett.* **2001**, *28*, 3263–3266. [[CrossRef](#)]

9. Crétaux, J.F.; Bergé-Nguyen, M.; Calmant, S.; Jamangulova, N.; Satylkanov, R.; Lyard, F.; Perosanz, F.; Verron, J.; Montazem, A.S.; Le Guilcher, G.; et al. Absolute calibration or validation of the altimeters on the Sentinel-3A and the Jason-3 over Lake Issykkul (Kyrgyzstan). *Remote Sens.* **2018**, *10*, 1679. [[CrossRef](#)]
10. Tu, J.; Gu, D.; Wu, Y.; Yi, D. Error modeling and analysis for InSAR spatial baseline determination of satellite formation flying. *Math. Probl. Eng.* **2012**, *2012*, 140301. [[CrossRef](#)]
11. Montenbruck, O.; Gill, E.; Kroes, R. Rapid orbit determination of LEO satellites using IGS clock and ephemeris products. *GPS Solut.* **2005**, *9*, 226–235. [[CrossRef](#)]
12. Gu, D.; Ju, B.; Liu, J.; Tu, J. Enhanced GPS-based GRACE baseline determination by using a new strategy for ambiguity resolution and relative phase center variation corrections. *Acta Astronaut.* **2017**, *138*, 176–184. [[CrossRef](#)]
13. Kroes, R.; Montenbruck, O.; Bertiger, W.; Visser, P. Precise GRACE baseline determination using GPS. *GPS Solut.* **2005**, *9*, 21–31. [[CrossRef](#)]
14. Ju, B.; Gu, D.; Herring, T.A.; Allende-Alba, G.; Montenbruck, O.; Wang, Z. Precise orbit and baseline determination for maneuvering low earth orbiters. *GPS Solut.* **2015**, *21*, 53–64. [[CrossRef](#)]
15. Jäggi, A.; Arnold, D. Precise Orbit Determination. In *Global Gravity Field Modeling from Satellite-to-Satellite Tracking Data*; Naeimi, M., Flury, J., Eds.; Part of the Lecture Notes in Earth System Sciences Book Series; Springer International Publishing: Cham, Switzerland, 2017; pp. 35–80.
16. NanoSats Database. World's Largest Database of Nanosatellites, over 2500 Nanosat and CubeSats. Available online: <https://www.nanosats.eu/> (accessed on 30 April 2020).
17. Douglas, E.S.; Cahoy, K.L.; Knapp, M.; Morgan, R.E. CubeSats for Astronomy and Astrophysics. Submitted to the Astro 2020 Decadal Survey Call for APC Whitepapers. *arXiv* **2019**, arXiv:1907.07634v2.
18. Poghosyan, A.; Golkar, A. CubeSat evolution: Analyzing CubeSat capabilities for conducting science missions. *Prog. Aerosp. Sci.* **2017**, *88*, 59–83. [[CrossRef](#)]
19. Han, K.; Wang, H.; Tu, B.; Jin, Z. Pico-Satellite Autonomous Navigation with Magnetometer and Sun Sensor Data. *Chin. J. Aeronaut.* **2011**, *24*, 46–54. [[CrossRef](#)]
20. Kahr, E.; Montenbruck, O.; O'Keefe, K.; Skone, S.; Urbanek, J.; Bradbury, L.; Fenton, P. GPS tracking on a nanosatellite—The CanX-2 flight experience. In Proceedings of the 8th International ESA Conference on Guidance, Navigation & Control System, Karlovy Vary, Czech Republic, 5–10 June 2011.
21. Lantto, S.; Gross, J.N. Precise Orbit Determination Using Duty Cycled GPS Observations. In Proceedings of the 2018 AIAA Modeling and Simulation Technologies Conference, AIAA SciTech Forum, Kissimmee, FL, USA, 8–12 January 2018; AIAA: Reston, VA, USA, 2018.
22. Montenbruck, O.; Ramos-Bosch, P. Precision real-time navigation of LEO satellites using global positioning system measurements. *GPS Solut.* **2008**, *12*, 187–198. [[CrossRef](#)]
23. Wesam, E.M.; Zhang, X.; Lu, Z.; Liao, W. Kalman filter implementation for small satellites using constraint GPS data. *IOP Conf. Ser. Mater. Sci. Eng.* **2017**, *211*, 012015. [[CrossRef](#)]
24. Kahr, E.; Montenbruck, O.; O'Keefe, K.P.G. Estimation and analysis of two-line elements for small satellites. *J. Spacecr. Rocket.* **2013**, *50*, 433–439. [[CrossRef](#)]
25. Bittner, D.E. Advances in MEMS IMU Cluster Technology for Small Satellite Applications. Graduate Theses, Dissertations, and Problem Reports, 5216. Master's Thesis, The Benjamin M. Statler College of Engineering and Mineral Resources, West Virginia University, Morgantown, WV, USA, 2015.
26. Morris, J.; Zemerick, S.; Grubb, M.; Lucas, J.; Jaridi, M.; Gross, J.N.; Christian, J.A.; Vassiliadis, D.; Kadiyala, A.; Dawson, J.; et al. Simulation-to-Flight 1 (STF-1): A mission to enable Cubesat software-based verification and validation. In Proceedings of the 54th AIAA Aerospace Sciences Meeting, AIAA SciTech Forum, San Diego, CA, USA, 4–8 January 2016.
27. Johnston, G.; Riddell, A.; Hausler, G. The International GNSS Service. In *Springer Handbook of Global Navigation Satellite Systems*, 1st ed.; Teunissen, P.J.G., Montenbruck, O., Eds.; Springer International Publishing: Cham, Switzerland, 2017; pp. 967–982.
28. Noll, C.E. The Crustal Dynamics Data Information System: A resource to support scientific analysis using space geodesy. *Adv. Space Res.* **2010**, *45*, 1421–1440. [[CrossRef](#)]
29. Sun, X.; Han, C.; Chen, P. Precise real-time navigation of LEO satellites using a single-frequency GPS receiver and ultra-rapid ephemerides. *Aerosp. Sci. Technol.* **2017**, *67*, 228–236. [[CrossRef](#)]

30. Ivanov, A.B.; Masson, L.A.; Rossi, S.; Belloni, F.; Mullin, N.; Wiesendanger, R.; Rothacher, M.; Hollenstein, C.; Männel, B.; Willi, D.; et al. CUBETH: Nano-satellite mission for orbit and attitude determination using low-cost GNSS receivers. In Proceedings of the 66th International Astronautical Congress, IAC-15-B4.4.5, Jerusalem, Israel, 12–16 October 2015.
31. Yang, Y.; Yue, X.; Tang, G.; Cui, H.; Song, B. Orbit Determination Using Combined GPS + Beidou Observations for Low Earth Cubesats: Software Validation in Ground Testbed. In *China Satellite Navigation Conference (CSNC) 2015 Proceedings*; Sun, J., Liu, J., Fan, S., Lu, X., Eds.; Part of the Lecture Notes in Electrical Engineering Book Series (Volume 342); Springer: Berlin/Heidelberg, Germany, 2015; Volume III, pp. 321–334.
32. Hoque, M.M.; Jakowski, N. Ionospheric propagation effects on GNSS signals and new correction approaches. In *Global Navigation Satellite Systems: Signal, Theory and Applications*; Jin, S., Ed.; IntechOpen: Rijeka, Croatia, 2012; pp. 381–404.
33. Mander, A.; Bisnach, S. GPS-based precise orbit determination of Low Earth Orbiters with limited resources. *GPS Solut.* **2013**, *17*, 587–594. [[CrossRef](#)]
34. Dach, R.; Lutz, S.; Walser, P.; Fridez, P. *Bernese GNSS Software Version 5.2*; University of Bern, Bern Open Publishing: Bern, Switzerland, 2015.
35. Li, K.; Zhou, X.; Wang, W.; Gao, Y.; Zhao, G.; Tao, E.; Xu, K. Centimeter-Level Orbit Determination for TG02 Spacelab Using Onboard GNSS Data. *Sensors* **2018**, *18*, 2671. [[CrossRef](#)] [[PubMed](#)]
36. Beutler, G. Variational Equations. In *Methods of Celestial Mechanics*; Part of the Astronomy and Astrophysics Library Book Series; Springer: Berlin/Heidelberg, Germany, 2005; pp. 175–207.
37. Montenbruck, O.; Gill, E. *Satellite Orbits: Models, Methods and Applications*, 4th ed.; Springer: Berlin/Heidelberg, Germany, 2012.
38. Jäggi, A.; Hugentobler, U.; Beutler, G. Pseudo-stochastic orbit modeling techniques for low Earth orbiters. *J. Geod.* **2006**, *80*, 47–60. [[CrossRef](#)]
39. Pavlis, N.K.; Holmes, S.A.; Kenyon, S.C.; Factor, J.K. An Earth Gravitational Model to Degree 2160: EGM2008. In Proceedings of the European Geosciences Union General Assembly 2008, Vienna, Austria, 13–18 April 2008.
40. Standish, E.M. *JPL Planetary and Lunar Ephemerides, DE405/LE405, JPL IOM 312; F-98-048*; JPL: Pasadena, CA, USA, 1998.
41. Petit, G.; Luzum, B. *IERS Conventions*; IERS Technical Note No. 36; Verlag des Bundesamts für Kartographie und Geodäsie: Frankfurt am Main, Germany, 2010; 179p, ISBN 3-89888-989-6.
42. Lyard, F.; Lefevre, F.; Letellier, T.; Francis, O. Modelling the global ocean tides: Modern insights from FES2004. *Ocean. Dyn.* **2006**, *56*, 394–415. [[CrossRef](#)]
43. Flechtner, F.; Morton, P.; Watkins, M.; Webb, F. Status of the GRACE Follow-On Mission. In *Gravity, Geoid and Height Systems*; Marti, U., Ed.; Part of the International Association of Geodesy Symposia Book Series (Volume 141); Springer: Cham, Switzerland, 2014; pp. 117–121.
44. Wen, H.Y.; Kruizinga, G.; Paik, M.; Landerer, F.; Bertiger, W.; Sakumura, C.; Bandikova, T.; McCullough, C. Gravity Recovery and Climate Experiment Follow-On (GRACE-FO) Level-1 Data Product User Handbook. JPL D-56935 (URS270772), 11 September 2019. Available online: https://podaac-tools.jpl.nasa.gov/drive/files/allData/gracefo/docs/GRACE-FO_L1_Handbook.pdf (accessed on 26 May 2020).
45. Hadas, T.; Bosy, J. IGS RTS precise orbits and clocks verification and quality degradation over time. *GPS Solut.* **2015**, *19*, 93–105. [[CrossRef](#)]
46. IGS Real-Time Service, Monitoring. Available online: <http://www.igs.org/rtts/monitor> (accessed on 25 June 2020).
47. *IGC Products, Decoded Clock and Orbit Solutions from IGS Real-Time Product Streams*; NASA Crustal Dynamics Data Information System (CDDIS): Greenbelt, MD, USA, 2018. Available online: <http://cdsis.nasa.gov/gnss/products/rtpp> (accessed on 28 May 2020).
48. Kazmierski, K.; Sośnica, K.; Hadas, T. Quality assessment of multi-GNSS orbits and clocks for real-time precise point positioning. *GPS Solut.* **2018**, *22*, 11. [[CrossRef](#)]
49. The International GNSS Service. IGS Products. Available online: <http://www.igs.org/products> (accessed on 7 May 2020).

50. Gatsonis, N.A.; Lu, Y.; Blandino, J.; Demetriou, M.A.; Paschalidis, N. Micro Pulsed Plasma Thrusters for Attitude Control of a Low Earth Orbiting CubeSat. In Proceedings of the 54th AIAA Aerospace Sciences Meeting, AIAA SciTech Forum, San Diego, CA, USA, 4–8 January 2016.
51. Henderson, D.M. *Euler Angles, Quaternions, and Transformation Matrices for Space Shuttle Analysis*; JSC Report 12960 (77-FM-37); NASA: Washington, DC, USA, 1977.






© 2020 by the authors. Licensee MDPI, Basel, Switzerland. This article is an open access article distributed under the terms and conditions of the Creative Commons Attribution (CC BY) license (<http://creativecommons.org/licenses/by/4.0/>).

5 Precise Orbit Determination of CubeSats Using Proposed Observations Weighting Model

The actual GNSS observations collected onboard CubeSats for POD are collected by COTS sensors and have a fast-changing space geometry between GNSS satellites and CubeSats, which require better stochastic functions than the traditional elevation-angle dependant models that were developed mainly for ground applications. This chapter which is covered by the following publication, proposes an SNR-based model for the CubeSat POD and evaluates this model using a set of CubeSats' actual observations:

Allahviridi-Zadeh, A., El-Mowafy, A., Wang, K. (2022). Precise Orbit Determination of CubeSats Using Proposed Observations Weighting Model. In: International Association of Geodesy Symposia. Springer, Berlin, Heidelberg. DOI: 10.1007/1345_2022_160

Precise Orbit Determination of CubeSats Using Proposed Observations Weighting Model

Amir Allahviridi-Zadeh , Ahmed El-Mowafy , and Kan Wang 

Abstract

CubeSats can be used for many space missions and Earth science applications if their orbits can be determined precisely. The Precise Orbit Determination (POD) methods are well developed for large LEO satellites during the last two decades. However, CubeSats are built from Commercial Off-The-Shelf (COTS) components and have their own characteristics, which need more investigations. In this paper, precise orbits of 17 3U-CubeSats in the Spire Global constellation are determined using both the reduced-dynamic and the kinematic POD methods. The limitations in using elevation-dependent weighting models for CubeSats POD are also discussed and, as an alternative approach, a weighting model based on the Signal-to-Noise Ratio (SNR) has been proposed. One-month processing of these CubeSats revealed that around 40% of orbits can be determined at the decimeter accuracy, while 50% have accuracy at centimeters. Such precise orbits fulfil most mission requirements that require such POD accuracy. Internal validation methods confirmed the POD procedure and approved the distinction of weighting based on SNR values over the elevation angles.

Keywords

CubeSats · Precise orbit determination (POD) · Signal-to-noise ratio (SNR) · Weighting model

1 Introduction

CubeSats are small low-cost and low-power satellites that can be used for many space missions. Precise Orbit Determination (POD) of CubeSats is essential for some missions such as radio-occultation, Interferometric Synthetic Aperture Radar (InSAR), satellite altimetry, gravity field recovery, and future mega-constellations as an augmentation system for positioning and navigation (Allahviridi-Zadeh and El-

Mowafy 2022). POD of CubeSats using the observations of Global Navigation Satellite Systems (GNSS) can be performed using the reduced-dynamic and the kinematic methods in post-mission or real-time (Allahviridi-Zadeh et al. 2022a). In this study, we analyze the POD of CubeSats from the Spire CubeSat Constellation (Spire Global, Inc.), comparing elevation angle-dependent and Signal-to-Noise ratio (SNR) based weighting models.

The Spire Global constellation of nanosatellites consists of more than 145 3U-CubeSats ($10 \times 10 \times 30$ cm) that were launched mostly in Sun-synchronous and various other orbits with different altitudes (445–600 km). Most are equipped with the STRATOS GNSS receiver module to receive 1-Hz dual-frequency GPS signals (L1C/A and L2L) using a compatible zenith-mounted GNSS antenna. It also simultaneously collects 50-Hz signals dual-frequency multi-GNSS signals through the high-gain, side-mounted antennas from setting or rising GNSS satellites to perform Radio Occul-

A. Allahviridi-Zadeh (✉) · A. El-Mowafy
GNSS-SPAN Group, School of Earth and Planetary Sciences, Curtin
University, Perth, Australia
e-mail: amir.allahviridizadeh@curtin.edu.au

K. Wang
National Time Service Center, Chinese Academy of Sciences, Xi'an,
China

University of Chinese Academy of Sciences, Beijing, China

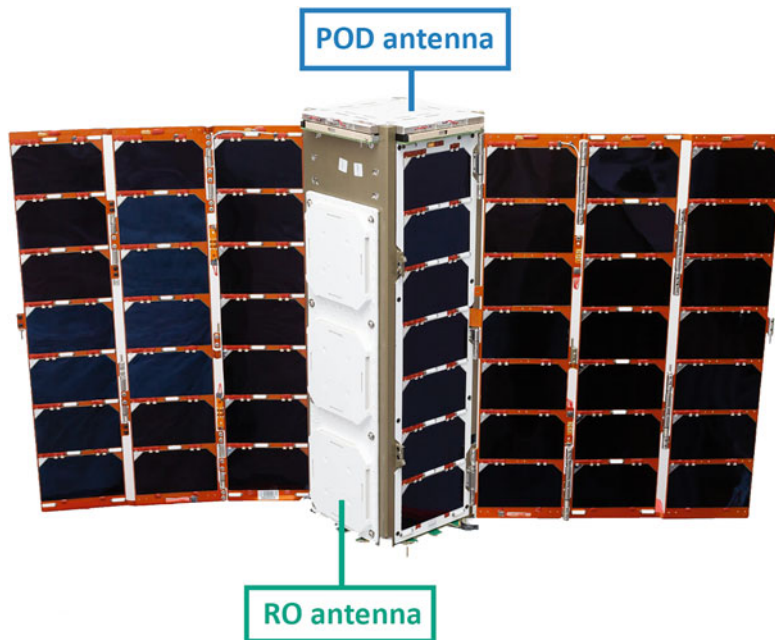


Fig. 1 Structure of the Spire 3U RO CubeSat (Credit: Spire Global, Inc.)

tation (RO). The location of the POD and RO high-gain antennas on the Spire’s CubeSats are depicted in Fig. 1.

2 Precise Orbit Determination

The reduced-dynamic POD (RD-POD) is considered the main method in this study. It is based on exploiting available dynamic models as well as GNSS observations to estimate the CubeSat’s state vector, which includes position and velocity, clock offsets, float ambiguities, and some piece-wise constant stochastic accelerations to compensate for deficiencies in dynamic models (Allahviridi-Zadeh et al. 2022a). The type of data used, processing information, and models in the RD-POD processing are provided in Table 1.

2.1 Weighting Models

Equal weighting of GNSS observations can be considered for the POD of Low Earth Orbit (LEO) satellites. However, this model is not optimal due to factors causing mis-modelled errors, such as higher-order ionosphere scintillation, near field multipath, etc. One may suggest using the elevation-angle dependent (defined here for brevity as elevation-dependent) weighting models such as $\sin^2\theta$. The analysis of the observation residuals in the validation step (see Sect. 2.3.3) reveals that this type of models is not optimal for reflecting the actual noise level of the CubeSats observations. This is due to the fact that these models

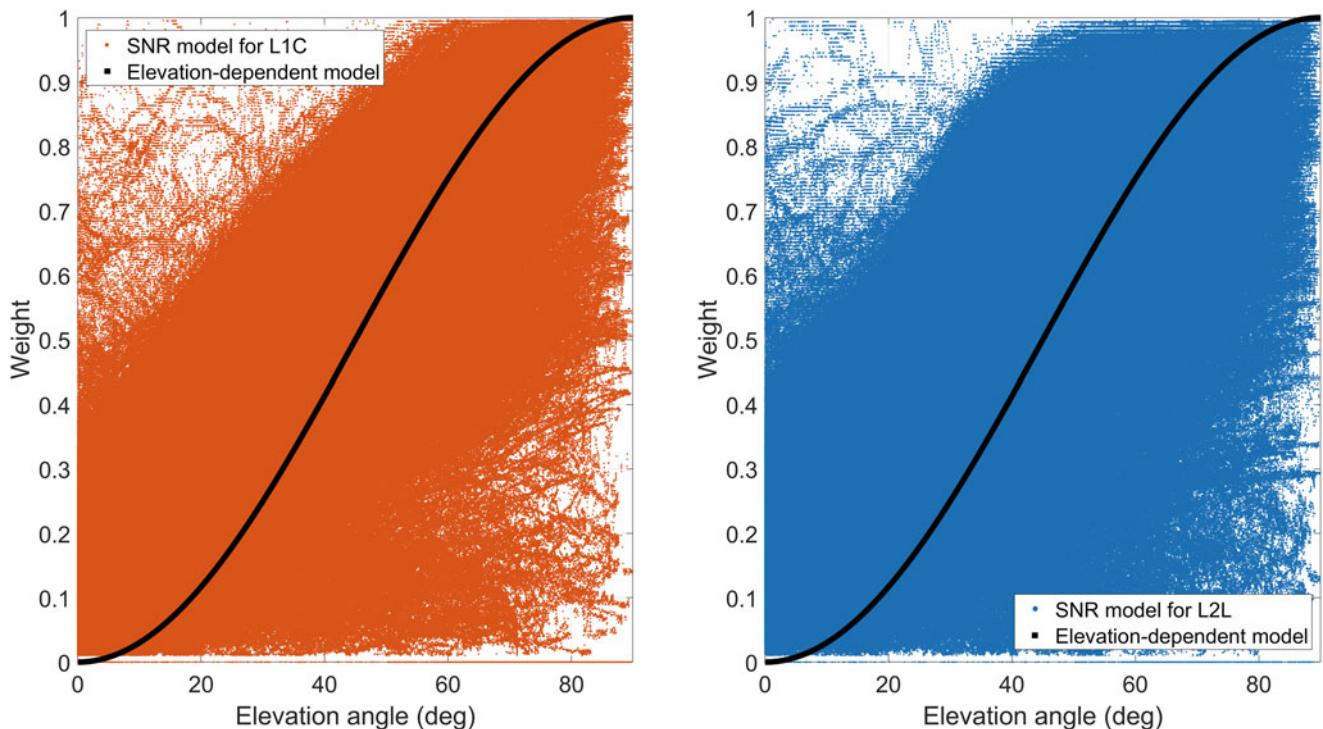
are developed to account for the effect of the tropospheric delays and multipath, mainly for users on the Earth surface (Hobiger and Jakowski 2017), whereas CubeSats fly above the troposphere layer. Besides, in order to correctly apply the elevation-dependent model, the CubeSat should effectively record the attitude information, such as the quaternions. This, however, may not be available for CubeSats with low-power budget. Hence, we propose to use a direct signal quality indicator, i.e. the SNR, which equals to the ratio of the signal power to the noise power of the modulated signal at the correlator output. The proposed SNR-based model for weighting the observations (Φ_i) can be expressed as:

$$W(\Phi_i) = \left(0.1 + 0.9 * \left(\frac{\Delta SNR_{i,\min}}{\Delta SNR_{\max,\min}} \right) \right)^2 \quad (1)$$

where $\Delta SNR_{i,\min}$ is the difference between the observation SNR value and the minimum SNR of all observations, and $\Delta SNR_{\max,\min}$ is the difference between the maximum and minimum SNR values among all observations. The coefficients 0.1 and 0.9 on the right-hand side of Eq. 1 are used to give the maximum weight, i.e., 1, to the observation which has the highest SNR value, and a very low weight, i.e., 0.01, to the observation with the lowest SNR. A similar model has been developed for baseline processing (Luo 2013), however, the way of choosing the maximum and minimum SNR values and applying weights for double differences are different. Figure 2 compares the weights generated from applying the elevation-dependent weighting model ($\sin^2\theta$) and the SNR-based model (Eq. 1) for different elevation angles (θ) for one-month observations of CubeSat PRN099. Two

Table 1 CubeSats POD processing models and parameters

| Item | Description |
|--|--|
| Gravity field/Earth tide/Relativity/Other planets | EGM 2008 (Pavlis et al. 2008)/FES2004 (Lyard et al. 2006)/IERS 2010 (Petit and Luzum 2010)/DE405 (Standish 1998) |
| Observation model | 1-Hz dual-frequency GPS Ionosphere-Free |
| A-priori code and phase standard deviation | 0.1 m, 1 mm (Zenith, L1) |
| Empirical acceleration | piece-wise constant accelerations |
| Attitude information, Quaternions, Antenna phase center offsets (PCO) and variations (PCV) | Provided by Spire Global, Inc. and applied (Allahviridi-Zadeh 2021b) |
| Weighting model (tested) | Elevation-dependent or SNR-based models |
| GNSS orbits and clocks | IGS-RTS and CODE final |

**Fig. 2** Observation weights from the SNR- and the elevation-dependent weighting models for one month (16/12/2020–15/01/2021) of L1C (left) and L2L (right) signals from all available GPS satellites as observed on CubeSat PRN099

models behave differently in weighting the observations. For example, the SNR-based model gives higher weights to the observations from low elevation angles for both L1C and L2L signals compared with the elevation-dependent model depending on the received signal strength. It can be more realistic for signals in space, since they are not affected by the troposphere, and the amount of near-field multipath is low, mainly due to the CubeSat structure (see Fig. 1). Realistic weighting is crucial in the POD of the low-power CubeSats since they are allowed to record the observations for a limited time based on their power budget and mission requirements (personal communication with the CubeSat developers (Allahviridi-Zadeh 2021a)). Therefore, losing observations due to incorrect weighting may even lead to the unavailability of POD procedure for the Kinematic mode. It does not generally though take place for the satellites that

record GNSS observations continuously, since the RD-POD of these satellites can run even in the presence of duty-cycled GNSS data (i.e., available at certain percentage of the orbit due to the need of the low available onboard power to sensors other than GNSS) (Wang et al. 2020).

2.2 POD Results

One month (from 16 December 2020 to 15 January 2021) of all available observations of 17 3U-CubeSats from the Spire Global constellation are processed in this study. A list of these CubeSats and their specifications are given in Allahviridi-Zadeh et al. 2022b. The observations comprise several segments each day. Each segment has around 1.5 h (orbital period) of 1-Hz dual-frequency GPS data. The

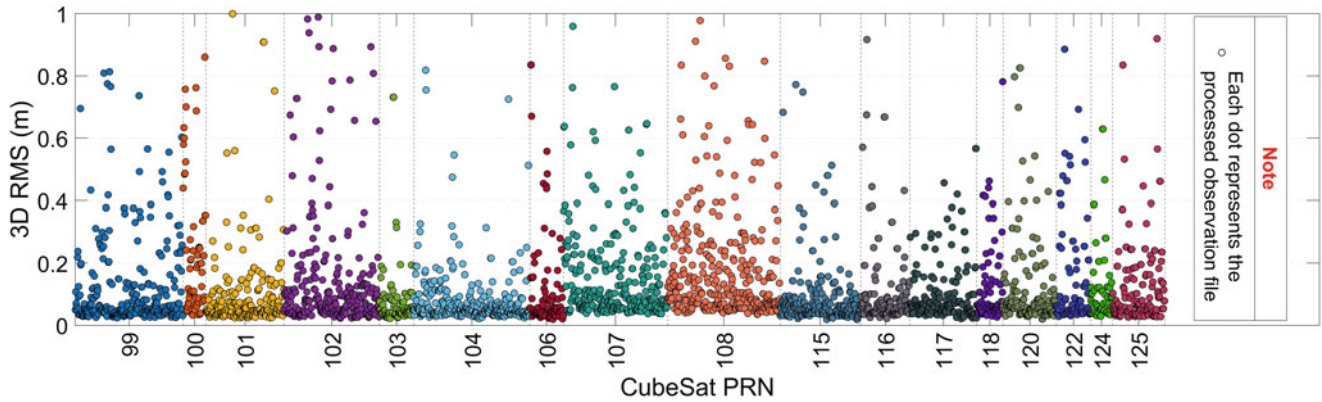


Fig. 3 3D-RMS of differences between RD-POD and Kinematic POD (Kin-POD) for all CubeSats. Each segment related to each CubeSat PRN contains all processed file during one month (16/12/2020–15/01/2021)

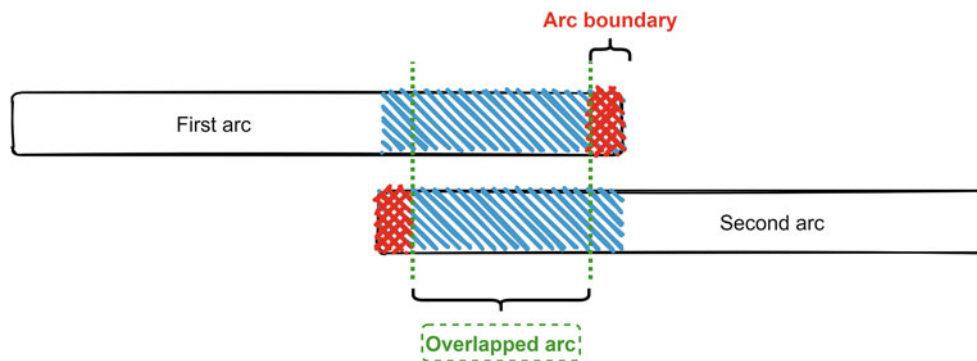


Fig. 4 Overlapped arc between two consecutive orbits. The red cross hatches indicate the arc boundaries

related observable-specific signal biases for L1C and L2L are synchronized with the applied precise GNSS orbits and clocks (Schaer 2016). A comparison between the reduced-dynamic orbits, as the most precise obtainable orbits in this study, and the kinematic orbits are plotted in Fig. 3 in the radial (R), along-track (S), and cross-track (W) directions. In this comparison, 40% of kinematic orbits have 3D root mean square (3D-RMS) of decimeters, while half of them have accuracies at a few centimeters. Such orbits can fulfil the requirements of different space missions and earth-science applications such as radio occultation, InSAR, the Earth monitoring, etc. (Allahviridi-Zadeh et al. 2021).

2.3 POD Validation

The Spire CubeSats are not equipped with Satellite Laser Ranging (SLR) reflectors, and thus, external validation is not possible. Therefore, the internal methods including the overlapping arcs, residuals analysis, and goodness of fit checks are used to validate the POD results. Their results are described in the following sections.

2.3.1 Overlapping Arcs

The overlapping validation is performed by testing two consecutive arcs longer than 24 h (e.g. 30 h) and checking the differences in the overlapped part. The estimated CubeSats orbits are all around 1.5 h arcs due to the length of the observation segments. All possible overlapped arcs between all estimated orbits of each CubeSat, except for the arc boundaries, are considered for this validation method. Figure 4 shows a sample of the overlapped arc between two consecutive orbits.

The RMS of the overlapped differences for RD-POD and Kinematic POD (Kin-POD) in all directions are plotted in Fig. 5. Small RMS values indicate validation of the POD procedure. The overall average reduction in RMS for the Kin-POD, are also observed when using the SNR-based weighting (dark colours) against the elevation-dependent model (light colours). This confirms the benefits of using the SNR-based model for the CubeSat's kinematic POD. The average percentage of the RMS reduction for all CubeSats are provided in Table 2. In the RD-POD, the overlapping results applying both models are similar. This could be

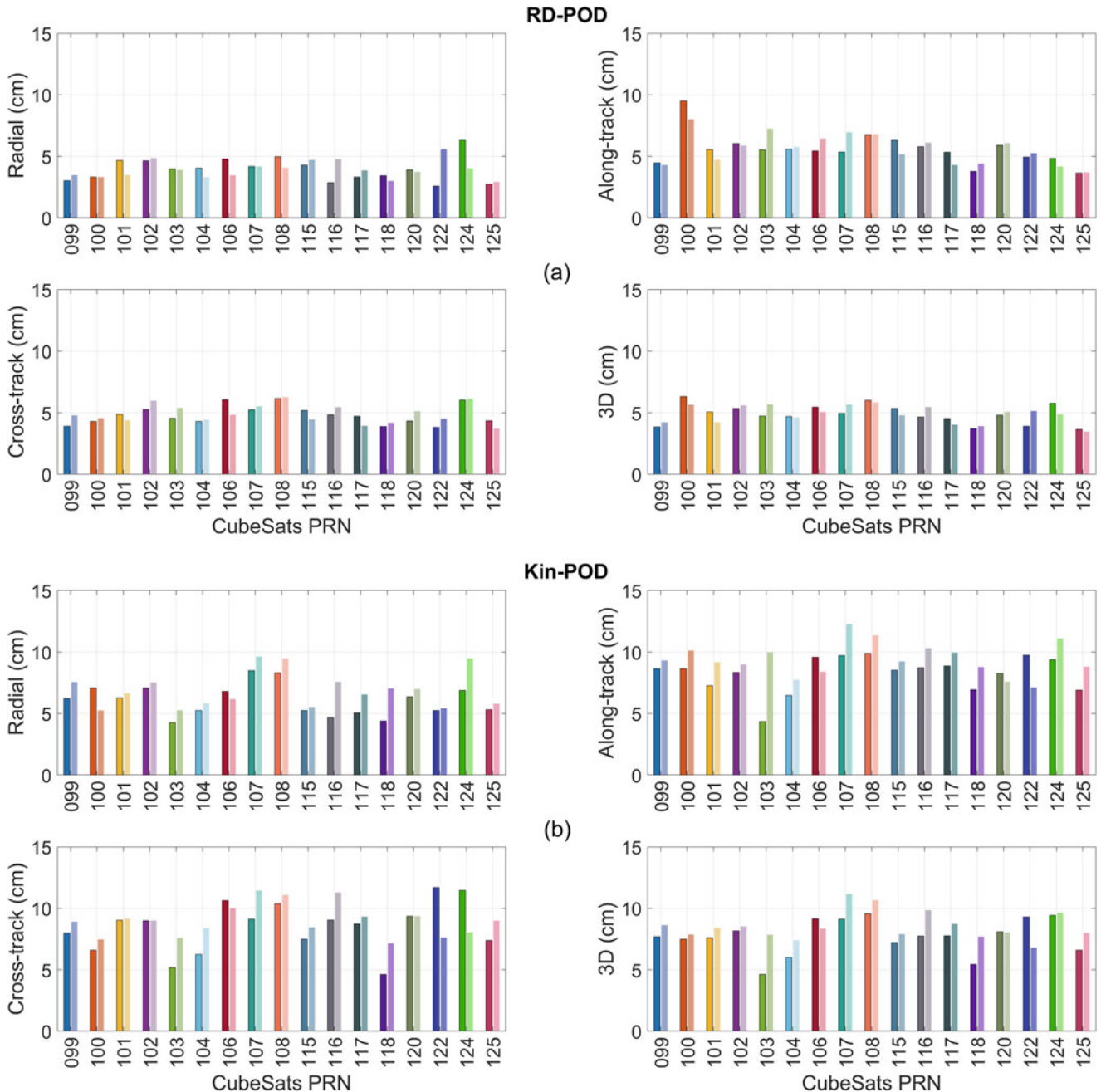


Fig. 5 RMS of overlapping validation for RD-POD (a) and Kin-POD (b). (Dark colours: using the SNR-based model – Light colours: using the elevation-dependent model)

due to the impact of using similar dynamic models and estimating the piecewise accelerations in the RD-POD using both weighting models.

2.3.2 Goodness of Fit

The a-posteriori variance can be expressed as:

$$\hat{\sigma}_0^2 = \frac{\|\hat{e}\|_W^2}{dof}$$

(2) where $(\|\hat{e}\|_W^2 = \hat{e}^T W \hat{e})$ is the weighted squared norm of the observation residuals (\hat{e}) using the observation weight

Table 2 Mean percentage of the RMS reduction due to the proposed SNR-based model compared to the elevation-dependent model for all CubeSats in all directions

| POD | Radial (%) | Along-Track (%) | Cross-Track (%) | 3D (%) |
|-----|-------------|-----------------|-----------------|------------|
| RD | 0.0 | 0.1 | 0.0 | 0.1 |
| Kin | 11.2 | 11.1 | 5.7 | 9.5 |

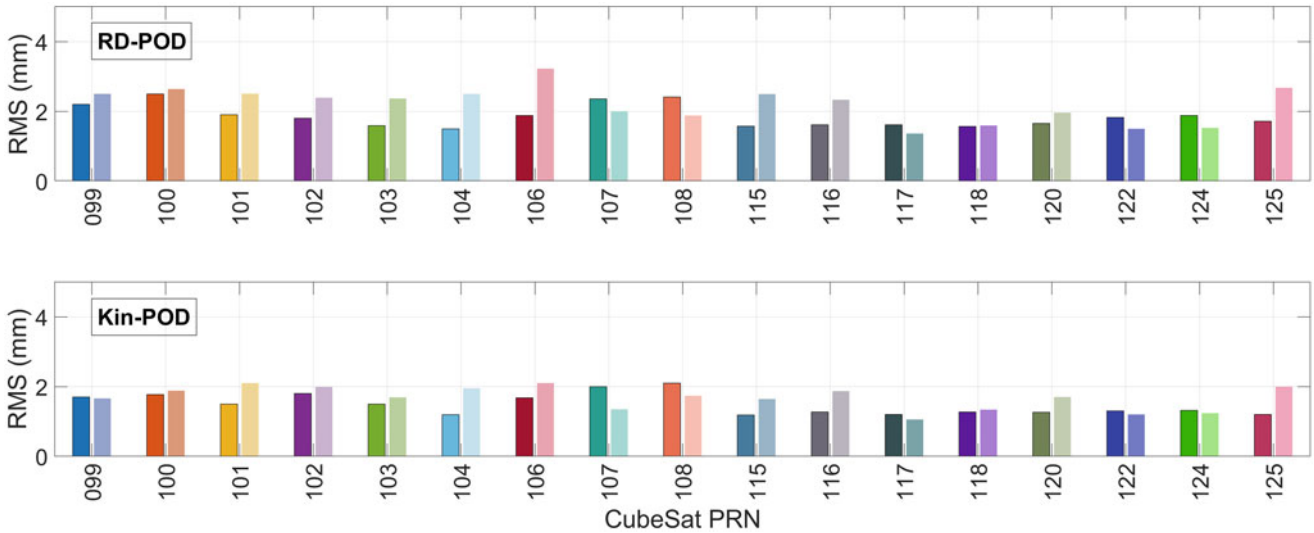


Fig. 6 RMS of the a-posteriori sigma for all CubeSats for RD-POD (top) and Kin-POD (bottom). (Dark colours: using the SNR-based model—Light colours: using the elevation-dependent model)

Table 3 Mean value of the a-posteriori STD of all CubeSats from RD-POD and Kin-POD

| POD | Mean value of the a-posteriori sigma (mm) | |
|-----|---|---------------------------|
| | SNR-based model | Elevation-dependent model |
| RD | 1.85 | 2.20 |
| Kin | 1.48 | 1.67 |

matrix (W) and dof denotes the degrees of freedom. The ratio of a-posteriori variance to the a-priori variance (see Table 1) can be used as a self-consistency check of the goodness of fit using the following chi-squared test with selected confidence region (α) (Strang and Borre 1997):

$$\frac{\hat{\sigma}_0^2}{\sigma_0^s} < \frac{\chi_{dof,1-\alpha}^2}{dof} \quad (3)$$

The a-posteriori standard deviation (STD) values of all CubeSats are plotted in Fig. 6. They are all less than 3 mm which represents an acceptable fitting model to the POD problem. The mean of all a-posteriori STD values for all tested CubeSats are given in Table 3. In total, 16% and 11% reduction in the a-posteriori STD values are observed in the case of POD using SNR-based weighting model for RD-POD and Kin-POD, respectively.

2.3.3 Residual Analysis

The final validation check is the observation residual analysis. As a representative example, the GPS ionosphere-free (IF) phase residuals for CubeSat PRN-099 are plotted in Fig. 7. The ambiguities were estimated as float values in our POD processing. The residuals are at sub-centimeter to centimeter

level mainly due to the onboard COTS receiver/antenna, as well as using the IF-LC which increases the noise compared to the use of uncombined signals. However, the reduction of the residuals is obvious for the POD using the SNR-based model. Similar trends are observed for other CubeSats.

The CubeSats cross the eclipse region several times per day. Although the solar radiation pressure is significantly low due to the absence of sunlight, there is a thermal re-radiation as an additional effect of the solar radiation pressure in these regions (Švehla 2018). A cylindrical model proposed by Allahviridi-Zadeh (2013, 2022) and Allahverdi-Zadeh et al. (2016) is used to estimate the eclipse region and analyse the residual behaviours. No significant changes on residuals can be observed for crossing this region. The reason is that such effect has been captured by the estimation of stochastic accelerations in the POD procedure.

3 Conclusion

The proposed SNR-based weighting model reduced the IF phase residuals compared to the traditional elevation angle-dependent model. The internal validation including comparing overlapping arcs and the a-posteriori STD confirmed the improved performance of CubeSats' POD using the proposed SNR-based weighting model. The generated CubeSats orbits have a precision that fulfils the requirements of different space and Earth science applications. The impact of using such a weighting model on ambiguity resolution is among our next studies.

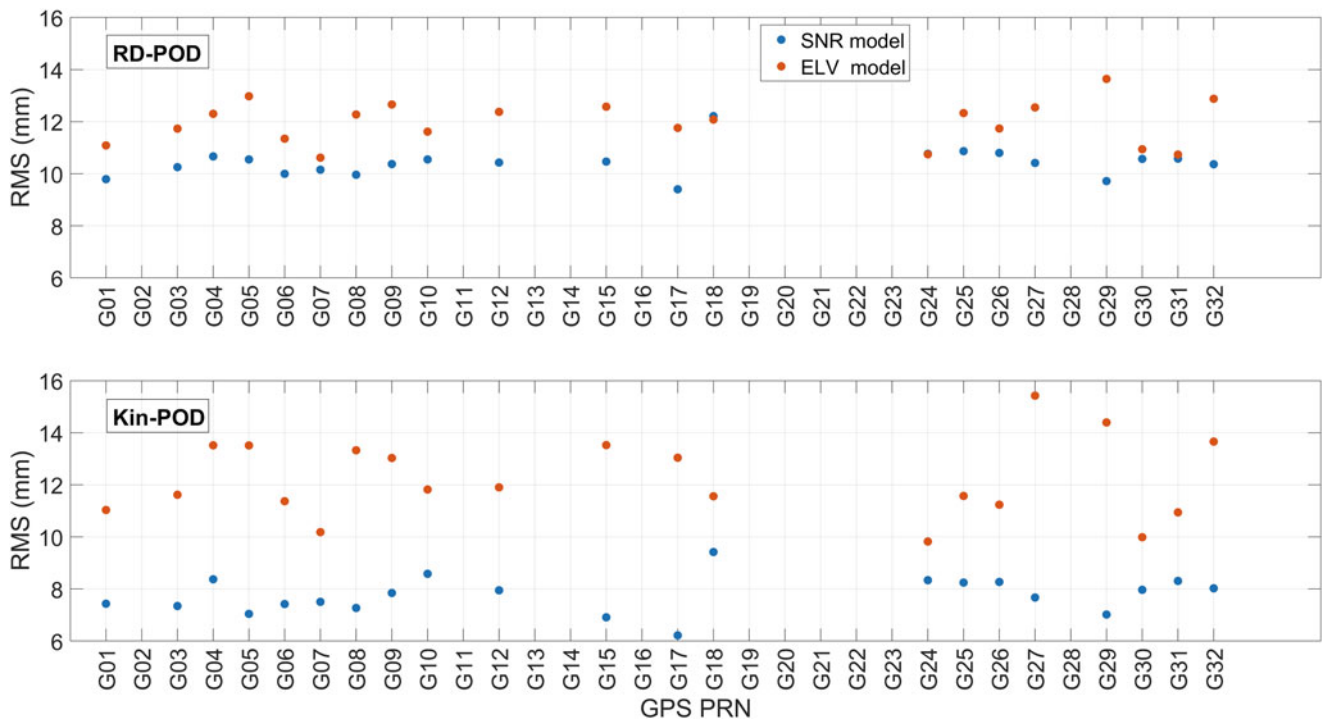


Fig. 7 The RMS of IF phase residuals from the RD-POD (top) and the Kin-POD (bottom) for CubeSat PRN099. The RMS values are derived from one month of all observations of all GPS satellites

Acknowledgments We would like to thank Spire Global, Inc for providing the nanosatellite data for scientific research. Special thanks to Dallas Masters, Ph.D., Director of Earth observations/GNSS and his team for our discussions on the satellite structure and for providing the required information. This work is funded by the Australian Research Council under the discovery project “Tracking Formation-Flying of Nanosatellites Using Inter-Satellite Links” (DP 190102444). Third author receives fund from the Chinese Academy of Science (CAS) “Light of West China” Program (No. XAB2018YDYLO1).

References

- Allahverdi-Zadeh A, Asgari J, Amiri-Simkooei AR (2016) Investigation of GPS draconitic year effect on GPS time series of eliminated eclipsing GPS satellite data. *J Geod Sci* 6. <https://doi.org/10.1515/jogs-2016-0007>
- Allahverdi-Zadeh A (2013) Evaluation of the GPS observable effects located in the earth shadow on permanent station position time series. MSc thesis, Geomatics Engineering Department, University of Isfahan. <https://doi.org/10.13140/RG.2.2.28151.32167>
- Allahverdi-Zadeh A (2021a) Software Defined Radio (SDR) as a GNSS receiver in future CubeSats. In: Internship with Binar Space Program – Innovation Central Perth. Curtin University, Perth, Western Australia. <https://doi.org/10.13140/RG.2.2.28290.20166>
- Allahverdi-Zadeh A (2021b) Phase centre variation of the GNSS antenna onboard the CubeSats and its impact on precise orbit determination. In: Proceedings of the GSA Earth Sciences Student Symposium, Western Australia (GESSS-WA), Perth, Australia, 25 November 2021. <https://doi.org/10.13140/RG.2.2.10355.45607/1>
- Allahverdi-Zadeh A, Wang K, El-Mowafy A (2021) POD of small LEO satellites based on precise real-time MADOCA and SBAS-aided PPP corrections. *GPS Solut* 25:31. <https://doi.org/10.1007/s10291-020-01078-8>
- Allahverdi-Zadeh A (2022) Shadow toolbox. figshare. Software. <https://doi.org/10.6084/m9.figshare.19085546.v1>
- Allahverdi-Zadeh A, El-Mowafy A (2022) The impact of precise inter-satellite ranges on relative precise orbit determination in a smart CubeSats constellation, EGU General Assembly 2022, Vienna, Austria, 23–27 May 2022, EGU22-2215, <https://doi.org/10.5194/egusphere-egu22-2215>
- Allahverdi-Zadeh A, Wang K, El-Mowafy A (2022a) Precise orbit determination of LEO satellites based on undifferenced GNSS observations. *J Surv Eng* 148:03121001. [https://doi.org/10.1061/\(ASCE\)SU.1943-5428.0000382](https://doi.org/10.1061/(ASCE)SU.1943-5428.0000382)
- Allahverdi-Zadeh A, Awange J, El-Mowafy A, Ding T, Wang K (2022b) Stability of CubeSat clocks and their impacts on GNSS radio occultation. *Remote Sens* 14:362. <https://doi.org/10.3390/rs14020362>
- Hobiger T, Jakowski N (2017) Atmospheric signal propagation. In: Teunissen PJG, Montenbruck O (eds) Springer handbook of global navigation satellite systems. Springer International Publishing, Cham, pp 165–193. https://doi.org/10.1007/978-3-319-42928-1_6
- Luo X (2013) Observation weighting using signal quality measures. In: GPS stochastic modelling: signal quality measures and ARMA processes. Springer, Berlin, pp 137–162. https://doi.org/10.1007/978-3-642-34836-5_5
- Lyard F, Lefevre F, Letellier T, Francis O (2006) Modelling the global ocean tides: modern insights from FES2004. *Ocean Dyn* 56:394–415. <https://doi.org/10.1007/s10236-006-0086-x>
- Pavlis N, Kenyon S, Factor J, Holmes S (2008) Earth gravitational model 2008. In: SEG technical program expanded abstracts 2008. SEG technical program expanded abstracts. Society of Exploration Geophysicists, pp 761–763. <https://doi.org/10.1190/1.3063757>
- Petit G, Luzum B (2010) IERS conventions. (IERS Technical Note; 36) Frankfurt am Main: Verlag des Bundesamts für Kartographie und Geodäsie, p 179. ISBN 3-89888-989-6
- Schaer S (2016) SINEX BIAS—Solution (Software/technique) Independent Exchange Format for GNSS BIASes Version 1.00. In: IGS

- workshop on GNSS biases, Bern, Switzerland. http://ftp.aiub.unibe.ch/bcwg/format/sinex_bias_100.pdf
- Spire Global Inc. <https://spire.com/>. Accessed 13 August 2021
- Strang G, Borre K (1997) Linear algebra, geodesy, and GPS. Wellesley-Cambridge Press
- Švehla D (2018) Geometrical theory of satellite orbits and gravity field. Springer, Online. <https://doi.org/10.1007/978-3-319-76873-1>
- Wang K, Allahviridi-Zadeh A, El-Mowafy A, Gross JN (2020) A sensitivity study of POD using dual-frequency GPS for cubesats data limitation and resources. Remote Sens 12(13):2107. <https://doi.org/10.3390/rs12132107>

Open Access This chapter is licensed under the terms of the Creative Commons Attribution 4.0 International License (<http://creativecommons.org/licenses/by/4.0/>), which permits use, sharing, adaptation, distribution and reproduction in any medium or format, as long as you give appropriate credit to the original author(s) and the source, provide a link to the Creative Commons license and indicate if changes were made.

The images or other third party material in this chapter are included in the chapter's Creative Commons license, unless indicated otherwise in a credit line to the material. If material is not included in the chapter's Creative Commons license and your intended use is not permitted by statutory regulation or exceeds the permitted use, you will need to obtain permission directly from the copyright holder.



6 Stability of CubeSat Clocks and Their Impacts on GNSS Radio Occultation

In the previous chapters, the required algorithms and models were developed and validated to overcome data acquisition limitations and reach the targeted accuracy in the CubeSats POD. However, the POD process output does not only include the computation of precise orbits but also estimating receiver clocks, which are affected by the orbit estimation procedure and the quality of the oscillators. Therefore, the first part of the following paper that covers this chapter explains the essential factors in reducing the short-term stability of CubeSats' clocks and proposes some remedies. The second part of the paper shows the benefits of replacing large LEO satellites with CubeSats by evaluating and comparing the products of two actual LEO and CubeSat constellations:

Allahviridi-Zadeh, A., Awange, J., El-Mowafy, A., Ding, T., & Wang, K. (2022). Stability of CubeSat Clocks and Their Impacts on GNSS Radio Occultation. *Remote Sensing*, 14(2) (pp 1-26), 362. DOI: 10.3390/rs14020362



Article

Stability of CubeSat Clocks and Their Impacts on GNSS Radio Occultation

Amir Allahviridi-Zadeh ¹, Joseph Awange ¹, Ahmed El-Mowafy ¹, Tong Ding ¹ and Kan Wang ^{2,3,*}

¹ School of Earth and Planetary Sciences (Spatial Sciences), Curtin University, GPO Box U1987, Perth, WA 6845, Australia; amir.allahviridizadeh@curtin.edu.au (A.A.-Z.); j.awange@curtin.edu.au (J.A.); a.el-mowafy@curtin.edu.au (A.E.-M.); tong.ding@curtin.edu.au (T.D.)

² National Time Service Center, Chinese Academy of Sciences, Xi'an 710600, China

³ University of Chinese Academy of Sciences, Beijing 100049, China

* Correspondence: wangkan@ntsc.ac.cn

Abstract: Global Navigation Satellite Systems' radio occultation (GNSS-RO) provides the upper troposphere-lower stratosphere (UTLS) vertical atmospheric profiles that are complementing radiosonde and reanalysis data. Such data are employed in the numerical weather prediction (NWP) models used to forecast global weather as well as in climate change studies. Typically, GNSS-RO operates by remotely sensing the bending angles of an occulting GNSS signal measured by larger low Earth orbit (LEO) satellites. However, these satellites are faced with complexities in their design and costs. CubeSats, on the other hand, are emerging small and cheap satellites; the low prices of building them and the advancements in their components make them favorable for the GNSS-RO. In order to be compatible with GNSS-RO requirements, the clocks of the onboard receivers that are estimated through the precise orbit determination (POD) should have short-term stabilities. This is essential to correctly time tag the excess phase observations used in the derivation of the GNSS-RO UTLS atmospheric profiles. In this study, the stabilities of estimated clocks of a set of CubeSats launched for GNSS-RO in the Spire Global constellation are rigorously analysed and evaluated in comparison to the ultra-stable oscillators (USOs) onboard the Constellation Observing System for Meteorology, Ionosphere, and Climate (COSMIC-2) satellites. Methods for improving their clock stabilities are proposed and tested. The results (i) show improvement of the estimated clocks at the level of several microseconds, which increases their short-term stabilities, (ii) indicate that the quality of the frequency oscillator plays a dominant role in CubeSats' clock instabilities, and (iii) show that CubeSats' derived UTLS (i.e., tropopause) atmospheric profiles are comparable to those of COSMIC-2 products and in situ radiosonde observations, which provided external validation products. Different comparisons confirm that CubeSats, even those with unstable onboard clocks, provide high-quality RO profiles, comparable to those of COSMIC-2. The proposed remedies in POD and the advancements of the COTS components, such as chip-scale atomic clocks and better onboard processing units, also present a brighter future for real-time applications that require precise orbits and stable clocks.

Keywords: CubeSats; precise orbit determination (POD); GNSS radio occultation (GNSS-RO); clock stability; COSMIC-2 profiles



Citation: Allahviridi-Zadeh, A.; Awange, J.; El-Mowafy, A.; Ding, T.; Wang, K. Stability of CubeSat Clocks and Their Impacts on GNSS Radio Occultation. *Remote Sens.* **2022**, *14*, 362. <https://doi.org/10.3390/rs14020362>

Academic Editor: Yunbin Yuan

Received: 17 December 2021

Accepted: 11 January 2022

Published: 13 January 2022

Publisher's Note: MDPI stays neutral with regard to jurisdictional claims in published maps and institutional affiliations.



Copyright: © 2022 by the authors. Licensee MDPI, Basel, Switzerland. This article is an open access article distributed under the terms and conditions of the Creative Commons Attribution (CC BY) license (<https://creativecommons.org/licenses/by/4.0/>).

1. Introduction

Global Navigation Satellite Systems' Radio Occultation (GNSS-RO) is an atmospheric remote sensing/atmospheric sounding technique currently being employed to complement the radiosonde [1] and reanalysis [2,3] products in order to improve the derived upper tropopause-lower stratosphere (UTLS) atmospheric profiles used in numerical weather prediction (NWP) models that generate global weather forecasting [4], as well as climate change studies [5,6]. GNSS-RO operates in such a way that the precise phase observations of a rising or setting GNSS satellite, which increase while passing through the atmospheric

layers, are collected by the receivers onboard low Earth orbit (LEO) satellites. The measured phase delays (also called excess phases) are used to derive bending angles, which form the key observable used to retrieve the atmospheric profiles of temperature and pressure needed for NWP models as well as climate change studies (see, e.g., [7,8]). GNSS-RO theory, including the inversion of the phase delays to the atmospheric refractivity using Abel transformation, is well documented in different literature, e.g., [7–13].

Different larger LEO satellites, such as Gravity Recovery and Climate Experiment (GRACE [14]), Meteorological Operational (MetOp [15]), and Constellation Observing System for Meteorology, Ionosphere, and Climate (COSMIC-1 [14], and COSMIC-2 [16]), are equipped with the RO antennas suited for the GNSS-RO [17]. However, these satellites are utilised with the high-grade components in their buses and payloads, which increase their complexity, budget, and the time required for building and launching. In terms of costs, for example, COSMIC-1 and -2 required more than USD 100 and USD 460 million, respectively, to be completed [18]. As opposed to the larger LEO satellites above, low-cost CubeSats such as 3U CanX-2 [19] and 3U ARMADILLO [20] are currently being tested for GNSS-RO applications. CubeSats in general are small low-cost satellites with limited power budgets that are built from the commercial off-the-shelf (COTS) components in $10 \times 10 \times 10 \text{ cm}^3$ units (1U). A 3U CubeSat can cost USD 20 K–USD 200 K depending on the onboard payload. The launch cost could be less than USD 40 K, which can be significantly reduced for mass launches in a constellation since several CubeSats will have a ride-share. The complexity and required budget, as well as the building time, of CubeSats are much less than those of larger LEO satellites, where these factors may even prevent the continuation of larger LEO missions, as evidenced in the second phase of COSMIC-2 that was cancelled due to funding problems [21]. Moreover, the technological advancements in the COTS components and the possibility of launching them in a constellation make them comparable to the larger LEO satellites in terms of their applicability in a wide range of space and earth science applications.

The mega constellation of CubeSats launched by Spire Global Inc. [<https://spire.com> accessed on 12 January 2022] is an example of CubeSats' constellation that provides different services such as global weather monitoring using the GNSS-RO procedure, maritime domain awareness, and automatic dependent surveillance-broadcast. This constellation consists of more than 145 3U CubeSats ($10 \times 10 \times 30 \text{ cm}^3$) equipped mostly with STRATOS GNSS receivers that collect 50-Hz dual-frequency GNSS-RO signals. These signals and those that are collected by the zenith antenna mounted for the precise orbit determination (POD) are processed in the analysis center to provide daily globally distributed and high-quality atmospheric vertical profiles that bring substantial benefits to the performance of the NWP models [22].

To achieve accurate UTLS atmospheric profiles, however, the orbital accuracy of LEO satellites used for GNSS-RO should be at several centimeters level, and the velocity components, mainly along-track direction, should be better than 0.2 mm/s [23]. The orbital precisions and accuracies of the Spire CubeSats have already been estimated using the reduced-dynamic POD (RD-POD) and internally validated in [24] and found to be at an acceptable range for the GNSS-RO application. Besides the orbital parameters, the accuracy of the estimated clocks and their stabilities are essential for GNSS-RO since the high-rate observations, e.g., at 50 Hz sample intervals, should be precisely time-tagged based on the estimated clock offsets. As such, any error or instability in these clocks affects the measured phase observations and subsequently the derived GNSS-RO atmospheric profiles.

The accuracy of the estimated clocks and their stabilities are influenced by the quality of the oscillators and the remaining GNSS errors in the RD-POD models [25]. Larger LEO satellites (e.g., GRACE and COSMIC-2) are generally equipped with highly accurate oscillators that provide high stabilities at the 10^{-12} to 10^{-14} level [26,27]. However, this level of stability can be degraded by any unmodelled errors in the RD-POD procedure or the GNSS data quality. For example, the reduction in the clock stabilities to the 10^{-9} to 10^{-11} level, which is observed for COSMIC satellites, has been related to the quality of

the GPS observations due to the inclined POD antenna orientation and its field of view, the accuracy of the attitude control systems, and the quality and the type of the onboard GPS receiver [26]. In addition, some periodic variations due to the GPS orbital period have been found in the GRACE clock analysis and proposed to be considered in the clock modelling [28]. For CubeSats, however, besides the general studies that show the CubeSats' evolution (e.g., [29]) and their capabilities in the earth science applications (e.g., [30]), most studies have concentrated on evaluating the stabilities of the onboard CubeSats' oscillators and developing compatible atomic clocks based on CubeSats' limitations. For example, Warren et al. [31] analysed the developed atomic clocks based on optical pumping for the CubeSats while Rybak et al. [32] simulated the performance of the chip-scale atomic clocks for the navigation of a CubeSat in lunar orbit. To the best of the authors' knowledge, no literature exists on the assessment and evaluation of CubeSats' clock stabilities due to un-modelled errors in the POD procedure and their propagated impacts on the determined GNSS-RO profiles.

This study aims at assessing and evaluating the CubeSats' clock stabilities and their possible impacts on the derived UTLS atmospheric products. The specific objectives of the study are (i) assessing CubeSats' clock stabilities resulting from un-modelled errors during the RD-POD procedure and evaluating possible remedies, and (ii) analysing the derived GNSS-RO profiles from unstable CubeSats' clocks in comparison to COSMIC-2. Section 2 starts by presenting the RD-POD procedure and the excess phase derivation before assessing CubeSats' clock instabilities emanating from GNSS observational quality, hardware biases, un-modelled phase center variations, and relativistic effects. To have a better understanding of the ranges of the errors in the RD-POD compared to the quality of oscillators and their influences on the CubeSats' clocks, the estimated clocks are compared to those of COSMIC-2 that have USOs. These are also analysed for the first time from the stability of receiver clocks' point of view. Possible remedies in the RD-POD procedure to improve the accuracy of the estimated clocks are evaluated and discussed in addition to addressing the practical solutions for the unstable CubeSats' clocks in GNSS-RO. To evaluate the CubeSats' GNSS-RO atmospheric profiles derived from the excess phase observations while the CubeSats' clock errors are removed using the complex solutions, they are compared in Section 3 to those of COSMIC-2 profiles and in situ radiosonde observations, which provide a completely independent data source for validation. Section 4 summarises and concludes the study.

2. CubeSats' Clock Analysis

2.1. POD and Excess Phase Derivation

GNSS RO's excess phase is derived from the phase observation ($\Delta\Phi_{r,j}^s$) between the GNSS satellite s and the CubeSat's onboard receiver r for the frequency j through

$$\Delta\Phi_{r,j}^s = \rho_r^s + c(dt_r - dt^s) - dI_{r,j}^s + dA_r^s + \epsilon_j \quad (1)$$

where ρ_r^s is the true range between the GNSS satellite and the CubeSat, and c is the speed of light that transforms the satellite and receiver clock offsets (dt^s and dt_r) into computed ranges. The phase delays due to the ionosphere and the neutral atmosphere are indicated by $dI_{r,j}^s$ and dA_r^s , respectively, while ϵ_j denotes the unmodelled observation noises. The phase observation in Equation (1) ignores the phase ambiguities since the time derivatives of the phase observations are the actual parameters of interest in GNSS-RO [33]. The wind-up effect, relativity term, phase center offsets (PCO) and variations (PCV), and clock hardware biases are first applied in Equation (1). Besides the available precise orbits and clocks of the GNSS satellites from network processing, precise orbits and the onboard receiver clock offsets of CubeSat are also required in order to derive the excess phase in Equation (1). From the excess phase, bending angles are then derived provided that the along-track component of the velocity vectors and the excess Doppler shifts are available [10].

The satellite's state vector including the orbital and velocity components, as well as the onboard clock offsets, are estimated using the RD-POD method that is mainly based on the precise phase observations collected by the zenith POD antenna, which takes advantage of the available extensive dynamic models, as well as estimating some pre-defined stochastic accelerations to compensate for the dynamic model deficiencies [34]. The observations used in the RD-POD are subjected to the following pre-processing steps for outlier detection:

- Identification of large magnitude outliers through single-differencing between GNSS satellites, and then comparing them with low-degree polynomials in order to eliminate them from the POD processing.
- Detection of cycle slips by forming the ionosphere-free linear combinations and checking the differences between two consecutive epochs.
- Detection of millisecond clock jumps from which new ambiguities are introduced.

In the above pre-processing steps, the a priori coarse orbits generated from code observations are used whenever CubeSat's coordinates are required. However, these orbits are not good enough for reliable data screening. Therefore, the pre-processing steps are carried out iteratively (see [34] for more details). Table 1 provides the model and parameters that are used to solve the following least-squares problem for the CubeSats' RD-POD procedure [35]:

$$E(\Delta\Phi_{r,IF}^s) = [A_o, A_d, A_a][X_o, X_d, X_a]^T + cdt_r + \lambda_{IF}N_{IF} \quad (2)$$

where E is the expectation operator, $\Delta\Phi_{r,IF}^s$ is the linearised ionospheric-free phase observations, and A_o , A_d , and A_a are the design matrices containing the required partial derivatives of the observations and dynamic models with respect to the orbital components, dynamic parameters, and stochastic accelerations, respectively. The unknown X_o vector includes the orbit and velocity elements. The coefficients related to the dynamic models and the stochastic accelerations are combined into the X_d and X_a matrices, respectively. The ionosphere-free (IF) wavelength (λ_{IF}) transforms the IF phase ambiguities (N_{IF}) into computed ranges. The partial derivatives in Equation (2) are derived through the numerical integration of the variational equation [34,36]. The unknown parameters are generally derived using the so-called pre-elimination and back-substitution method [37].

Table 1. POD processing models and parameters.

| Item | Description |
|--|---|
| Dynamic models | Gravity field: Earth Gravitational Model (EGM 2008) [38] |
| | Tidal corrections: Updated Finite Element Solution tidal model (FES2004) [39] |
| | Relativity: International Earth rotation and Reference systems Service (IERS 2010) [40] |
| | Planets ephemeris: Jet Propulsion Laboratory Development Ephemeris (JPL DE405) [41] |
| Observation model | Dual-frequency GPS Ionosphere-Free (1 Hz) |
| | Removing the required GNSS satellites using the cylindrical shadow model [42] |
| | A priori code standard deviation of 0.1 m, a priori phase standard deviation of 1 mm (Zenith, L1) |
| | Satellite attitude information: Obtained as quaternions |
| | PCO and PCV for GNSS satellites: igs14.atx [43] |
| | PCO and PCV for CubeSats: LEMUR_ant-1931.atx (Provided by Spire Global Inc.) |
| | GNSS orbits and clocks: Center for Orbit Determination in Europe (CODE) final products [44] |
| GNSS satellite phase biases: CODE P1C1 and P2C2 Differential Code Biases (DCB) are applied to be consistent with the precise ephemeris | |
| Stochastic accelerations | Velocity changes (pulses) at certain epochs at every 15 min |
| | Piece-wise constant accelerations at 6 min intervals |

2.2. Assessment of the CubeSats' Clock Instabilities

GNSS and CubeSats' clock offsets should be stable enough to be interpolated at the 50 Hz time tags of the phase observations in order to derive the excess phase observation from Equation (1). On the one hand, all GNSS satellites are equipped with high-grade atomic clocks, where their clock offsets are estimated through rigorous network processing [45]. The available GNSS precise clocks are, therefore, stable enough to be interpolated using polynomials to the high-rate observation time tags [46–48]. On the other hand, CubeSats' clock stabilities are estimated through the RD-POD processing, and depend on the GNSS observation noises, near field multipath due to the CubeSat's structure, the accuracy of GNSS orbits and clocks used in the RD-POD processing, deficiencies of the dynamic models regarding the non-gravitational forces, unmodelled hardware biases, and the quality of the oscillators [25]. Due to these factors, the modified Allan deviation (*MDEV*) with the averaging time (τ) [49] is used to analyse the stability of the clock errors:

$$MDEV(\tau) = \sqrt{\frac{1}{2m^2\tau^2(n-3m+1)} \sum_{k=1}^{n-3m+1} \left(\sum_{i=k}^{k+m-1} (dt_{r,i+2m} - 2dt_{r,i+m} + dt_{r,i}) \right)^2} \quad (3)$$

where n is the number of clock samples, m is the averaging factor to compute τ from the sampling interval t_0 as $\tau = mt_0$, and dt_r is the estimated clock offsets from the RD-POD processing. In the analysis undertaken in this study, the clock offsets of 17 CubeSats from the Spire Global constellation are estimated through a comprehensive RD-POD procedure and their stabilities are computed from Equation (3) for a period of one month (16 December 2020 to 15 January 2021). A list of the CubeSats analysed in this study and their specifications are presented in Table 2, with their structure and antenna locations shown in Figure 1.

Table 2. Specifications of seventeen CubeSats employed in this study. SSO: Sun-Synchronous Orbit, LTAN: Local Time of Ascending Node, LTDN: Local Time of Descending Node (provided by Spire Global Inc.).

| ID | CubeSat's Name | COSPAR ID | Altitude (km) | Orbit Type | Mass Size |
|-----|-----------------------|------------|---------------|------------------------|---|
| 099 | LEMUR-2-JOHANLORAN | 2019-018G | | | |
| 100 | LEMUR-2-BEAUDACIOUS | 2019-018H | 505 | SSO (LTAN 09:30) | |
| 101 | LEMUR-2-ELHAM | 2019-018J | | | |
| 102 | LEMUR-2-VICTOR-ANDREW | 2019-018K | | | |
| 103 | LEMUR-2-WANLI | 2019-038S | | | |
| 104 | LEMUR-2-LILLYJO | 2019-038L | | | |
| 106 | LEMUR-2-EJATTA | 2019-038Z | 530 | SSO (LTAN 15:05) | |
| 107 | LEMUR-2-MORAG | 2019-038T | | | |
| 108 | LEMUR-2-GREGROBINSON | 2019-038AB | | | ~5 kg 0.1 × 0.1 × 0.3 m ³ (3U CubeSat) |
| 115 | LEMUR-2-JPGSQUARED | 2019-089D | 550 | Orbit inclination: 37° | |
| 116 | LEMUR-2-ETHANOAKES | 2020-061AC | 540 | SSO (LTDN 10:30) | |
| 117 | LEMUR-2-THEODOSIA | 2019-089M | 550 | Orbit inclination: 37° | |
| 118 | LEMUR-2-SCHMIDTFALL | 2020-061AV | | | |
| 120 | LEMUR-2-DJUPROERA | 2020-061AW | | | |
| 122 | LEMUR-2-SQUAREJAWS | 2020-061AX | 540 | SSO (LTDN 10:30) | |
| 124 | LEMUR-2-OSCARLATOR | 2020-061AD | | | |
| 125 | LEMUR-2-URSA-AVION | 2020-061AY | | | |

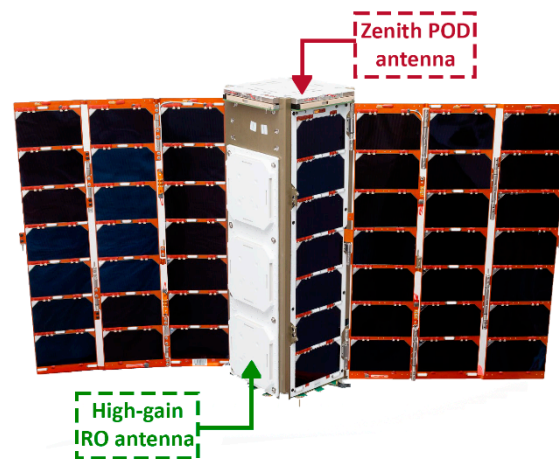


Figure 1. Structure of the Spire 3U RO CubeSat (source: Spire Global, Inc.).

The required observation segments, attitude information, and phase center values of the CubeSats are provided by Spire Global, Inc. Each observation segment contains from 45 min to 3 h, mostly around 1.5 h, dual-frequency GPS observations collected by the zenith POD antenna of the CubeSats (see Figure 1). Figure 2 shows the MDEV of the estimated clocks for different averaging times between 1 s and 1.5 h that are computed from Equation (3). The stability of the clock errors varies between 10^{-11} and 10^{-3} , with about 95% of the computed MDEV being in the 10^{-8} to 10^{-4} range.

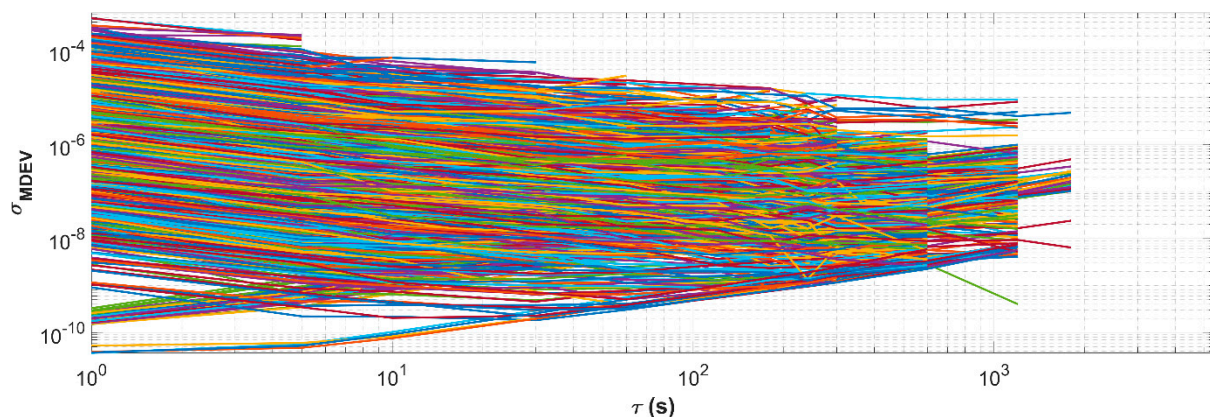


Figure 2. MDEV of the estimated clocks of all 17 CubeSats from the RD-POD over the testing period (31 days: 16 December 2020–15 January 2021). Different colours are dedicated to the different observation segments.

Next, an in-depth analysis of CubeSats' clock instabilities emanating from GNSS observational quality, onboard hardware biases, unmodelled phase center variations, and relativistic effects are presented. In addition, the quality of the onboard CubeSats' oscillators is also analysed. From the analysis of the above instability triggers, some remedies are proposed and evaluated as summarised in Figure 3.

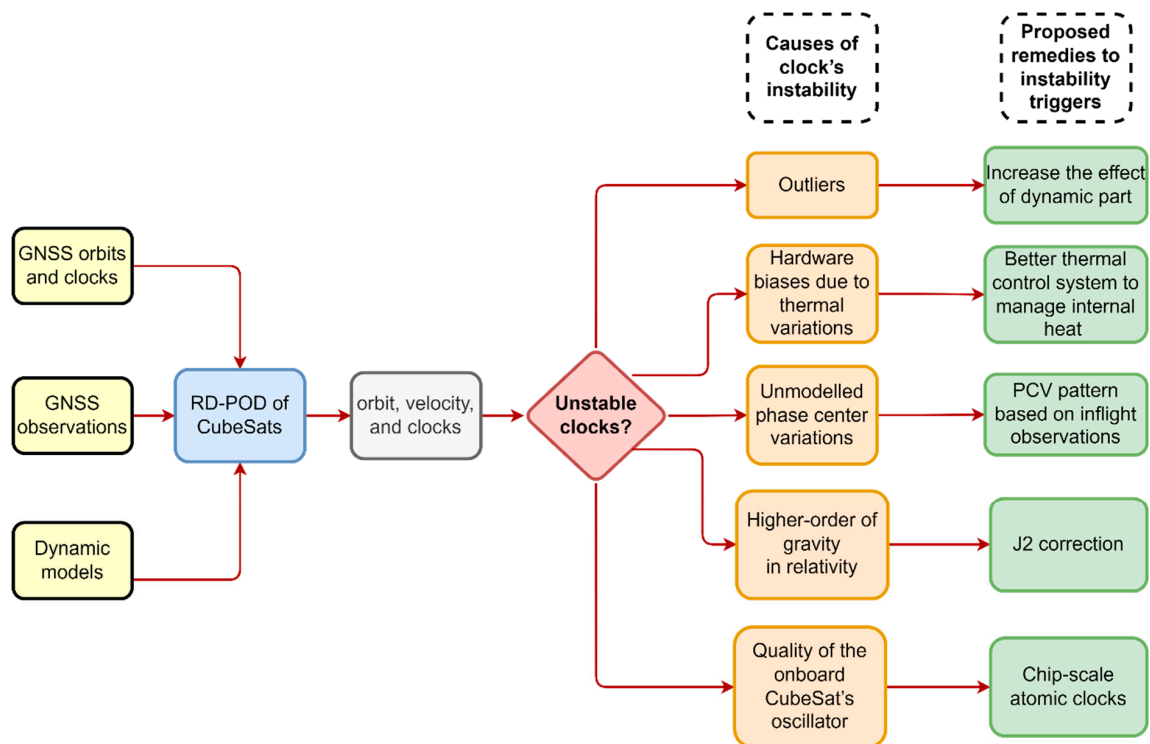


Figure 3. Flowchart indicating CubeSats' clock instability assessment and the proposed remedies.

2.2.1. Quality of GNSS Observations

The RD-POD is available with a short time or even with the duty-cycled data, i.e., when the observations are not continuously collected by the receiver due to the power limitations in CubeSats [35]. However, the number of observations that are marked as outliers in the pre-processing step and filtered out from the rest of the POD procedure affects the precision of the estimated clocks. To illustrate this effect, the relation between the outlier ratio and the clock stabilities for short averaging times are plotted in Figure 4 for all 17 CubeSats. The stabilities of the estimated clocks are generally worse than 10^{-5} when more than 50% of the observations are considered outliers. This value degrades to 10^{-3} when more than 90% of the observations are rejected (i.e., considered outliers). Hence, the noisy observations that cannot pass the pre-processing steps decrease the degrees of freedom and affect the stability of the estimated clocks. Figure 4 contains only the values pertaining to short averaging times (i.e., 1, 5, 10, and 30 s), which is of interest to GNSS-RO. Nonetheless, similar trends are observed for longer averaging times.

The stochastic accelerations that are estimated in the POD procedure as compensations for the deficiencies in the non-gravitational dynamic models are initially set to every 15 min for the velocity changes and at 6 min intervals for the piece-wise constant accelerations. These values, which have been tested in different studies (e.g., [35,46,50]), are selected based on the length of the observations, sample intervals, and computational power unit (CPU). However, since the GNSS-dependent part of the RD-POD is weak for the observation segments with a large number of outliers, the impact of the dynamic-dependent part in RD-POD needs to be increased to compensate for this weakness. Therefore, the numbers of the stochastic accelerations for the observations with outliers larger than 50% are doubled compared to the values given in Table 2, i.e., every 7.5 min for the velocity changes and at 3 min intervals for the piece-wise constant accelerations. The MEDVs of the estimated clocks with the new settings are compared with the clock stabilities provided in Figure 2, and the mean values for this comparison are provided in Table 3. The stability refinement due to the higher number of stochastic accelerations for the short averaging time (1 s) is at 10^{-6} level, which decreases for longer averaging times. This indicates that more stochastic

accelerations for the observation segments with large outliers can improve the short-time stability of the estimated clocks in the RD-POD procedure.

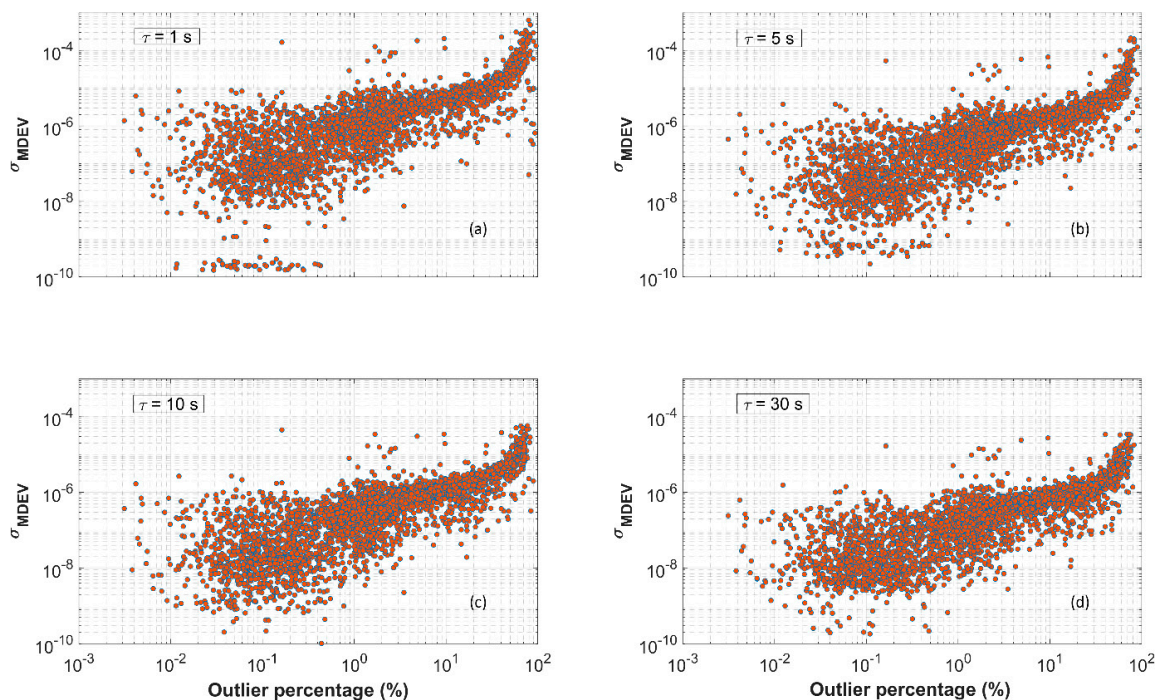


Figure 4. MDEV of the 17 CubeSats' clocks for short averaging times plotted against the percentage of the observations that are considered outliers in the pre-processing steps. In the subfigures, each dot represents the MDEV of one observation segment for one CubeSat over the testing period. The subfigures (a–d) indicate averaging times 1, 5, 10, and 30 s, respectively.

Table 3. Mean values of the MDEV changes of the CubeSats' clocks when the numbers of stochastic accelerations are doubled compared to the default settings for the CubeSats observations with a high rate of outliers (>50%).

| Averaging Time | Mean |
|----------------|-------------------------|
| 1 s | 4.2422×10^{-6} |
| 5 s | 3.9271×10^{-6} |
| 10 s | 8.3397×10^{-7} |
| 30 s | 1.8289×10^{-7} |
| 60 s | 1.8873×10^{-7} |
| 120 s | 2.7663×10^{-7} |
| 300 s | 6.2265×10^{-8} |

2.2.2. Hardware Biases in Onboard CubeSat's Receiver

The satellite hardware biases have been applied in the observations to be consistent with the ionosphere-free linear combination (IF-LC) of code observations (P1/P2), used to generate the precise GNSS orbits and clocks. However, the onboard CubeSats' receiver hardware biases are lumped with the receiver clock offsets, leading to instabilities in the estimated clock offsets in the RD-POD. These biases vary due to the complex space environment, the temperature variations in its region [51], and the internal heat transfer between different components. These heating sources are analysed using the single or multi-node models before the launch. Both passive and active thermal control systems are designed to keep the temperature of the satellite within the acceptable range [52,53]. However, the

thermal variations onboard a satellite from one side are hardly predictable [54], and from the other side, can reach the same order of magnitude of the COTS clock noises, thus making them hard to distinguish [55]. To gain better insight into the thermal effects, the clock stabilities of the CubeSats when crossing shadow regions are compared with those passing through the sunlight region due to the fact that solar radiation pressures are mostly absent in shadow regions [56], and consequently the temperature drops in this part of the orbit. Based on the cylindrical model depicted in Figure 5, the CubeSat is detected in the shadow region if the following two criteria hold:

$$\begin{cases} \frac{r_c r_s}{\|r_s\|} < 0 \\ \left| r_c - \left(\frac{r_c r_s}{\|r_s\|} \right) \right| < a_e \end{cases} \quad (4)$$

where the vectors r_c and r_s are the geocentric coordinates of the CubeSat and the Sun, a_e is the equatorial radius of the earth, $\| \cdot \|$ denotes the norm of the vector, and $| \cdot |$ gives the absolute value. This model was also used for detecting GNSS satellites in the shadow of the earth in order to remove those with unpredictable Yaw motions in this region from the RD-POD process [42].

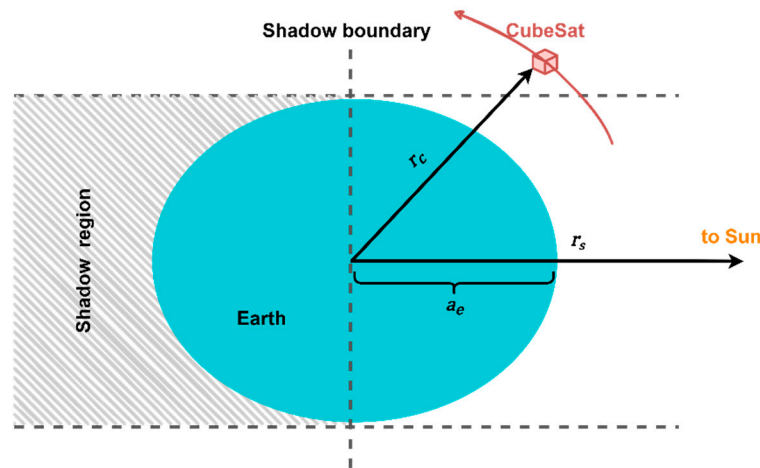


Figure 5. Cylindrical model for detecting CubeSats located in the shadow of the earth.

Around 35% of the whole observations are generally in the shadow region. The mean values comparing the clock stabilities in the shadow region and the other estimated clocks (non-shadow) for the short averaging times (1 to 30 s) are given in Table 4, varying from 10^{-5} to 10^{-8} . This shows better stabilities for the clocks in the shadow regions compared to the clocks in sunlight and confirms the impact of the thermal variations of the LEO region on the estimated clocks.

Table 4. Mean values of MDEV differences between when the CubeSats are in the shadow and when they are out of the shadow region.

| CubeSat ID | Mean | | | |
|------------|-------------------------|-------------------------|-------------------------|-------------------------|
| | $\tau = 1 \text{ s}$ | $\tau = 5 \text{ s}$ | $\tau = 10 \text{ s}$ | $\tau = 30 \text{ s}$ |
| 099 | 2.8099×10^{-6} | 1.8482×10^{-6} | 4.8800×10^{-7} | 3.5617×10^{-7} |
| 100 | 1.5454×10^{-6} | 6.1293×10^{-7} | 2.5558×10^{-7} | 1.2716×10^{-7} |
| 101 | 9.8588×10^{-7} | 6.3366×10^{-8} | 1.8324×10^{-7} | 2.3903×10^{-7} |
| 102 | 4.8431×10^{-6} | 1.5803×10^{-6} | 5.5428×10^{-7} | 3.9989×10^{-7} |
| 103 | 1.1581×10^{-5} | 1.7409×10^{-6} | 1.4120×10^{-6} | 6.4800×10^{-7} |
| 104 | 7.5333×10^{-7} | 3.3848×10^{-7} | 1.6251×10^{-7} | 1.3164×10^{-7} |
| 106 | 1.0016×10^{-6} | 6.7556×10^{-7} | 4.7897×10^{-7} | 2.7246×10^{-7} |
| 107 | 1.3704×10^{-6} | 2.4749×10^{-6} | 8.0511×10^{-7} | 4.5053×10^{-7} |

Table 4. Cont.

| CubeSat ID | Mean | | | |
|------------|-------------------------|-------------------------|-------------------------|-------------------------|
| | $\tau = 1$ s | $\tau = 5$ s | $\tau = 10$ s | $\tau = 30$ s |
| 108 | 3.3448×10^{-6} | 9.0071×10^{-7} | 9.6554×10^{-7} | 6.0439×10^{-7} |
| 115 | 1.5440×10^{-6} | 8.5576×10^{-7} | 6.8720×10^{-7} | 2.7086×10^{-7} |
| 116 | 9.3402×10^{-7} | 4.7609×10^{-7} | 3.4113×10^{-7} | 2.3037×10^{-7} |
| 117 | 1.1685×10^{-6} | 5.2623×10^{-7} | 3.9324×10^{-7} | 3.0497×10^{-7} |
| 118 | 2.8515×10^{-6} | 1.6011×10^{-6} | 4.9824×10^{-7} | 4.4380×10^{-7} |
| 120 | 2.9299×10^{-6} | 1.3750×10^{-6} | 1.8455×10^{-7} | 1.0158×10^{-7} |
| 122 | 5.3061×10^{-7} | 1.2508×10^{-7} | 5.2173×10^{-8} | 1.5620×10^{-7} |
| 124 | 1.0540×10^{-7} | 6.9540×10^{-8} | 5.8206×10^{-8} | 3.2678×10^{-8} |
| 125 | 1.2551×10^{-7} | 1.4559×10^{-8} | 1.4114×10^{-8} | 2.4155×10^{-8} |

2.2.3. Unmodelled Phase Center Variations

The Phase Center Offsets (PCO) and Phase Center Variations (PCV) of the CubeSat's POD antenna are applied in the RD-POD. These nominal values are estimated using ground calibration methods such as the anechoic chamber and robotic tests. However, these methods do not consider the actual space environment or the multipath effects due to CubeSat structure (see Figure 1) and possible neighbouring satellites in the orbit. Therefore, re-calibration based on inflight GNSS observations and the residual approach is required [57]; otherwise, some parts of the unmodelled (or miss-modelled) PCV values are absorbed by the estimated clocks. To perform the residual approach, the precise orbits of the CubeSats derived from the RD-POD and the precise orbits of the GNSS satellites from the CODE final products are used to estimate the phase residuals for different azimuths and elevation angles. The mean values of these bin-wise residuals are then considered the new PCV values and used in another round of RD-POD for all CubeSats. This procedure is performed iteratively with at least two iterations, each time with a new PCV pattern generated from the residuals of the previous run, which is applied in the POD of the next iteration. The iteration process ensures that the impacts of the residuals are correctly applied. As an example, the left pattern in Figure 6 shows the nominal PCV values estimated using the ground calibration method, while the right pattern reflects the impacts of the unmodelled PCVs for all the tested CubeSats on the phase residuals after two iterations. The impacts of the CubeSat structure and the unfolded solar panels are obvious in the pattern.

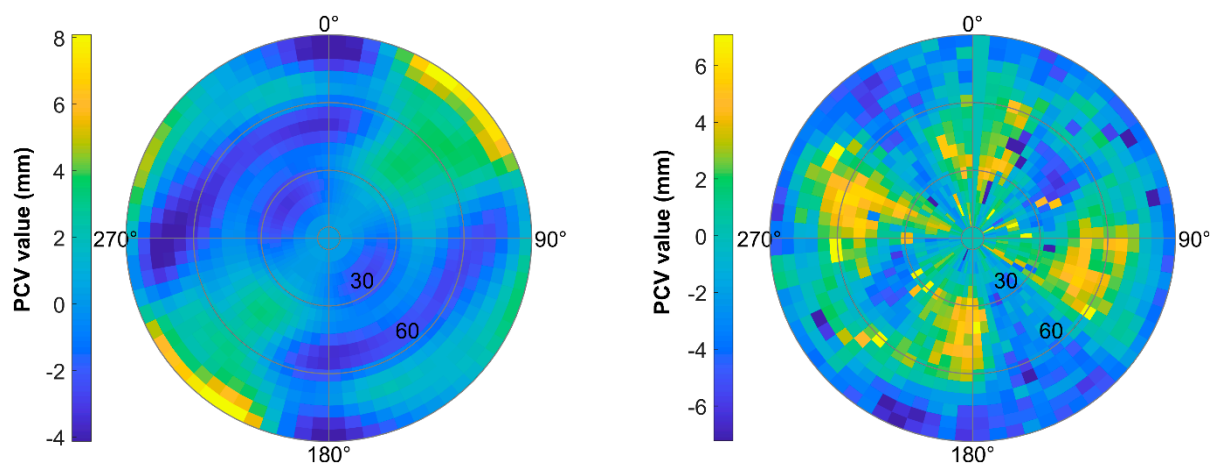


Figure 6. PCV patterns with 5° resolution for the CubeSat antenna (Lemur 3.1.0) from the antenna calibration (left) and the inflight observations using the residual approach (right). The inner circles are marked with the elevation angles, and the azimuth values are tagged on the outer circle. The azimuth 0° coincides with the positive x-axis of the CubeSats' body frame (approximately the positive velocity direction) in the zero-quaternion case.

The estimated PCVs are applied in a new run of RD-POD for all CubeSats, and the mean values of the improvements in the short-term stabilities, i.e., the MDEV reductions, are presented in Table 5. The improvement is generally higher for shorter averaging times and varied in the range of 10^{-11} to 10^{-9} for different CubeSats over the whole testing period. The observation residuals also decreased from 7 to 6 mm after applying the new PCV patterns [58].

Table 5. Mean values of the MDEV reductions after applying new PCV patterns in the RD-POD for short averaging times.

| CubeSat ID | Mean of the MDEV Reduction | | | |
|------------|----------------------------|--------------------------|--------------------------|--------------------------|
| | $\tau = 1 \text{ s}$ | $\tau = 5 \text{ s}$ | $\tau = 10 \text{ s}$ | $\tau = 30 \text{ s}$ |
| 099 | 1.1300×10^{-9} | 7.3386×10^{-9} | 8.0030×10^{-9} | 1.4970×10^{-10} |
| 100 | 1.3419×10^{-9} | 8.6637×10^{-9} | 7.7906×10^{-9} | 1.2419×10^{-9} |
| 101 | 1.1937×10^{-9} | 3.7906×10^{-9} | 2.1707×10^{-9} | 2.5780×10^{-9} |
| 102 | 5.1661×10^{-9} | 6.3604×10^{-9} | 7.5512×10^{-9} | 7.0404×10^{-9} |
| 103 | 7.6031×10^{-10} | 1.7196×10^{-10} | 1.9582×10^{-10} | 1.3144×10^{-10} |
| 104 | 1.2214×10^{-9} | 1.1005×10^{-9} | 5.9672×10^{-10} | 1.9739×10^{-10} |
| 106 | 2.5850×10^{-9} | 2.5345×10^{-10} | 4.2752×10^{-10} | 4.4856×10^{-10} |
| 107 | 1.4757×10^{-9} | 3.7337×10^{-9} | 4.5135×10^{-9} | 1.6850×10^{-10} |
| 108 | 7.2797×10^{-10} | 8.4711×10^{-10} | 3.5868×10^{-9} | 1.353×10^{-10} |
| 115 | 3.8695×10^{-9} | 2.4038×10^{-9} | 1.3947×10^{-9} | 7.8002×10^{-10} |
| 116 | 9.6599×10^{-10} | 4.9457×10^{-9} | 3.3635×10^{-10} | 6.4411×10^{-10} |
| 117 | 4.9848×10^{-9} | 3.5505×10^{-9} | 2.9508×10^{-9} | 3.5893×10^{-10} |
| 118 | 4.5214×10^{-10} | 8.1125×10^{-10} | 3.7160×10^{-9} | 1.1742×10^{-10} |
| 120 | 4.9896×10^{-9} | 3.4873×10^{-10} | 8.3837×10^{-11} | 9.9838×10^{-10} |
| 122 | 1.7535×10^{-9} | 1.8092×10^{-9} | 4.6117×10^{-10} | 5.7452×10^{-10} |
| 124 | 4.4049×10^{-9} | 4.9378×10^{-9} | 1.4370×10^{-9} | 3.7034×10^{-10} |
| 125 | 3.5682×10^{-9} | 1.5480×10^{-9} | 2.8436×10^{-9} | 4.1328×10^{-10} |

2.2.4. Higher-Order of the Earth's Gravity in the Relativity Effect

The once and twice per revolution periodic variations due to the relativistic effects cause systematic errors on the onboard clocks and affect the stability of the estimated clock offsets in RD-POD [25]. To correct them, the following J2 correction, which is usually applied for the GNSS satellite to consider the effect of gravitational potential due to the earth's oblateness [59], is considered for the CubeSats:

$$\delta t_{J_2} = -\frac{3J_2 a_E^2}{2a^2 c^2} \sqrt{GMa} \sin^2 i \sin 2u \quad (5)$$

where J_2 is the zonal coefficient, a is the semi-major axis of the satellite orbit, c is the speed of light, GM is the gravitational constant of the earth, i is the orbit inclination and u is the argument of latitude. This correction is added to the following model, which reflects the delays in GNSS signals due to the central gravity of the Earth or Shapiro effect, and the deviation of the CubeSat's clock due to the relativity effect [60]:

$$\delta t = \frac{2GM}{c^3} \ln \left(\frac{\|r_g\| + \|r_c\| + \rho_c^g}{\|r_g\| + \|r_c\| - \rho_c^g} \right) - 2 \frac{(r_c \cdot v_c)}{c^2} + \delta t_{J_2} \quad (6)$$

where r_g and r_c indicate the geocentric coordinates of the GNSS satellite and the CubeSat, respectively, v_c represents the geocentric velocity vector of the CubeSat, and ρ_c^g is the geometric distance between the CubeSat and the GNSS satellite. The mean values of the estimated clocks after applying the above corrections compared with the unmodelled J2 corrections are provided in Table 6 for each of the 17 CubeSats considered here. These values are in 10^{-11} to 10^{-8} level and their impacts may not be obvious for the unstable CubeSats' clocks (see Figure 2). However, it is useful to apply the J2 correction and even

higher zonal and tesseral gravitational harmonics for the analysis of LEO satellites equipped with onboard ultra-stable oscillators (USO).

Table 6. Mean values of the clock differences between with/without applying J_2 corrections in the RD-POD.

| CubeSat ID | Mean (s) | CubeSat ID | Mean (s) |
|------------|--------------------------|------------|--------------------------|
| 099 | 2.1591×10^{-10} | 115 | 5.6549×10^{-11} |
| 100 | 2.7670×10^{-10} | 116 | 3.9839×10^{-10} |
| 101 | 1.5468×10^{-10} | 117 | 6.8971×10^{-11} |
| 102 | 4.6668×10^{-11} | 118 | 1.0467×10^{-8} |
| 103 | 3.8903×10^{-11} | 120 | 7.2278×10^{-10} |
| 104 | 5.1731×10^{-11} | 122 | 6.3187×10^{-11} |
| 106 | 1.1238×10^{-10} | 124 | 8.8691×10^{-11} |
| 107 | 8.3909×10^{-9} | 125 | 1.6217×10^{-10} |
| 108 | 6.0123×10^{-9} | | |

2.2.5. Quality of the Onboard CubeSat's Oscillator

The quality of the frequency oscillator in the CubeSats affects their short- and long-term stabilities. These CubeSats are not equipped with USOs, and therefore, the presence of the instabilities due to the relatively low quality of the oscillators are expected. As a comparison, the USOs stability of GRACE satellites has been reported at $1 - 3 \times 10^{-13}$ for $1 \text{ s} < \tau < 10^3 \text{ s}$ [27]. For example, Figure 7 (top) shows the estimated clock of CubeSat 099 over the testing period. Several jumps are observed that can be attributed to when attempting synchronizing the oscillator with the GPS time and to prevent clock biases from becoming too large. Some of them are drawn in bold in the figure for better visibility. Similar jumps are seen in the clocks of the other tested CubeSats. As a comparison, the estimated clocks of the COSMIC-2A 1 satellite that is equipped with USO are plotted in Figure 7 (bottom). These clocks are estimated using around 1.5 h observation segments with a 10 s sample interval in the RD-POD procedure by the University of Corporation for Atmospheric Research (UCAR) COSMIC Program [61]. All clock jumps for this satellite were less than 1 millisecond, thus confirming the high quality of the USOs in comparison to the CubeSats' oscillators. A similar range of clock jumps has been observed for the other LEO satellites in the COSMIC-2 constellation.

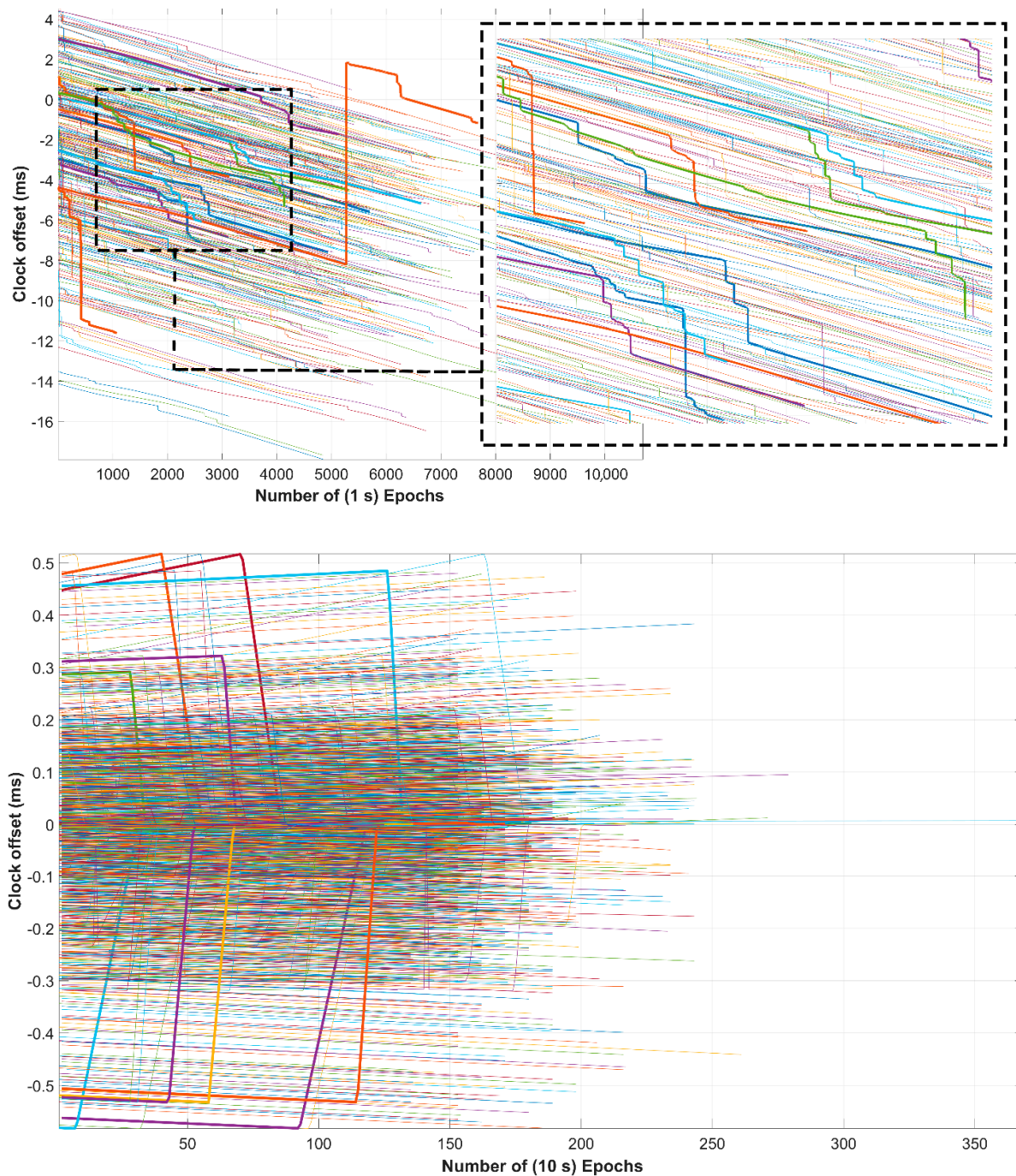


Figure 7. Estimated clock offsets from all observation segments of CubeSat 099 (**top**) and COSMIC-2A 1 (**bottom**) over the testing period. Several millisecond jumps are observed for CubeSat’s oscillator compared to the USO’s onboard COSMIC-2. Some of the clocks are plotted in bold for better visibility.

2.3. The Impacts of the Proposed Changes in RD-POD for CubeSats’ Clocks

All of the following changes are applied in the RD-POD of all CubeSats as a final step, and the clocks are estimated again to show their combined impacts of the discussed effects on clock stabilities, with:

- Doubling the number of stochastic accelerations;
- Applying the new PCV patterns based on inflight observations;
- Applying the higher order of gravitational potential in the relativity model.

The mean values for the clock improvements for each of the CubeSats after applying the above changes are shown in Figure 8. The improvements are in microseconds, generally around 20 microseconds for all CubeSats, except 80 microseconds for CubeSat 103, which is due to the higher number of observation segments with large outliers (>50%) for this particular CubeSat compared to the others. The line segments inside the bars represent the maximum and minimum Root Mean Squared (RMS) of the improvements among all the estimated clocks.

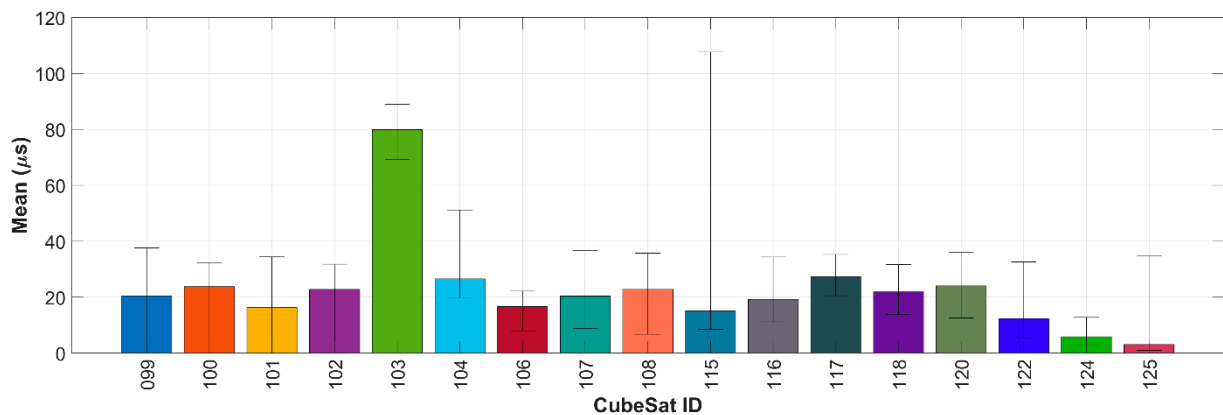


Figure 8. Mean of the improvements in comparing the estimated CubeSats' clocks before and after applying the proposed corrections in the RD-POD procedure. The lines inside each bar show the minimum and maximum RMS of the improvements over the testing period.

The improvements in the short-term stabilities of the estimated clocks for each CubeSat compared to the clocks before applying the proposed correction are plotted in Figure 9. In addition to the general stability improvements that are obvious for all tested CubeSats, the short-term stabilities for $\tau = 1$ s have higher improvements than the other averaging times. Note that the MDEV reductions for CubeSat 124, which are not visible in Figure 9 due to the scale of the Y-axis, follow the similar trends of the other CubeSats.

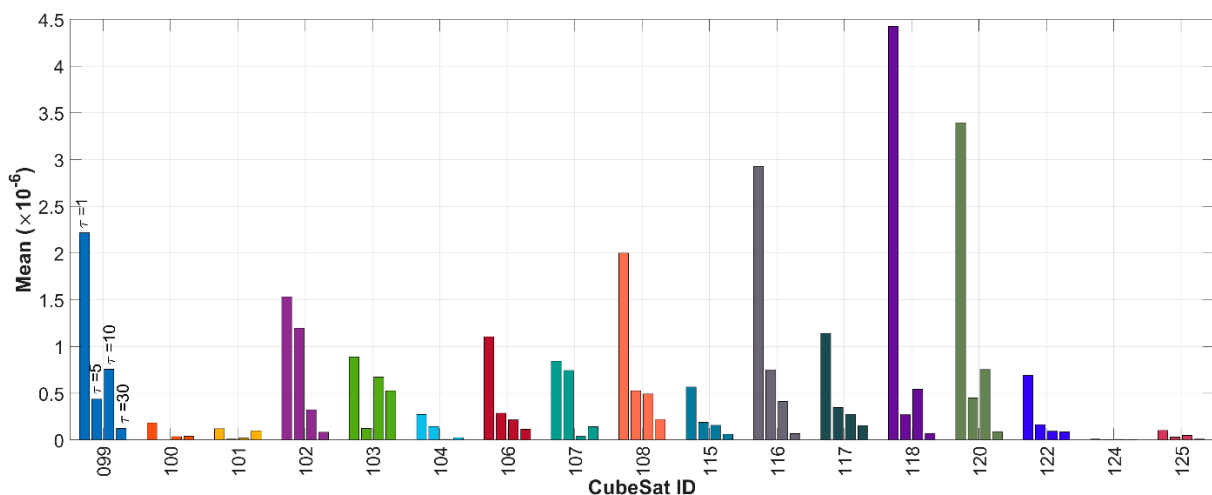


Figure 9. Mean of the MDEV reductions in the short-term stabilities after applying the proposed corrections compared to the first estimation of clocks, i.e., before applying the proposed remedies. Each CubeSat has four bars related to short averaging times (1, 5, 10, and 30 s, respectively). They are tagged for CubeSat 099 as an example.

Although the short-term and, in total, long-term stabilities are improved after applying the proposed corrections in the RD-POD, the range of the final clock stabilities are still not in the acceptable range to be used directly in high-rate applications such as GNSS-RO.

It shows that the quality of the frequency oscillator plays a dominant role among the discussed CubeSats' clock instabilities. To have a comparison with the USO clocks onboard the COSMIC-2 satellites, the MDEVs of the clock offsets of the COSMIC-2 constellation are plotted in Figure 10. The stabilities of these clocks are in the range of 10^{-13} to 10^{-8} , which are generally better than the CubeSats' clocks even with the above changes applied in the POD procedures. The short-term stabilities for τ less than 10 s are not available for COSMIC-2 satellites since the POD products from UCAR are provided with sample intervals of 10 s. The current POD accuracies and the estimated clock stabilities of COSMIC-2 meet the requirements for the GNSS-RO, and the estimated values can be directly used to retrieve the excess phase (Equation (1)) in a zero-difference processing approach discussed in [62]. However, COSMIC-2 satellites are equipped with the same USOs that are available onboard GRACE and GRACE-FO satellites, i.e., TriG-GNSS receivers. Comparing the stability ranges of COSMIC-2 in Figure 10 and the values reported in [27] for GRACE, i.e., $1 - 3 \times 10^{-13}$ for $1 \text{ s} < \tau < 10^3 \text{ s}$, reveals that there are some errors in the RD-POD of COSMIC-2, such as the PCO error mentioned by UCAR [63], as well as the issue of the offset between center of mass and the antenna reference point [64]. Therefore, the proposed corrections discussed above should also be considered in the RD-POD of the COSMIC-2 to increase the accuracy of RD-POD and stabilities of the estimated clocks.

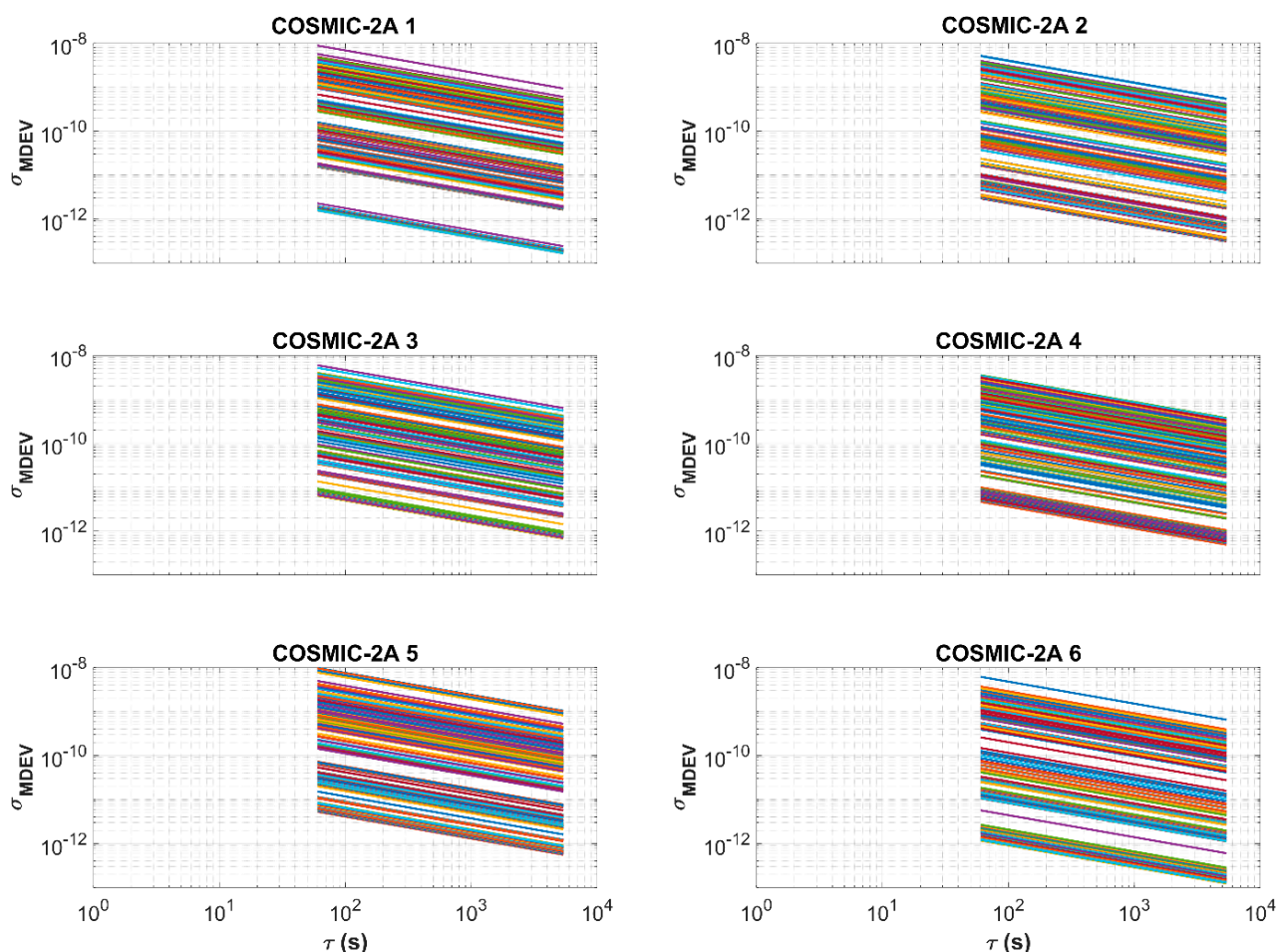
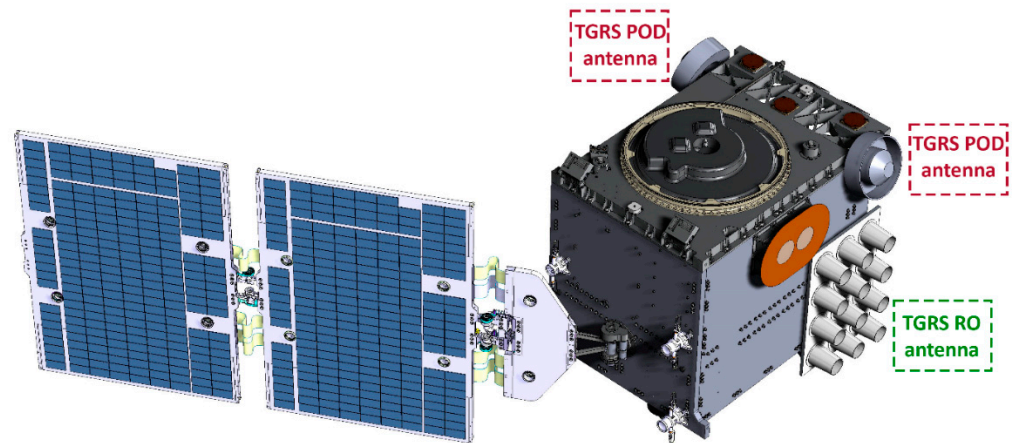


Figure 10. MDEV of the estimated clocks of COSMIC-2 satellites. Different colours are dedicated to the different observation segments of each COSMIC-2 satellite. The duration of the observation segments is varied from 30 min to 2 h, generally around 1.5 h with a sample interval of 10 s.

To compare with the CubeSats, the specifications of the COSMIC-2 satellites and their structure are provided in Table 7 and Figure 11.

Table 7. COSMIC-2 satellite specifications (the ESA Earth Observation Portal (eoPortal)).

| Satellite | COSPAR ID | Altitude (km) | Orbit Type | Mass Size |
|---------------------------|-----------|---------------|--|---|
| FORMOSAT 7A (COSMIC-2A 1) | 2019-036L | ~520–550 | Approximately Circular orbit, 24° Inclination, 97 min period | ~277 kg (launch wet mass) 1.25 × 1 × 1.25 m ³ (stowed spacecraft) |
| FORMOSAT 7B (COSMIC-2A 2) | 2019-036N | | | |
| FORMOSAT 7C (COSMIC-2A 3) | 2019-036E | | | |
| FORMOSAT 7D (COSMIC-2A 4) | 2019-036M | | | |
| FORMOSAT 7E (COSMIC-2A 5) | 2019-036V | | | |
| FORMOSAT 7F (COSMIC-2A 6) | 2019-036Q | | | |

**Figure 11.** COSMIC-2 satellite structure (credit: Surrey Satellite Technology).

As a conclusion for this section, the estimated CubeSats' clocks after applying the proposed corrections represent higher short-term stabilities. However, due to the remaining instabilities, they cannot be directly used for the time-tag interpolation in the high-rate (50 Hz) excess phase observations in Equation (1). There are two solutions to this problem. The practical solution that is used by Spire (Personal Communication) is to eliminate the onboard clock offsets by forming the single difference (SD) between a reference GNSS satellite (R) and the occulting one (O), and estimate the excess phases to within several centimeters as follows:

$$SD_{r,j}^{OR} = \Delta\Phi_{r,j}^O - \Delta\tilde{\Phi}_{r,IF}^R - \rho_r^O + \rho_r^R + c(dt^O - dt^R) = dI_{r,j}^s + dA_r^s \quad (7)$$

where $\Delta\tilde{\Phi}_{r,IF}^R = \Delta\Phi_{r,1}^R - c\Delta\Phi_{r,1}^R - \Delta\Phi_{r,2}^R$ denotes the ionosphere-free phase observations to the reference GNSS satellite to remove the dominant first-order part of the ionosphere delays for the reference satellite link, and to reduce the noise level using the 2-s smoothing window in $\langle \cdot \rangle$ operator [65,66]. The subscripts 1 and 2 indicate 1st and 2nd signal frequencies. The profiles derived from applying this solution is evaluated in the next section. However, the SD solution suffers from the complexity in computation as well as the amplification of the noises of the reference satellite link in the model [48]. These issues are not limited only to the computation of the excess phase but also to the derivation of the following excess Doppler shift needed for the derivation of the RO profiles:

$$\frac{d}{dt}(SD_{r,j}^{OR}) = \frac{d}{dt}(\Delta\Phi_{r,j}^O) - \frac{d}{dt}(\Delta\tilde{\Phi}_{r,IF}^R) - \frac{d}{dt}(\rho_r^O - \rho_r^R - c(dt^O - dt^R)) = \frac{d}{dt}(dI_{r,j}^s) + \frac{d}{dt}(dA_r^s) \quad (8)$$

where the notation $\frac{d}{dt}(\cdot)$ indicates the time derivative.

As an alternative solution, the excess phases can be derived directly using the undifferenced approach if the CubeSats are equipped with better clocks, such as the Cesium Chip-Scale Atomic Clock (C-CSAC) and Rubidium Miniature Atomic Clock (R-MAC).

These clocks are low-power and low-mass atomic clocks that have stabilities (Allan Deviation) at the range of 3.3×10^{-12} for C-CSAC and 9.5×10^{-13} for R-MAC. The C-CSAC has been tested on CHOMPTT (CubeSat Handling of Multisystem Precision Time Transfer) for the optical time transfer and provides the in-orbit short time stability of 75×10^{-12} ($\tau = 1$) and the accuracy of 200 picoseconds [67]. This level of stability is comparable to the ultra-stable oscillators onboard larger LEO satellites (see Figure 10). Equipping the CubeSats with these high-grade atomic clocks, as well as applying proposed corrections in the POD procedure, substantially increases the estimated clock stability that leads to the use of these clocks directly in the excess phase derivation in Equation (1). It can decrease the complexity of the model and provide the excess phase in real-time, which is useful for numerical weather prediction (NWP) forecasting models. In addition to the GNSS-RO application, the stability and accuracy of the above atomic clocks are high enough for the navigation requirements [67], which can be used for building an augmentation service for Positioning, Navigation, and Timing (PNT) purposes from mega-constellations of CubeSats. In this way, the availability of precise GNSS orbits and clocks in space from, e.g., the Australia/New Zealand Satellite Based Augmentation System (AU/NZ SBAS) or Japanese Quasi-Zenith Satellite System (QZSS) for the onboard POD would be a big step forward [46]. However, there are some limitations, such as the onboard processing budget of the CubeSats and developing more efficient POD procedures that are currently under investigation.

The ambiguities in Equation (2) are estimated as float values in the RD-POD procedure, which affects the final accuracy of the RD-POD outputs. The ambiguity resolution methods addressed in [34] can be applied to estimate them as integer values and increase the POD accuracy. However, fixing the ambiguities to the integer values generally increases the mid-to-long-term stability of the clocks, which is not of interest for the GNSS-RO applications. The integer ambiguity resolution of the CubeSats is among our future investigations.

In the following section, the atmospheric profiles derived from the excess phases of these CubeSats after applying the single-difference approach are evaluated by comparing them with those of COSMIC-2 profiles and radiosonde observations.

3. Evaluation of the CubeSats' Derived GNSS-RO Profiles

The RO atmospheric temperature profiles from the COSMIC-2 constellation and the data from the radiosonde observations, provided by the National Centers for Environmental Information (NCEI) through the Integrated Global Radiosonde Archive [68], are used to evaluate the CubeSats RO profiles derived from the SD excess phase in Equation (7). Available occultations from COSMIC-2 satellites and these 17 CubeSats over the testing period (16 Dec 2020 to 15 Jan 2021) are plotted in Figure 12 (top). Note that the number of occultations for the CubeSats is related to only 17 tested CubeSats and not all 145 CubeSats flying in the Spire Global constellation. Despite the Spire occultations being available for all ranges of latitudes (even from the only 17 tested CubeSats in Figure 12 (bottom left)), the COSMIC-2 does not provide the RO products for the high latitude and the polar regions (Figure 12 (bottom right)). This is mainly due to the type of the orbits and their inclinations as provided in Table 7. The second launch of the COSMIC-2 constellation with six satellites (COSMIC-2B) in higher inclined orbits (72°) was supposed to fill this gap; however, it was cancelled due to financial problems in building and launching these large LEO satellites [21]. This confirms the benefits of the affordable CubeSats compared with the expensive larger LEO satellites.

The radiosonde observations of four stations on four different dates are used to compare the temperature profiles. These radiosonde stations are located at Bogra in Bangladesh (BGM41883), Yap in the Caroline Islands (FMM91413), Manzanillo in Mexico (MXM76654), and Tan Son Hoa in Vietnam (VMM48900). Figure 13 compares the temperature profiles of CubeSats, COSMIC-2, and nearby radiosonde observations. Both CubeSats and COSMIC-2 profiles agree with the radiosonde observations to better than 1°C for the vertical heights less than 20 km. Table 8 provides the mean and the standard deviation values for these agreements for different altitudes. The temperature values from both constellations are

close to each other for the heights below 30 km, with the best temperature agreement observed around the UTLS (tropopause) region between 10 and 20 km, i.e., 1.49 and 1.19 °C for CubeSats and COSMIC-2, respectively. The differences for the heights above 30 km are large.

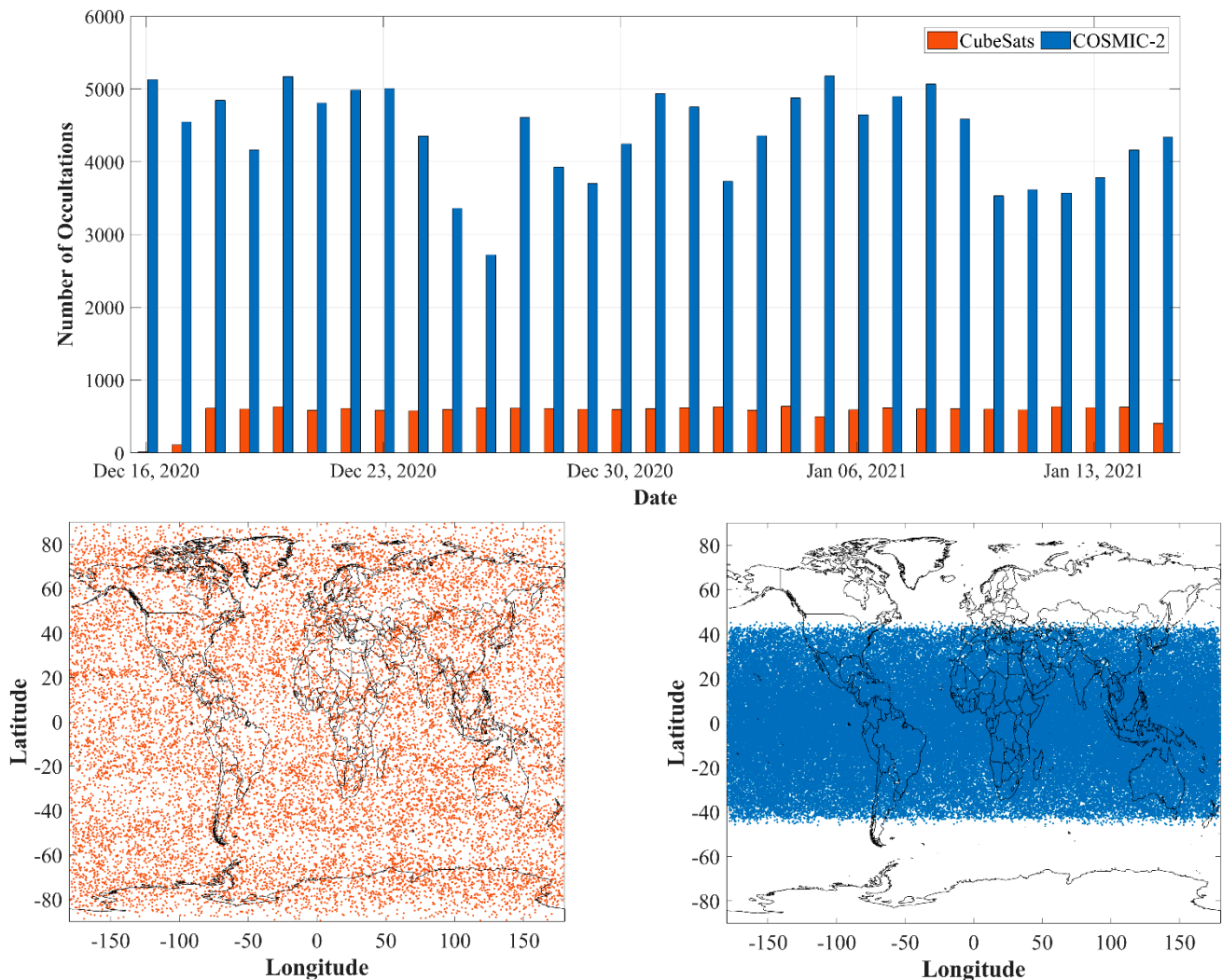


Figure 12. Number of occultations for the COSMIC-2 constellation and 17 CubeSats (**top**), Geographical coverage of the 17 tested CubeSats (**bottom left**), and COSMIC-2 constellation (**bottom right**) over the testing period (16 December 2020–15 January 2021).

Table 8. Mean and standard deviation (STD) of the differences between the CubeSats and COSMIC-2 temperature values and the radiosonde observations for different heights.

| Height (km) | CubeSats | | COSMIC-2 | |
|-------------|-----------|----------|-----------|----------|
| | Mean (°C) | STD (°C) | Mean (°C) | STD (°C) |
| 5–10 | 3.59 | 7.86 | 4.67 | 7.73 |
| 10–20 | 1.49 | 2.12 | 1.19 | 2.10 |
| 20–30 | 5.25 | 2.5 | 4.62 | 2.62 |
| 30–40 | 9.4 | 6.01 | 7.23 | 4.77 |

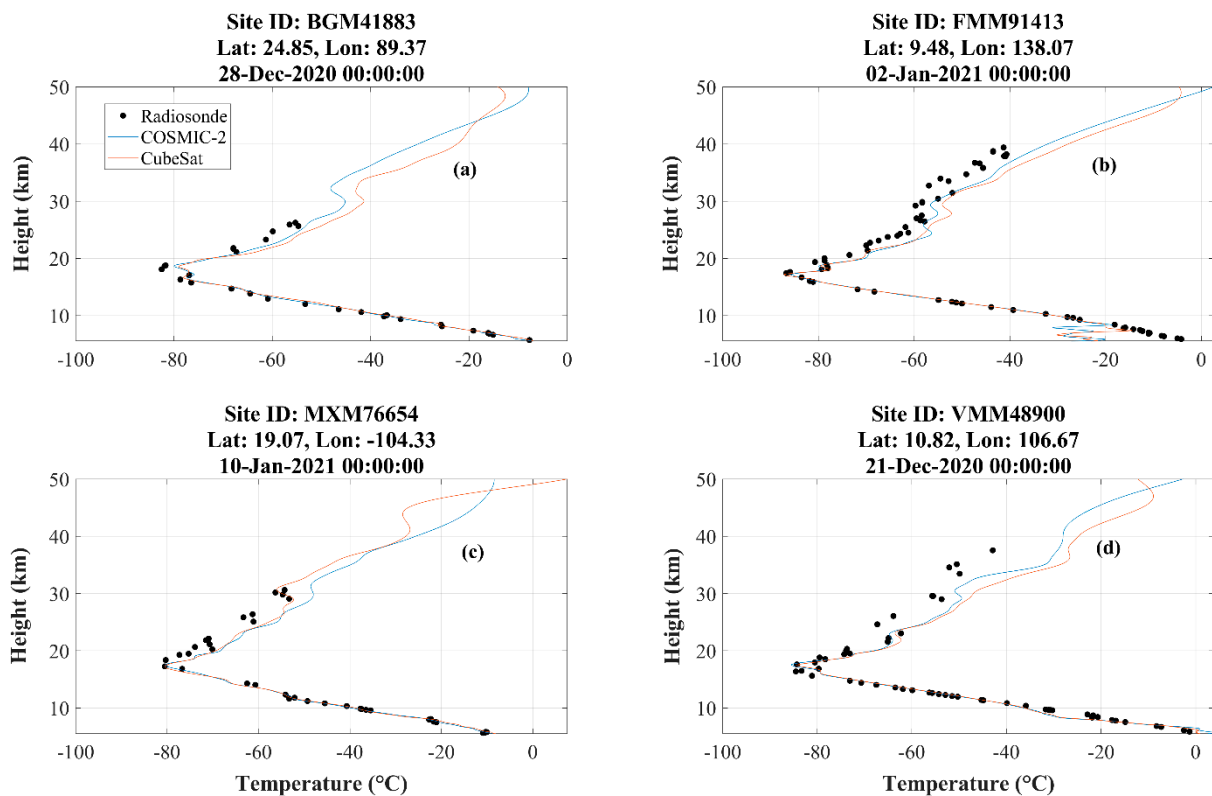


Figure 13. Comparing the CubeSats and COSMIC-2 with radiosonde observations as a reference in terms of temperature and height. The profiles related to each site are provided in subfigures (a–d).

Additional evaluation of CubeSats' derived GNSS-RO is obtained by plotting temperature versus pressure in Figure 14, which further shows the agreement between the CubeSats and the COSMIC-2 products compared to radiosonde observations. The agreements between the temperature values for pressures less than 300 hPa for CubeSats, COSMIC-2, and the radiosonde observations are obvious even with the visual inspection. However, Table 9 provides the means and standard deviations of this agreement. The perfect agreement of less than 0.1 °C for the pressures less than 100 hPa is observed in the CubeSat data, which is even better than 0.68 °C for COSMIC-2. The large biases in the station FFM (Figure 14b) for the pressures higher than 300 hPa cause the large values of mean and the standard deviation of the temperature for that pressure range.

Table 9. Mean and standard deviation (STD) of the differences between CubeSats and COSMIC-2 temperature values and the radiosonde observations for different pressures levels.

| Pressure (hPa) | CubeSats | | COSMIC-2 | |
|----------------|-----------|----------|-----------|----------|
| | Mean (°C) | STD (°C) | Mean (°C) | STD (°C) |
| <100 | 0.12 | 2.77 | 0.68 | 2.81 |
| 100–300 | 0.54 | 1.69 | 0.63 | 1.61 |
| 300> | 21.23 | 20.59 | 20.68 | 18.67 |

The refractivity comparisons between the CubeSats and the COSMIC-2 profiles for four random dates, i.e., 21 and 27 of December 2020 and 1 and 10 January 2021, are plotted in Figure 15. The RMS value for the differences between the refractivity from CubeSats and COSMIC-2 for the heights more than 10 km is 0.11, indicating an agreement between the two profiles. This value reaches 4.7 for heights lower than 10 km.

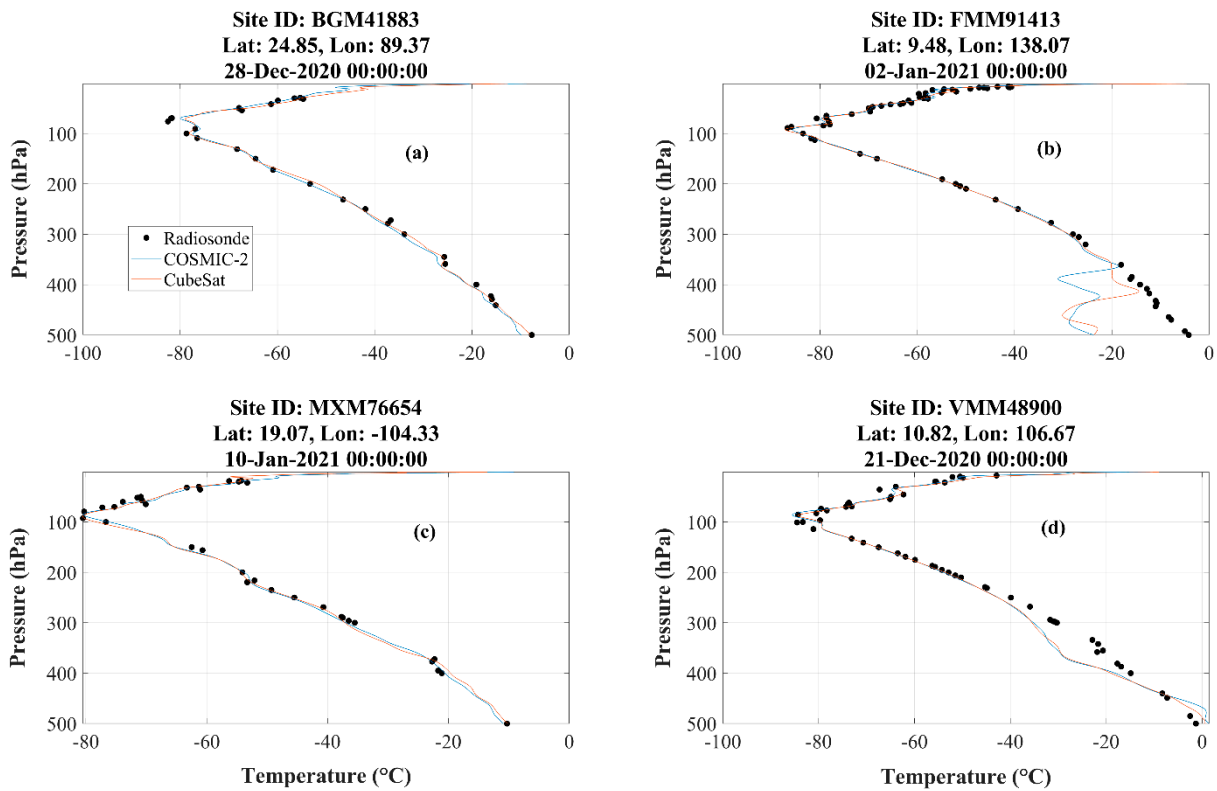


Figure 14. Comparing CubeSats and COSMIC-2 with the radiosonde observations as a reference in terms of the temperature and pressure. The profiles related to each site are provided in subfigures (a–d).

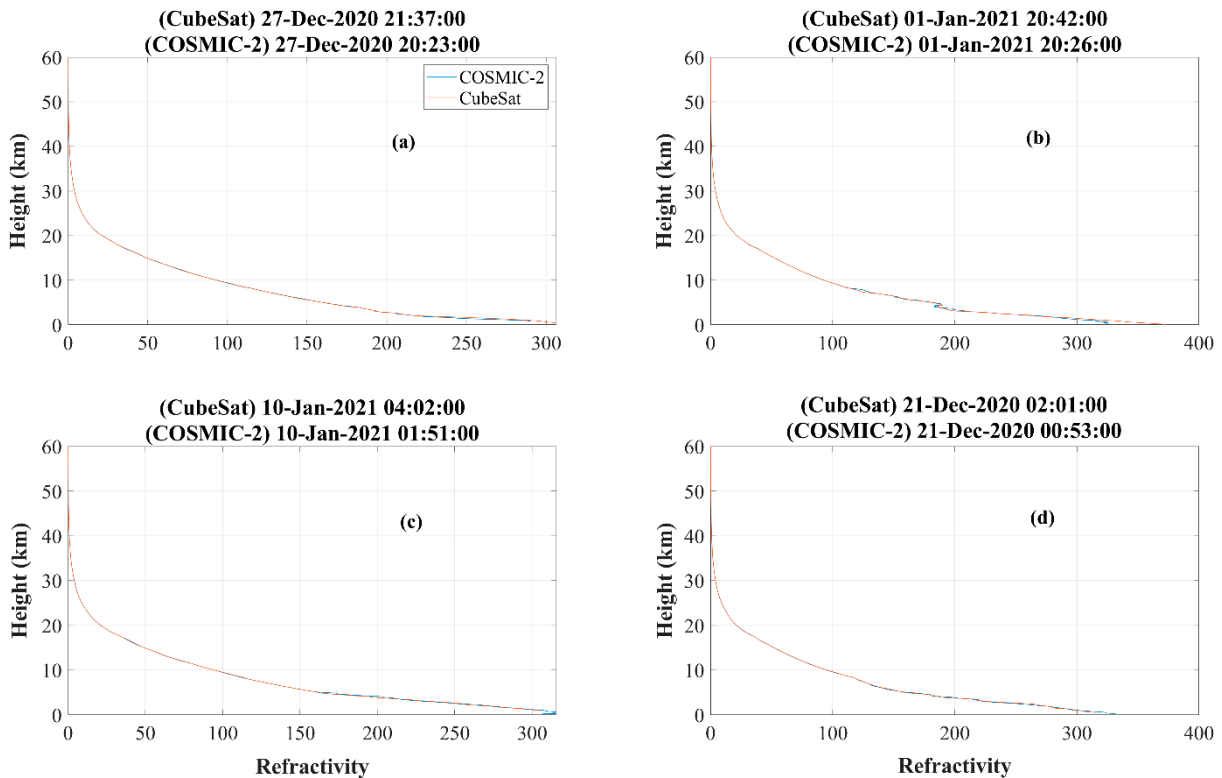


Figure 15. Comparing CubeSats and COSMIC-2 in terms of the refractivity and height. The profiles related to each date are provided in subfigures (a–d).

Finally, the Kling-Gupta Efficiency metric (*KGE*, Equation (9)) that combines the correlation (*C*), bias (β), and the variability (γ) is used to provide an overall performance of CubeSats and COSMIC-2 products against in situ radiosondes [69]:

$$KGE = 1 - \sqrt{(C - 1)^2 + (\beta - 1)^2 + (\gamma - 1)^2} \quad (9)$$

where $\beta = \frac{\mu}{\mu_0}$ is the ratio of the estimated and the observed mean, and $\gamma = \frac{\sigma/\mu}{\sigma_0/\mu_0}$ is the ratio of the estimated and observed variations derived from the means and the standard deviations. The radiosonde observations from 562 globally distributed stations shown in Figure 16 are used to compute the *KGE* values. To estimate the correlation, the observations from 50 stations co-located with the CubeSats and COSMIC-2 profiles are selected. Each pair of linear correlation is calculated between CubeSats, COSMIC-2, and radiosonde observations, and the mean of the correlation coefficient is used in Equation (9). The estimated *KGE* values for the CubeSats and the COSMIC-2 profiles against radiosonde observations are given in Table 10, where the values closer to 1 represent better agreement with the radiosonde observations. From the results in Table 10, it can be seen that CubeSats have close *KGE* values to COSMIC-2, thus indicating a good agreement of both products.

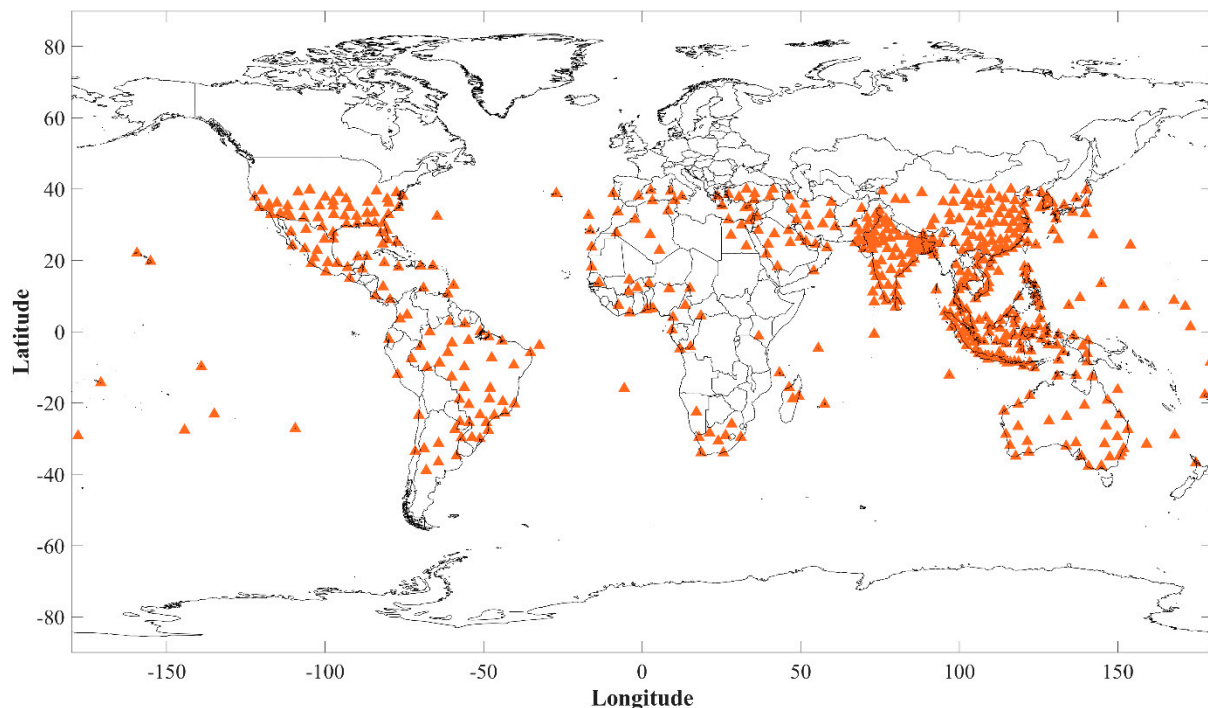


Figure 16. Locations of the radiosonde stations used for the validation using *KGE* metric.

Table 10. *KGE* values for the CubeSats and COSMIC-2 profiles against the radiosonde observations.

| Profile | CubeSats | COSMIC-2 |
|----------------------|----------|----------|
| Height–Temperature | 0.862 | 0.884 |
| Pressure–Temperature | 0.697 | 0.782 |

4. Summary and Conclusions

The stabilities of the CubeSats' clocks that are estimated in the RD-POD procedure are important for high-rate applications such as GNSS-RO. These stabilities are affected by the following factors:

- The ratio of the outliers in the observations derived from pre-processing steps;
- The number of stochastic accelerations that are estimated in the POD procedure;

- The CubeSats' hardware biases due to, e.g., the thermal variations in space;
- The nominal PCV values derived from ground calibration methods that do not consider the inflight situation;
- The higher order of geopotential forces and their effects on relativity;
- The quality of the frequency oscillator;
- The float ambiguities and their impacts on the estimated clocks.

The impacts of these clock instability triggers were assessed for a set of CubeSats that have been launched for GNSS-RO. The stabilities of the CubeSats' clocks are worse than 10^{-5} when the ratio of observation outliers is higher than 50%. This value can even drop to the 10^{-3} level for the high percentage of outliers (>90%). By increasing the number of stochastic accelerations including the estimation of velocity pulses at every 7.5 min and using constant accelerations for 3 min intervals, the short-term stabilities have been refined to the 10^{-8} to 10^{-6} level. To represent the impact of clock hardware biases due to thermal variations on the clock stabilities, a cylindrical shadow model was used to detect the CubeSat's positions in the shadow of the earth, where the temperature drops and the direct sunlight as the dominant heat source is absent. The comparison of the estimated clocks for these regions with the clocks from the orbit in the sunlight revealed the impact of thermal variations on clock stabilities. Better thermal control systems may be required to handle the internal heat transfer between the COTS components of the CubeSats as well as the external heat sources. The new phase center variation (PCV) patterns are derived from the mean values of the observation residuals for different elevation and azimuth angles. Despite the nominal PCV values that are computed from ground calibrations, this pattern represents the actual multipath effect due to the CubeSat's structure. The short-term stability improvements of the clocks after using this pattern varies from 10^{-11} to 10^{-9} for different CubeSats. Applying the J2 correction due to the earth's oblateness in addition to the signal delays resulting from the central gravity and the clock deviations because of the relativity effect improves the CubeSat's clock stability at the 10^{-11} to 10^{-8} level. In the analysis of the CubeSats' clocks, several-millisecond-long jumps were observed, which seems to be due to the quality of the frequency oscillator. Such large jumps are not available for COSMIC-2 satellites that are equipped with ultra-stable oscillators. To show the impacts of all the aforementioned instability triggers, a final RD-POD round for all CubeSats is performed by applying all possible corrections together in the POD procedure. The results show improvements of several microseconds in the estimated clocks compared to the uncorrected clock estimations, thus confirming the improvement in the short-term stabilities after applying the proposed corrections. However, comparing with the COSMIC-2 clocks reveals the dominant role of the quality of the oscillators in the CubeSats' clock instabilities. To deal with this limitation for the GNSS-RO application and derive the excess phase observations, single difference combinations between the reference GNSS satellite and the occulted one are formed. The integer ambiguity resolution in the POD procedure is among future studies and its impacts on the short-term stabilities are not investigated in this study. However, it is expected to be substantially less than the impact of the quality of the frequency oscillator.

The evaluations of the profiles derived from the CubeSats' excess phase observations are in great agreement with those of the COSMIC-2 constellation, as well as the in situ radiosonde observations that provided an external validation source. The temperature profiles largely agree with those of COSMIC-2 at the UTLS (tropopause) region between 10 and 20 km, i.e., a mean of 1.49 ± 2.12 °C (CubeSats) and 1.19 ± 2.10 °C (COSMIC-2). The CubeSats (0.12 ± 2.77 °C) surprisingly outperformed the COSMIC-2 satellites (0.68 ± 2.81 °C) in the temperature-pressure profiles for the pressures less than 100 hPa. The refractivity comparisons between CubeSats and COSMIC-2 satellites show great agreements for heights more than 10 km. The KGE metrics for both CubeSats and COSMIC-2 in comparison with radiosonde observations are very close to each other, indicating CubeSats' capability for atmospheric sounding. This level of quality and the fact that CubeSat constellations can cover the whole earth, including the high-altitude and polar regions, in contrast to

COSMIC-2, show their importance in the future of GNSS-RO, which would be significant to numerical weather prediction models for global weather forecasting.

Although short-term stability and accuracy at the nanosecond level (or even better) can be derived by the availability of the chip-scale and miniature atomic clocks for the CubeSats, there are still some limitations that need more advancements in technology, such as increasing the processing power, as well as, in theory, providing more efficient algorithms for the onboard POD. This will be subject to future studies.

Author Contributions: A.A.-Z., J.A. and A.E.-M. designed the work, A.A.-Z. processed and analysed the CubeSats clocks. T.D. processed the GNSS-RO profiles and A.A.-Z. and J.A. analysed them. A.A.-Z., J.A., A.E.-M. and K.W. contributed to the writing of the paper. All authors have read and agreed to the published version of the manuscript.

Funding: This research is funded by the Australian Research Council under the discovery project: Tracking Formation-Flying of Nanosatellites Using Inter-Satellite Links (DP 190102444), the National Time Service Center, Chinese Academy of Sciences (CAS) (No. E167SC14) and the CAS “Light of West China” Program (No. XAB2018YDYL01).

Institutional Review Board Statement: Not applicable.

Informed Consent Statement: Not applicable.

Data Availability Statement: The CubeSats data and products for the tested period are provided by Spire Global Inc., the COSMIC-2 data and products are available at the UCAR data center <https://www.ucar.edu/> accessed on 1 November 2021, and the CODE final products are from <http://ftp.aiub.unibe.ch/> accessed on 1 November 2021. The data are processed with Bernese GNSS software v 5.2.

Acknowledgments: We would like to thank Spire Global Inc. for providing the CubeSats data for scientific research. Special thanks are given to the Spire’s Earth observations/GNSS team for our discussions on the satellite structure and for providing the required information. The availability of COSMIC-2 data and products by the UCAR COSMIC Program is highly appreciated.

Conflicts of Interest: The authors declare no conflict of interest.

References

1. Feng, S.; Fu, Y.; Xiao, Q. Trends in the global tropopause thickness revealed by radiosondes. *Geophys. Res. Lett.* **2012**, *39*. [[CrossRef](#)]
2. Shangguan, M.; Wang, W.; Jin, S. Variability of temperature and ozone in the upper troposphere and lower stratosphere from multi-satellite observations and reanalysis data. *Atmos. Chem. Phys.* **2019**, *19*, 6659–6679. [[CrossRef](#)]
3. Xian, T.; Homeyer, C.R. Global tropopause altitudes in radiosondes and reanalyses. *Atmos. Chem. Phys.* **2019**, *19*, 5661–5678. [[CrossRef](#)]
4. Ruston, B.; Healy, S. Forecast Impact of FORMOSAT-7/COSMIC-2 GNSS Radio Occultation Measurements. *Atmos. Sci. Lett.* **2021**, *22*, e1019. [[CrossRef](#)]
5. Santer, B.D.; Wehner, M.F.; Wigley, T.M.L.; Sausen, R.; Meehl, G.A.; Taylor, K.E.; Ammann, C.; Arblaster, J.; Washington, W.M.; Boyle, J.S.; et al. Contributions of Anthropogenic and Natural Forcing to Recent Tropopause Height Changes. *Science* **2003**, *301*, 479–483. [[CrossRef](#)] [[PubMed](#)]
6. Santer, B.D.; Sausen, R.; Wigley, T.M.L.; Boyle, J.S.; AchutaRao, K.; Doutriaux, C.; Hansen, J.E.; Meehl, G.A.; Roeckner, E.; Ruedy, R.; et al. Behavior of tropopause height and atmospheric temperature in models, reanalyses, and observations: Decadal changes. *J. Geophys. Res. Atmos.* **2003**, *108*, ACL 1-1–ACL 1-22. [[CrossRef](#)]
7. Awange, J.L. *Environmental Monitoring Using GNSS: Global Navigation Satellite Systems*; Springer Science & Business Media: Amsterdam, The Netherlands, 2012. [[CrossRef](#)]
8. Awange, J. *GNSS Environmental Sensing*; Springer International Publishers: Amsterdam, The Netherlands, 2018; Volume 10, pp. 973–978. [[CrossRef](#)]
9. Awange, J.L.; Grafarend, E.W. GPS meteorology in environmental monitoring. In *Solving Algebraic Computational Problems in Geodesy and Geoinformatics: The Answer to Modern Challenges*; Awange, J.L., Grafarend, E.W., Eds.; Springer: Berlin/Heidelberg, Germany, 2005; pp. 217–244.
10. Elgered, G.; Wickert, J. Monitoring of the neutral atmosphere. In *Springer Handbook of Global Navigation Satellite Systems*; Teunissen, P.J.G., Montenbruck, O., Eds.; Springer International Publishing: Cham, Switzerland, 2017; pp. 1109–1138. [[CrossRef](#)]
11. Awange, J.; Kiema, J. *Environmental Geoinformatics, Extreme Hydro-Climatic and Food Security Challenges: Exploiting the Big Data*, 2nd ed.; Springer: Cham, Switzerland, 2019. [[CrossRef](#)]
12. Awange, J.; Kiema, J. *Environmental Geoinformatics*; Springer: Berlin/Heidelberg, Germany, 2013; pp. 973–978. [[CrossRef](#)]

13. Nascimento, A.A.; Awange, J.L.; Gonçalves, R.M.; Khandu. South America's tropopause variability in relation to global teleconnection (2001–2017): A GNSS-radio occultation assessment. *J. Atmos. Sol. Terr. Phys.* **2020**, *209*, 105379. [[CrossRef](#)]
14. Wickert, J.; Schmidt, T.; Michalak, G.; Heise, S.; Arras, C.; Beyerle, G.; Falck, C.; König, R.; Pingel, D.; Rothacher, M. GPS Radio Occultation with CHAMP, GRACE-A, SAC-C, TerraSAR-X, and FORMOSAT-3/COSMIC: Brief Review of Results from GFZ. In *New Horizons in Occultation Research: Studies in Atmosphere and Climate*; Steiner, A., Pirscher, B., Foelsche, U., Kirchengast, G., Eds.; Springer: Berlin/Heidelberg, Germany, 2009; pp. 3–15.
15. von Engeln, A.; Andres, Y.; Marquardt, C.; Sancho, F. GRAS radio occultation on-board of Metop. *Adv. Space Res.* **2011**, *47*, 336–347. [[CrossRef](#)]
16. Schreiner, W.S.; Weiss, J.P.; Anthes, R.A.; Braun, J.; Chu, V.; Fong, J.; Hunt, D.; Kuo, Y.H.; Meehan, T.; Serafino, W.; et al. COSMIC-2 Radio Occultation Constellation: First Results. *Geophys. Res. Lett.* **2020**, *47*, e2019GL086841. [[CrossRef](#)]
17. Khandu; Awange, J.L.; Wickert, J.; Schmidt, T.; Sharifi, M.A.; Heck, B.; Fleming, K. GNSS remote sensing of the Australian tropopause. *Clim. Chang.* **2011**, *105*, 597–618. [[CrossRef](#)]
18. Yen, N. Status and Aims of the FORMOSAT-7/COSMIC-2 Mission. 2014. Available online: <https://www.ecmwf.int/node/13747> (accessed on 1 November 2021).
19. Sarda, K.; Grant, C.; Eagleson, S.; Kekez, D.D.; Shah, A.; Zee, R.E. Canadian Advanced Nanospace Experiment 2: On-Orbit Experiences with a Three-Kilogram Satellite. In Proceedings of the AIAA/USU Conference on Small Satellites, Logan, UT, USA, 9–11 September 2008. Available online: <https://www.worldcat.org/title/big-business-small-satellites-22nd-annual-aiaausu-conference-on-small-satellites-conference-proceedings-and-presentations-august-11-to-14-2007-logan-utah-usa/oclc/425278726> (accessed on 20 November 2021).
20. eoPortal-a. ARMADILLO (Attitude Related Maneuvers and Debris Instrument in Low (L) Orbit). Available online: <https://directory.eoportal.org/web/eoportal/satellite-missions/a/armadillo> (accessed on 25 August 2021).
21. eoPortal-b. STP-2-FormoSat-7/COSMIC-2. Available online: <https://directory.eoportal.org/web/eoportal/satellite-missions/content/-/article/formosat-7> (accessed on 25 August 2021).
22. Bowler, N.E. An assessment of GNSS radio occultation data produced by Spire. *Q. J. R. Meteorol. Soc.* **2020**, *146*, 3772–3788. [[CrossRef](#)]
23. Montenbruck, O. Space applications. In *Handbook of Global Navigation Satellite Systems*; Teunissen, P.J.G., Montenbruck, O., Eds.; Springer: Cham, Switzerland, 2017; pp. 933–964. [[CrossRef](#)]
24. Allahviridi-Zadeh, A.; El-Mowafy, A. Precise Orbit Determination of CubeSats Using a Proposed Observations Weighting Model. In Proceedings of the Scientific Assembly of the International Association of Geodesy (IAG), China Surveying and Mapping Mansion, Beijing, China, 28 June 2021. [[CrossRef](#)]
25. Wang, K.; El-Mowafy, A. LEO satellite clock analysis and prediction for positioning applications. *Geo. Spat. Inf. Sci.* 2021; in press. [[CrossRef](#)]
26. Tseng, T.-P.; Zhang, K.; Hwang, C.; Hugentobler, U.; Wang, C.-S.; Choy, S.; Li, Y.-S. Assessing antenna field of view and receiver clocks of COSMIC and GRACE satellites: Lessons for COSMIC-2. *GPS Solut.* **2014**, *18*, 219–230. [[CrossRef](#)]
27. Weinbach, U.; Schön, S. Improved GPS receiver clock modeling for kinematic orbit determination of the GRACE satellites. In Proceedings of the 2012 European Frequency and Time Forum, Gothenburg, Sweden, 23–27 April 2012; pp. 157–160. [[CrossRef](#)]
28. Tseng, T.-P.; Shum, C.K.; Yang, T.-Y. Characterizing receiver clock behaviors onboard Low Earth Orbiters: A case study of GRACE satellites. *Geod. Geodyn.* **2019**, *10*, 276–281. [[CrossRef](#)]
29. Poghosyan, A.; Golkar, A. CubeSat evolution: Analyzing CubeSat capabilities for conducting science missions. *Prog. Aerosp. Sci.* **2017**, *88*, 59–83. [[CrossRef](#)]
30. Selva, D.; Krejci, D. A survey and assessment of the capabilities of Cubesats for Earth observation. *Acta Astronaut.* **2012**, *74*, 50–68. [[CrossRef](#)]
31. Warren, Z.; Huang, M.; Kettering, H.; Stapleton, A.; Camparo, J. A versatile testbed for CubeSat atomic clock development: EOM vs Laser Current Modulation. In Proceedings of the 49th Annual Precise Time and Time Interval Systems and Applications Meeting, Reston, VA, USA, 1–29 January 2018; pp. 100–106. [[CrossRef](#)]
32. Rybak, M.M.; Axelrad, P.; Seubert, J.; Ely, T. Estimation of Thermal and Stochastic Variations of Chip Scale Atomic Clocks for Navigation of a Lunar CubeSat. In Proceedings of the 51st Annual Precise Time and Time Interval Systems and Applications Meeting, San Diego, CA, USA, 21–24 January 2020; pp. 221–233. [[CrossRef](#)]
33. Hajj, G.A.; Kursinski, E.R.; Romans, L.J.; Bertiger, W.I.; Leroy, S.S. A technical description of atmospheric sounding by GPS occultation. *J. Atmos. Sol. Terr. Phys.* **2002**, *64*, 451–469. [[CrossRef](#)]
34. Allahviridi-Zadeh, A.; Wang, K.; El-Mowafy, A. Precise Orbit Determination of LEO Satellites Based on Undifferenced GNSS Observations. *J. Surv. Eng.* **2022**, *148*, 03121001. [[CrossRef](#)]
35. Wang, K.; Allahviridi-Zadeh, A.; El-Mowafy, A.; Gross, J.N. A Sensitivity Study of POD Using Dual-Frequency GPS for CubeSats Data Limitation and Resources. *Remote Sens.* **2020**, *12*, 2107. [[CrossRef](#)]
36. Montenbruck, O.; Gill, E. *Satellite Orbits: Models, Methods and Applications*; Springer: Berlin/Heidelberg, Germany, 2000. [[CrossRef](#)]
37. Dach, R.; Lutz, S.; Walser, P.; Fridez, P. *Bernese GNSS Software, version 5.2*; Bern Open Publishing: Bern, Switzerland, 2015.
38. Pavlis, N.; Kenyon, S.; Factor, J.; Holmes, S. Earth gravitational model 2008. In *SEG Technical Program Expanded Abstracts 2008*; SEG Technical Program Expanded Abstracts; Society of Exploration Geophysicists: Tulsa, OK, USA, 2008; pp. 761–763. [[CrossRef](#)]

39. Lyard, F.; Lefevre, F.; Letellier, T.; Francis, O. Modelling the global ocean tides: Modern insights from FES2004. *Ocean Dynam.* **2006**, *56*, 394–415. [[CrossRef](#)]
40. Petit, G.; Luzum, B. IERS Conventions. 2010. Available online: <https://www.iers.org/IERS/EN/Publications/TechnicalNotes/tn36.html> (accessed on 1 November 2021).
41. Standish, E. JPL Planetary and Lunar Ephemerides, DE405/LE405, JPL IOM 312. F-98_048 1998. Available online: https://ipnpr.jpl.nasa.gov/progress_report/42-196/196C.pdf (accessed on 1 November 2021).
42. Allahverdi-Zadeh, A.; Asgari, J.; Amiri-Simkooei, A.R. Investigation of GPS draconitic year effect on GPS time series of eliminated eclipsing GPS satellite data. *J. Geod. Sci.* **2016**, *6*, 93–102. [[CrossRef](#)]
43. Rothacher, M.; Schmid, R. *ANTEX: The Antenna Exchange Format Version 1.4. Format Specification*; IGS Central Bureau: Pasadena, CA, USA, 2010.
44. Bock, H.; Dach, R.; Jäggi, A.; Beutler, G. High-rate GPS clock corrections from CODE: Support of 1 Hz applications. *J. Geod.* **2009**, *83*, 1083. [[CrossRef](#)]
45. Weiss, J.P.; Steigenberger, P.; Springer, T. Orbit and clock product generation. In *Springer Handbook of Global Navigation Satellite Systems*; Teunissen, P.J.G., Montenbruck, O., Eds.; Springer International Publishing: Cham, Switzerland, 2017; pp. 983–1010. [[CrossRef](#)]
46. Allahverdi-Zadeh, A.; Wang, K.; El-Mowafy, A. POD of small LEO satellites based on precise real-time MADOCA and SBAS-aided PPP corrections. *GPS Solut.* **2021**, *25*, 31. [[CrossRef](#)]
47. Griggs, E.; Kursinski, E.R.; Akos, D. Short-term GNSS satellite clock stability. *Radio Sci.* **2015**, *50*, 813–826. [[CrossRef](#)]
48. Tseng, T.-P.; Chen, S.-Y.; Chen, K.-L.; Huang, C.-Y.; Yeh, W.-H. Determination of near real-time GNSS satellite clocks for the FORMOSAT-7/COSMIC-2 satellite mission. *GPS Solut.* **2018**, *22*, 47. [[CrossRef](#)]
49. Riley, W.J. *Handbook of Frequency Stability Analysis*; US Department of Commerce, National Institute of Standards and Technology. 2008. Available online: <https://safe.nrao.edu/wiki/pub/Main/ToddHunter/nist1065.pdf> (accessed on 1 November 2021).
50. Kroes, R. *Precise Relative Positioning of Formation Flying Spacecraft Using GPS*. Optima Grafische Communicatie, PO Box 84115, 3009 BC Rotterdam, The Netherlands. 2006. Available online: <https://www.ncgeo.nl/downloads/61Kroes.pdf> (accessed on 1 November 2021).
51. Wang, L.; Chen, R.; Li, D.; Zhang, G.; Shen, X.; Yu, B.; Wu, C.; Xie, S.; Zhang, P.; Li, M. Initial assessment of the LEO based navigation signal augmentation system from Luojia-1A satellite. *Sensors* **2018**, *18*, 3919. [[CrossRef](#)]
52. Gilmore, D.G.; Donabedian, M. *Spacecraft Thermal Control Handbook: Cryogenics*; AIAA: Reston, VA, USA, 2002; Volume 2.
53. Boushon, K.E. *Thermal Analysis and Control of Small Satellites in Low Earth Orbit*. M.S.A.E.; Missouri University of Science and Technology: Ann Arbor, MI, USA, 2018.
54. Hauschild, A.; Montenbruck, O. Real-time clock estimation for precise orbit determination of LEO-satellites. In Proceedings of the 21st International Technical Meeting of the Satellite Division of The Institute of Navigation (ION GNSS 2008), Savannah, GA, USA, 16–19 September 2008; pp. 581–589.
55. Pirazzi, G.; Mazzoni, A.; Biagi, L.; Crespi, M. Preliminary performance analysis with a GPS+ Galileo enabled chipset embedded in a smartphone. In Proceedings of the 30th International Technical Meeting of the Satellite Division of The Institute of Navigation (ION GNSS+ 2017), Portland, OR, USA, 25–29 September 2017; pp. 101–115. [[CrossRef](#)]
56. Svehla, D. *Geometrical Theory of Satellite Orbits and Gravity Field*; Springer: Berlin/Heidelberg, Germany, 2018. [[CrossRef](#)]
57. Jäggi, A.; Dach, R.; Montenbruck, O.; Hugentobler, U.; Bock, H.; Beutler, G. Phase center modeling for LEO GPS receiver antennas and its impact on precise orbit determination. *J. Geod.* **2009**, *83*, 1145. [[CrossRef](#)]
58. Allahverdi-Zadeh, A. Phase centre variation of the GNSS antenna onboard the CubeSats and its impact on precise orbit determination. In Proceedings of the GSA Earth Sciences Student Symposium, Western Australia (GESS-WA), Perth, Australia, 25 November 2021. [[CrossRef](#)]
59. Ashby, N. Relativity in the Global Positioning System. *Living Rev. Relativ.* **2003**, *6*, 1–42. [[CrossRef](#)] [[PubMed](#)]
60. Hauschild, A. Basic observation equations. In *Springer Handbook of Global Navigation Satellite Systems*; Teunissen, P.J.G., Montenbruck, O., Eds.; Springer International Publishing: Cham, Switzerland, 2017; pp. 561–582. [[CrossRef](#)]
61. UCAR. UCAR COSMIC Program, COSMIC-2 Data Products Near Real-Time Operational Datasets. UCAR/NCAR-COSMIC. 2019. Available online: <https://www.cosmic.ucar.edu/what-we-do/cosmic-2/data/> (accessed on 28 October 2021).
62. Beyerle, G.; Schmidt, T.; Michalak, G.; Heise, S.; Wickert, J.; Reigber, C. GPS radio occultation with GRACE: Atmospheric profiling utilizing the zero difference technique. *Geophys. Res. Lett.* **2005**, *32*. [[CrossRef](#)]
63. Weiss, J.-P. FORMOSAT-7/COSMIC-2 Neutral Atmosphere Initial Operating Capability Data Release. 2020. Available online: https://data.cosmic.ucar.edu/gnss-ro/cosmic2/nrt/F7C2_NA_IOC_Data_Release_Memo.pdf. (accessed on 1 November 2021).
64. Weiss, J.-P.; Hunt, D.; Schreiner, W.; VanHove, T.; Arnold, D.; Jaeggi, A. COSMIC-2 Precise Orbit Determination Results. In Proceedings of the EGU General Assembly Conference Abstracts 2020, Online, 4–8 May 2020.
65. Li, Y.; Hwang, C.; Tseng, T.; Huang, C.; Bock, H. A Near-Real-Time Automatic Orbit Determination System for COSMIC and Its Follow-On Satellite Mission: Analysis of Orbit and Clock Errors on Radio Occultation. *IEEE Trans. Geosci. Remote Sens.* **2014**, *52*, 3192–3203. [[CrossRef](#)]
66. Xia, P.; Ye, S.; Jiang, K.; Chen, D. Estimation and evaluation of COSMIC radio occultation excess phase using undifferenced measurements. *Atmos. Meas. Tech.* **2017**, *10*, 1813–1821. [[CrossRef](#)]

67. Conklin, J.W.; Nydam, S.; Ritz, T.; Barnwell, N.; Serra, P.; Hanson, J.; Nguyen, A.N.; Priscal, C.; Stupl, J.; Jaroux, B. Preliminary results from the chomptt laser time-transfer mission. In Proceedings of the 3rd Annual AIAA/USU Conference on Small Satellites, Logan, UT, USA, 6 August 2019.
68. IGRA. Integrated Global Radiosonde Archive. 2021. Available online: <https://www.ncei.noaa.gov/products/weather-balloon/integrated-global-radiosonde-archive> (accessed on 1 November 2021).
69. Gupta, H.V.; Kling, H.; Yilmaz, K.K.; Martinez, G.F. Decomposition of the mean squared error and NSE performance criteria: Implications for improving hydrological modelling. *J. Hydrol.* **2009**, *377*, 80–91. [[CrossRef](#)]

7 POD of small LEO satellites based on precise real-time MADOCA and SBAS-aided PPP corrections

In addition to the algorithms discussed so far in this thesis, the CubeSats POD also requires real-time precise orbits and clocks of GNSS satellites for (near) real-time applications. This chapter is covered by the following paper, which extends the developed POD algorithms used in the previous chapters to use PPP corrections that are available through space links.

Allahvirdi-Zadeh, A., Wang, K., & El-Mowafy, A. (2021). POD of small LEO satellites based on precise real-time MADOCA and SBAS-aided PPP corrections. *GPS solutions*, 25(2) (pp 1-14). DOI: 10.1007/s10291-020-01078-8



POD of small LEO satellites based on precise real-time MADOCA and SBAS-aided PPP corrections

Amir Allahviridi-Zadeh¹ · Kan Wang¹ · Ahmed El-Mowafy¹

Received: 16 July 2020 / Accepted: 22 December 2020

© The Author(s), under exclusive licence to Springer-Verlag GmbH, DE part of Springer Nature 2021

Abstract

For real-time precise orbit determination (POD) of low earth orbit (LEO) satellites, high-accuracy global navigation satellite system (GNSS) orbit and clock products are necessary in real time. Recently, the Japanese multi-GNSS advanced demonstration of orbit and clock analysis precise point positioning (PPP) service and the new generation of the Australian/New Zealand satellite-based augmentation system (SBAS)-aided PPP service provide free and precise GNSS products that are directly broadcast through the navigation and geostationary earth orbit satellites, respectively. With the high quality of both products shown in this study, a 3D accuracy of centimeters can be achieved in the post-processing mode for the reduced-dynamic orbits of small LEO satellites having a duty cycle down to 40% and at sub-dm to dm level for the kinematic orbits. The results show a promising future for high-accuracy real-time POD onboard LEO satellites benefiting from the precise free-of-charge PPP corrections broadcast by navigation systems or SBAS.

Keywords MADOCA · SBAS · LEO · POD · PPP

Introduction

The precise orbit determination (POD) of the low earth orbiters (LEO) has been investigated for decades. With the help of Global Navigation Satellite System (GNSS) observations collected onboard, high POD accuracy can be achieved using both the reduced-dynamic method (Wu et al. 1991) and the kinematic method (Švehla and Rothacher 2003). The former approach delivers typically higher accuracy, i.e., at centimeters, combining comprehensive dynamic models with the GNSS measurements, while the latter is based on the kinematic precise point positioning (PPP) method based on purely GNSS measurements. In both POD approaches, when using undifferenced observations, precise GNSS satellite clocks and orbits are required, which can be obtained with some latencies, e.g., using the final or rapid products

from the International GNSS Service (IGS) (Johnston et al. 2017). Similar corrections can be obtained from other analysis centers such as the Center for Orbit Determination in Europe (CODE), or in real time, e.g., using the IGS real-time service (RTS) (Hadas and Bosy 2015). The (near)-real-time POD is essential for applications like atmospheric sounding or urgent Interferometric Synthetic Aperture Radar (InSAR). As examples for the near-real-time POD, the Metop-A satellite has achieved cm orbital accuracy by using the Real-Time Clock Estimation system (RETICLE) products from the German Aerospace Center (DLR) with less than 10 s latency and the products from the GNSS Receiver for Atmospheric Sounding (GRAS) Support Network (GSN) with different latencies ranging from 10 to 90 min (Montenbruck et al. 2013). Using the IGS ultra-rapid products, the orbital accuracy of the GRACE and TerraSAR-X satellites has also reached dm level (Montenbruck et al. 2005; Wermuth et al. 2012). In addition to the Internet-linked real-time GNSS products, the precise orbits and clocks can also be obtained directly through the geostationary earth orbit (GEO) link from commercial services (Tegedor et al. 2017). As tested in a simulation study for the onboard LEO POD, a promising 3D accuracy of sub-dm level can be achieved using the Fugro G4 service (Hauschild et al. 2016).

✉ Kan Wang
kan.wang@curtin.edu.au

Amir Allahviridi-Zadeh
Amir.Allahviridizadeh@curtin.edu.au

Ahmed El-Mowafy
A.El-Mowafy@curtin.edu.au

¹ School of Earth and Planetary Sciences, Curtin University, Perth, Australia

In recent years, in addition to the commercial services mentioned above, high-precision real-time multi-constellation GNSS orbits and clocks are broadcast free-of-charge directly from navigation satellites or GEO satellite of the Satellite-Based Augmentation System (SBAS). Examples are the Multi-GNSS Advanced Demonstration of Orbit and Clock Analysis (MADOCA) precise point positioning (PPP) service of the Japanese Quasi-Zenith Satellite System (QZSS) and the new generation of the Australian/New Zealand (AU/NZ) SBAS-aided PPP service. The MADOCA service, operated by the Japan Aerospace Research and Development Agency (JAXA), provides the precise orbit and clock corrections for GPS, GLONASS, and QZSS, through an Internet link and from the QZSS satellites via the L6E signal (GPAS 2017). Using MADOCA precise corrections, the 3D accuracy of the PPP results is shown to be at a dm level after convergence for ground receivers (Zhang et al. 2019). For SBAS-aided PPP service, precise corrections are broadcast by the GEO satellite Inmarsat-4F1 within the new generation of AU/NZ SBAS test bed. This provides PPP service via L1 (for GPS L1/L5 signals) and L5 (for GPS L1/L5 and Galileo E1/E5a signals) (Barrios et al. 2018). Note that the initial phase of SBAS-aided PPP service has supported the GPS L1/L2 signals instead of those on L1/L5 to enable a good measurement geometry and simulate the conditions when more satellites broadcast L5 signals are available. For SBAS-aided L5 PPP service, e.g., tests have also demonstrated a dm-level 3D accuracy for static stations in the open-sky situations (Sobreira et al. 2018) and at decimeters for road transport in suburban environments (El-Mowafy et al. 2020). Although both products (MADOCA and SBAS) have currently regional service over the Asia–Pacific region, in this research, we investigate their potential benefits to the LEO POD, expecting that similar services can be provided by more regional/global navigation satellite systems or SBASs in the future, and global coverage can be reached.

For the first time in this study, POD results are assessed using MADOCA L6E PPP corrections and SBAS-aided L5 PPP corrections that are received through free satellite links. Making use of the real data of two typical LEO satellites from GRACE Follow-On (Flechtner et al. 2014) and Sentinel-3 mission (ESA 2012), the POD is performed in both the reduced-dynamic and the kinematic modes, and applying precise GNSS orbits and clocks of these two services. The results are compared with those achieved using IGS final products and other Internet-linked real-time services, e.g., IGS RTS products, IGS ultra-rapid products, and National Centre for Space Studies (CNES) products (Laurichesse et al. 2013). For the reduced-dynamic mode, the accuracy of LEO satellite velocities using different products, computed from the difference between them, and the velocities provided in the reference products are also analyzed, including analysis for small satellites that may not be able to track the

GNSS signals continuously due to their power constraints, such as CubeSats (Wang et al. 2020). The duty cycle, i.e., collecting data within a pre-defined percentage of time due to the power constraints of small satellites that necessities rotating access to power among different sensors, is tested down to 40%, and corresponding influences on the orbital accuracy are assessed.

We first assess the precise orbits and clocks of MADOCA L6E PPP service and SBAS-aided L5 PPP service by comparing them with IGS/CODE final products as reference. The LEO POD processing strategy is then briefly explained for both the kinematic and dynamic modes, followed by a comprehensive analysis of the POD results using different products, for the reduced-dynamic and the kinematic modes and applying different duty cycles. The study is concluded with an outlook for the near future.

Analysis of the precise orbits and clocks used for POD

In different analysis centers, data collected from a network of continuously operating reference stations (CORS) are processed using different observation models to estimate parameters such as station coordinates and clocks, tropospheric delays, satellite orbits and clocks, ambiguities, and inter-system biases (Weiss et al. 2017). For the products considered in our study, MADOCA L6E PPP products are computed based on multi-GNSS observations of a global network (JAXA 2020), uploaded to the QZSS satellites, and broadcast through L6E signal to users. The network used to estimate the precise orbits and clocks for AU/NZ SBAS consists of stations from the Australian regional GNSS network, the south pacific GNSS network, the Land Information New Zealand (LINZ) PositionZ network, and the IGS network. GNSS satellite orbit and clock corrections are estimated at Uralla station in New South Wales, Australia, and transferred to the Inmarsat-4F1 GEO satellite through the uplink system (Barrios et al. 2018).

In the following subsections, the accuracy of orbit and clock products of MADOCA L6E PPP service and SBAS-aided L5 PPP service is analyzed and compared with IGS/CODE final products (IGS final 2020), considered as a reference, since IGS final products are known to be among the most accurate available products.

Orbit comparison

The IGS orbits are weighted sums of the reduced-dynamic orbits estimated by different IGS analysis centers and contain the center of mass (CoM) positions of GNSS satellites in the earth-centered earth-fixed (ECEF) frame, i.e., the IGS14 during our test period in August 2018. The MADOCA orbits

also refer to the CoM. However, the orbits of SBAS-aided PPP service are computed with respect to the antenna phase center (APC). To have a consistent comparison, the SBAS orbits are corrected in the inertial system with the offset between the APC and the CoM as follows:

$$r_I^{CoM} = r_I - x_{SRF}e_x - y_{SRF}e_y - z_{SRF}e_z \tag{1}$$

where r_I^{CoM} and r_I denote the orbital position vectors in the inertial system referred to the CoM and the APC, respectively. The vector $(x_{SRF}, y_{SRF}, z_{SRF})^T$ is the vector from the CoM to the APC expressed in the satellite reference frame (SRF), which is transformed into the inertial system using the unit vectors e_x, e_y and e_z with (Subirana et al. 2013):

$$e_z = -\frac{r_I}{\|r_I\|}, e_y = e_z \times e_s, e_x = e_y \times e_z \tag{2}$$

$$e_s = \frac{r_{sun} - r_I^{CoM}}{\|r_{sun} - r_I^{CoM}\|} \approx \frac{r_{sun}}{\|r_{sun}\|} \tag{3}$$

where r_{sun} is the position of the sun in the inertial frame derived from Jet Propulsion Laboratory Development Ephemeris (JPL DE405) (Montenbruck and Gill 2000) and $\|\cdot\|$ denotes the norm of the vector. The correction is performed with the help of the Bernese GNSS Software version 5.2 (Dach et al. 2015) having the approximation given in (3).

The corrected orbits of the MADOCA L6E PPP service and SBAS-aided L5 PPP services, after transforming the latter to the CoM, are compared with IGS orbits for seven days from August 14–20, 2018, as a suitable representative period. The sampling interval of the orbit comparison is 30 s. The root mean square error (RMSE) for all available

GPS satellites is shown in Fig. 1 in the radial, along-track, and cross-track directions. Figure 1 shows that the RMSE values are mostly at a few cm, and the orbital accuracy in the radial direction is better than in the other two directions, mostly below 5 cm for both products. Also, it is visible that MADOCA orbits generally have a 3D RMSE below or around 5 cm. This orbital accuracy of MADOCA products is consistent with those reported in (Zhang et al. 2019). The jump of the red dots on the first test day is caused by abnormal behaviors of satellite G26 orbits in MADOCA products. Large clock jumps are also visible for the same satellite on the same day, which will be shown later.

The average orbital RMSE is given in Table 1 over the seven test days. It can be observed that MADOCA L6E and SBAS-aided L5 PPP services have worse orbital accuracy in the along-track direction, i.e., in the direction of the satellite movement than in the other two directions. MADOCA products have shown good orbital consistency with IGS final orbits, i.e., with a 3D RMSE below 4 cm on average.

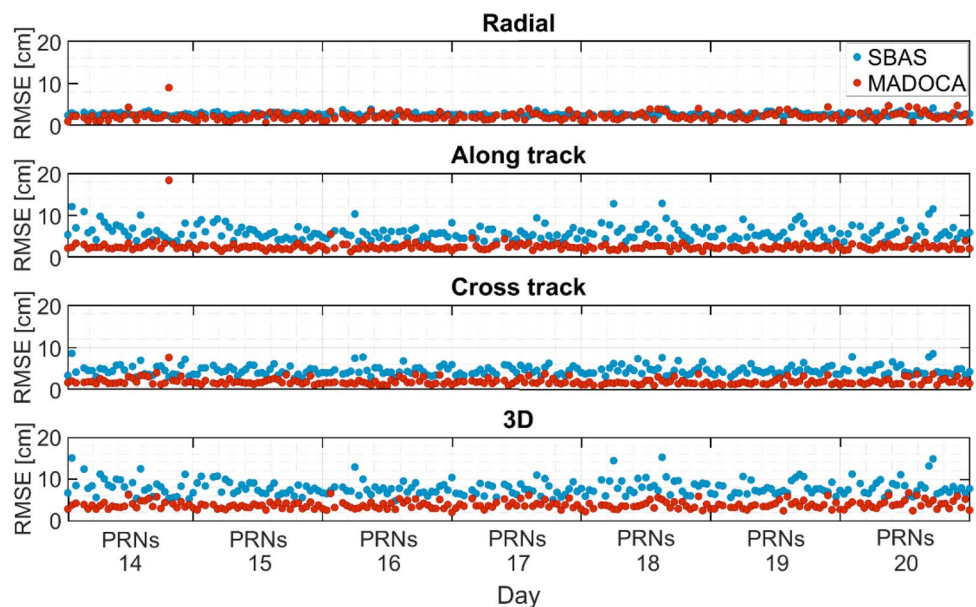
Clock comparison

To remove the impact of different time references and enable the clock comparison, we first difference the satellite clocks

Table 1 Average orbital RMSE of MADOCA L6E and SBAS-aided L5 PPP services from August 14–20, 2018

| Product | Radial (cm) | Along-track (cm) | Cross-track (cm) | 3D (cm) |
|-------------------|-------------|------------------|------------------|---------|
| MADOCA L6E PPP | 2.1 | 2.5 | 1.8 | 3.8 |
| SBAS-aided L5 PPP | 2.5 | 5.9 | 4.5 | 7.9 |

Fig. 1 RMSE of the orbits in MADOCA L6E PPP service (red) and SBAS-aided L5 PPP service (blue) with respect to IGS final orbits in the radial (top), along-track (2nd row), cross-track (3rd row) directions, and the 3D RMS (bottom) for August 14–20, 2018. The area of each day is divided into 31 sections, representing 31 PRNs. Each dot represents the result of one GPS satellite on the corresponding day



of MADOCA L6E and SBAS-aided L5 PPP products with IGS final clocks and then subtract the mean clock differences for all available satellites (Yao et al. 2017). The residual Δdr_i^s is expressed as follows:

$$\Delta dr_i^s = dr_{i,IGS}^s - dr_{i,X}^s - \sum_{n=1}^{n_s} \frac{dr_{i,IGS}^n - dr_{i,X}^n}{n_s} \quad (4)$$

where $dr_{i,IGS}^s$ and $dr_{i,X}^s$ denote the clock offsets for satellite s at epoch i from IGS final products and MADOCA or SBAS-aided PPP products (denoted as X), respectively. The number of satellites at epoch i is indicated by n_s . As the constant biases in Δdr_i^s do not significantly influence ambiguity float processing results, the daily standard deviations (STDs) of Δdr_i^s in ns, shown in Fig. 2 for each satellite and each test day, are used for the assessment. The sampling

interval of the clock comparison is 30 s. Figure 2 shows that STD values for MADOCA clocks (red) are generally less than 0.15 ns, and the STDs of SBAS-aided L5 PPP service (blue) are also mostly within 0.2 ns. The 7-day average STD amount to about 0.08 and 0.16 ns, respectively, for MADOCA L6E and SBAS-aided L5 PPP services. Similar to the orbital products, a jump in the red dot on the first day is visible for the G26 clocks.

The short-term stability of the GNSS clocks is essential for high-rate applications such as real-time PPP and radio occultation (Hauschild et al. 2013). To analyze stability of MADOCA and SBAS-aided PPP clocks, we compute their modified Allan deviation (MDEV) (Griggs et al. 2015) and compare with that of CODE final clocks. The results are illustrated in Fig. 3 and Table 2. Note that the outlier G26 on August 14, 2020 (see Fig. 2) was not used for the

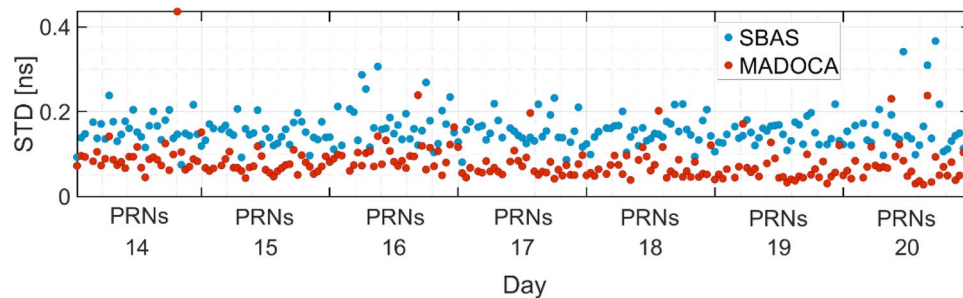


Fig. 2 Standard deviations of the satellite clock residuals from MADOCA L6E PPP service (red) and SBAS-aided L5 PPP service (blue) from August 14–20, 2018. The clocks are compared with IGS

final satellite clocks. The area of each day is divided into 31 sections, representing 31 PRNs. Each dot represents the result of one GPS satellite on the corresponding day

Fig. 3 Modified Allan deviation (σ_{MDEV}) of all GPS clocks from CODE final products (top), MADOCA L6E PPP service (middle), and SBAS-aided L5 PPP service (bottom) from August 14–20, 2018

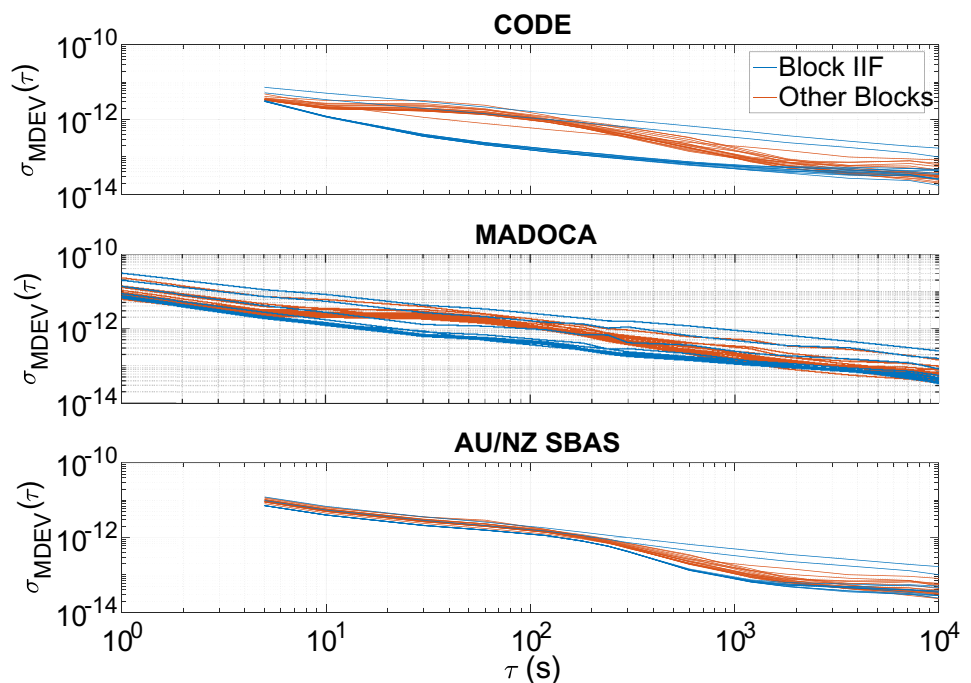


Table 2 Mean MDEV of the CODE, MADOCA, and SBAS-aided PPP (L5) clocks for all Block IIF satellites with different averaging times

| | Averaging time (s) | Mean MDEV ($\times 10^{-12}$) | | | | |
|--------|--------------------|---------------------------------|------|------|------|------|
| | | 5 | 10 | 30 | 60 | 120 |
| CODE | 3.67 | 1.71 | 0.73 | 0.48 | 0.33 | 0.27 |
| MADOCA | 3.41 | 2.38 | 1.20 | 0.95 | 0.69 | 0.54 |
| SBAS | 7.88 | 4.41 | 2.32 | 1.72 | 1.22 | 0.89 |

Clocks from August 14–20, 2018, were used in the calculations

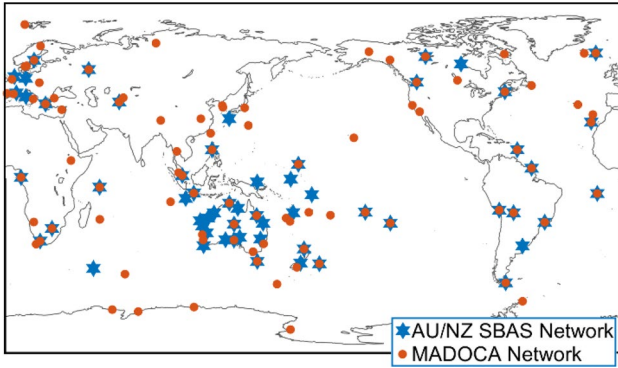


Fig. 4 Network distribution of MADOCA (red) and AU/NZ SBAS services (blue)

calculations. For GPS Block IIF satellites equipped with high-quality rubidium clocks, it can be observed that the short-term stabilities of MADOCA and SBAS-aided PPP clocks are slightly worse than CODE final clocks. However, for MADOCA clocks, a MDEV of about 3×10^{-12} , 1×10^{-12} and 5×10^{-13} can still be reached at an averaging time of 5 s, 30 s, and 180 s, respectively.

The quality difference between MADOCA L6E and SBAS-aided L5 products can be attributed to from the following:

- The network density and distribution used for the two products are different. As shown in Fig. 4, MADOCA uses a network of about 90 stations (JAXA 2020), while the network used in the AU/NZ SBAS contains about 60 stations (Barrios et al. 2018). A better global distribution of the network can be observed for MADOCA.
- The constellations used in network processing are different. MADOCA uses observations of GPS, GLONASS, Galileo, BDS, and QZSS (JAXA 2020), while SBAS-aided L5 products are generated using GPS and Galileo signals (personal communication).
- The models used in the network processing are different. For example, MADOCA uses the empirical DBY solar radiation pressure (SRP) model and updates 12 coefficients regularly (Takasu et al. 2015), while AU/NZ SBAS estimates 5 empirical SRP coefficients in the real-time filter (Tobías et al. 2014).

- The update interval of the real-time filter is 1 s for MADOCA, while for AU/NZ SBAS it amounts to 2 s (personal communication).
- The SBAS-aided PPP corrections are codified to the AU/NZ SBAS GEO link’s spare bits, which has a limited bandwidth. Compared to using SBAS-aided PPP corrections in the radio technical commission for maritime services (RTCM) format, obvious degradations were reported in PPP results (Rubinov et al. 2019). A different GEO message format is considered to be defined to eliminate this constraint (personal communication).

Processing strategy

In this study, using Bernese GNSS Software version 5.2 (Dach et al. 2015), the orbits of LEO satellites are post-processed based on the batch least-squares estimation in both the reduced-dynamic and the kinematic modes. The reduced-dynamic orbit determination is based on solving the following satellite equation of motion as a second-order differential equation by using numerical integration methods:

$$a = -GM \frac{r}{\|r\|^3} + a_p \tag{5}$$

where a is the total acceleration vector, GM is the gravitational constant, and r indicates the satellite position vector. The term a_p represents the acceleration vector caused by all other perturbations, which is a function of the satellite positions, velocities, time, and the estimable dynamic parameters, including the constant and periodic dynamic parameters and stochastic velocity changes or constant accelerations in short time intervals (Beutler et al. 2003; Dach et al. 2015). A summary of this procedure is depicted in Fig. 5 with the processing details given in Table 3. The POD procedure starts by generating the code-based kinematic positions, which are later combined with the dynamic models to produce an initial coarse orbit. Using GNSS phase observations, this initial orbit is improved during an iterative scheme along with the phase-screening step. In addition to the receiver clock offset and ambiguity terms under the ionosphere-free (IF) combination, 6 Keplerian elements at the initial state are estimated together with additional dynamic parameters to compensate

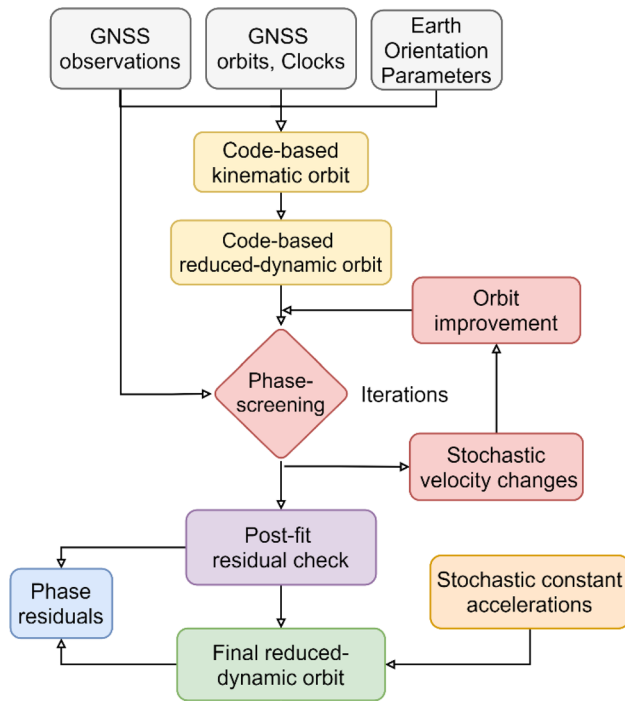


Fig. 5 Flowchart of the reduced-dynamic POD

for model deficiencies of the existing dynamic models used in the processing. This includes 3 constant and 6 periodic dynamic parameters, and stochastic velocity changes within pre-defined intervals, e.g., every 15 min in this study. These estimable parameters are obtained with the least-squares adjustment using GPS observations, and the design matrix is constructed with the help of the partial derivatives of the orbital positions with respect to Kepler elements at the initial condition, the constant/periodic dynamic parameters and stochastic parameters based on the following variational equations (Montenbruck and Gill 2000):

$$\frac{d}{dt}(\tilde{\Phi}, \tilde{S}) = \begin{pmatrix} 0_{3 \times 3} & I_{3 \times 3} \\ \partial_{r,a} & \partial_{v,a} \end{pmatrix}_{6 \times 6} (\tilde{\Phi}, \tilde{S}) + \begin{pmatrix} 0_{3 \times 6} & 0_{3 \times n_p} \\ 0_{3 \times 6} & \partial_p a \end{pmatrix}_{6 \times (6+n_p)} \quad (6)$$

where $\tilde{\Phi} = \partial_{r_0, v_0} (r_t^T, v_t^T)^T$ contains partial derivatives of the LEO position and velocity at time t with respect to the initial state vector and $\tilde{S} = \partial_p (r_t^T, v_t^T)^T$ comprises the corresponding partial derivatives with respect to the dynamic parameters p . The number of the dynamic parameters is denoted by n_p . Note that the partial derivatives with respect to the stochastic parameters can be obtained by forming linear combinations of those with respect to the osculating elements (Dach et al. 2015). With Keplerian elements at the initial condition and all dynamic parameters estimated, a phase-based reduced-dynamic orbit is produced with the numerical integration of (5). In the end, the reduced-dynamic orbit is further improved by estimating stochastic accelerations within shorter time intervals, e.g., every 6 min.

The kinematic orbits are also estimated based on the dual-frequency GNSS observations using PPP method in addition to the reduced-dynamic orbits. The receiver clock offset and 3D orbital positions are estimated at each epoch independently together with the IF ambiguity terms. In this study, the reduced-dynamic and the kinematic LEO orbits are computed and compared using different real-time products from MADOCA L6E service, SBAS-aided L5 PPP service, and several other Internet-provided real-time services. Details are given in the next section.

Test results

This section presents the final orbits of two satellites from typical LEO missions, i.e., Sentinel-3B satellite from the Sentinel-3 mission and satellite GRACE-FO 1 from the GRACE Follow-On mission are evaluated as representative examples of LEO satellites for seven days from August 14–20, 2018. Using the precise satellite clocks and orbits

Table 3 LEO POD processing models and parameters

| Item | Description |
|---|---|
| Gravity field | EGM 2008 (120 × 120) (Pavlis et al. 2008) |
| Solid earth/ocean tide | IERS 2010 (Petit and Luzum 2010)/ FES2004 (50 × 50) (Lyard et al. 2006) |
| Sun, moon, and other planet ephemerides | DE405 (Standish 1998) |
| Relativity | IERS 2010 |
| Observation sampling interval | 30 s |
| Observation combination | GPS dual-frequency IF combination |
| Code and phase standard deviations | 0.1 m, 1 mm (Zenith, L1) |
| Elevation cutoff angle | 5 degrees |

EGM is the acronym of the earth gravity model, and IERS stands for the International Earth Rotation and Reference Systems Service

delivered by MADOCA PPP L6E service and SBAS-aided L5 PPP service, the LEO orbits are computed in both the reduced-dynamic and the kinematic modes. They are compared with the reference orbits provided by the European Space Agency (ESA) for Sentinel-3B (Fernández 2019) and the JPL for GRACE-FO 1 (Wen et al. 2019).

For comparison, in addition to GPS products from SBAS-aided L5 PPP service and MADOCA PPP L6E service, other precise real-time orbit and clock products were also used for generating the POD solutions. This includes the products from CNES (Laurichesse et al. 2013), the ultra-rapid products from IGS (IGS ultra-rapid 2020), and the products from IGS RTS (IGS RTS 2020). These, however, need ground uplink to LEO satellites, unlike MADOCA and SBAS-aided PPP products, which can be received from higher satellites, thus facilitating real-time onboard computation. Furthermore, IGS final products, which have a latency of 12 to 18 days, were also utilized for the LEO orbit processing for comparison. Table 4 summarizes the information of different GPS products used to process daily arcs (i.e., processing period). Note that 18 h observed part and 6 h predicted part of IGS ultra-rapid products were used for processing the daily arcs. As an example, for arcs ending at 24:00 in GPS time (GPST), the last available ultra-rapid products are provided at 21:00, which contain 18 h observed part (from 00:00 to 18:00) and 6 h predicted part (from 18:00 to 24:00). It can be used in such a case.

To deal with the power constraints of small satellites (Lantto and Gross 2018), e.g., CubeSats, for the reduced-dynamic orbits, duty cycling, i.e., collecting data in a pre-defined portion of time, is enabled for the testing with the duty cycle varying from 100 to 40%. This implies possible intermittent tracking of GPS signals, and in our tests, for a duty cycle of $D\%$, only the first $D\%$ of the data in each hour

are used for the processing. The ambiguities are newly set up after each power-off period.

In the next two subsections, the orbital positions using different GPS products are assessed in radial, along-track, and cross-track directions with respect to the corresponding reference orbits (from ESA and JPL), as mentioned before.

Reduced-dynamic orbits

Using MADOCA L6E PPP products and SBAS-aided L5 PPP products, the orbital errors of GRACE-FO-1 are illustrated in Fig. 6 in the radial, along-track, and cross-track directions for the day August 15, 2018, as a representative example. The duty cycle varies from 100 to 40%. Figure 6 shows that the orbital differences generally range from sub-dm to dm level. The errors in the along-track direction are shown to be larger than in the other two directions. The average RMSE in the three directions are given for both test satellites and the seven test days in Table 5. Note that the average RMSE is computed based on the daily RMSE, which used the POD results from the beginning of the first power-on period to the end of the last power-on period in each day. The radial RMSE values are in the range of 1–3 cm even for a duty cycle of 40% and below 2 cm when using MADOCA products. For example, the latter case fulfills the requirement of 1–2 cm radial accuracy for the altimetry missions (Montenbruck 2017). Making use of both products, 3D RMSE at several centimeters can be achieved for post-processed reduced-dynamic orbits even at a duty cycle of 40%, which satisfies the requirement of the near-real-time POD with sub-dm accuracy that is suitable, for example, for InSAR missions (Montenbruck 2017).

Using the IGS final and other real-time products as listed in Table 4, the average 3D RMSE over the seven days of testing is illustrated in Fig. 7 applying different duty cycles. It can be observed that the 3D RMSE generally increases with the decreasing of duty cycles. The line segment in each bar indicates the range of the daily RMSE over the test period, and large ranges are mostly observed at the low duty cycle of 40% (red bars), which indicates a relatively large variation of the accuracy from day to day. The results using SBAS-aided L5 PPP products are slightly worse than those computed using CNES real-time products and IGS RTS products, but better than those using IGS ultra-rapid products. The orbital results generated using MADOCA L6E PPP products have shown to be the best with the smallest RMSE among all tested real-time products.

With a duty cycle of 100%, using the 3D orbital errors for the test period from August 14–20, 2018, the maximum errors within a certain percentage of all 3D orbital errors are illustrated in Fig. 8. Figure 8 shows that for both test satellites, 95% of the 3D orbital errors are within or around 1 dm using MADOCA L6E PPP products (black) and SBAS-aided

Table 4 Details of different GPS products used for the processing

| Products | Indicator | Transfer | Sampling interval (s) | | Source |
|-------------------|-----------|---------------|-----------------------|--------|--------|
| | | | Orbits | Clocks | |
| MADOCA L6E PPP | MDC | Internet/QZSS | 30 | 30 | JAXA |
| SBAS-aided L5 PPP | SBS | Internet/GEO | 5 | 5 | GMV |
| IGS final | IGS | Internet | 900 | 30 | IGS |
| CNES real time | CNE | Internet | 300 | 5 | CNES |
| IGS RTS | IGC | Internet | 30 | 30 | IGS |
| IGS ultra-rapid | IGP | Internet | 900 | 900 | IGS |

Note that the sampling intervals of different real-time products are given based on the real-time orbit and clock files provided by the servers of the corresponding analysis centers and for SBAS-aided L5 PPP service, provided by the GMV team

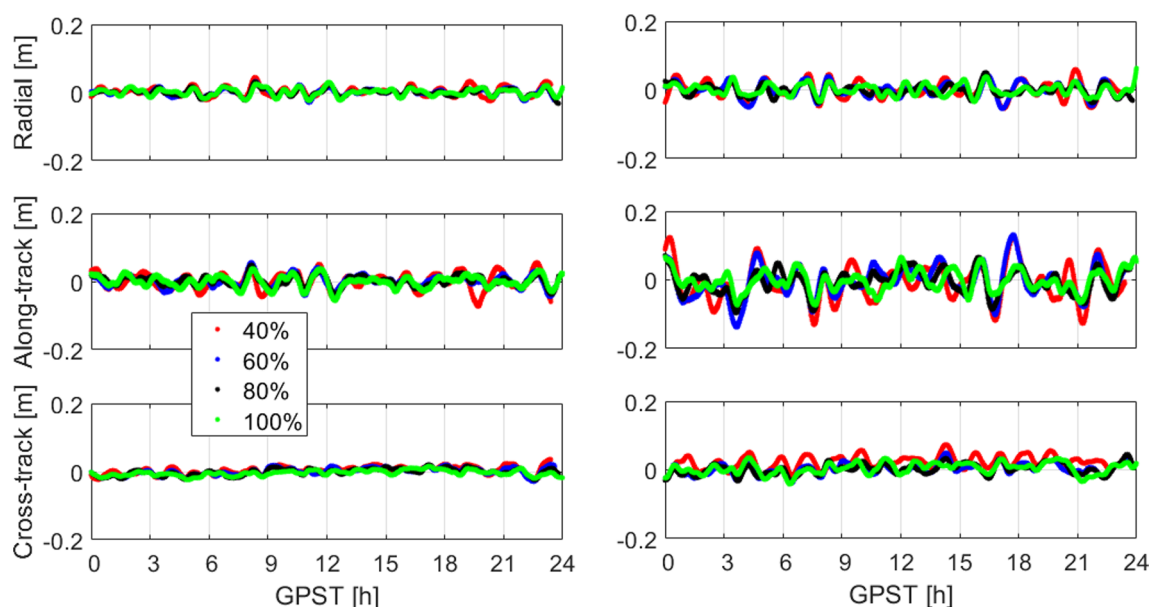


Fig. 6 Orbital differences between the reduced-dynamic orbits and the reference orbits applying (left) MADOCA L6E PPP products and (right) SBAS-aided L5 PPP products. The data of GRACE-FO 1 on August 15, 2018, were used for the plot

Table 5 Average RMSE of the reduced-dynamic orbits from August 14–20, 2018, using MADOCA L6E PPP products and SBAS-aided L5 PPP products

| Duty cycle | Radial (m) | Along-track (m) | Cross-track (m) | 3D (m) |
|----------------------------|-------------|-----------------|-----------------|-------------|
| MADOCA L6E PPP products | | | | |
| 100% | 0.011/0.016 | 0.018/0.027 | 0.009/0.020 | 0.023/0.037 |
| 80% | 0.009/0.015 | 0.016/0.026 | 0.010/0.021 | 0.021/0.036 |
| 60% | 0.010/0.016 | 0.019/0.029 | 0.012/0.024 | 0.025/0.041 |
| 40% | 0.011/0.019 | 0.023/0.037 | 0.014/0.031 | 0.029/0.052 |
| SBAS-aided L5 PPP products | | | | |
| 100% | 0.019/0.023 | 0.037/0.046 | 0.019/0.034 | 0.046/0.062 |
| 80% | 0.018/0.023 | 0.036/0.046 | 0.024/0.036 | 0.047/0.063 |
| 60% | 0.020/0.024 | 0.042/0.051 | 0.027/0.044 | 0.054/0.071 |
| 40% | 0.024/0.028 | 0.055/0.062 | 0.037/0.043 | 0.070/0.080 |

The results for the satellites GRACE-FO 1 and Sentinel-3B are separated by “/,” respectively

L5 PPP products (cyan). Even with the duty cycle reduced to 40%, 95% of the 3D orbital errors using products of these two services are still within 0.14 m.

In addition to the satellite positional errors, the satellite velocity errors are also computed for both test satellites using different GPS products in the along-track direction, as the accuracy of the along-track velocity needs to be better than 0.05 to 0.2 mm/s for missions such as GNSS radio occultation (Montenbruck 2017). As shown in Fig. 9, the along-track velocities computed using MADOCA L6E and SBAS-aided L5 PPP products have comparable accuracy

to those generated using CNES and IGS RTS products, i.e., smaller than 0.05 mm/s on average for all the investigated duty cycles from 40 to 100%. In the cross-track and the radial directions, the average velocity RMSE using these two products (MADOCA and SBAS) is also at a similar level, i.e., within 0.05 mm/s. The velocity RMSE at the radial direction is found to be larger than those in the other two directions. It is noted that in addition to the orbital and velocity accuracy, based on the method used for radio occultation retrieval, short-term clock stability should also be considered (Hauschild et al. 2013, Griggs et al. 2015). This is not, however, within the scope of this study.

Recall that compared with the other real-time products, MADOCA L6E PPP products and SBAS-aided L5 PPP products can be directly broadcast from QZSS satellites and the geostationary (GEO) SBAS satellite, respectively, and do not necessarily require an internet link. Although the current QZSS constellation and the GEO satellite Inmarsat-4F1 used for AU/NZ SBAS test bed have a regional service over the Asia–Pacific region, the shown results illustrate a bright future when more navigation systems and SBASs could broadcast free precise orbit and clock products to users, so that global coverage of such signals can be achieved. Compared with the orbits computed based on the broadcast ephemeris with a 3D RMSE at sub-meter level (Montenbruck and Ramos-Bosch 2008), the precise satellite orbits and clocks from MADOCA L6E PPP service and SBAS-aided L5 PPP service are able to provide significantly better LEO POD accuracy, even with a low duty cycle. This could

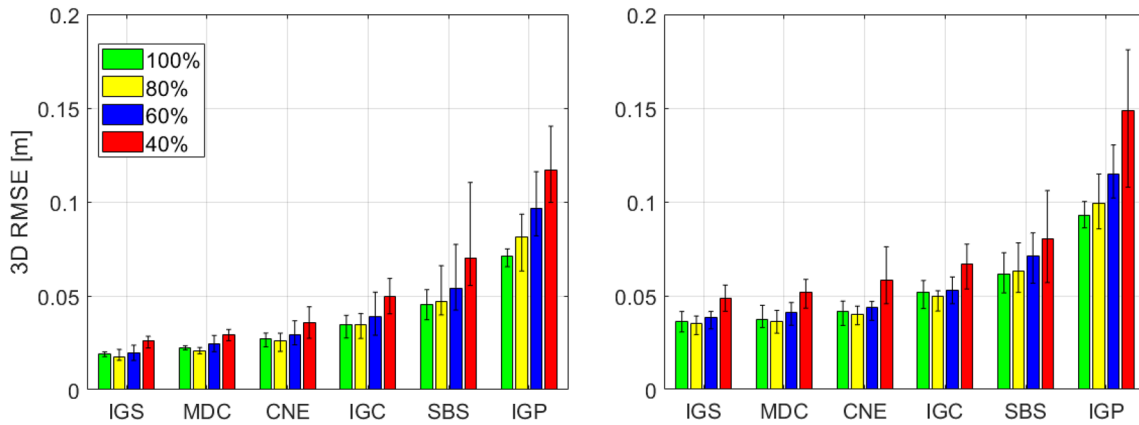


Fig. 7 Average 3D RMSE of the reduced-dynamic orbits applying different duty cycling (shown as the colored percentage in the legend) for (left) GRACE-FO 1 and (right) Sentinel-3B using different GPS

products from August 14–20, 2018. The line segments inside each bar illustrate the minimum and maximum daily 3D RMSE over the test period. The abbreviations in the x-axis are given in Table 4

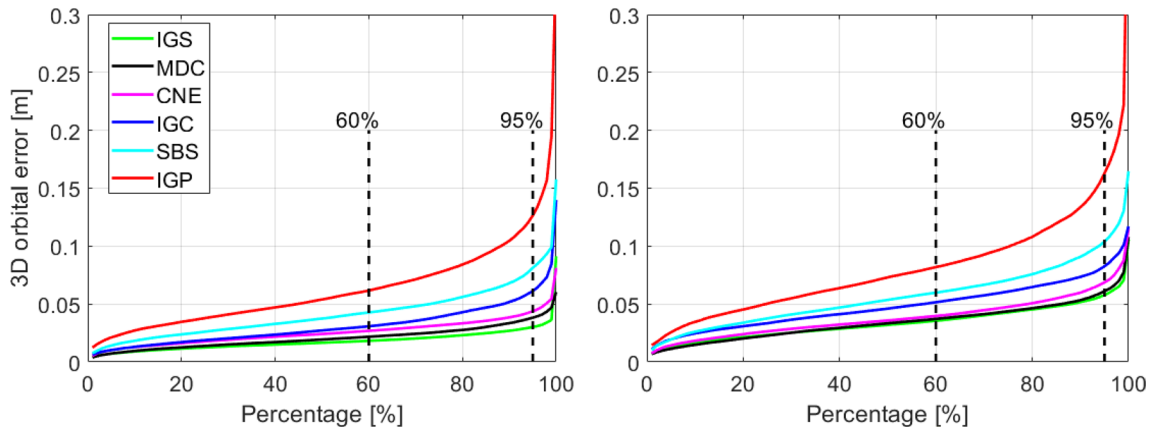


Fig. 8 Maximum 3D errors of the reduced-dynamic orbits within a certain percentage of all 3D orbital errors from August 14–20, 2018, after using different providers of GNSS observation corrections for (left) GRACE-FO1 and (right) Sentinel-3B. The duty cycle is set to 100%

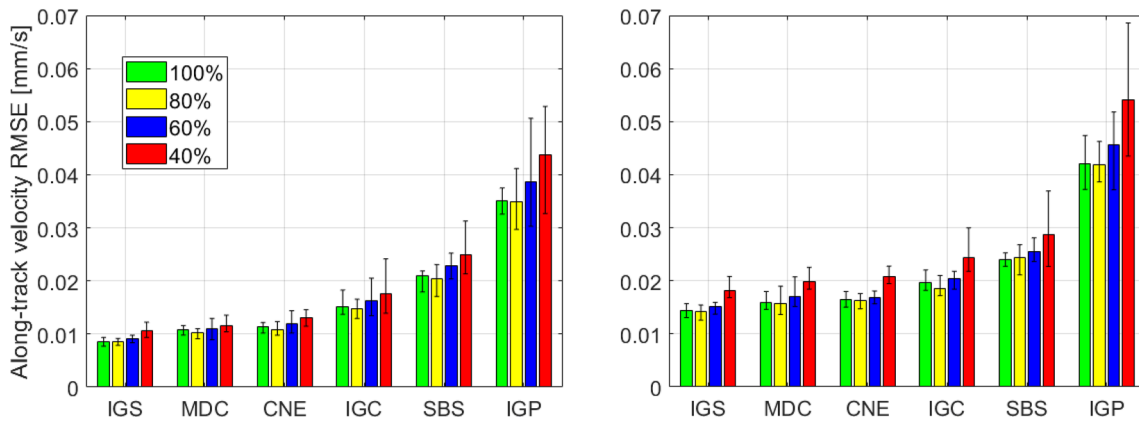


Fig. 9 Average velocity RMSE in the along-track direction for (left) GRACE-FO 1 and (right) Sentinel-3B using different GPS products from August 14–20, 2018. The line segments inside each bar illus-

trate the minimum and maximum daily velocity RMSE in the along-track direction over the test period. The legend refers to the percentage values for duty cycling

also indicate good potential for real-time onboard POD for small LEO satellites, such as CubeSats, in the future.

Kinematic orbits

Compared with the post-processed orbits computation, the onboard real-time POD processing has more substantial constraints on the computational load and thus needs to balance between the complexity of the dynamic models used and the POD accuracy. As an extreme case, the kinematic orbits are presented in this subsection, with the final least-squares adjustment (Fig. 5) performed based only on GPS measurements. Here, a 100% duty cycle is assumed when processing the kinematic orbits. Note that the accuracy of the kinematic orbits post-processed in this study should be similar to that of the converged orbits processed in real time, provided that GPS L1 and L2 observations are tracked with 100% duty cycle, and processed with comprehensive dynamic models as described in the section on processing strategy.

As an example, the kinematic orbits are shown together with the reduced-dynamic orbits in Fig. 10 for GRACE-FO

1 on August 15, 2018, applying MODACA L6E PPP products (left panel) and SBAS-aided L5 PPP products (right panel). Without applying dynamic models, the kinematic POD orbital errors (red dots) have shown a larger range. The degradation of the kinematic POD results is especially obvious in the radial direction due to the strong correlation between the LEO receiver clock offset and the radial component of the orbit (Rothacher and Beutler 1998).

Averaging over all the seven test days, we show the RMSE values in Table 6 for the radial, along-track, and cross-track directions for both GRACE-FO 1 and Sentinel-3B satellites. An outlier detection and exclusion scheme was applied for the kinematic solutions in each direction to screen out large outliers before calculating the RMSE. This process is performed such that the absolute value of the normalized orbital error (assumed normally distributed) in each direction is compared with a threshold K , defined with a significance probability level α arbitrarily taken as 10^{-4} , where

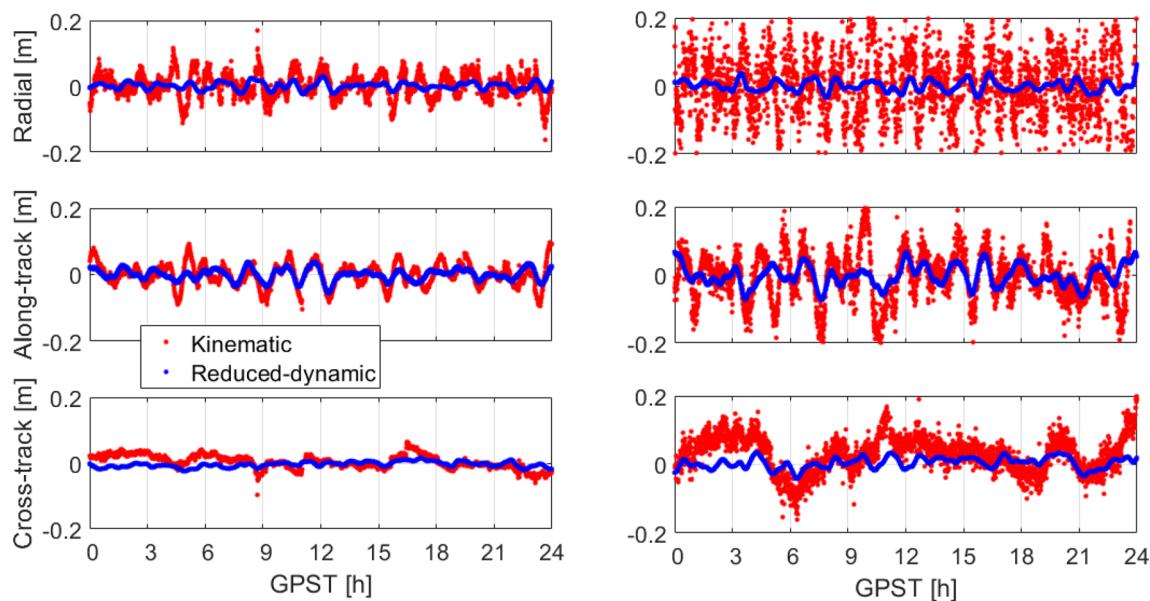


Fig. 10 Kinematic and reduced-dynamic orbits for GRACE-FO-1 on August 15, 2018, using (left) MADOCA L6E PPP products and (right) SBAS-aided L5 PPP products

Table 6 Average RMSE of the kinematic orbits from August 14–20, 2018, using MADOCA L6E PPP products and SBAS-aided L5 PPP products

| Product | Radial (m) | Along-track (m) | Cross-track (m) | 3D (m) |
|-------------------|-------------|-----------------|-----------------|-------------|
| MADOCA L6E PPP | 0.034/0.046 | 0.032/0.045 | 0.022/0.043 | 0.052/0.077 |
| SBAS-aided L5 PPP | 0.102/0.110 | 0.081/0.098 | 0.060/0.079 | 0.143/0.167 |

The results for GRACE-FO 1 and Sentinel-3B are separated with “/,” respectively

$$K = Q^{-1}\left(1 - \frac{\alpha}{2}\right) \tag{7}$$

for which Q^{-1} denotes the inverse CDF of a normal distribution. In case that the absolute normalized error is larger than K in any of the three directions, the orbits at the corresponding time point are not used for computing the RMSE. Table 6 shows that the 3D RMSE of the kinematic orbits can generally reach sub-dm to dm level using MADOCA and SBAS (L5) PPP products among the three directions, and the RMSE of the radial orbits is larger than those in the other two directions.

A comparison of the kinematic orbits produced using different precise GPS orbits and clocks is illustrated in Fig. 11. Similar to the reduced-dynamic orbits, the results applying SBAS-aided L5 PPP products are slightly worse than those using CNES (CNE) and IGS RTS (IGC) products, but are better than those using IGS ultra-rapid (IGP) orbits and

clocks. The MADOCA L6E PPP products can produce better kinematic orbits than all other tested real-time products. A larger RMSE can generally be observed in the radial direction (blue bars) than in the along-track (yellow bars) and the cross-track directions (green bars). In general, it can be observed that the kinematic solutions using MADOCA L6E and SBAS-aided L5 PPP products are at a comparable level to the results applying other real-time precise products, however, without the requirement of an internet link.

Using the 3D errors of the kinematic orbits over the seven test days, including also outliers, the maximum errors within different percentages of all 3D orbital errors are illustrated for the two test satellites in Fig. 12. It can be observed that the maximum errors within 60% of all errors are at sub-dm to dm level using the products from MADOCA (black) and SBAS-aided L5 PPP services (cyan). 95% of the kinematic orbital errors are within or around 1 dm using MADOCA

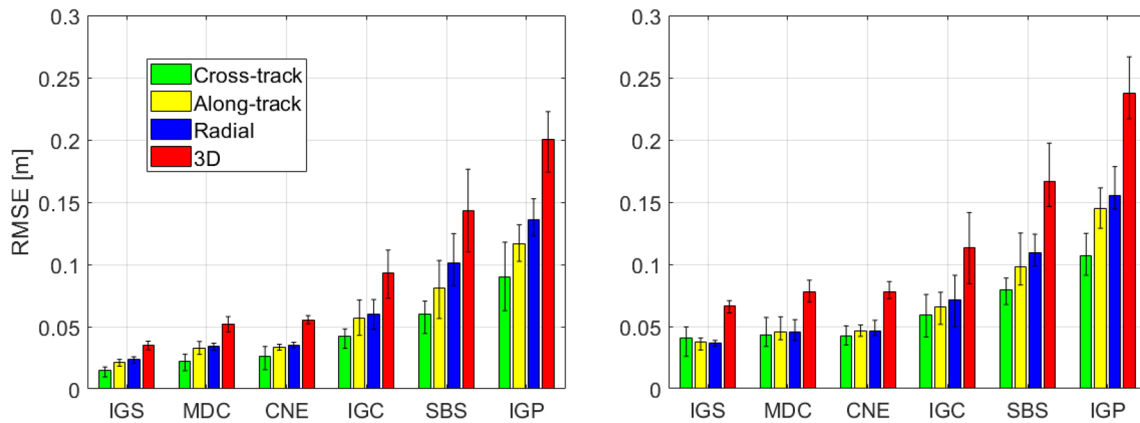


Fig. 11 Average RMSE of the kinematic orbits (for the 3D, cross-track, along-track, and radial directions) for (left) GRACE-FO 1 and (right) Sentinel-3B using different GPS products from August 14–20,

2018. The line segments inside each bar illustrate the minimum and maximum daily RMSE over the test period

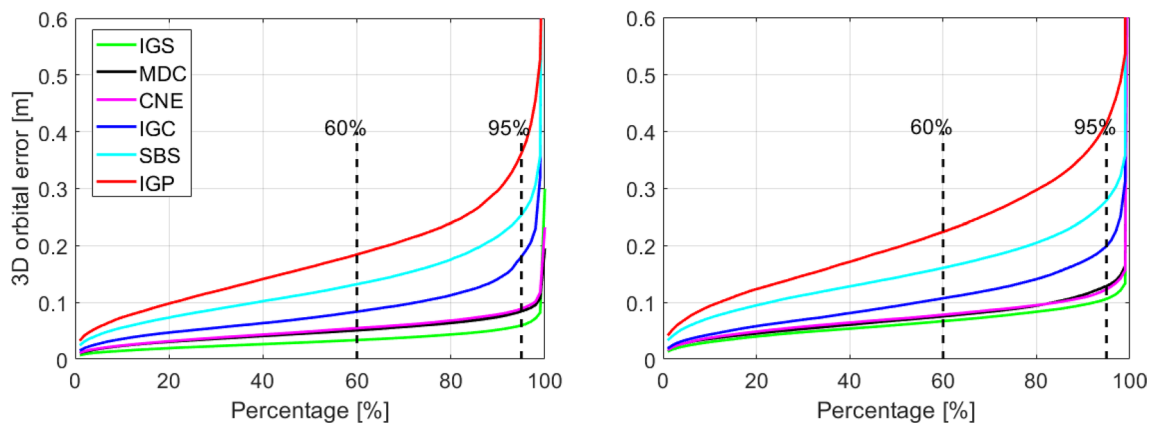


Fig. 12 Maximum 3D errors of the kinematic orbits within a certain percentage of all 3D orbital errors from August 14–20, 2018, using different providers of GPS observation corrections for (left) GRACE-FO 1 and (right) Sentinel-3B satellites. The duty cycle is set to 100%

L6E PPP products and are within 3 dm using SBAS-aided PPP L5 products.

Conclusion

Nowadays, different real-time services provide precise GNSS satellite orbits and clock corrections to users, benefiting the POD of spaceborne receivers onboard LEO satellites. While most real-time services on the ground require an Internet link to transmit their products, in recent years, non-commercial services have broadcast multi-constellation GNSS orbits and clock corrections directly from navigation satellites or GEO SBAS satellites. The Japanese MADOCA L6E PPP service and AU/NZ SBAS-aided L5 PPP service are two good examples for this purpose.

This study shows that GPS orbit and clock corrections of these two products are of high accuracy. Using these two products, the orbital accuracy of the tested LEO satellites ranges at several centimeters even with a duty cycle down to 40% in the reduced-dynamic mode, which is comparable to those using other high-quality Internet-linked real-time products and fulfills the requirement for applications like InSAR. The results demonstrated that 95% of the reduced-dynamic orbital errors are within or around 1 dm using the two new tested products with a duty cycle of 100%. Among all the three directions, the accuracy of the radial component using MADOCA PPP products is below 2 cm even having a 40% duty cycle, which fulfills the requirement of satellite altimetry. The velocity accuracy is within 0.05 mm/s in the along-track direction, which is useful for the GNSS radio occultation missions. The 3D orbital accuracy is at sub-dm to dm level in the kinematic mode using MADOCA and SBAS-aided (L5) PPP products. The orbits computed using MADOCA products have generally shown better accuracy than the results using all other tested real-time products, including those from CNES and IGS RTS. The orbits computed using SBAS-aided L5 PPP products have also overperformed those using IGS ultra-rapid products.

The results shown in this study, on the one side, demonstrate the high-quality of MADOCA and SBAS-aided real-time GNSS products and, on the other side, illustrate a bright future for precise onboard LEO POD, which benefits from these high-precision, satellite-linked, and free-of-charge GNSS products instead of using low-accuracy broadcast ephemeris. Furthermore, for small satellites with power constraints, such as CubeSats, good orbital accuracy is shown to be achievable, albeit in the post-processing mode mimicking real-time applications after convergence, using these two products even with a duty cycle down to 40%.

Acknowledgement We would like to thank the GMV team for providing the GNSS satellite orbits and clocks of the SBAS-aided L5

PPP service. Special thanks are given to Julián Barrios from GMV and Hiroshi Takiguchi from JAXA for discussions of the processing details of the MADOCA and the SBAS-aided PPP products. The work is funded by the Australian Research Council Discovery Project: Tracking Formation-Flying of Nanosatellites Using Inter-Satellite Links (DP 190102444).

Data availability The MADOCA L6E PPP products were obtained from the JAXA <ftp://mgmds01.tksc.jaxa.jp/mdc1/>. The IGS final, ultra-rapid, and the RTS products were obtained from the NASA CDDIS <https://cdis.nasa.gov/archive/gnss/products/rtp/>. The CNES real-time products were obtained from http://www.ppp-wizard.net/products/REAL_TIME/. The data of GRACE-FO-1 were obtained from the NASA JPL <https://podaac-tools.jpl.nasa.gov/drive/files/allData/gracefo/L1B/JPL/RL04/ASCII/>. The observation data and the reference orbits of the Sentinel-3B were obtained from the ESA via <https://scihub.copernicus.eu/gnss/#/home> and <https://sentinel.esa.int/web/sentinel/missions/sentinel-3/ground-segment/pod/products-requirements>, respectively. The SBAS-aided PPP L5 corrections are available from the corresponding author on reasonable request. The data are processed with the Bernese GNSS Software version 5.2.

References

- Barrios J, Caro J, Calle JD, Carbonell E, Pericacho JG, Fernández G, Esteban VM, Fernández MA, Bravo F, Torres B (2018) Update on Australia and New Zealand DFMC SBAS and PPP System Results. In Proceedings of ION GNSS+ 2018. Institute of Navigation, Miami, Florida, USA, September 24–28, pp 1038–1067
- Beutler G, Schildknecht T, Hugentobler U, Gurtner W (2003) Orbit determination in satellite geodesy. *Adv Space Res* 31(8):1853–1868. [https://doi.org/10.1016/S0273-1177\(03\)00171-6](https://doi.org/10.1016/S0273-1177(03)00171-6)
- Dach R, Lutz S, Walser P, Fridez P (2015) Bernese GNSS Software Version 5.2. University of Bern, Bern Open Publishing. <https://doi.org/10.7892/boris.72297>
- El-Mowafy A, Cheung N, Rubinov E (2020) First results of using the second generation SBAS in Australian urban and suburban road environments. *J Spat Sci* 65:99–121. <https://doi.org/10.1080/14498596.2019.1664943>
- ESA (2012) SENTINEL-3, ESA's Global Land and Ocean Mission for GMES Operational Services. European Space Agency. https://sentinel.esa.int/documents/247904/351187/S3_SP-1322_3.pdf
- Fernández M (2019) Sentinel-3 Properties for GPS POD, Copernicus Sentinel-1, -2 and -3 Precise Orbit Determination Service (SENTINELSPOD), GMV-GMESPOD-TN-0027, Version 1.7. <https://sentinels.copernicus.eu/documents/247904/3372613/Sentinel-3-GPS-POD-Properties.pdf>
- Flechtner F, Morton P, Watkins M, Webb F (2014) Status of the GRACE follow-on mission. In: Gravity, geoid and height systems, IAG Symposia, vol 141. Springer, Cham, pp 117–121. https://doi.org/10.1007/978-3-319-10837-7_15
- GPAS-Global Positioning Augmentation Service Corporation (2017) L6E MADOCA Data Format http://file.gpas.co.jp/L6E_MADOC_A_DataFormat_E.pdf
- Griggs E, Kursinski ER, Akos D (2015) Short-term GNSS satellite clock stability. *Radio Sci* 50(8):813–826. <https://doi.org/10.1002/2015RS005667>
- Hadas T, Bosy J (2015) IGS RTS precise orbits and clocks verification and quality degradation over time. *GPS Solut* 19:93–105. <https://doi.org/10.1007/s10291-014-0369-5>
- Hauschild A, Montenbruck O, Steigenberger P (2013) Short-term analysis of GNSS clocks. *GPS Solut* 17:295–307. <https://doi.org/10.1007/s10291-012-0278-4>

- Hauschild A, Tegedor J, Montenbruck O, Visser H, Markgraf M (2016) Precise onboard orbit determination for LEO satellites with real-time orbit and clock corrections. In Proceedings of ION GNSS + 2016. Institute of Navigation, Portland, Oregon, USA, September 12–16, pp 3715–3723
- IGS final (2020) International GNSS Service, GNSS Final Combined Orbit Solution Product. Greenbelt, MD, USA: NASA Crustal Dynamics Data Information System (CDDIS). https://doi.org/10.5067/gnss/gnss_igsorb_001
- IGS RTS (2020) International GNSS Service, Decoded orbit solution (30 second) from IGS real-time product streams. NASA Crustal Dynamics Data Information System (CDDIS), Greenbelt. https://doi.org/10.5067/gnss/gnss_igsrtclk30_001
- IGS ultra-rapid (2020) International GNSS Service, GNSS ultra-rapid combined orbit solution product. NASA Crustal Dynamics Data Information System (CDDIS), Greenbelt. https://doi.org/10.5067/gnss/gnss_igsuorb_001
- JAXA (2020) MADOCA real-time estimate condition. JAXA. https://ssl.tksc.jaxa.jp/madoca/public/public_message_en.html
- Johnston G, Riddell A, Hausler G (2017) The international GNSS service. In: Teunissen PJG, Montenbruck O (eds) Springer handbook of global navigation satellite systems. Springer, Cham. https://doi.org/10.1007/978-3-319-42928-1_33
- Lantto S, Gross JN (2018) Precise orbit determination using duty cycled GPS observations. In: 2018 AIAA modeling and simulation technologies conference, Kissimmee, Florida, USA, January 8–12, 2018. <https://doi.org/10.2514/6.2018-1393>
- Laurichesse D, Cerri L, Berthias JP, Mercier F (2013) Real time precise GPS constellation and clocks estimation by means of a Kalman filter. In: Proceedings of ION GNSS + 2013. Institute of Navigation, Nashville, TN, USA, September 16–20, pp 1155–1163
- Lyard F, Lefevre F, Letellier T, Francis O (2006) Modelling the global ocean tides: modern insights from FES2004. *Ocean Dyn* 56:394–415. <https://doi.org/10.1007/s10236-006-0086-x>
- Montenbruck O (2017) Space applications. In: Teunissen PJG, Montenbruck O (eds) Springer handbook of global navigation satellite systems. Springer, Cham, pp 933–964. https://doi.org/10.1007/978-3-319-42928-1_32
- Montenbruck O, Gill E (2000) Satellite orbits: models, methods and applications. Springer, Berlin. <https://doi.org/10.1007/978-3-642-58351-3>
- Montenbruck O, Ramos-Bosch P (2008) Precision real-time navigation of LEO satellites using global positioning system measurements. *GPS Solut* 12:187–198. <https://doi.org/10.1007/s10291-007-0080-x>
- Montenbruck O, Gill E, Kroes R (2005) Rapid orbit determination of LEO satellites using IGS clock and ephemeris products. *GPS Solut* 9:226–235. <https://doi.org/10.1007/s10291-005-0131-0>
- Montenbruck O, Hauschild A, Andres Y, von Engeln A, Marquardt C (2013) (Near-) real-time orbit determination for GNSS radio occultation processing. *GPS Solut* 17:199–209. <https://doi.org/10.1007/s10291-012-0271-y>
- Pavlis N, Kenyon S, Factor J, Holmes S (2008) Earth gravitational model 2008. In: SEG technical program expanded abstracts 2008. SEG technical program expanded abstracts. Society of Exploration Geophysicists, pp 761–763. <https://doi.org/10.1190/1.3063757>
- Petit G, Luzum B (2010) IERS conventions. (IERS Technical Note; 36) Frankfurt am Main: Verlag des Bundesamts für Kartographie und Geodäsie, p 179. ISBN 3-89888-989-6
- Rothacher M, Beutler G (1998) The role of GPS in the study of global change. *Phys Chem Earth* 23:1029–1040. [https://doi.org/10.1016/S0079-1946\(98\)00143-8](https://doi.org/10.1016/S0079-1946(98)00143-8)
- Rubinov E, Marshall C, Ng L, Tengku AR (2019) Positioning performance of SBAS and PPP technology from the Australia and New Zealand SBAS test-bed. In: Proceedings of the 15th south east asian survey congress (SEASC2019), Darwin, Australia, August 15–18, 1–15. Accessed on December 16, 2020 at <https://frontiersi.com.au/wp-content/uploads/2020/11/Rubinov-2019-Results-of-SBAS-Test-bed-SEASC2019.pdf>
- Sobreira H, Bougard B, Barrios J, Calle JD (2018) SBAS Australian-NZ Test Bed: Exploring New Services. In Proceeding of ION GNSS + 2018. Institute of Navigation, Miami, Florida, September 24–28, pp 2119–2133
- Standish E (1998) JPL planetary and lunar ephemerides, DE405/LE405, JPL IOM 312. F-98_048
- Subirana JS, Zornoza JJ, Hernández-Pajares M (2013) GNSS data processing. Volume I: Fundamentals and algorithms. ESA TM-23/1, May 2013. ESA Communications, Noordwijk, the Netherlands
- Švehla D, Rothacher M (2003) Kinematic and reduced-dynamic precise orbit determination of low earth orbiters. *Adv Geosci* 1:47–56. <https://doi.org/10.5194/adgeo-1-47-2003>
- Takasu T, Miyoshi M, Kaori K, Satoshi K (2015) QZSS-1 Precise orbit determination by MADOCA. In: International symposium on GNSS, Kyoto, Japan, Nov 16–18, 2015
- Tegedor J, Orpen O, Melgard T, Lapucha D, Visser H (2017) G4 multi-constellation precise point positioning service for high accuracy offshore navigation. *Int J Mar Navig Saf Sea Transp* 11(3):425–429. <https://doi.org/10.12716/1001.11.03.05>
- Tobías G, Calle JD, Navarro P, Rodríguez I, Rodríguez D (2014) magicGNSS' Real-Time POD and PPP Multi-GNSS Service. In: Proceedings of ION GNSS + 2014. Institute of Navigation, Tampa, Florida, USA, September 8–12, pp 1046–1055
- Wang K, Allahviridi-Zadeh A, El-Mowafy A, Gross JN (2020) A sensitivity study of POD using dual-frequency GPS for CubeSats data limitation and resources. *Remote Sens* 12(13):2107. <https://doi.org/10.3390/rs12132107>
- Weiss JP, Steigenberger P, Springer T (2017) Orbit and clock product generation. In: Teunissen PJG, Montenbruck O (eds) Springer handbook of global navigation satellite systems. Springer, Cham, pp 983–1010. https://doi.org/10.1007/978-3-319-42928-1_34
- Wen HY, Kruizinga G, Paik M, Landerer F, Bertiger W, Sakumura C, Bandikova T, McCullough C (2019) Gravity recovery and climate experiment follow-on (GRACE-FO). Level-1 Data Product User Handbook vol JPL D-56935 (URS270772)
- Wermuth M, Hauschild A, Montenbruck O, Kahle R (2012) TerraSAR-X precise orbit determination with real-time GPS ephemerides. *Adv Space Res* 50:549–559. <https://doi.org/10.1016/j.asr.2012.03.014>
- Wu SC, Yunck TP, Thornton CL (1991) Reduced-dynamic technique for precise orbit determination of low earth satellites. *J Guid Control Dyn* 14:24–30. <https://doi.org/10.2514/3.20600>
- Yao Y, He Y, Yi W, Song W, Cao C, Chen M (2017) Method for evaluating real-time GNSS satellite clock offset products. *GPS Solut* 21:1417–1425. <https://doi.org/10.1007/s10291-017-0619-4>
- Zhang S, Du S, Li W, Wang G (2019) Evaluation of the GPS precise orbit and clock corrections from MADOCA real-time products. *Sensors* 19(11):2580. <https://doi.org/10.3390/s19112580>

Publisher's Note Springer Nature remains neutral with regard to jurisdictional claims in published maps and institutional affiliations.

Amir Allahviridi-Zadeh is a Ph.D. student in the School of Earth and Planetary Sciences, Curtin University. His research interests include precise orbit determination of LEO satellites, especially CubeSats, as well as their applications in space missions.

Kan Wang received her Ph.D. in GNSS advanced modeling from ETH Zurich in 2016 and is a research fellow in the School of Earth and Planetary Sciences, Curtin University. Her research interests include high-precision GNSS positioning, LEO precise orbit determination, SBAS, and integrity monitoring.

Ahmed El-Mowafy obtained his Ph.D. from the University of Calgary, Canada, in 1995 and is the Leader of the GNSS Satellite Positioning and Navigation Group, and Director of Graduate Research, School of Earth and Planetary Sciences, Curtin University, Australia. He has extensive publications in precise positioning and navigation using GNSS, quality control, integrity monitoring, and estimation theory.

8 Real-time CubeSats POD with a new software

The POD procedure explained in Chapter 3 delivers precise orbits of CubeSats at high accuracies (cf. Chapters 3-6). However, it is based on extensive post-processing of the observations in a batch mode, which is not suitable for onboard POD processing. The necessity of real-time CubeSats POD motivated the development of the “LeoPod” software package in this thesis based on sequential least-squares filtering. In this chapter, the structure and the models of LeoPod software are discussed in detail.

The LeoPod software has two main processing options: Absolute and Relative POD using the kinematic approach and in the near future, the reduced-dynamic. Therefore, the latter is not discussed in this thesis. The following subsections present the absolute and relative kinematic POD using LeoPod software.

The LeoPod software is a joint work between the GNSS-SPAN group at Curtin University (Australia) and the National Time Service Center, Chinese Academy of Sciences. The contribution of the latter to developing the kinematic POD part of the LeoPod software is acknowledged.

Note: The symbols used in the following equations are already defined in the previous chapters and inside the relevant papers. New symbols are defined inside the text

8.1 Kinematic POD using LeoPod software

Kinematic POD is very sensitive to the quality of the observations, and in the presence of undetected outliers, the estimated orbits are biased. These orbits are also unavailable during the duty cycles for low-power CubeSats since the GNSS sensor is not activated, and accordingly, there are no observations in these periods. Therefore, the kinematic POD discussed in the following sections is based on one condition that GNSS observations are continuously available. The reduced-dynamic POD part of our software that is currently under development is equipped with dynamic models for orbit propagation. This feature would suit small CubeSats with enabled duty cycles and interrupted observations.

In the following, the details of the kinematic POD part of the software are provided:

- 1- The input data include precise orbits and clocks of GNSS satellites, EOP files, RINEX observations of the CubeSat, and attitude files:
 - a. As thoroughly discussed in Chapter 7, precise corrections of GNSS orbits and clocks can be broadcast by systems such as QZSS satellites or SouthPAN in space. These corrections are provided in bandwidth-efficient State Space Representation (SSR) format for the former system through the L6E signal of Block II satellite of this

navigation system, known as the MADOCA L6E PPP service. The following algorithms are applied in LeoPod software to compute the precise orbits and clocks from these corrections at the requested epochs (El-Mowafy et al. 2017):

- GNSS satellite's orbit r^s :

$$r^s = r - \delta r = r - [e_R \quad e_S \quad e_W][\delta_R \quad \delta_S \quad \delta_W]^T \quad (8.1)$$

where r is the vector of satellite coordinates generated from the broadcast ephemeris that is corrected using δr in the compact SSR message. This term comprises the three corrections in the RSW directions, δ_R , δ_S , δ_W , respectively, with their relevant unit vectors as follows:

$$e_R = e_S \times e_W, \quad e_S = \frac{\dot{r}(t)}{\|\dot{r}(t)\|}, \quad e_W = \frac{r(t) \times \dot{r}(t)}{\|r(t) \times \dot{r}(t)\|} \quad (8.2)$$

\dot{r} is the satellite's velocity estimated from the broadcast ephemeris and $\| \cdot \|$ denotes the norm of the vector.

- GNSS satellite's clock offsets dt^s :

$$dt^s = a_0 + a_1(t_{oe} - t_{tr}) + a_2(t_{oe} - t_{tr})^2 - \frac{\delta t}{c} \quad (8.3)$$

The coefficients a_0 , a_1 , and a_2 are available in the broadcast ephemeris, t_{oe} is the ephemeris reference time and t_{tr} indicates the transmission time. The compact SSR provides the correction term δt in meters, which is transformed into the time scale (s) by applying the speed of light (c).

- b. The general algorithm for SouthPAN products is similar to Equations (8.1) and (8.3), except for providing the orbit corrections with respect to the APC (and not the Center of Mass, CoM). The transformation between these two points can be applied using Equation 1 in Chapter 7.
- c. The EOP files are provided by IERS and are used whenever the transformations between inertial and Earth-fixed frames are required (see Equations 3.1 and 3.2).
- d. The RINEX raw GNSS observations of the Spire CubeSats (constellation) are used in this thesis in different scenarios. These CubeSats are equipped with the STRATOS GNSS receiver collecting 1-Hz dual-frequency GPS signals (L1C and L2L). We need

first to consider the consistency between GNSS products and the observations collected at the CubeSats that will be combined in IF form. There are two approaches that can be performed for this task. The first approach is to transform the GNSS clock offsets (δt_{P1P2}^s) that are derived initially from the IF-LC of P1/P2 observations of the network used to compute the corrections as follows:

$$\delta t_{C1C2}^s = \delta t_{P1P2}^s - \left(\frac{f_1^2}{f_1^2 - f_2^2} DCB_{P1C1} \right) + \left(\frac{f_2^2}{f_1^2 - f_2^2} DCB_{P2C2} \right) \quad (8.4)$$

where δt_{C1C2}^s would be consistent with the CubeSats IF observations by applying the relevant DCB .

The second approach is to correct the IF observations of the CubeSats as follows:

$$P_{r,IF}^s = \frac{f_1^2 C1C_{r,1}^s - f_2^2 C2L_{r,2}^s}{f_1^2 - f_2^2} + \left(\frac{c f_1^2 DCB_{P1C1}}{f_1^2 - f_2^2} \right) - \left(\frac{c f_2^2 DCB_{P2C2}}{f_1^2 - f_2^2} \right) \quad (8.5)$$

where c is the speed of light, which transforms the DCB values from time to range.

- e. The CubeSats attitude files are generated from the star cameras and include quaternions to convert from the body-fixed CubeSat's Reference Frame (CRF) to the inertial true of epoch (ITOE) frame. In the zero-quaternion, called nominal attitude, the body-fixed CRF of the Spire CubeSats is defined as follows:

- Z : Opposite to the POD antenna pointed towards the nadir direction,
- Y : Points towards the negative orbit normal,
- X : points towards YXZ direction (approximately the direction of flight or the positive velocity direction).

Representing the attitude by the quaternions q_x, q_y, q_z, q_0 , the attitude matrix is computed as follows (Kuipers 1999):

$$R_{ATT} = (q_0^2 + q_x^2 + q_y^2 + q_z^2)^{-1} \begin{bmatrix} q_0^2 + q_x^2 - q_y^2 - q_z^2 & 2(q_x q_y - q_0 q_z) & 2(q_0 q_y + q_x q_z) \\ 2(q_0 q_z + q_x q_y) & q_0^2 - q_x^2 + q_y^2 - q_z^2 & 2(q_y q_z - q_0 q_x) \\ 2(q_x q_z - q_0 q_y) & 2(q_0 q_x + q_y q_z) & q_0^2 - q_x^2 - q_y^2 + q_z^2 \end{bmatrix} \quad (8.6)$$

The attitude information of CubeSat is required in three cases. First, when applying the antenna sensor offset, which is the offset between the CoM and the ARP; second,

when applying the phase centre variations in different azimuth and elevation angles; and third, when computing the phase wind-up effect.

- 2- The second step starts with coarsely estimating the epoch-wise CubeSat's coordinates and receiver clock offset using IF code observations. Referring to Equation 5 in Chapter 2, the linearized model for the iterative least-squares adjustment at each epoch equals:

$$E \left(\underbrace{\begin{bmatrix} P_{r,IF}^{s_1} - \tilde{P}_{r,IF}^{s_1} & \dots & P_{r,IF}^{s_m} - \tilde{P}_{r,IF}^{s_m} \end{bmatrix}^T}_{\Delta y} \right) = \underbrace{\begin{bmatrix} -\text{LoS}_{x,r}^{s_1} & -\text{LoS}_{y,r}^{s_1} & -\text{LoS}_{z,r}^{s_1} & 1 \\ \vdots & \vdots & \vdots & \vdots \\ -\text{LoS}_{x,r}^{s_m} & -\text{LoS}_{y,r}^{s_m} & -\text{LoS}_{z,r}^{s_m} & 1 \end{bmatrix}}_J \underbrace{\begin{bmatrix} dx \\ dy \\ dz \\ cdt_r \end{bmatrix}}_{\Delta x}, \quad (8.7)$$

$$D(\Delta y) = I_m$$

where LoS refers to the line-of-sight unit vector from the CubeSat to the GNSS satellite and m is the number of IF code observations. The relativistic corrections should be applied to the clocks (cf. Equation 6 in Chapter 6). The estimated parameters are used as initial values for the main least-squares adjustment explained later. This step continues with the data screening of code observations using the following Fault Detection and Exclusion (FDE) approach:

Considering the O-C term from the last iteration of the least-squares (Δy), the following chi-square statistic is computed and compared with the threshold $\chi_\alpha^2(df, 0)$ (Blanch et al. 2012):

$$\chi^2 = \Delta y^T Q_y^{-1} \Delta y - \Delta y^T Q_y^{-1} J (J^T Q_y^{-1} J)^{-1} J^T Q_y^{-1} \Delta y \quad (8.8)$$

In the case of detecting outliers, i.e., when $T_q > \chi_\alpha^2$, the normalised residuals are estimated as follows:

$$v_N = \frac{\Delta y - J \hat{x}}{\sqrt{\text{diag}(Q_y - J Q_x^{-1} J^T)}} \quad (8.9)$$

and the Chi-square test is repeated while the rows and columns corresponding to the biggest normalized residuals are removed from the matrices in Equation (8.8), and the identified outliers will be excluded from processing.

- 3- The next step is to detect cycle slips using the Melbourne-Wübbena combination shown in Equation (3.6) and the following Geometry-Free combination:

$$GF = \Phi_{r,1}^s - \Phi_{r,2}^s \quad (8.10)$$

which is influenced by cycle slips, ionospheric variations, and noises. The time differences in GF and MW combinations are tested with the empirical threshold proposed by Zhou et al. (2018) to detect cycle slips. The FDE based on the Chi-square test mentioned earlier is applied in the least-squares filtering to find undetected cycle slips. However, this step is performed here to prevent applying any estimated ambiguities from the previous epoch into the model as pseudo-observations when a cycle slip occurs (see Step 5).

- 4- The Kinematic POD applied in LeoPod software is based on precise point positioning (PPP) methodology, and the following corrections are applied to the systematic errors:
 - a. Tidal corrections: This displacement is a combination of Earth tides due to the moon and sun, polar tides, and permanent tidal effects (cf. IERS Technical Note No. 36- Petit and Luzum 2010) and should be applied to the estimated coordinates of the CubeSats.
 - b. Antenna corrections, including the antenna offsets (PCO and PCV) and phase wind-up values, should be applied to all observations. The antenna sensor offset should be transformed from the satellite reference frame to the inertial frame. For the GNSS satellites, the transformation is performed using Equation 1 in Chapter 7; however, the appropriate nominal attitude of each GNSS satellite block should be considered (cf. Allahverdi et al. 2016, Allahviridi-Zadeh 2022). For the CubeSats, it is estimated by applying the attitude matrix (8.6) to the antenna sensor offset in the CubeSat's reference frame (O_{CRF}) as follows:

$$O_{ITOE} = R_{ATT} O_{CRF} \quad (8.11)$$

These values should be transformed from the ITOE to the Earth-fixed frame using P_m and E_r rotation matrices in Equation (3.1), which is applied to estimate the epoch-wise kinematic coordinates with respect to the CoM.

The GNSS antenna PCO and PCV are provided in the IGS ANTEX file (igs14.atx) for the GNSS observations. They are extracted and applied in computing the O-C term inside the sequential least-squares filtering in step 5. Spire Global Inc. provides the PCO and the PCV for the CubeSats used in this thesis. These values are provided in the CRF (cf. step 1e) and should be transformed to the Earth-fixed frame similar to the antenna offset explained above. The empirical PCV patterns based on the residual approach are also estimated and applied in a relevant study (Allahviridi-Zadeh 2021).

The phase wind-up corrections applied to the IF phase observations are as follows:

$$w_{IF} = \frac{f_1^2 w_1 - f_2^2 w_2}{f_1^2 - f_2^2} \quad (8.12)$$

where the correction on each frequency w_j is estimated as follows (Hauschild 2017):

$$w_j = \text{sgn}(e_k \cdot (D' \times D)) \cos^{-1} \left(\frac{D' \cdot D}{\|D'\| \|D\|} \right) \quad (8.13)$$

where sgn is the Sign function. D' and D denote dipole vectors defined by the unit vectors of the CubeSats antenna (e_x, e_y, e_z) and the GNSS antenna (e'_x, e'_y, e'_z) as follows:

$$\begin{aligned} D &= e_x - e_k (e_k \cdot e_x) + e_k \times e_y \\ D' &= e'_x - e_k (e_k \cdot e'_x) - e_k \times e'_y \end{aligned} \quad (8.14)$$

and e_k is the unit vector pointing from the GNSS antenna to the CubeSats antenna that are estimated using CubeSats and GNSS coordinates in the inertial frame (I) and the GNSS antenna unit vectors:

$$e_k = \frac{r_I^{CubeSat} - r_I^{GNSS}}{\sqrt{\|e'_y\|^2 + \|r_I^{CubeSat} - r_I^{GNSS}\|^2}}, \quad e'_y = \frac{e'_z \times r_I^{Sun}}{\|e'_z \times r_I^{Sun}\|}, \quad e'_z = -\frac{r_I^{GNSS}}{\|r_I^{GNSS}\|}, \quad e'_x = e'_y \times e'_z \quad (8.15)$$

The CubeSat antenna unit vectors in IOTE are determined based on the definition of the Antenna Reference Frame (ARF), i.e., using boresight (Br) and azimuth (Az) directions of the antenna as follows:

$$e_x = R_{ATT} Az, \quad e_z = R_{ATT} Br, \quad e_y = e_z \times e_x \quad (8.16)$$

- 5- The last step is to perform the sequential least-squares filtering based on Equation 9 presented in Chapter 2, while the FDE procedure explained in step 2 should be performed in each iteration. The design matrix in this step for IF code and phase observations is expressed as follows:

$$J_r = \begin{bmatrix} -\text{LoS}_{x,r}^{s_1} & -\text{LoS}_{y,r}^{s_1} & -\text{LoS}_{z,r}^{s_1} & 1 & 0 & 0 & \dots & 0 \\ \vdots & \vdots & \vdots & \vdots & \vdots & \vdots & \vdots & \vdots \\ -\text{LoS}_{x,r}^{s_m} & -\text{LoS}_{y,r}^{s_m} & -\text{LoS}_{z,r}^{s_m} & 1 & 0 & 0 & \dots & 0 \\ -\text{LoS}_{x,r}^{s_1} & -\text{LoS}_{y,r}^{s_1} & -\text{LoS}_{z,r}^{s_1} & 1 & 1 & 0 & \dots & 0 \\ \vdots & \vdots & \vdots & \vdots & \vdots & \vdots & \dots & \vdots \\ -\text{LoS}_{x,r}^{s_m} & -\text{LoS}_{y,r}^{s_m} & -\text{LoS}_{z,r}^{s_m} & 1 & 0 & 0 & \dots & 1 \end{bmatrix} \quad (8.17)$$

The estimated ambiguities in each iteration are considered as pseudo-observations in the next epoch if no cycle slips are detected. The relevant part of these pseudo-observations in the design matrix is shown as $J_{x'}$ in Equation 9 given in Chapter 2.

Figure 1 illustrates a flowchart of these steps.

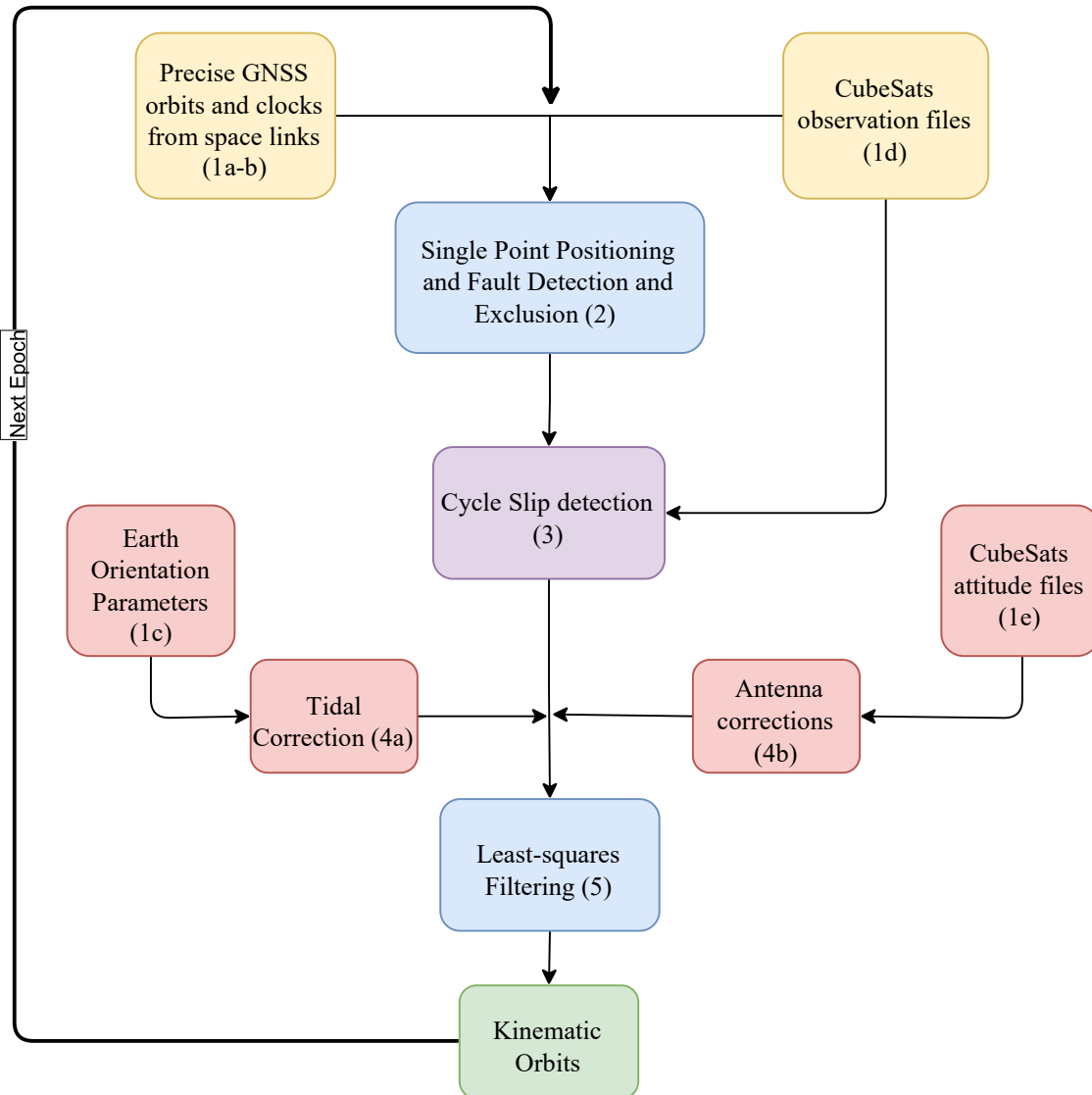


Figure 1 Flowchart of CubeSat POD using LeoPod software. The relevant step numbers are provided in parentheses.

8.2 Relative Kinematic POD using LeoPod software

Real-time onboard POD for CubeSats is still an issue due to the limited power and processing units' capabilities on CubeSats, noisy COTS components, including the receiver, antenna and unstable oscillators (cf. Chapter 6). The proposed solution is to augment the relative POD using the precise inter-satellite ranges in a smart formation flying or constellation of CubeSats (Allahviridi-Zadeh and El-Mowafy 2022, El-Mowafy et al. 2022a, El-Mowafy et al. 2022b). The benefits of this solution include removing the impact of receiver-dependent errors such as clock offsets, reducing the satellite orbital error, strengthening the model using precise ranges, and reducing the onboard computational burden significantly. This section covers the required models for this solution, the implementation procedure in the LeoPod software, and the testing results for real CubeSats.

The procedure of the relative POD is generally similar to the kinematic POD explained in section 8.1. However, the relative POD in the LeoPod software is based on using the following double-differenced IF observations between two CubeSats (r_1, r_2) and two GNSS satellites (s_1, s_2) where s_1 is considered as the reference satellite:

$$\begin{aligned} P_{r_2,IF}^{s_{12}} &= \rho_{r_2}^{s_{12}} + e_{r_2,IF}^{s_{12}} \\ \Phi_{r_2,IF}^{s_{12}} &= \rho_{r_2}^{s_{12}} + \lambda_{IF} n_{r_2,IF}^{s_{12}} + \varepsilon_{r_2,IF}^{s_{12}} \end{aligned} \quad (8.18)$$

and augmenting the model using precise ranges (PR) between two CubeSats at each epoch. These ranges are derived from the estimated reduced-dynamic POD explained in Chapter 3. Considering the baseline between two CubeSats as b_{r_2} , the augmented design matrix at each epoch with m number of common-in-view satellites is expressed as:

$$J = \begin{bmatrix} -\text{LoS}_{r_2}^{s_{12}} & 0 & 0 & \cdots & 0 & 0 \\ \vdots & \vdots & \vdots & \vdots & \vdots & \vdots \\ -\text{LoS}_{r_2}^{s_{1m}} & 0 & 0 & \cdots & 0 & 0 \\ -\text{LoS}_{r_2}^{s_{12}} & 1 & 0 & \cdots & 0 & 0 \\ \vdots & \vdots & \vdots & \vdots & \vdots & \vdots \\ -\text{LoS}_{r_2}^{s_{1m}} & 0 & 0 & \cdots & 1 & 0 \\ \frac{b_{r_2}}{PR_{r_2}} & 0 & 0 & \cdots & 0 & 0 \end{bmatrix}_{(4m-4) \times (3+(m-1))} \quad (8.19)$$

This is used in the sequential least-squares filtering to solve for the following unknowns:

$$x = \left[b_{r_2,X} \quad b_{r_2,Y} \quad b_{r_2,Z} \quad n_{r_2,IF}^{s_{12}} \quad n_{r_2,IF}^{s_{12}} \quad \cdots \quad n_{r_2,IF}^{s_{12}} \right]^T \quad (8.20)$$

where the first three columns are baseline components in X, Y, and Z directions, respectively. The processing steps, including the FDE, are similar to the kinematic POD. Precise inter-satellite ranges should be predicted for the near future and broadcasted to the CubeSats to implement the proposed solution in real-time scenarios. The prediction can be performed using the reduced-dynamic orbits computed on the ground; however, these orbits should be updated with the new GNSS observations to avoid significant discrepancies due to the deficiencies in the dynamic models for LEO satellites (cf. Chapter 2). The other requirement to implement the proposed solution is between CubeSats-communication-links. These links are achievable by equipping CubeSats with low-power software-defined radio (SDR), which enables sending and receiving, and even processing signals using its Field Programmable Gate Arrays (FPGA) (Allahviridi-Zadeh 2021). Figure 2 shows a flowchart for the proposed solution.

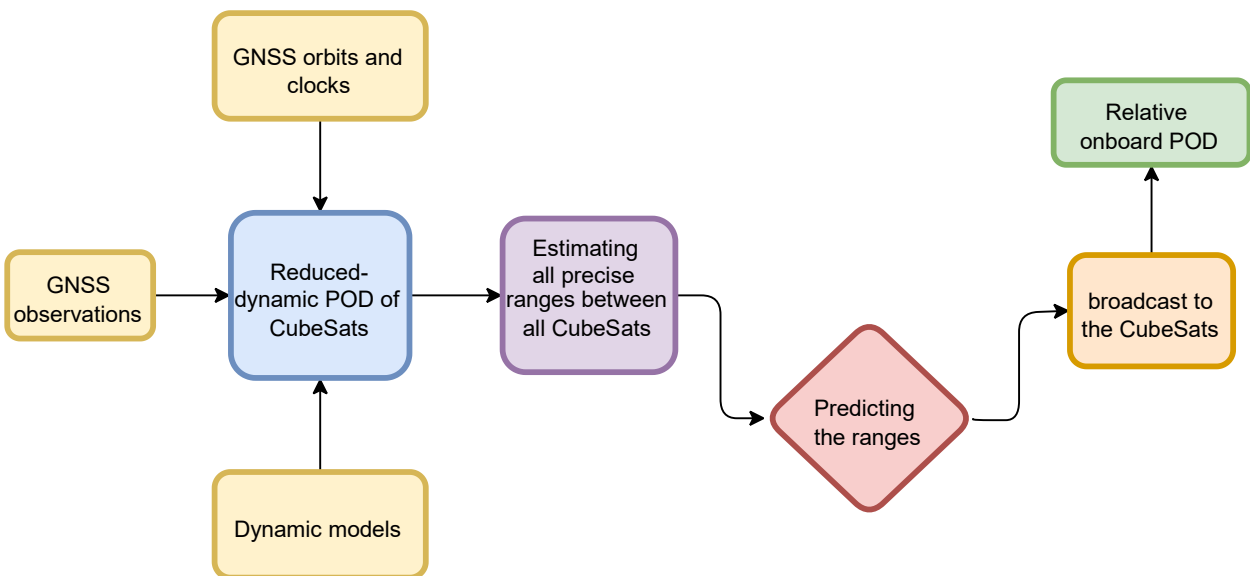


Figure 2 Flowchart for the relative POD augmented with the precise inter-satellite ranges

The observations of nine Spire CubeSats for 5 January 2021 are used to test and analyze the orbital improvement using the proposed solution. A list of these CubeSats is provided in Table 2 of Chapter 6. A Raspberry Pi 4 is used for relative POD to mimic the onboard processing. A comparison of the specifications of this CPU with a real CubeSat CPU is given in Table 1.

Table 1 The specifications of the CPU used for relative POD testing compared to a real CubeSat CPU

| Specifications | Tested CPU | CubeSat's CPU |
|--------------------------|----------------------------|----------------------|
| Processor | Quad-core ARM Cortex (A72) | Dual-core ARM Cortex |
| RAM | 8G DDR4 | 8 GB DDR3 |
| Power Consumption | 3.8-5.5 W | 1.6 to 2.85 W |

The following testing scenario is performed for all nine CubeSats:

- At each run, one CubeSat is set as the deputy satellite, and the others are the chief satellites
- The coordinates of the chief satellite are considered as known values in Equation 8.20, and therefore, the coordinates of the deputy CubeSat can be achieved
- The precise range (or baseline) between the deputy and the chief satellite is derived from their precise positions calculated from the reduced-dynamic POD.
- The precise orbits used to generate the baseline in previous steps are validated using internal validation methods. The accuracy of the orbit from this validation step is mainly at a few centimeters which is used to weigh the baselines in the model.
- The test is limited to baseline lengths of less than 1000 km
- The estimated coordinates of the deputy satellite are compared with its reference orbit, and the RMS values of the differences are provided in Table 2 for all tested CubeSats.

The results show that the orbital components with the dm-level accuracy are achievable when the baseline length between the deputy and chief CubeSats is shorter than 1000 km. The orbital accuracy dropped by increasing the baseline length mainly due to the low number of common-in-view GNSS satellites and the absorbed biases in the ambiguities. For example, the orbital accuracy dropped to around 1 meter for the baselines larger than 2000 km. For the baselines larger than 7000 km, there were no common-in-view satellites. Comparing the orbital components with and without applying the precise ranges in the model shows that implementing the precise ranges improves the estimated orbits with 0.33, 0.28, and 0.16 cm in X, Y, and Z directions, respectively.

Table 2 RMS values for comparison of CubeSats orbits generated from the augmented relative POD with the reduced-dynamic POD for baselines less than 1000 km

| Orbital components | RMS (m) | | | | | | | | |
|--------------------|---------|---------|---------|---------|---------|---------|---------|---------|---------|
| | PRN 099 | PRN 100 | PRN 101 | PRN 102 | PRN 103 | PRN 104 | PRN 106 | PRN 107 | PRN 122 |
| X | 0.47 | 0.48 | 0.61 | 0.45 | 0.38 | 0.56 | 0.51 | 0.49 | 0.57 |
| Y | 0.49 | 0.43 | 0.55 | 0.56 | 0.38 | 0.54 | 0.52 | 0.40 | 0.56 |
| Z | 0.52 | 0.56 | 0.52 | 0.55 | 0.45 | 0.59 | 0.48 | 0.56 | 0.53 |

The precise navigation of the smart constellation (or smart formation flying) of CubeSats is a new term in this field that requires more investigation. For example, in the proposed solution, the transformation delays due to the large distances between CubeSats and the signal disruption due to the unstable oscillators of SDR are not considered. The first challenge can be solved by limiting the distances between the chief and deputy CubeSats to less than, e.g., 1000 km. The second one, a hardware limitation, can be solved by integrating the SDR with chip-scale atomic clocks (cf. Chapter 6), where various research institutions are currently developing very small and relatively inexpensive atomic clocks.

9 Conclusions

9.1 Summary of the thesis outcomes

Precise orbits are essential for different applications in space and Earth sciences performed by LEO satellites. The state-of-the-art POD of geodetic LEO satellites is well developed, mainly using kinematic and reduced-dynamic methods. The first method uses high-quality GNSS observations and determines the satellite orbits and receiver clock offsets in a least-squares adjustment. Therefore, it mainly depends on the availability and quality of the GNSS observations, an efficient data screening process, and the availability of corrections for precise positioning. The second method is based on solving the equation of motion of the satellite and considering the dynamic forces acting on the satellite and GNSS observations when available. Although there are some models to estimate these effects, some deficiencies exist in the non-gravitational models that prevent solving the equation of motion using analytical solutions. Therefore, some dynamic parameters, velocity changes, and stochastic accelerations are estimated in the reduced-dynamic POD to compensate for the dynamic model deficiencies. This estimation requires calculating the partial derivatives of the satellite state vector with respect to the requested parameters using numerical integration. The partial derivatives are combined with the partial derivatives of GNSS observations with respect to the receiver clock offset and ambiguities to be used in a least-squares adjustment to estimate the unknown parameters. The outputs are used to update the orbit and reach sub-dm-level accuracy, and are evaluated by external validation approaches such as satellite laser ranging (SLR) observations and internal validation methods such as comparing overlapping arcs and residual analysis. This procedure is performed for almost all geodetic LEO satellites in the post-mission mode. All of the required procedures, models, and modifications for CubeSat POD in post-mission were explained in this thesis. They are applied in a batch least-squares estimation implemented in Bernese GNSS processing software, which was discussed in Chapter 3.

Having geodetic LEO satellites in space requires a complex design, building and launching procedure and a large budget that reaches hundreds of millions of dollars. This significant limitation motivated the investigation of using small satellites with less complexity and lower budgets as an alternative option for universities, research institutions, and small companies. Technology advances opened a new era for CubeSats as small satellites built with one or more 10 cm-sized cubes from COTS components. To be suitable for the applications currently performed by geodetic satellites, the orbits of CubeSats must be available with high accuracy. However, there are some limitations for the CubeSats to achieve such accuracy. The first one is the limited available power for all sensors in the bus and payloads, which inevitably lead to reduced GNSS sensor availability and interrupted GNSS

observations, especially in the eclipse region. The power limitation also yields the lower processing unit on the bus of CubeSats to perform onboard POD. The second primary limitation is the COTS components' quality, which may result in noisy observations, unstable oscillators, faulty ADCS, and imperfect thermal control systems. Some of these limitations in CubeSats POD were investigated in the thesis, and viable solutions are proposed.

To address the first limitation, the onboard GNSS observations of geodetic LEO satellites were used to generate observations influenced by duty cycling. The primary data constraints on CubeSat POD, including the continuity, completeness, and sampling interval of the recorded observations and the availability of attitude information, were investigated by the duty-cycled observations. Performing the developed CubeSat POD with daily observations that experienced 20% to 80% duty cycles provided precise orbits with RMSE equal to 3.5 to 1.6 cm. Such duty cycles are equivalent to switching the GNSS sensor on for 12 to 48 minutes per hour and collecting observations with sampling intervals of 10 s. The average number of satellites in the above test was about nine. However, this number can be reduced due to the constraint in the number of channels tracking GNSS satellites. The 3D RMSE values increased to around 5 cm when the maximum number of tracked satellites was set to 6, and the receiver was switched on for 12 minutes per hour. Adding more constraints, such as collecting observations with lower sampling intervals, resulted in reducing the GNSS part of the reduced-dynamic POD and increasing the 3D RMSE values. The sub-dm level of accuracy is achievable with sample intervals of 120 s and a duty cycle of 60%. The degradation in accuracy in the orbital components is considerable when these factors are simultaneously considered. In the post-mission mode and considering a sufficient degree and order of dynamic models is explained in the thesis in addition to estimating the stochastic accelerations to compensate for the model deficiencies. Sub-dm-level to dm level of orbital accuracy that is suitable for different applications is shown to be achievable even when applying the constraints mentioned earlier. However, when combining these constraints, the duty-cycle portion and the sampling interval should not be lower than 40% and larger than 1 min, respectively. This investigation can help the CubeSat designers correctly manage the power to reach the required accuracy of the mission.

The other limitation impacting CubeSats POD is the quality of COTS sensors. The GNSS observations collected by these sensors are not optimally weighted using traditional stochastic functions, such as the traditional elevation angle-dependant models. On the one hand, these models are developed for the observations travelled through the troposphere layer and to limit the effect of multipath on ground users, which is not the case for CubeSats. Some signals observed from GNSS satellites by CubeSats can also have negative elevation angles, and are still useful observations. On the other hand, these models reduce the impacts of observations received from the low-elevation

angles, which may be critical for the COTS sensors with low channel numbers. Therefore, a stochastic model based on SNR values was developed and tested using one month of observations collected by 17 CubeSats of the same type in the Spire Global constellation. Comparing the weight values estimated with the developed and traditional models showed that some observations from low-elevation angles may be helpful for CubeSats POD. The reduced-dynamic and the kinematic POD using the actual CubeSats were evaluated using internal validation methods. All overlapped orbits had RMS values less than 5 cm, and the residual analysis of the orbital components confirmed the estimated precise orbits. Comparing the POD results from applying the SNR models and the elevation angle dependant models confirmed the improvements in using the developed model.

Receiver clock offsets are one of the outputs of the CubeSat POD process, which are affected by the quality of the COTS sensors and the deficiencies in the dynamic models. The short-term instabilities observed in these clocks from the tested CubeSats are mainly in the 10^{-8} to 10^{-4} range, which is an obstacle for clock modelling in high-rate applications such as GNSS radio occultation. The impacts of the factors that cause the short-term instabilities were extensively investigated in this thesis for the first time, and solutions were proposed. The first factor is the number of outliers in the observations that decreases the impact of the GNSS part in CubeSats POD. When more than half of the observations are screened out of the POD process, the number of stochastic accelerations should be doubled. This would change the MDEV values at 10^{-6} for short averaging times less than 10 s. The other factors include biases in the model, like hardware biases due to the internal and external heat variations, unmodelled phase centre variations of the antenna, and the relativistic effect due to the higher order gravity forces. The stabilities in the shadow regions were compared with the sunlight to show the effect of thermal variation in the hardware biases. The better clock stabilities achieved when the temperature drops confirmed the importance of controlling the impacts of heat sources on the clocks. The mean of MDEV reduction after estimating the PCV pattern based on the residual approach and applying the CubeSats POD is at the level of 10^{-9} for short averaging times. Implementing the J2 corrections in the POD procedure slightly improved the stabilities, mainly at 10^{-8} to 10^{-11} . The analysis confirmed that applying all of these solutions can improve the estimated clocks at several microseconds, equivalent to the MDEV reduction at 10^{-6} level for short averaging times. However, comparing the improved clocks with the ultra-stable oscillators highlights the high impact of the sensor quality, i.e. the quality of onboard oscillators, as the main factor affecting the short-term clock stabilities.

The appropriate method for removing the clock influence on time-tagging the high-rate RO observations of CubeSats with unstable clocks was also addressed. In an example with real data, it was confirmed that CubeSats can perform the mission with the same quality as geodetic satellites.

The GNSS-RO products of COSMIC-2 constellations equipped with six geodetic LEO satellites were compared with the products of the Spire Global constellations of more than 145 3U-CubeSats. The evaluation with external sources revealed that the CubeSats provide RO atmospheric profiles at the same level as geodetic LEO satellites. Taking advantage of the less complex and much less budget of CubeSats than geodetic LEO satellites, the former can provide global coverage, which is useful for global environmental studies.

In the real-time mode, the precise orbits and clock corrections of the GNSS satellites are required to perform onboard kinematic or semi-dynamic POD. These corrections are provided through space links such as SouthPAN and MADOCA services. The accuracy, stability, and impacts of these corrections on CubeSat POD were investigated for the first time in the thesis. Compared to the IGS final products, the 3D RMSE of the orbit corrections for the MADOCA service equalled 3.8 cm, while the test-bed SouthPAN provided 7.9 cm. The STD of clock corrections of MADOCA was generally less than 0.15 ns, slightly better than SouthPAN test-bed products which gave 0.2 ns. Considering that SouthPAN was in the test-bed stage at the time of this evaluation, the better accuracy of the MADOCA products is mainly due to the differences in the density of their networks, types of observations, intervals of solutions, differences in dynamic models, and bandwidth availability for the carrier wave. However, the acceptable accuracy for the CubeSats POD with duty-cycled data was achieved. The 3D RMSE values of POD using MADOCA corrections were less than 5 cm for duty cycles ranging from 100% to 40%. This almost doubled when the SouthPAN test-bed products were used. Using the PPP corrections is even extendable to the larger LEO satellites when accessing these corrections in space. For example, applying MADOCA corrections in the kinematic POD of GARCEFO 1 and Sentinel-3B satellites delivered orbits with 5 and 7 cm accuracy, respectively. These values increased to 14 and 16 cm when the test-bed SouthPAN products were used in the POD model.

Precise navigation of CubeSats is a matter of interest when flying in a formation or a constellation. To perform the real-time CubeSat POD with the limited processing units, a software named LeoPod was developed based on sequential least-squares filtering. The last chapter explained the models used to develop this CubeSats POD software package. However, the CubeSats' limitations have negative impacts on real-time POD. Therefore, a relative POD based on using double differenced observations of the common-in-view GNSS satellites were developed to meet the power and computational expectations and reduce the impact of the receiver-dependant errors. The precise inter-satellite ranges from the reduced-dynamic orbits were used to augment the relative POD and strengthen the model. The precise ranges can be predicted and broadcasted to the CubeSats, and in the case of the between-satellite link using SDR, the relative POD can be performed onboard. The tests with the GNSS observations of nine CubeSats showed that the onboard POD with dm level of accuracy is achievable

if the baselines are less than 1000 km. The proposed solution was tested in a Raspberry Pi 4 module to mimic the onboard processing. Reaching this accuracy is a step toward augmented navigation systems for the smart formation flying or CubeSats constellation.

9.2 Recommendations and future work

Common CubeSats' limitations and their impacts on CubeSats POD were discussed in the thesis. However, CubeSats POD is an open research area that needs more investigation. CubeSats are usually equipped with space-based single-frequency GPS receivers. The availability of dual-frequency GPS receivers for the CubeSats and making use of IF observations are discussed in this thesis. However, new multi-frequency multi-constellation modules will be available for the CubeSats. Additional signals from different GNSS constellations increase the complexity of POD in both post-mission and real-time modes but may provide a good number of observations, particularly with the fast CubeSat motion and the rapid change in their geometry with GNSS satellites. Therefore, applying different positioning, navigation, and timing techniques is inevitable and require further research.

As an example, the POD based on the undifferenced uncombined methods can increase the number of observations in processing, resulting in higher impacts of the GNSS part in the reduced-dynamic POD and more information for kinematic POD. It is also possible to add some dynamic models for receiver and satellite biases to strengthen the POD model. Multi-frequency undifferenced methods can better leverage the availability of multi-frequency data to better estimate ionospheric delay parameters, which would also be helpful for some applications.

The PPP-IAR approach, which utilized corrections to the satellite phase biases to achieve integer ambiguity resolution for a single receiver, is a promising technique to improve the accuracy of CubeSats POD and needs further investigation. The availability of precise products with global coverage from, e.g., Galileo HAS service, and Fugro's SpaceStar[®] service brings the opportunity of onboard POD and needs more studies.

Another concept that needs to be studied for CubeSats is the array-aided PPP (A-PPP). Equipping CubeSats with an antenna array with known geometry would be useful for array-aided ambiguity resolution. It could improve the precision of the estimated parameters by at least two orders of magnitude for POD and allows for attitude determination using GNSS, albeit with a low accuracy due to the short baselines between the antennas. The A-PPP concept can also be extended to the differential A-PPP for the formation of CubeSats while the model is augmented with precise inter-satellite ranges. In addition to the complexity in the model for the integer ambiguity resolution, the availability of an array of antennae onboard a CubeSat is challenging. The small size of the array in

CubeSats would be another challenge in attitude determination since any slight bias in the considered short baselines between the antennas can significantly affect attitude determination.

It is recommended to equip CubeSats with SDR for the relative POD with the methods developed in this thesis and the A-PPP concept. It would enhance the number of receiving GNSS signals while providing inter-satellite communications. The FPGA of the SDR would also be helpful for some onboard processing. However, there were some instabilities in their clocks that may have negative impacts on receiving GNSS signals. Integrating SDR with chip-scale atomic clocks would be a solution to this issue.

References

This Chapter provides the references for Chapters 1, 3, and 8 only. The additional references for Chapters 2, 4-6 are listed at the end of the enclosed papers.

- Allahviridi-Zadeh, A. (2013) Evaluation of the GPS observable effects located in the earth shadow on permanent station position time series. MSc thesis, Geomatics Engineering Department, University of Isfahan. <https://doi.org/10.13140/RG.2.2.28151.32167>
- Allahviridi-Zadeh, A. (2021a). Phase centre variation of the GNSS antenna onboard the CubeSats and its impact on precise orbit determination. In: GSA Earth Sciences Students Symposium - WA (GESSS-WA), 25th Nov 2021, Perth, Western Australia, (pp 1-21). <https://doi.org/10.13140/RG.2.2.10355.45607/1>
- Allahviridi-Zadeh, A. (2021b). Software Defined Radio (SDR) as a GNSS receiver in future CubeSats. Presentation to the Binar Space Program - Innovation Central Perth, Curtin University, Western Australia (pp 1-12). <https://doi.org/10.13140/RG.2.2.28290.20166>
- Allahviridi-Zadeh, A. (2022). Shadow toolbox. figshare. Software. <https://doi.org/10.6084/m9.figshare.19085546.v1>
- Allahverdi-Zadeh, A., J. Asgari, and A. R. Amiri-Simkooei. 2016. "Investigation of GPS draconitic year effect on GPS time series of eliminated eclipsing GPS satellite data." *Journal of Geodetic Science*. 6 (1): 2016. <https://doi.org/10.1515/jogs-2016-0007>
- Allahviridi-Zadeh, A. and El-Mowafy, A. (2022). The impact of precise inter-satellite ranges on relative precise orbit determination in a smart CubeSats constellation, EGU General Assembly 2022, Vienna, Austria, 23–27 May 2022, EGU22-2215 (pp 1-18), <https://doi.org/10.5194/egusphere-egu22-2215>
- Arnold, D., Meindl, M., Beutler, G. et al. (2015). CODE's new solar radiation pressure model for GNSS orbit determination. *Journal of Geodesy* 89, (pp 775–791). <https://doi.org/10.1007/s00190-015-0814-4>
- Blanch, J., Walter, T., Enge, P., Lee, Y., Pervan, B., Rippl, M., & Spletter, A. (2012). Advanced RAIM user algorithm description: Integrity support message processing, fault detection, exclusion, and protection level calculation. In Proceedings of the 25th International Technical Meeting of The Satellite Division of the Institute of Navigation (ION GNSS 2012) (pp 2828-2849).
- El-Mowafy, A., Deo, M. & Kubo, N. (2017). Maintaining real-time precise point positioning during outages of orbit and clock corrections. *GPS Solution* 21, (pp 937–947). <https://doi.org/10.1007/s10291-016-0583-4>
- El-Mowafy, A. and Wang, K. and Allahviridi-Zadeh, A. (2022a). The potential of LEO mega-constellations in aiding GNSS to enable positioning in challenging environments. In: XXVII FIG Congress, 11-15 September 2022, Warsaw, Poland.
- El-Mowafy, A. and Wang, K. and Allahviridi-Zadeh, A. (2022b). LEO aiding GNSS positioning in challenging environments. In: XXVII FIG Congress, 11-15 September 2022, Warsaw, Poland. <https://doi.org/10.13140/RG.2.2.31587.84000>

- European Space Agency (ESA) (2019), New financial resources for Copernicus space component. https://www.esa.int/Applications/Observing_the_Earth/Copernicus/New_financial_resources_for_Copernicus_space_component (accessed on 5 July 2022)
- Foster, C., Hallam, H., & Mason, J. (2015). Orbit determination and differential-drag control of Planet Labs CubeSat constellations. arXiv preprint arXiv:1509.03270, (pp 1-13). <https://doi.org/10.48550/arXiv.1509.03270>
- Gangestad, J., Hardy, B., & Hinkley, D. (2013). Operations, orbit determination, and formation control of the AeroCube-4 CubeSats. In Small Sat Conference, 15 August 2013, (pp 1-8). <https://digitalcommons.usu.edu/smallsat/2013/all2013/116/> (accessed on 5 July 2022)
- Geoscience of Australia (GA) (2020): SouthPAN to position Australia and New Zealand into the future, <https://www.ga.gov.au/news-events/news/latest-news/southpan-to-position-australia-and-new-zealand-into-the-future> (accessed on 5 July 2022)
- Hauschild, A. (2017). Basic Observation Equations. In: Teunissen, P.J., Montenbruck, O. (eds) Springer Handbook of Global Navigation Satellite Systems. Springer Handbooks. Springer, Cham, Chapter 19 (pp 561-582). https://doi.org/10.1007/978-3-319-42928-1_19
- Jäggi, A., U. Hugentobler, and G. Beutler. (2006). Pseudo-stochastic orbit modeling techniques for low-Earth orbiters. *Journal of Geodesy* 80 (1): 47–60. <https://doi.org/10.1007/s00190-006-0029-9>.
- Jäggi, A. (2007). Pseudo-stochastic orbit modelling of Low Earth Satellites using the Global Positioning System. Geodätisch-geophysikalische Arbeiten in der Schweiz: Vol. 73. Swiss Geodetic Commission (pp 1-220). <http://www.sgc.ethz.ch/sgc-volumes/sgk-73.pdf> (accessed on 5 July 2022)
- Kahr, E., Montenbruck, O., & O’Keefe, K. P. (2013). Estimation and analysis of two-line elements for small satellites. *Journal of Spacecraft and Rockets*, 50 (2), (pp 433-439). <https://doi.org/10.2514/1.A32352>
- Kovář, P.; Puričar, P.; Kovářová, K. (2022). Study of the Two-Line Element Accuracy by 1U CubeSat with a GPS Receiver. *Sensors* 2022, 22, 2902. <https://doi.org/10.3390/s22082902>
- Li, B., Zhang, Y., Huang, J., & Sang, J. (2021). Improved orbit predictions using two-line elements through error pattern mining and transferring. *Acta Astronautica*, 188, (pp 405-415). <https://doi.org/10.1016/j.actaastro.2021.08.002>
- Mander, A., Bisnath, S. (2013). GPS-based precise orbit determination of Low Earth Orbiters with limited resources. *GPS Solutions* 17, (pp 587-5940). <https://doi.org/10.1007/s10291-012-0303-7>
- Montenbruck, O. (2017). Space Applications. In: Teunissen, P.J., Montenbruck, O. (eds) Springer Handbook of Global Navigation Satellite Systems. Springer Handbooks. Springer, Cham, Chapter 32 (pp 933-964). https://doi.org/10.1007/978-3-319-42928-1_32
- Omar, S., Guglielmo, D., Mauro, G. D., Martin, T., & Bevilacqua, R. (2018). CubeSat mission to demonstrate aerodynamically controlled re-entry using the drag de-orbit device (D3). <https://digitalcommons.usu.edu/smallsat/2018/all2018/335/> (accessed on 21 July 2022)
- Petit, G., & Luzum, B. (2010). IERS conventions (technical note, 36). <https://iers-conventions.obspm.fr/content/tn36.pdf> (accessed on 5 July 2022)

- Roscoe, C. W., Westphal, J. J., & Mosleh, E. (2018). Overview and GNC design of the CubeSat Proximity Operations Demonstration (CPOD) mission. *Acta Astronautica* 153, (pp 410-421). <https://doi.org/10.1016/j.actaastro.2018.03.033>
- San-Juan, J. F., Pérez, I., San-Martín, M., & Vergara, E. P. (2017). Hybrid SGP4 orbit propagator. *Acta Astronautica* 137, (pp 254-260). <https://doi.org/10.1016/j.actaastro.2017.04.015>
- Smith, M. (2018). Nasa's GRACE-FO, Five Iridium Satellites Share A Ride To Space, Spacepolicyonline.com. <https://spacepolicyonline.com/news/nasas-grace-fo-five-iridium-satellites-share-a-ride-to-space/> (accessed on 5 July 2022)
- Teunissen, Peter. (2000). Adjustment theory: an introduction. Series on Mathematical Geodesy and Positioning. VSSD Press. Delft, Netherlands.
- Vallado, D., & Crawford, P. (2008). SGP4 orbit determination. In AIAA/AAS Astrodynamics Specialist Conference and Exhibit (p. 6770). <https://doi.org/10.2514/6.2008-6770>
- Vidal-Valladares, M. G., & Díaz, M. A. (2022). A Femto-Satellite Localization Method Based on TDOA and AOA Using Two CubeSats. *Remote Sensing* 14(5), 1101. <https://doi.org/10.3390/rs14051101>
- Wang, K., Allahviridi-Zadeh, A., El-Mowafy, A., Gross, J.N. (2020). A Sensitivity Study of POD Using Dual-Frequency GPS for CubeSats Data Limitation and Resources. *Remote Sensing* 2020, 12, 2107. <https://doi.org/10.3390/rs12132107>
- Wesam, E. M., Zhang, X., Lu, Z., & Liao, W. (2017). Kalman filter implementation for small satellites using constraint GPS data. In IOP Conference Series: Materials Science and Engineering. IOP Publishing 211 (1), (p. 012015). <https://doi.org/10.1088/1757-899X/211/1/012015>
- Yen, N. (2014). Status and Aims of the FORMOSAT-7/COSMIC-2 Mission. Available online: <https://www.ecmwf.int/node/13747> (accessed on 5 July 2022)
- Zhang, K., Li, X., Wu, J., Yuan, Y., Li, X., Zhang, X., & Zhang, W. (2021). Precise orbit determination for LEO satellites with ambiguity resolution: Improvement and comparison. *Journal of Geophysical Research: Solid Earth*, 126, e2021JB022491. <https://doi.org/10.1029/2021JB022491>
- Zhou, F., Dong, D., Li, W., Jiang, X., Wickert, J., & Schuh, H. (2018). GAMP: An open-source software of multi-GNSS precise point positioning using undifferenced and uncombined observations. *GPS Solutions* 22(2), (pp 1-10). <https://doi.org/10.1007/s10291-018-0699-9>

Every reasonable effort has been made to acknowledge the owners of copyright material. I would be pleased to hear from any copyright owner who has been omitted or incorrectly acknowledged."

Appendix A: Copyright Permission Statements

I have obtained, where necessary, permission from the copyright owners to use any third-party copyright material reproduced in the thesis or to use any of my own published work (e.g., journal articles) in which the copyright is held by another party (e.g., publisher, co-author). The permissions are all provided below.

Amir Allahvirdizadeh

The permission for the following **Springer** publication is attached in the forthcoming pages:

- Allahviridi-Zadeh, A., Wang, K., & El-Mowafy, A. (2021). POD of small LEO satellites based on precise real-time MADOCA and SBAS-aided PPP corrections. *GPS solutions*, 25(2), 1-14. DOI: 10.1007/s10291-020-01078-8

05/07/2022, 09:05

RightsLink Printable License

SPRINGER NATURE LICENSE
TERMS AND CONDITIONS

Jul 04, 2022

This Agreement between Curtin University -- Curtin Allahviridi-Zadeh ("You") and Springer Nature ("Springer Nature") consists of your license details and the terms and conditions provided by Springer Nature and Copyright Clearance Center.

License Number 5342210919131

License date Jul 04, 2022

Licensed Content
Publisher Springer Nature

Licensed Content
Publication GPS Solutions

Licensed Content Title POD of small LEO satellites based on precise real-time
MADOCA and SBAS-aided PPP corrections

Licensed Content Author Amir Allahviridi-Zadeh et al

Licensed Content Date Jan 11, 2021

<https://s100.copyright.com/AppDispatchServlet>

1/7

05/07/2022, 09:05

RightsLink Printable License

Type of Use Thesis/Dissertation

Requestor type academic/university or research institute

Format electronic

Portion full article/chapter

Will you be translating? no

Circulation/distribution 50000 or greater

Author of this Springer
Nature content yes

Title PhD Thesis and posting the thesis in Curtin's repository

Institution name Curtin University

Expected presentation
date Jul 2022

Requestor Location Curtin University
GPO Box U 1987 WA

Perth, WA 6845
Australia
Attn: Curtin University

<https://s100.copyright.com/AppDispatchServlet>

2/7

05/07/2022, 09:05

RightsLink Printable License

Total 0.00 AUD

Terms and Conditions

Springer Nature Customer Service Centre GmbH Terms and Conditions

This agreement sets out the terms and conditions of the licence (the **Licence**) between you and **Springer Nature Customer Service Centre GmbH** (the **Licensor**). By clicking 'accept' and completing the transaction for the material (**Licensed Material**), you also confirm your acceptance of these terms and conditions.

1. Grant of Licence

- 1.1. The Licensor grants you a personal, non-exclusive, non-transferable, world-wide licence to reproduce the Licensed Material for the purpose specified in your order only. Licences are granted for the specific use requested in the order and for no other use, subject to the conditions below.
- 1.2. The Licensor warrants that it has, to the best of its knowledge, the rights to license reuse of the Licensed Material. However, you should ensure that the material you are requesting is original to the Licensor and does not carry the copyright of another entity (as credited in the published version).
- 1.3. If the credit line on any part of the material you have requested indicates that it was reprinted or adapted with permission from another source, then you should also seek permission from that source to reuse the material.

2. Scope of Licence

- 2.1. You may only use the Licensed Content in the manner and to the extent permitted by these Ts&Cs and any applicable laws.
- 2.2. A separate licence may be required for any additional use of the Licensed Material, e.g. where a licence has been purchased for print only use, separate permission must be obtained for electronic re-use. Similarly, a licence is only valid in

<https://s100.copyright.com/AppDispatchServlet>

3/7

05/07/2022, 09:05

RightsLink Printable License

the language selected and does not apply for editions in other languages unless additional translation rights have been granted separately in the licence. Any content owned by third parties are expressly excluded from the licence.

- 2.3. Similarly, rights for additional components such as custom editions and derivatives require additional permission and may be subject to an additional fee. Please apply to Journalpermissions@springernature.com/bookpermissions@springernature.com for these rights.
- 2.4. Where permission has been granted **free of charge** for material in print, permission may also be granted for any electronic version of that work, provided that the material is incidental to your work as a whole and that the electronic version is essentially equivalent to, or substitutes for, the print version.
- 2.5. An alternative scope of licence may apply to signatories of the [STM Permissions Guidelines](#), as amended from time to time.

3. Duration of Licence

- 3.1. A licence for is valid from the date of purchase ('Licence Date') at the end of the relevant period in the below table:

| Scope of Licence | Duration of Licence |
|--------------------|---|
| Post on a website | 12 months |
| Presentations | 12 months |
| Books and journals | Lifetime of the edition in the language purchased |

4. Acknowledgement

- 4.1. The Licensor's permission must be acknowledged next to the Licensed Material in print. In electronic form, this acknowledgement must be visible at the same time as the figures/tables/illustrations or abstract, and must be hyperlinked to the journal/book's homepage. Our required acknowledgement format is in the Appendix below.

<https://s100.copyright.com/AppDispatchServlet>

4/7

5. Restrictions on use

5. 1. Use of the Licensed Material may be permitted for incidental promotional use and minor editing privileges e.g. minor adaptations of single figures, changes of format, colour and/or style where the adaptation is credited as set out in Appendix 1 below. Any other changes including but not limited to, cropping, adapting, omitting material that affect the meaning, intention or moral rights of the author are strictly prohibited.
5. 2. You must not use any Licensed Material as part of any design or trademark.
5. 3. Licensed Material may be used in Open Access Publications (OAP) before publication by Springer Nature, but any Licensed Material must be removed from OAP sites prior to final publication.

6. Ownership of Rights

6. 1. Licensed Material remains the property of either Licensor or the relevant third party and any rights not explicitly granted herein are expressly reserved.

7. Warranty

IN NO EVENT SHALL LICENSOR BE LIABLE TO YOU OR ANY OTHER PARTY OR ANY OTHER PERSON OR FOR ANY SPECIAL, CONSEQUENTIAL, INCIDENTAL OR INDIRECT DAMAGES, HOWEVER CAUSED, ARISING OUT OF OR IN CONNECTION WITH THE DOWNLOADING, VIEWING OR USE OF THE MATERIALS REGARDLESS OF THE FORM OF ACTION, WHETHER FOR BREACH OF CONTRACT, BREACH OF WARRANTY, TORT, NEGLIGENCE, INFRINGEMENT OR OTHERWISE (INCLUDING, WITHOUT LIMITATION, DAMAGES BASED ON LOSS OF PROFITS, DATA, FILES, USE, BUSINESS OPPORTUNITY OR CLAIMS OF THIRD PARTIES), AND WHETHER OR NOT THE PARTY HAS BEEN ADVISED OF THE POSSIBILITY OF SUCH DAMAGES. THIS LIMITATION SHALL APPLY NOTWITHSTANDING ANY FAILURE OF ESSENTIAL PURPOSE OF ANY LIMITED REMEDY PROVIDED

HEREIN.

8. Limitations

8. 1. **BOOKS ONLY:** Where 'reuse in a dissertation/thesis' has been selected the following terms apply: Print rights of the final author's accepted manuscript (for clarity, NOT the published version) for up to 100 copies, electronic rights for use only on a personal website or institutional repository as defined by the Sherpa guideline (www.sherpa.ac.uk/romeo/).
8. 2. For content reuse requests that qualify for permission under the [STM Permissions Guidelines](#), which may be updated from time to time, the STM Permissions Guidelines supersede the terms and conditions contained in this licence.

9. Termination and Cancellation

9. 1. Licences will expire after the period shown in Clause 3 (above).
9. 2. Licensee reserves the right to terminate the Licence in the event that payment is not received in full or if there has been a breach of this agreement by you.

Appendix 1 — Acknowledgements:

For Journal Content:

Reprinted by permission from [the Licensor]: [Journal Publisher (e.g. Nature/Springer/Palgrave)] [JOURNAL NAME] [REFERENCE CITATION (Article name, Author(s) Name), [COPYRIGHT] (year of publication)]

For Advance Online Publication papers:

Reprinted by permission from [the Licensor]: [Journal Publisher (e.g. Nature/Springer/Palgrave)] [JOURNAL NAME] [REFERENCE CITATION (Article name, Author(s) Name), [COPYRIGHT] (year of publication), advance online publication, day month year (doi: 10.1038/sj.[JOURNAL ACRONYM].)]

For Adaptations/Translations:

Adapted/Translated by permission from [the Licensor]: [Journal Publisher (e.g. Nature/Springer/Palgrave)] [JOURNAL NAME] [REFERENCE CITATION (Article name, Author(s) Name), [COPYRIGHT] (year of publication)]

Note: For any republication from the British Journal of Cancer, the following credit line style applies:

Reprinted/adapted/translated by permission from [the Licensor]: on behalf of Cancer Research UK: : [Journal Publisher (e.g. Nature/Springer/Palgrave)] [JOURNAL NAME] [REFERENCE CITATION (Article name, Author(s) Name), [COPYRIGHT] (year of publication)]

For Advance Online Publication papers:

Reprinted by permission from The [the Licensor]: on behalf of Cancer Research UK: [Journal Publisher (e.g. Nature/Springer/Palgrave)] [JOURNAL NAME] [REFERENCE CITATION (Article name, Author(s) Name), [COPYRIGHT] (year of publication), advance online publication, day month year (doi: 10.1038/sj. [JOURNAL ACRONYM])]

For Book content:

Reprinted/adapted by permission from [the Licensor]: [Book Publisher (e.g. Palgrave Macmillan, Springer etc) [Book Title] by [Book author(s)] [COPYRIGHT] (year of publication)]

Other Conditions:

Version 1.3

Questions? customercare@copyright.com or +1-855-239-3415 (toll free in the US) or +1-978-646-2777.

The following papers are published in **MDPI Remote Sensing** under the open access licence provided in the quotes below. All articles published by MDPI are immediately available worldwide under an open-access license. No special permission is required to reuse all or part of the article published by MDPI, authored or co-authored by me, including figures and tables. Any part of the article may be reused without permission for articles published under an open-access Creative Commons CC BY license, provided that the original article is clearly cited. Permission for the MDPI publication can be found at <http://www.mdpi.com/about/openaccess>

Papers:

- Wang, K., Allahviridi-Zadeh, A., El-Mowafy, A., & Gross, J. N. (2020). A sensitivity study of POD using dual-frequency GPS for CubeSats data limitation and resources. *Remote Sensing*, 12(13), 2107. DOI: 10.3390/rs12132107

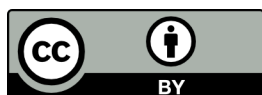
Attribution:



Copyright: © 2020 by the authors. Licensee MDPI, Basel, Switzerland. This article is an open-access article distributed under the terms and conditions of the Creative Commons Attribution (CC BY) license (<http://creativecommons.org/licenses/by/4.0/>).

- Allahviridi-Zadeh, A., Awange, J., El-Mowafy, A., Ding, T., & Wang, K. (2022). Stability of CubeSat Clocks and Their Impacts on GNSS Radio Occultation. *Remote Sensing*, 14(2), 362. DOI: 10.3390/rs14020362

Attribution:



Copyright: © 2022 by the authors. Licensee MDPI, Basel, Switzerland. This article is an open-access article distributed under the terms and conditions of the Creative Commons Attribution (CC BY) license (<https://creativecommons.org/licenses/by/4.0/>).

The following paper is published in the **ASCE Journal of Surveying Engineering** under the open-access licence provided below. The CC BY license allows authors to retain copyright but licenses the use of the article to ASCE as the publisher. Others may use all or portions of the paper's content without seeking permission from the ASCE or the author. Any such use must contain an attribution to the original author.

- Allahviridi-Zadeh, A., Wang, K., & El-Mowafy, A. (2022). Precise Orbit Determination of LEO Satellites Based on Undifferenced GNSS Observations. *Journal of surveying engineering*, 148(1), 03121001. DOI: 10.1061/(ASCE)SU.1943-5428.0000382

Attribution:

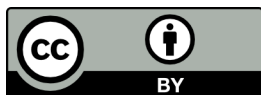


This work is made available under the terms of the Creative Commons Attribution 4.0 International license, <https://creativecommons.org/licenses/by/4.0/>

The following paper is published in **Springer International Association of Geodesy Symposia** under the open access licence provided below.

El-Mowafy, A., Wang, K. (2022). Precise Orbit Determination of CubeSats Using Proposed Observations Weighting Model. In: International Association of Geodesy Symposia. Springer, Berlin, Heidelberg. DOI: 10.1007/1345_2022_160

Attribution:



This work is made available under the terms of the Creative Commons Attribution 4.0 International license, <https://creativecommons.org/licenses/by/4.0/>

Appendix B: Statement of Contributions by Co-Authors

This thesis presents 4 first-author and 1 second-author papers that are published in journals. The authors' contributions to these papers are provided in this appendix.

I, Amir Allahvirdizadeh, wrote the manuscript, derived the analytical expressions and provide the numerical results. In the case of co-authorship, Prof. Ahmed El-Mowafy and Prof. Kan Wang provided their comments to improve the manuscripts for submission. *All the above holds for the following publications:*

- 1- Allahviridi-Zadeh, A., Wang, K., & El-Mowafy, A. (2022). Precise Orbit Determination of LEO Satellites Based on Undifferenced GNSS Observations. *Journal of surveying engineering*, 148(1), 03121001. DOI: 10.1061/(ASCE)SU.1943-5428.0000382
- 2- Allahviridi-Zadeh, A., Wang, K., & El-Mowafy, A. (2021). POD of small LEO satellites based on precise real-time MADOCA and SBAS-aided PPP corrections. *GPS solutions*, 25(2), 1-14. DOI: 10.1007/s10291-020-01078-8
- 3- Allahviridi-Zadeh, A., El-Mowafy, Wang, K. (2022). Precise Orbit Determination of CubeSats Using Proposed Observations Weighting Model. *International Association of Geodesy Symposia*, Springer (accepted)

Amir Allahvirdizadeh _____

I, as a Co-Author, endorse that this level of contributions by the candidate indicated above is appropriate.

Ahmed El-Mowafy _____

Kan Wang _____

For the following paper, I, Amir Allahvirdizadeh, designed the work by consulting Prof. Ahmed El-Mowafy and Prof. Joseph Awange. I processed and analysed the CubeSats clocks. Mr Tong Ding processed the GNSS-RO profiles and I and Prof. Joseph Awange analysed them. I wrote the manuscript and Prof. Joseph Awange, Prof. Ahmed El-Mowafy and Prof. Kan Wang provided their comments to improve the manuscripts for submission.

- 4- Allahviridi-Zadeh, A., Awange, J., El-Mowafy, A., Ding, T., & Wang, K. (2022). Stability of CubeSat Clocks and Their Impacts on GNSS Radio Occultation. *Remote Sensing*, 14(2), 362. DOI: 10.3390/rs14020362.

Amir Allahvirdizadeh _____

I, as a Co-Author, endorse that this level of contributions by the candidate indicated above is appropriate.

Joseph Awange _____

Ahmed El-Mowafy _____

Tong Ding _____

Kan Wang _____

For the following paper, Prof. Kan Wang and Prof. Ahmed El-Mowafy designed the work. Prof. Kan Wang and I, Amir Allahvirdizadeh, contributed to the data processing analyses. All authors contributed to the writing of the paper.

- 5- Wang, K., Allahvirdi-Zadeh, A., El-Mowafy, A., & Gross, J. N. (2020). A sensitivity study of POD using dual-frequency GPS for CubeSats data limitation and resources. *Remote Sensing*, 12(13), 2107. DOI: 10.3390/rs12132107

Amir Allahvirdizadeh _____

I, as a Co-Author, endorse that this level of contributions by the candidate indicated above is appropriate.

Kan Wang _____

Ahmed El-Mowafy _____

Jason N. Gross _____

Appendix C: Proof of Peer-Reviewed and Accepted Publications

Provided below is the proof that the following conference paper is peer-reviewed and published in the International Association of Geodesy Symposia:

- Allahviridi-Zadeh, A., El-Mowafy, A., Wang, K. (2022). Precise Orbit Determination of CubeSats Using Proposed Observations Weighting Model. In: International Association of Geodesy Symposia. Springer, Berlin, Heidelberg. DOI: 10.1007/1345_2022_160

From: em.iags.2ac0.7afb0e.7e93235c@editorialmanager.com on behalf of [Jeff Freymueller](#)
To: [Amir Allahvirdizadeh](#)
Subject: IAGS: Your manuscript entitled Precise Orbit Determination of CubeSats Using Proposed Observations Weighting Model
Date: Friday, 29 April 2022 9:13:08 PM

Ref.:

Ms. No. IAGS-D-21-00007

Precise Orbit Determination of CubeSats Using Proposed Observations Weighting Model

International Association of Geodesy Symposia

Dear Mr. Allahvirdi-Zadeh,

I am pleased to inform you that your work has now been accepted for publication in International Association of Geodesy Symposia.

Thank you for submitting your work to this journal.

With kind regards

Jeff Freymueller
Editor-in-Chief
International Association of Geodesy Symposia

Reviewer #1: This manuscript presents an interesting study on precise orbit determination processing dualfrequency GPS data (L1C and L2L) with an SNR-based weighting scheme. The authors focus on micro/cube satellites as their rapidly growing numbers and broad geophysical applications require developing novel methods for their orbit determination. Moreover, the well-established methods for larger LEOs may not suit these small CubeSats. Therefore, the authors propose their own weighting scheme based on SNR (eq. 1) and compare it to the classic satellite elevation-dependent one.

The validation is based on the analysis of overlapping arcs and IF residual analysis. In each case, there is a clear reduction in residuals when POD is carried out using their SNR-based weighting approach. The manuscript is well-written and easy to follow. I have no points to address; hence my recommendation is to publish this manuscript as is.

PublicationOfficeSPS@springernature.com

Recipients of this email are registered users within the Editorial Manager database for this journal. We will keep your information on file to use in the process of submitting, evaluating and publishing a manuscript. For more information on how we use your personal details please see our privacy policy at <https://www.springernature.com/production-privacy-policy>. If you no longer wish to receive messages from this journal or you have questions regarding database management, please email our publication office, stating the journal name(s) and your email address(es):

In compliance with data protection regulations, you may request that we remove your personal registration details at any time. (Use the following URL: <https://www.editorialmanager.com/iags/login.asp?a=r>). Please contact the publication office if you have any questions.